Downloaded from orbit.dtu.dk on: May 04, 2023

DTU Library

Nickel/Yttria-Stabilised Zirconia Cermet Anodes for Solid Oxide Fuel Cells

Primdahl, Søren

Publication date:
1999

Document Version
Publisher's PDF, also known as Version of record

Link back to DTU Orbit

Citation (APA):
Primdahl, S. (1999). *Nickel/Yttria-Stabilised Zirconia Cermet Anodes for Solid Oxide Fuel Cells*. Risø National Laboratory. Denmark. Forskningscenter Risoe. Risoe-R No. 1137(EN)

General rights
Copyright and moral rights for the publications made accessible in the public portal are retained by the authors and/or other copyright owners and it is a condition of accessing publications that users recognise and abide by the legal requirements associated with these rights.

- Users may download and print one copy of any publication from the public portal for the purpose of private study or research.
- You may not further distribute the material or use it for any profit-making activity or commercial gain
- You may freely distribute the URL identifying the publication in the public portal

If you believe that this document breaches copyright please contact us providing details, and we will remove access to the work immediately and investigate your claim.

NICKEL/YTTRIA-STABILISED ZIRCONIA CERMET ANODES FOR SOLID OXIDE FUEL CELLS

Søren Primdahl

Primdahl, Søren
Nickel/yttria-stabilised zirconia cermet anodes for solid oxide fuel cells

Thesis
University of Twente, Faculty of Chemical Technology, The Netherlands
and Risø National Laboratory, Materials Research Department, Denmark.

ISBN 90-36513375

Also published in Denmark by Risø National Laboratory as

Risø-R-1137(EN)
ISBN 87-550-2605-2 (internet)

NICKEL/YTTRIA-STABILISED ZIRCONIA CERMET ANODES FOR SOLID OXIDE FUEL CELLS

PROEFSCHRIFT

ter verkrijging van
de graad van doctor aan de Universiteit Twente,
op gezag van de rector magnificus,
prof.dr. F.A. van Vught,
volgens besluit van het College voor Promoties
in het openbaar te verdedigen
op vrijdag 17 september 1999 te 13.15 uur

door

Søren Primdahl
geboren op 16 juli 1967
te Skanderborg, Denemarken

Dit proefschrift is goedgekeurd door de promotor

Prof. Dr. Ir. H. Verweij

en de assistant promotor

Dr. H. J. M. Bouwmeester

Preface

Development of solid oxide fuel cells (SOFC) for applications in industry and the consumer market is a multidisciplinary challenge. The necessary reduction of cost and improvement of performance implies extensive knowledge of a complex and mainly ceramic system at elevated temperatures. This thesis deals with only a part of this system, the Ni/yttria-stabilized anode exposed to hydrogen/water mixtures.
The work described here was produced within a period of about 3 years, as part of a full time research position at Risø National Laboratory. As the conditions for a Ph.D. study in the Danish educational system was found not to comply with a full time position, an arrangement was found for this thesis to be evaluated at the University of Twente, The Netherlands. The work carried out and presented here was financed by The Danish Energy Agency and the Danish utility corporation ELSAM within the national DK-SOFC program, and by EC within the Joule II and Joule/Thermie frameworks.

I would like to express my gratitude to the entire SOFC group at Risø National Laboratory, for providing an excellent working environment both scientifically, technically and on a personal level. With a group of this size and composition, there is always a network of experience, advice and inspiration to rely on, and an expert to turn to when a new challenge is faced.
It is due to acknowledge Carsten Bagger, Mogens Mogensen and Søren Linderoth, the project leaders of the various SOFC projects I have been involved in, for providing ample challenge, freedom with responsibility, and especially for keeping me out of administration during this period.
Also a word of appraisal for colleagues at University of Twente, to Prof. Henk Verweij for engaging in this cooperation, to Henny Bouwmeester for guidance and inspiring discussions, and to Bernard Boukamp for writing the program EQUIVCRT on which most of the data interpretation is based.
I am, in particular, grateful to Mogens Mogensen, my local mentor and discussion partner, for guidance, inspiration and encouragement. Without his commitment this thesis would not have had the present quality or consistency.

Last but not least, I would like to thank my wife Annette for her patience, and also my children Katrine and Morten for having time for me, when I have taken time for them.

Søren Primdahl
Risø National Laboratory, *August 1999.*

"Having opened a can of worms,
the only way to recan them is by using a larger can"
Unknown, quite possibly a researcher

Contents

Summary **1**

1 **Introduction to Ceramic Fuel Cells** **3**
1.1 Introduction 4
1.2 Fuel Cells 4
1.3 Solid Oxide Fuel Cells 5
1.4 Materials for SOFC 7
1.5 Fabrication Techniques 9
1.6 Cell Development 10
1.7 Commercialization 12
1.8 Scope of this Thesis 12

2 **Solid Electrode Characterization** **15**
2.1 Introduction 16
2.2 Cell Geometry and Position of Reference Electrode 16
2.3 Current Collection and Polarization Resistance 18
2.4 Polarization and Ohmic Heating 20
2.5 Inductance and Impedance Spectroscopy 20
2.6 Active Electrode Thickness 21

3 **Impedance of Ni/YSZ Cermet Anodes** **23**
3.1 Introduction 24
3.2 Experimental 26
3.3 Results 28
3.4 Discussion 39
3.5 Conclusion 44

4 **Gas Conversion Impedance** **47**
4.1 Introduction 48
4.2 Experimental 49
4.3 Results and Discussion 51
4.4 Summary 59
4.5 Appendices 60

5 **Gas Diffusion Impedance** **67**
5.1 Introduction 68
5.2 Experimental 70
5.3 Results 73
5.4 Discussion 77
5.5 Conclusion 80
5.6 Appendices 81

6 **Anode Structure/Performance Relations** **85**
6.1 Introduction 86
6.2 Experimental 88
6.3 Results 90
6.4 Discussion 98
6.5 Conclusion 105

7 **Effect of Sintering Temperature on Anode Performance and Cell Strength** **109**
7.1 Introduction 110
7.2 Experimental Procedure 111
7.3 Results 112
7.4 Discussion 121
7.5 Conclusion 124

8 **Indications of the Electrode Reaction Limitations** **127**
8.1 Introduction 128
8.2 Experimental 128
8.3 Results 130
8.4 Discussion 134
8.5 Conclusion 136

9 **Durability and Thermal Cycling** **139**
9.1 Introduction 140
9.2 Experimental 142
9.3 Results 146
9.4 Discussion 156
9.5 Summary 160

10 **A Review on the H_2/H_2O/Ni/YSZ Electrode** **163**
10.1 Introduction 164
10.2 The Reaction Sites 164
10.3 Electrochemical Evidence 173
10.4 Cermet Technology 183

11 **Evaluation and Recommendations** **195**
11.1 Evaluation of Thesis Results 196
11.2 Recommendations 199

Summary

This thesis deals with the porous Ni/yttria-stabilized zirconia (YSZ) cermet anode on a YSZ electrolyte for solid oxide fuel cells (SOFC). Such anodes are predominantly operated in moist hydrogen at 700°C to 1000°C, and the most important technological parameters are the polarization resistance and the long-term stability.

The polarization resistance can be measured by a number of techniques, in the present work impedance spectroscopy has been used extensively. By impedance spectroscopy limiting processes in the anode polarization resistance may often be separated and characterized individually, provided they have a reasonable separation in time constants.

Three limiting processes are recognized in impedance spectra obtained on technological Ni/YSZ cermet anodes characterized against a stable reference electrode atmosphere. By parameter studies and illustrative experiments, the two contributions at low and medium frequency have been identified as gas conversion and diffusion limitations, respectively. Both of these effects are concentration limitations relating to the inefficient exchange of fuel gas in the test setup outside the porous cermet. A test setup geometry where these concentration effects are avoided for high-performance electrodes is recommended.

The high frequency limitation is demonstrated to relate to the cermet structure. The dependence on gas composition, temperature, adsorbed species (sulfur), isotopes (H/D), sintering temperature and cermet thickness is investigated. Despite these studies and several similar studies by others, the exact chemical or physical nature of the limiting step has not been incontestably identified. However, there is a general consensus in literature about the hydrogen oxidation process taking place on or near to the triple phase boundary (TPB) line, where open gas-filled pores, the continuous electrolyte phase (oxide ion conductor) and the continuous Ni phase (electronic conductor) meet.

The physical thickness of a cermet anode that contains active TPB sites contributing to the current density of an SOFC is demonstrated to be about 10 μm. This result has technological importance, as any overlying structure serves primarily as a current collector and needs not be optimized for transport of oxide ions.

The anode durability is investigated over 1300 to 1900 hrs at 300 mA/cm^2 and shown to be stable at 1050°C. At 1000°C a degradation rate of about 10 mΩcm^2/1000 hrs is observed, and at 850°C a degradation rate of about 100 mΩcm^2/1000 hrs is found. The degradation during thermal cycling from 1000°C to below 100°C is demonstrated to be negligible after a 30 mΩcm^2 loss of performance over the first 2 cycles.

By adding Mn to the Ni/YSZ cermet anode the polarization resistance is reduced by a factor of 2, yielding down to 60 and 30 mΩcm^2 in hydrogen with 3% water at 850°C and 1000°C, respectively.

Chapter 1

Introduction to Ceramic Fuel Cells[†]

Abstract

Fuel cells are considered one of the most promising assets of the future for highly effective conversion of fossil fuels into electricity and heat with a minimum of pollution. This chapter gives an introduction to fuel cells, in particular solid oxide fuel cells, which are studied intensively at Risø. The basic design of the cell, choice of materials and production techniques are presented. The complexity of the development task is illustrated by selected case stories.

[†] This chapter has been published in danish as S. Primdahl and M. J. Jørgensen, "Introduktion til Keramiske Brændselsceller", *J. Danish Ceram. Soc*. **2** 13-20 (1999)

1.1 Introduction

A reappearing problem in man's administration of natural energy resources is conversion from available to usable form. In particular, this concerns the conversion of chemical energy in the form of fossil resources and derivatives such as hydrogen and alcohols, into electrical energy. Partly due to industrialization and technological progress, it has become increasingly important to reduce the losses associated with the applied conversion techniques. Traditional conversion to electrical energy or propulsion is by combustion in combination with a generator or using a combustion engine, where the Carnot-cycle sets a limit to the efficiency. A fuel cell operating as a sort of continuously replenished battery provides an alternative, whereby electrical energy can be made available with small losses. If the fuel is clean, the effluents are in principle only water, heat and CO_2. Fuel cell plants can be modular in design, and the energy production can be adjusted to meet the actual demand, which is a convenient feature for a power source in a technological society.
The practical discovery of the fuel cell is often ascribed to Sir William Grove,[1] demonstrating the reversibility of electrolytic water-splitting in 1839. However, the very same discovery was reported by Sir Humphrey Dawy as early as 1802.[2] In 1899 Nernst contributed by demonstrating that certain oxides attained remarkably high electrical conductivity by doping with other oxides.[3] In the middle of this century the development accelerated. Several types of fuel cells were developed in the global race for conquering space. In the eighties focus on pollution and the demand for higher efficiency in the exploitation of fossil resources initiated a new wave of fuel cell developments. At present several types of fuel cells are approaching the consumer market within a limited number of years. The primary challenges are cost and durability, to be solved by materials selection and design engineering.

1.2 Fuel Cells

Today 5 types of fuel cells are commonly known, all named after the electrolyte material. Each type of fuel cell has certain characteristics, some of which are listed in Table 1.1. Among these are operation temperature, electric efficiency and demands for fuel composition defining the prospects of each type.

Table 1.1 The most important characteristics for five common types of fuel cells.

Name[1]	Alcaline FC	Solid Polymer Proton Conductor FC	Phosphoric Acid FC	Molten Carbonate FC	Solid Oxide FC
Abbreviation	AFC	SPFC/PEMFC[2]	PAFC	MCFC	SOFC
Electrolyte	KOH	Polymer	H_3PO_4	62% Li_2CO_3 + 38% K_2CO_3	$ZrO_2 + Y_2O_3$
Charge carrier	OH^-	H^+	H^+	CO_3^{2-}	O^{2-}
Fuel	Highly pure H_2	Pure H_2, (EtOH)[3]	CO-free H_2	H_2, CH_4, CO	H_2, CH_4, CO
Operation Temperature	80°C	80-260°C	200°C	650°C	800-1000°C
Electrical efficiency[3]	40%	40%	40%	60%	60%

[1] FC = fuel cell. [2] Polymer Electrolyte Membrane FC or Direct Methanol FC with methanol as fuel. [3] Compared with higher heating value for Methane.

Low temperature fuel cells (AFC, SPFC and PAFC) have a potential for propulsion of cars, where a short heating time is needed and the efficiency has to be compared with about 20% for a combustion engine.
High temperature fuel cells (MCFC and SOFC) are suitable for continuous power/heat production, where the cell temperature can be maintained. These types of cells in combination with a gas turbine can reach a total efficiency a factor of 2 higher than a coal-based power plant.[4]
In general the high temperature fuel cells exhibit higher efficiency and are less sensitive to fuel composition than low temperature fuel cells. At higher temperatures natural gas can be applied directly as a fuel. In some cases this will, however, require some level of catalyzed reforming, where higher hydrocarbons are decomposed and part of the CH_4 is converted into H_2, CO and CO_2.

An unfortunate property of the MCFC is that the presence of a molten alkaline salt poses considerable problems with corrosion and creep (transport by wetting metallic surfaces), and the risk of contaminating an internal reforming catalyst.
Based on these characteristics of the various types of fuel cells, the Danish Department of Energy concentrated the public funds for fuel cell research in a national research program dealing with SOFC in the late eighties. Since 1989 Risø National Laboratory, Haldor Topsøe A/S, IRD A/S (earlier Innovision A/S) and institutes at The Technical University of Denmark and The University of Odense have been cooperating in the Danish DK-SOFC program. The overall aim has been to achieve a Danish production of a SOFC, alternatively to obtain know-how to ensure a Danish participation in production of parts therefor. Simultaneously the participants have been involved in a number of international cooperations with industry and research organizations worldwide.

1.3 Solid Oxide Fuel Cells

1.3.1 Principle of Operation

The operating principle of the solid oxide fuel cell is illustrated in Figure 1.1. An electrolyte membrane is provided with two electrodes, exposed to air and hydrogen, respectively. The difference in oxygen activity of the two gases at the electrodes provides a driving force for motion of the oxide ions in the electrolyte. Oxide ions formed by dissociation of oxygen at the cathode under electron consumption migrate through the electrolyte to the anode, where they react with hydrogen to form water and release the electrons.

The electrochemical reactions occur in the electrodes within a distance of less than 10-20 μm from the electrolyte surface.[5,6] This zone is referred to as the functional layer. The part of the electrode exceeding this thickness is primarily a current collector structure, which must be porous to allow gas access to the functional layer. The electrolyte has to be gas impermeable to avoid direct mixing and combustion of the gases. The electrolyte is ceramic, and the electrodes are often based on ceramic materials. The cell produces current as long as the reactants (fresh gases) are provided to the electrodes. An open voltage of about 1 volt is attained when the cell is not loaded, defined by the Nernst potential of the different activity of oxygen on the electrodes. Therefore the cells must be connected in series in a stack to reach higher voltages necessary for most practical purposes. A stack can in principle comprise any number of cells depending on the desired power, and a fuel cell plant can be designed in modules of stacks in series- and parallel connections.

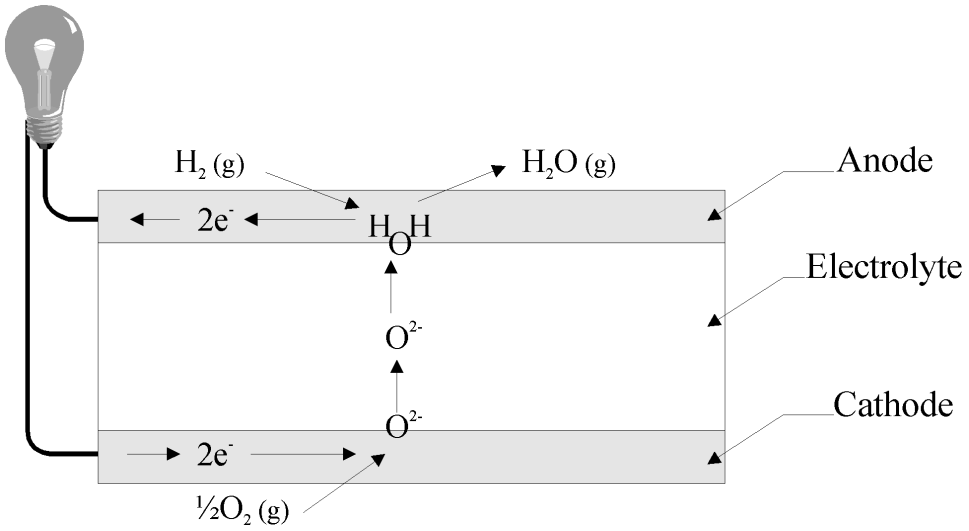

Figure 1.1 Sketch of solid oxide fuel cell operated on hydrogen and air.

An SOFC can be operated as an electrolyzer. By applying a current, water can be split to hydrogen as an energy carrier on the cathode side, and purified oxygen on the anode side. Unsteady power supplies such as wind turbines can be coupled with an electrolyzer to provide storage of energy as hydrogen, which can later be released when the need arises by operating the electrolyzer as an SOFC. Furthermore an SOFC has advantages in the wood and paper industry where the fuel can be established by gasification of waste products, for operating electrolyzer plants requiring DC with high current and low voltage, and for cathodic protection against corrosion. In the personal-transport sector the high temperature makes SOFC less appealing than SPFC, but for larger units such as trains and ships, SOFC may prove advantageous.

1.3.2 Stack Design

An SOFC stack can be established in a number of ways.[7] As cells are typically flat or tubular, two principal examples are given in Figure 1.2. A common feature of SOFC stacks is that a dense interconnect must be applied to ensure electric connections between cells and to separate the oxidizing and reducing gases between cells.
Apart from this, there are a number of principal differences of the two stacks presented. Planar cells are characterized by a need for sealing at operation temperature along the cell edges of both electrodes, to avoid direct gas mixing. Additionally gas manifolds are needed around the stack, and a channel structure must be incorporated in the interconnect surface to allow for gas access to the electrodes without significant pressure losses. The major advantages of the planar design are a low component volume and the short current path perpendicular to the cell plane, with very little in-plane current transport. The latter will potentially lead to low ohmic losses in the stack.
If fuel cells are to be operated as electrolyzers, the demands to sealing are high. If the SOFC is to be operated in combined electricity/heat devices, a certain level of direct gas mixing and burning can be accepted, provided that it does not happen in direct contact with the cells.
Tubular cells are operated with one gas inside and the other gas outside the porous tubes. The tubular design offers an advantage in fabrication size of each component, and the gases are readily kept separated up to the point of exhaust from the cells. At the same time the tubes can be prolonged out of the hot active zone to temperatures where seals and manifolds can be made from conventional materials. The disadvantage of the tubular design is the long current path in-plane through a cell, as only one point on the cell perimeter is in contact with the next cell. This leads to a critical role of the in-plane conductivity of the electrodes.

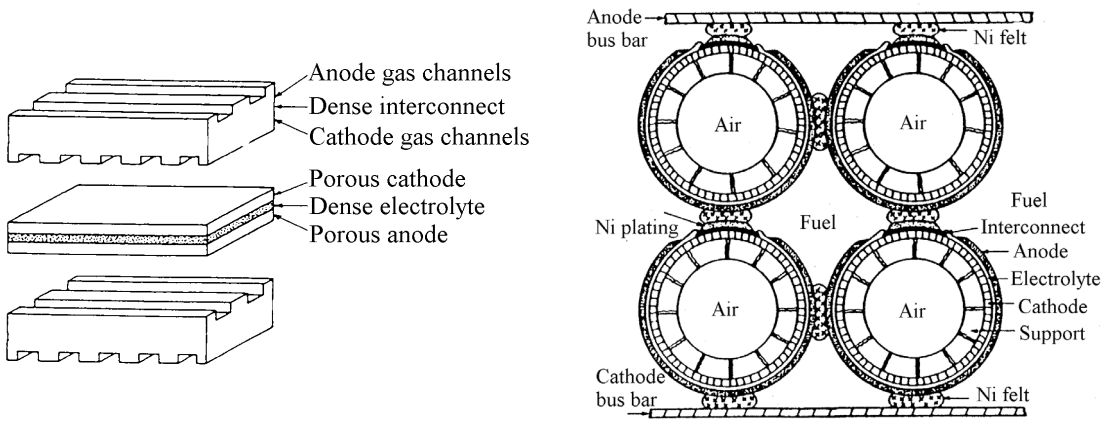

Figure 1.2 Sketch of two principal SOFC stack designs. Left: early planar design. Right: early tubular design.[7]

1.3.3 Efficiency

The electrical efficiency of a fuel cell can be defined in a number of ways, making comparison difficult.[8] A good indicator for cell performance is the area-specific internal resistance $R_{i,cell}$, at given conditions (temperature, current load, gas composition and gas utilization). $R_{i,cell}$ includes ionic resistance in the electrolyte, electronic resistance in the electrodes, and the reaction resistance in the anode and the cathode. It is a condition for comparison of cell results that the cells are contacted in the same way, as the in-plane electronic resistance in the electrodes can depend significantly on the distance between points of contact.
In the same way an area-specific internal stack resistance $R_{i,stack}$ can be defined. It comprises $R_{i,cell}$, electronic resistance in the interconnects and the contact resistance between electrodes and interconnects. $R_{i,stack}$ can be determined experimentally for "stacks" with only one cell, to yield a realistic estimate of the expected resistance obtained by scale-up.
$R_{i,stack}$ is a very important parameter during development, as an evaluation of the technology will often be based on cost per produced effect. If the resistance can be brought 30% down by a 10% more expensive selection of parameters or materials, the cost per kW is reduced by a factor of (100+10)%/(100-30)%=1.6.

1.4 Materials for SOFC

The selection of materials for SOFC is complicated by the high temperatures of sintering and operation, and the fact that most components are in contact with a number of other materials. Ceramics are primarily selected, based on functionality, compatibility and cost.

1.4.1 Functionality

The primary functional parameters are conductivity, catalytic properties and temperatures of stability and sintering. For instance the electrolyte must exhibit significant ionic conductivity and negligible electronic conductivity. For the interconnect the opposite qualities are favored. Both materials must be able to sinter to high density to avoid gas mixing. The electrodes must exhibit high electrocatalytic activity for the desired reactions, and good conductivity for both ions and electrons. In case direct oxidation of e.g. methane is not efficient, the anode should

preferably be a catalyst for methane reforming. The mixed conductivity is often obtained by applying a composite of two materials with each their dominant conductivity. Manifolds and glass seals must be able to densify by sintering, and exhibit no conductivity.

1.4.2 Compatibility

The compatibility of materials is essential to ensure reliable operation for thousands of hours at high temperature.[9]
Solid-solid reactions are an explicit problem during sintering of monolithic (materials sintered into one piece) stack components. The allowable sintering temperature is determined considering the formation of reaction products with undesirable properties on the interfaces, and the minimization of diffusion to maintain the properties of the pure materials.
Certain demands to compatibility of thermal expansion coefficient (TEC) for monolithic stack components and components sharing glass seals are set to maintain physical and electrical contact. Assuming that materials in a monolith are stress free at the maximum sintering temperature, the material exhibiting the higher TEC will experience tensile stress upon cooling. The magnitude of the tension is proportional to the change of temperature and the difference in TEC.[10]

Stability of materials towards the atmosphere can be a problem as most materials are sensitive to the oxygen partial pressure at higher temperatures. A number of components are exposed to more than one atmosphere during sintering and operation. In principle materials forming more than one phase within the oxygen partial pressures considered should be avoided. However, this criterion is not sufficient, as some ceramic materials can change their oxygen stoichiometry and molar volume, when the oxygen partial pressure of the atmosphere is changed.[11]

1.4.3 Cost

The cost of individual components is primarily governed by component volume, need for processing, required purity of the material and the general availability of the material on the market. It is evident that components should be made thin and from cheaper materials, or be replaced in part by components of a cheaper material.[12] Savings can also be found by accepting natural contaminants in raw materials where these will not reduce performance.

1.4.4 Choice of Materials

As a consequence of the above demands, the list of materials used actively at Risø for SOFC construction in Table 1.2 is fairly short. A number of alternative materials are investigated in literature and applied by other companies. A common feature of the ceramic SOFC materials is doping of pure oxides to obtain the required properties regarding conductivity and TEC.[11] Some materials are only applicable under certain conditions and with certain other materials, and new materials are still searched for.

Table 1.2 List of materials used in SOFC development at Risø.

	Chemical composition	Abbreviation	Comments
Electrolyte	$(ZrO_2)_{1-x}(Y_2O_3)_x$	YSZ	classic
	$(ZrO_2)_{1-x-z}(Y_2O_3)_x(Sc_2O_3)_z$	ScYSZ	better conductivity
Cathode	$La_{1-x}Sr_xMn_yO_{3\pm\delta}$/YSZ composite	LSM/YSZ	classic
	$Ln_{1-x}Sr_xMn_yO_{3\pm\delta}$/YSZ composite	LnSM/YSZ	Cheap, (Ln=lanthanides)
Anode	Ni/YSZ cermet	Ni/YSZ	classic for hydrogen, unfit for methane
	$Ce_{0.6}Gd_{0.4}O_{1.8}$	CG	for methane and hydrogen, mixed conductor
Interconnect	$(La_{1-y}Sr_y)CrO_{3\pm\delta}$ with dopants *x*	LSC*x*	classic at high temperature
	$Cr_{1-x}Fe_x(Y_2O_3)_y$	Cr-alloy	redox stable, moderate temp.
	$Fe_{1-x}Cr_x$	Ferritic steel	cheap, low temperature (<800°C)
Sealing	SiO_2 with additives	silicate glass	melting required
Manifold & Housing	$(MgO)_{1-x}$ $(Al_2O_3)_x$ Metals	spinel	non-conductor low temp. <800°C

1.5 Fabrication Techniques

A broad range of process techniques is available for fabrication of ceramic components. Simple wet ceramic shaping techniques such as slip casting, spray painting, extrusion, calendaring and tape casting are based on forming the outline of the component by shaping a paste or suspension of ceramic components and organic additives.[13]
These methods which all require sintering after shaping are attractive due to low cost and potential for effective scale-up. A general limitation is, that sintering of two materials in contact require some extent of reaction at the interface to obtain adhesion. Furthermore, matching of sintering contraction and TEC is critical to obtain shape-constant components.
Advanced gas-phase and plasma techniques such as physical vapor deposition (PVD), chemical and electrochemical vapor deposition (CVD and EVD) and ion beam deposition can form dense and well adhering layers or monoliths and do not require subsequent sintering at higher temperature.[14] This advantage has to be balanced against cost, as the processes are time-consuming, the vacuum equipment is expensive and the savings on scale-up are limited.
Tubular cells are often based on extrusion of a 1 to 3 mm thick support structure, which is sintered separately. To obtain dense electrolyte and interconnect layers CVD and EVD techniques are typically applied. A shift to the use of wet ceramic processing is considered an economic requirement for commercialization of tubular SOFC.[15]
Production of planar cells is often based on fabrication of the dense electrolyte by tape-casting and subsequent sintering, as this simple and cost effective process is developed to produce foils of controlled thickness. Electrodes can be produced in the same way as tape-cast sheets and laminated with the electrolyte prior to sintering, or as particle dispersions that are spray-painted directly onto the electrolyte prior to or after sintering of the electrolyte.

At the current state of development planar cells are often produced by simple, cheap processes, whereas production of tubular cells at present require partial use of more costly methods.

1.6 Cell Development

In the following examples from the development of planar SOFC at Risø are elaborated to illustrate how the materials demands and selection of fabrication methods are interacting.

1.6.1 Cell Design

Planar cells can be designed in several ways. Besides of the mentioned demands to materials, final stack design and operation temperature must be considered. The operation temperature can be decisive for the allowable thickness of components, and thereby for which components can be the structurally supporting member of a cell. Most developers initially chose an operation temperature of about 1000°C,[16] this choice was based on suppressing the resistance in the electrolyte and the electrodes, as these decrease with increasing temperature. The conductivity of YSZ at 1000°C is sufficient to form a self-supporting component, without the electrolyte resistance being the dominant limitation on cell performance. Such a supporting electrolyte is typically 100-300 μm thick,[7] Figure 1.3. The development of electrodes has lead to a point where they can be operated at lower temperature, e.g. 800°C. This offers economic advantages, as cheaper materials can be applied as interconnects, manifolds and cell housing. A lowering of the operation temperature causes an increase in the resistance of the cell. To counteract this, the electrolyte contribution must be reduced in combination with the use of improved electrodes. A factor of 2 improvement[17] is obtainable by co-doping the yttria doped zirconia with scandia. This is, however, not sufficient.

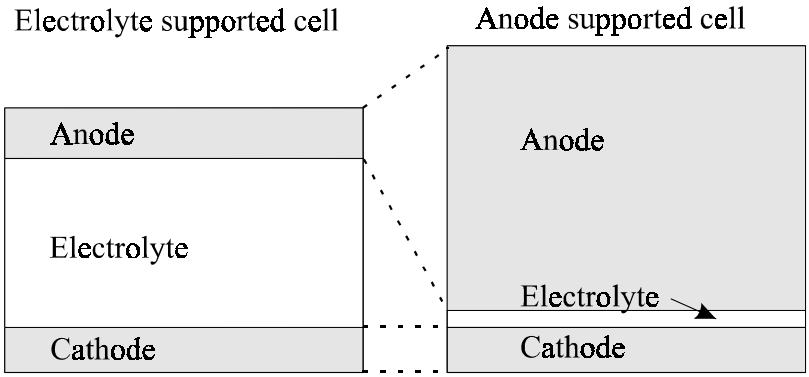

Figure 1.3 Illustration of two types of planar cells. Left electrolyte supported cell. Right: anode supported cell.

A significant reduction of the electrolyte thickness to e.g. 20-40 μm makes the electrolyte incapable of supporting the cell. Therefore the cell is constructed by depositing the electrolyte on a porous supporting structure, typically made from one of the electrode materials. Based on cost, only wet ceramic processes are considered. When selecting the supporting material it is important to consider the reactivity and the significance of sintering temperature on the electrode performance. The supporting structure and the electrolyte are often co-sintered, as it is difficult to sinter a dense electrolyte on a pre-sintered support. Co-sintering requires thorough control of the sintering behavior of the components to avoid warping and cracks caused by internal stress. The

sintering contraction can be manipulated to some extent by addition of organic additives and changing the powder particle size distribution.[18] The porosity can be increased by addition of organic fillers that burn out on sintering.
Densification of the electrolyte typically requires temperatures in excess of 1300°C. CG anodes and LSM/YSZ cathodes should not be sintered higher than 1100°C to avoid reaction with the electrolyte and to maintain performance. The performance of Ni/YSZ cermet anodes is not affected by sintering as high as 1500°C,[19] making this electrode a natural choice for the supporting structure, Figure 1.3. The thickness of a porous supporting structure is typically from 0.5 to 2 mm depending on fabrication methods and materials.[7]

1.6.2 Anode

Despite a long list of undesired properties of Ni in an SOFC, the Ni-based cermet with the electrolyte YSZ is still the most widespread used anode. This is primarily due to the excellent catalytic properties, the low reactivity with other components and a fairly low cost.
The anode is usually fabricated from a NiO/YSZ composite, reduced to Ni/YSZ cermet under start-up. For a reduced cermet anode re-oxidation will cause an expansion of more than 30 v/o in the Ni-phase. In the worst case this leads to fragmentation of the anode or detachment from the electrolyte. Therefore a Ni-based anode is not suitable for an SOFC operated as an electrolyzer unless a protective re-circulation of hydrogen is established.
Another drawback of Ni is reactivity at elevated temperature under high partial pressures of water, such as in partially spent fuel gas. Volatile $Ni(OH)_2$ is formed and exert a partial pressure of about 10^{-6} atm at 950°C.[20] This is not in itself critical, but due to the rapid passage of fuel gas, the formed $Ni(OH)_2$ is swept away, diminishing the long-term stability of the anode.
Finally Ni is an excellent catalyst for cracking of hydrocarbons under deposition of carbon. The carbon formation can cause clogging of gas channels, physical disintegration of the Ni-structure and fragmentation of the porous anode. Therefore Ni-based anodes are not suitable for direct operation in dry natural gas without modifications of the catalytic properties.
An alternative anode material is ceria, e.g. doped with gadolinia. As CeO_2 exhibits both ionic and some electronic conduction under reducing conditions, this material can be used for anodes without forming a composite.[21] However, the redox change of volume for ceria is a few pct when switching between oxidizing and reducing atmosphere. This is a consequence of part of the present Ce^{4+} being reduced to Ce^{3+} under release of oxygen from the lattice. By doping with 40 m/o $GdO_{3/2}$ this change of volume is severely reduced but not eliminated. Anodes fabricated from CG can attain a performance comparable to that of Ni/YSZ cermet anodes in hydrogen, and do not cause carbon formation in methane.[22]
The challenges of CG-anodes are establishment of adequate adhesion to the electrolyte without detrimental reactions,[21] and lowering the fairly high materials cost. To avoid this CG is only used for a less than 20 μm thick functional anode, whereas another and cheaper electron conducting material must be used for contacting and current collection.

1.6.3 Cathode

The classical material for the cathode is a strontium doped lanthanum manganite (LSM), with a high electrocatalytic activity for reduction of oxygen. One of the problems with this material is its reactivity towards the electrolyte, YSZ. Nevertheless the cathode often consists of a composite of these two materials. Under sintering and operation of the cathode, Mn migrates into the electrolyte where it dissolve in the lattice.[23] This in it self enhances sintering of the YSZ, and the morphology and especially the porosity of the composite depend on the Mn content. When LSM is substoichiometric regarding Mn, zirconates of lanthanum and strontium are formed by

reaction with the electrolyte.[24] These phases exhibit low conductivity, and should be avoided. This can be effected by using an LSM that is substoichiometric regarding La and Sr. Furthermore the sintering temperature should be kept at a minimum where sufficient adhesion to the electrolyte can be obtained. Application of a cheaper LSM-material based on less pure lanthanide sources (primarily La, Ce, Nd and Pr) is a possibility. However, the concentration of impurities varies, and some of them may cause undesired reactions with the electrolyte.[25]
Another alternative is strontium doped lanthanum cobaltates (LSCo), with a markedly higher electronic conductivity than LSM.[26] The disadvantages are reactivity of LSCo with YSZ forming non-conducting zirconates, and a fairly high deviation in TEC from other materials in the stack. LSCo may be used as a current collector with no direct contact to the electrolyte at lower temperatures. The higher TEC can be accommodated by establishing a graded zone between the pure LSCo and the LSM/YSZ functional cathode.

1.6.4 Interconnect

The redox change of volume is a common problem for selection of an interconnect material. In the classic $LaCrO_3$ based ceramic materials mechanical stress builds up when the element is exposed to air on the cathode side and reducing fuel gas on the anode side.[11] The interconnect tends to bend due to the pO_2 gradient, and to loose electrical contact or even fracture to let gases react directly in the stack. Metallic interconnects do not exhibit this type of redox volume changes. Instead it is critical that the metal forms a very thin and preferably electronically conducting protective layer upon oxidation of the metal on the cathode side.[27] Alternatively a protective layer can be applied by coating.

1.7 Commercialization

For SOFC to be a commercial product, competitive power generation must be attained. The cost of SOFC power generation is often given in cost/kW for the SOFC stack and for the surrounding equipment (balance of plant). In an EU SOFC-strategy from 1997, a stack cost of 500 ECU/kW is the aim.[28] Typically a lifetime in the order of 40.000 hrs is considered with an acceptable degradation rate of less than 1% per 1000 hrs.[9]

Plans for commercialization of SOFC-technology have been presented. Power/heat plants in the MW class based on tubular SOFC's in combination with a gas turbine is the primary aim for Siemens Westinghouse in the US and British Rolls-Royce. Fabrication of commercial units at Siemens Westinghouse is foreseen in the year 2001.[15] Sulzer Hexis in Switzerland is working on systems for domestic applications with a 1 kW electric +10 kW heat output.[29] The system is based on planar cells in combination with a conventional burner. These systems are also available at a non-commercial price. Commercialization is planned for 2001.

1.8 Scope of this Thesis

Characterization of limitations and improvement of performance for solid electrodes is a central issue in several projects dealing with SOFC at Risø. The aim of this thesis is to contribute to the understanding of Ni/YSZ cermet anodes operated in hydrogen/water mixtures and, if possible, to improve the performance.

The Ni/YSZ cermet anodes developed at Risø in 1990-1992[30] have been characterized by an impedance of 0.2 to 0.3 Ωcm^2 at 1000°C in hydrogen with 3% water. The impedance spectra contain two, [31] later realized to be three arcs, assumed to represent at least three limitations of physical or chemical nature.[32] Focus is on identifying the processes causing the limitations in these technological cermets with a fine structure. To some extent coarse cermets and Ni anodes are studied as well to identify relations between structure and performance. The long term behavior of cermet anodes under load has become an increasingly important issue, and a durability study is included in the work.

References

[1] W.R. Grove, *Phil. Mag*., **14** 127 (1839)
[2] H. Davy, *Nicholson's J. Nat. Phil*., 144 (1802)
[3] W. Nernst, *Z. Electrochem*., **6** 41 (1899)
[4] M. C. Williams, in *Third European SOFC Forum*, P. Stevens, Editor, European Fuel Cell Forum, Oberrohrdorf, CH. 27 (1998)
[5] M. Juhl, S. Primdahl, C. Manon and M. Mogensen, *J. of Power Sources* **61** 173 (1996)
[6] M. Brown, S. Primdahl and M. Mogensen, *J. Electrochem. Soc.* submitted (1999), chapter 6 in this thesis
[7] N. Q. Minh and T. Takahashi, *Science and technology of ceramic fuel cells*, Elsevier Science B. V. (1995)
[8] C. Bagger, S. Linderoth, M. Mogensen, P. V. Hendriksen, B. Kindl, S. Primdahl, P. H. Larsen, F. W. Poulsen, N. Bonanos and M. J. Jørgensen, in *SOFC VI*, accepted (1999)
[9] S. P. S. Badwal og K. Foger, *Materials Forum*, **21** 187 (1997)
[10] B. F. Sørensen and S. Primdahl, *J. Mat. Sci.* **33** 5291(1998)
[11] P. H. Larsen, P. V. Hendriksen and M. Mogensen, in *Third European SOFC Forum*, P. Stevens, Editor, European Fuel Cell Forum, Oberrohrdorf, CH. 181 (1998)
[12] F, Tietz, F. J. Dias and A. Naoumidis, in Third European SOFC Forum, P. Stevens, Editor, European Fuel Cell Forum, Oberrohrdorf, CH. 171 (1998)
[13] G. Y. Onoda og L. L. Hench, *Ceramic processing before firing*, John Wiley & Sons, Inc. (1978)
[14] P. Møller, Overfladeteknologi, ("Surface Technology", in danish), Teknisk forlag A/S, København, DK. (1998)
[15] S. C. Singhal, in *SOFC V*, U. Stimming, S. C. Singhal, H. Tagawa and W. Lehnert, Editors, **PV97-40**, The Electrochemical Society Proceedings Series, Pennington, NJ. 37 (1997)
[16] *SOFC I*, S. C. Singhal, Editor, **PV89-11**, The Electrochemical Society Proceedings Series, Pennington, NJ. (1997)
[17] N. Bonanos, Risø National Lab., Private communications (1999)
[18] S. Primdahl, M. J. Jørgensen, C. Bagger and B. Kindl, in *SOFC VI*, accepted (1999)
[19] S. Primdahl, B. F. Sørensen and M. Mogensen, *J. Am. Ceram. Soc.* submitted (1998), chapter 7 in this thesis
[20] A. Gubner, H. Landes, J. Metzger, H. Seeg and R. Stübner, in *SOFC V*, U. Stimming, S. C. Singhal, H. Tagawa and W. Lehnert, Editors, **PV97-40**, The Electrochemical Society Proceedings Series, Pennington, NJ. 844 (1997)
[21] O. Marina, S. Primdahl, C. Bagger and M. Mogensen, in *SOFC V*, U. Stimming, S.C. Singhal, H. Tagawa and W. Lehnert, Editors, **PV97-40**, The Electrochemical Society Proceedings Series, Pennington, NJ. 540 (1997)
[22] O. Marina, C. Bagger, S. Primdahl and M. Mogensen, *Solid State Ionics*, **123** 199 (1999)
[23] C. C. Apple, N. Bonanos, A. Horsewell and S. Linderoth, in preparation (1999)
[24] A. Mitterdorfer, M. Cantoni and L. J. Gauckler, in *Second European SOFC Forum*, U. Bossel, Editor. European Fuel Cell Forum, Oberrohrdorf, CH. 373 (1996)
[25] M. Mori, T. Yamamoto, H. Itoh and T. Abe. in *2nd Int. Fuel Cell Conference*, Kobe, Japan, 485 (1996)
[26] H. Yokokawa, N. Sakai, T. Kawada and M. Dokiya, *J. Electrochem. Soc*. **138** 2719 (1991)

[27] S. Linderoth and P. H. Larsen, in *Third European SOFC Forum*, P. Stevens, Editor, European Fuel Cell Forum, Oberrohrdorf, CH. 323 (1998)

[28] A Fuel Cell Research, Development and Demonstration Strategy for Europe up to 2005, EC, Brussels, 1998 Edition

[29] R. Diethelm, M. Schmidt, B. Doggwiler, Th. Gamper, M. Keller, K. Honegger and E. Batwi, in *Third European SOFC Forum*, P. Stevens, Editor, European Fuel Cell Forum, Oberrohrdorf, CH. 87 (1998)

[30] C. Bagger, in *1992 Fuel Cell Seminar*, Courtesy Associates Inc., Washington D.C. 241 (1992)

[31] M. Mogensen and T. Lindegaard, in *SOFC III*, S. C. Singhal and H. Iwahara, Editors, **PV 93-4,** The Electrochemical Society Proceedings Series, Pennington, NJ. 484 (1993)

[32] M. Mogensen, S. Primdahl and M. Juhl, in *SOFC V*, U. Stimming, S. C. Singhal, H. Tagawa and W. Lehnert, Editors. **PV 97-40**, The Electrochemical Society Proceedings Series, Pennington, NJ. 385 (1997)

Chapter 2

Solid Electrode Characterization[†]

Abstract

The technological development and electrochemical characterisation of solid electrodes require well defined, reproducible and error-free measurements of the electrode polarisation resistances. A number of pitfalls exist, which are often not adequately discussed in the extensive literature on this subject. This chapter addresses the following problems: i) Placement of reference electrodes in commonly used cell geometries, ii) ohmic heating in thick electrolytes under dc load, iii) the establishment of sufficient current collection on test-cells, which may be a problem even without dc load, iv) assessment of the series resistance at high frequency in impedance analysis and the importance of reducing inductive effects due to leads, and finally v) the effect of temperature on the active thickness of a composite electrode in relation to the determination of activation energies.

[†] This chapter has been published as S. Primdahl and P. V. Hendriksen "Pitfalls in Solid Electrode Characterisation" in *High Temperature Electrochemistry: Ceramics and Metals*, F. W. Poulsen, N. Bonanos, S. Linderoth, M. Mogensen and B. Zachau-Christiansen, Editors, 17th Risø International Symposium on Materials Science. Roskilde, DK. 403-410 (1996)

2.1 Introduction

This chapter states, explains and suggests remedies for a number of problems in characterising solid electrodes at elevated temperature. The problems presented and the solutions suggested are based on the authors' experience and observations from the literature.

2.2 Cell Geometry and Position of Reference Electrode

To measure the performance and characterise a single electrode (working electrode, WE), a reference electrode (RE) must be introduced to avoid unintended interference of the other current electrode (counter electrode, CE). Often a fourth lead is used in contact with the working electrode or as a separate electrode (RWE) to monitor the potential of the working electrode.

A part of the voltage drop observed between the WE and the RE is due to the electrochemical process (polarisation resistance, *Rp*) and a part is caused by purely ohmic losses in the electrolyte and the electrode, (series resistance, *Rs*).

Rp is normally calculated from

$$Rp = \frac{\varphi_w^o - \varphi_r^o}{I_o} - Rs\,, \tag{2.1}$$

where

$$Rs = \frac{\varphi_w^\infty - \varphi_r^\infty}{I_\infty}\,. \tag{2.2}$$

Here φ is electrode potential and I is current, subscripts w and r refers to WE and RE potentials respectively. 0 and ∞ indicate low-frequency and high-frequency limits, respectively.

In the case of asymmetric cells where, due to the overall cell geometry, the current density is not homogeneous, the above methodology may lead to erroneous results. The ratio *Rp/Rs* changes with frequency leading to changes in the current density distribution in the cell, which result in an apparent frequency dependence of *Rs*, i.e., $Rs^\infty \neq Rs^o$. Furthermore, in the case of an inhomogeneous current density it is very difficult to judge whether a reference electrode in a given position really function correctly. A correct positioning of the reference electrode is such that no resistance associated with the counter electrode contributes to (φ_w - φ_r) and all of the working electrode resistance is included.

It would be desirable to perform error-free single electrode measurements on actual fuel cell stack components, e.g. a cell on a YSZ tape, typically 200 μm thick, placed between two interconnects in a stack. However, due to complications arising from the positioning of reference electrodes this is not feasible. In practice the YSZ tape based cell can be mounted between Pt or Au mesh current collectors in a special test facility. In a circular geometry the reference electrodes may be placed concentric within the current electrode,[1] concentric outside it,[2] or as a separate part of the counter electrode placed opposite the working electrode.[3] For unpolarised measurements, the problem of placing reference electrodes on thin electrolytes can be elegantly avoided by the use of a symmetric two-electrode cell with identical electrodes on each side.[4] Based on principles

of symmetry and experience from aqueous electro-chemistry, a 3-electrode pellet has been designed at Risø to allow single electrode studies in controlled atmosphere with a reference electrode in air. The geometry is illustrated elsewhere,[5] see also the insert in Figure 2.1B.

In a modelling study[6] the validity of some of these geometries has been investigated with respect to determination of the electrode polarisation resistance. In the model all material layers are assumed to be ohmic. The polarisation resistance is represented by adding a thin material layer of thickness h in the interface between electrode and electrolyte. The conductivity of this fictive layer is defined as $\sigma=h/Rp^{true}$, where Rp^{true} is the polarisation resistance to be represented by the layer. The potential and current density distribution in the cell are determined by solving the Laplace equation ($\nabla^2\varphi=0$), which expresses conservation of charge inside a continuum obeying Ohms law. The equation is solved using the finite-element method and *Rp* is calculated from Eq. (2.1).

Results of such calculations are presented in Figure 2.1A for the case of a square cell based on a thin electrolyte, where the two current electrodes may be exactly opposite or slightly displaced relative to each other. The details of the geometry, as well as the values of *Rp* and *Rs* are given in the figure caption. When the cell is symmetric no error is made in deriving *Rp* from Eq. (2.1). However, if the electrodes are slightly displaced, on a length scale of the electrolyte thickness, *Rp* is severely under- or overestimated, depending on the direction of the displacement. There are two contributions to the error: The first is the change in *Rs* with frequency discussed above. A second and more important error arises when the reference electrode equipotential line intersects the electrolyte/electrode interface, i.e. part of the working electrode *Rp* is excluded from the measurement or part of the counter electrode *Rp* included, depending on the direction of the electrode displacement.

The above problems are less severe in a pellet-like cell geometry, since the current density distribution changes less with frequency than in the thin electrolyte case. This is because the changes in *Rp* with frequency are of less relative importance due to the large resistance of the electrolyte between WE and CE. Also it is easier to place the reference electrode where interference with the current electrodes is avoided.
The suitability of Risø 3-electrode pellets and similar geometries can be judged from Figure 2.1B, where the error in measuring *Rp* is estimated. Generally, the hole for the reference electrode should be as small as possible, and the distance between WE and RE must be two times larger than the bore radius to obtain reliable results for the considered *Rp*. In general, the requirements to the geometry become more severe with decreasing *Rp*.

These calculations show that electrochemical measurements on thin electrolyte cells require extreme control of the geometry. Measurements on thick pellets are far less sensitive to electrode alignment. Alternatively, if no dc loading is required a symmetric two-electrode method can be used on thin electrolytes. As a general principle, reference electrodes for potential monitoring should be as small as possible or placed along equipotential lines. This prevents a flow of current through the electrode which might disturb the current distribution in the electrolyte and polarise the reference electrode.

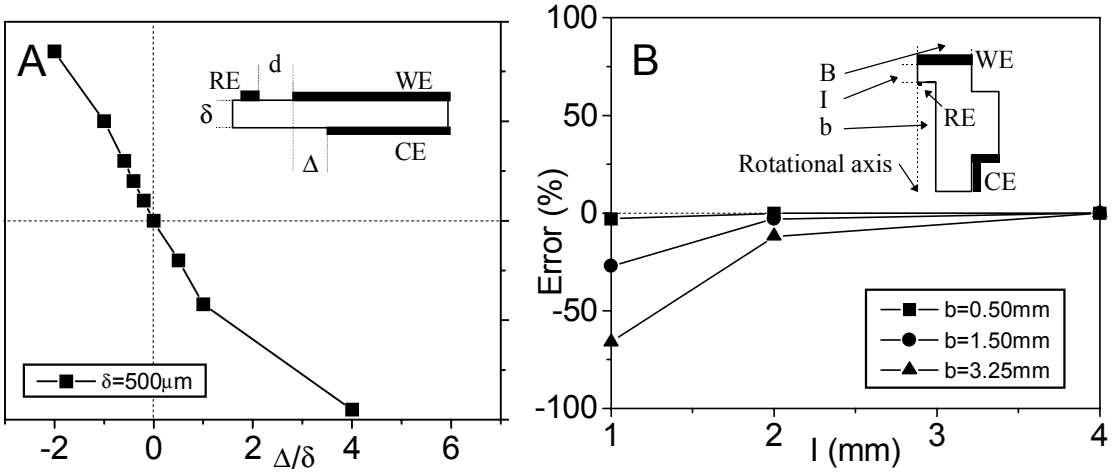

Figure 2.1 Calculated error in determination of *Rp* for different 3-electrode cell geometries.[6] *Rp* was 0.16 Ωcm^2, the resistivity of the electrolyte $R_{YSZ,Spec.}$ was 0.10 Ωm. A) Cross section of square electrodes on a thin electrolyte (δ) with a parallel reference electrode at a distance d=0.5-2.5 mm, see insert. The error is a function of the electrode displacement Δ, here normalised against δ. B) Risø 3-electrode pellet geometry, see insert. The calculated error is given as a function of the distance I between WE and RE for various bore radii b. Actual dimensions of Risø 3-electrode pellets are I=2 mm, b=1.50 mm and B=3.8 mm. For further details see Ref.[6]

2.3 Current Collection and Polarization Resistance

The quality of the current collection over the working electrode is significant for the study of *Rp* when operating with high current density. Most studies in literature are performed using a fine Pt or Au mesh pressed towards the electrode surface. The electrodes used in this study are integrated with a ceramic/cermet current collector, and a central current collection probe (1 mm sphere or a short 0.3 mm wire) is used. Recently, however, it has become clear that in-plane conductivity of some current collectors has been insufficient, causing an inhomogeneous current distribution. As a result, 1/*Rp* does not scale with electrode area and *Rs* is larger than expected from the geometry. The problem can be solved by using a better current collector or a smaller WE area. An example to illustrate this is given in Table 2.1 for lanthanum strontium manganite (LSM) based cathodes on an yttrium stabilised zirconia (YSZ) electrolyte.

Table 2.1 *Rp* and *Rs* measured on an LSM/YSZ composite cathode at 1000°C in a symmetric two-electrode geometry similar to Figure 2.2.

Sample area	Rp	Rs
0.35 cm^2	0.10 Ωcm^2	1.60 Ωcm^2
0.18 cm^2	0.07 Ωcm^2	1.74 Ωcm^2
0.033 cm^2	0.06 Ωcm^2	1.74 Ωcm^2
0.38 $cm^{2\,\#}$	0.05 Ωcm^2	0.21 Ωcm^2

50 µm of porous platinum on both electrodes.

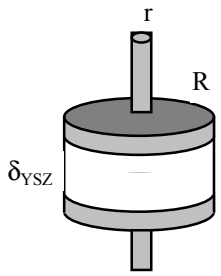

Figure 2.2 Model geometry. Two electrodes on a thin circular disk (radius R) of electrolyte with a central current collector (radius r).

The current collection may be improved by applying a layer of metallic paste such as fritless platinum. The thickness of platinum needed to obtain an almost ideal current distribution in the electrolyte may be calculated.[7] In this case, complications arising from the frequency dependence of *Rp* at the interfaces have been disregarded. An experimentally determined resistivity of $8 \cdot 10^{-5}$ Ωm at 1000°C is assigned to the porous Pt layer (*Einbrennplatin 308A, Demetron*). To examine only the effect of the Pt layer, the opposite electrode is assigned a much higher conductivity. In Table 2.2 the variation in *Rs* is given for three WE areas, with various thicknesses of platinum. A typical thickness of a brushed-on Pt paste layer is 20-30 µm.

Table 2.2 Calculated effect on *Rs* of various thicknesses of the porous platinum layer in the geometry of Figure 2.2. $\rho_{Pt} = 8 \cdot 10^{-5}$ Ωm, $R_{YSZ,Spec.} = 0.10$ Ωm, $\delta_{YSZ} = 200$ µm.

WE radius	Platinum thickness	Rs from model	Deviation from Rs_{min}
R=1 mm	>100 µm	4.78 Ω	≡Rs_{min}
	5 µm	4.78 Ω	0%
	1 µm	4.82 Ω	1%
R=4 mm	>500 µm	0.299 Ω	≡Rs_{min}
	100 µm	0.302 Ω	1%
	20 µm	0.315 Ω	6%
R=10 mm	>10,000 µm	0.0479 Ω	≡Rs_{min}
	900 µm	0.0484 Ω	1%
	100 µm	0.0530 Ω	12%

In conclusion, the quality of current collection from the electrochemically active electrode layer can invalidate the measurement of *Rp* even on electrodes of small area. Quite thick layers of porous platinum may be required to ensure a homogeneous current distribution on thin electrolytes.

2.4 Polarization and Ohmic Heating

Depending on the electrolyte geometry, conductivity and temperature, ohmic heating of the electrolyte may have to be considered in dc measurements with high current densities. For LSM based cathodes exhibiting an apparent activation energy of about 2eV,[8] a temperature change in the electrode of 5°C at 1000°C changes the performance by 7%.

Test rigs for 3-electrode pellets at Risø are equipped with a thin thermocouple in the reference electrode bore allowing a reliable measurement of the electrolyte temperature at each polarisation. In this experiment a porous pellet of LSM is placed in contact with the cathode to accommodate the high currents. The activation energy of the electrolyte conductivity is about 80 kJ/mol in TZ8Y (ZrO_2 with 8mol% Y_2O_3).[9,10] Bearing this in mind, the temperature increase can be calculated from the observed variation in *Rs* between WE and RE. Measured as well as calculated temperatures are illustrated in Figure 2.3 as a function of current density and polarization. Considering a temperature change of 5°C as acceptable, the maximum allowable current density according to Figure 2.3 is 500 mA/cm^2, corresponding to a polarisation of only -50 mV. The discrepancy between measured and calculated temperature is believed to be due to an inhomogeneous temperature distribution in the electrolyte pellet and surface cooling.

In summary, ohmic heating may be of importance for measurements obtained under polarisation on thick electrolytes. Due to the sometimes high activation energy of electrode processes a temperature increase of a few degrees may severely influence the measured *Rp*.

2.5 Inductance and Impedance Spectroscopy

One of the major uncertainties in *Rp* determined from impedance measurements originates from the limited accuracy of determining *Rs* at the high frequency intercept with the abscissa in Nyquist plots. The maximum applicable frequency is limited by the frequency analyser used, and often further constrained by phase errors in the potentiostat. Leads from instrumentation to the measurement rig are often protected against excessive inductance by driven shields (*Solartron*) or a forwarded potentiometerbox (*EG&G*). Ideally driven shields should be implemented all the way to the hot sample.

The major contribution to the inductance is associated with the platinum wires leading from the terminal box of a test rig to the hot sample. The simple way of bringing WE and CE/RE leads into a cylindrical oven from opposite ends must be avoided, as it introduces a large inductive loop around the oven coils. The inductance, in the order of 2-10 μH, distorts impedance spectra considerably above 1 kHz as illustrated in Figure 2.4A.[5] By comparison, running the leads in parallel out of the same end of the oven reduces the inductance to below 0.1 μH, in which case the spectra are distorted only above 10 kHz (Figure 2.4B), allowing a more detailed interpretation of the high frequency part.[11]

Numerical fitting of experimental data by routines such as EQUIVCRT[12] opens a possibility for estimating a poorly determined *Rs*. However, care should be taken not to over-interpret data. A small positive inductance (e.g. Figure 2.4B) gives a false sense of being able to estimate *Rs* rather precisely. It is worthwhile to see how far from the initial fit value *Rs* can be constrained before a substantially poorer fit is obtained.

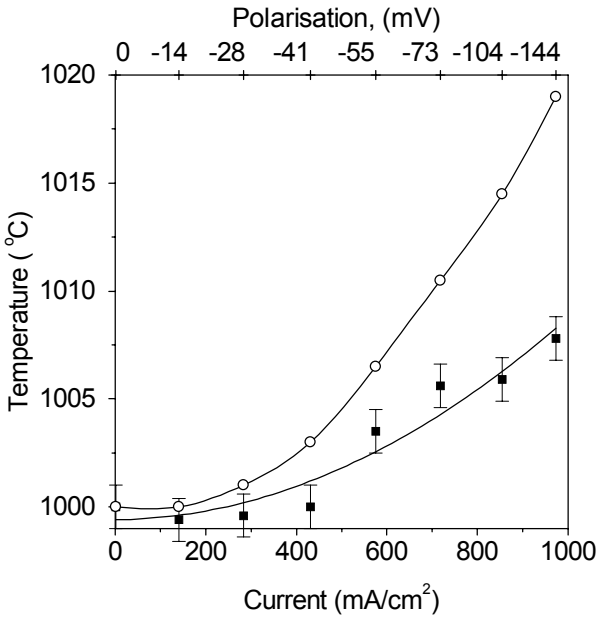

Figure 2.3 Measured (solid squares) and calculated (circles, from *Rs*) temperature in a Risø 3-electrode pellet due to ohmic heating as function of current and applied polarisation.

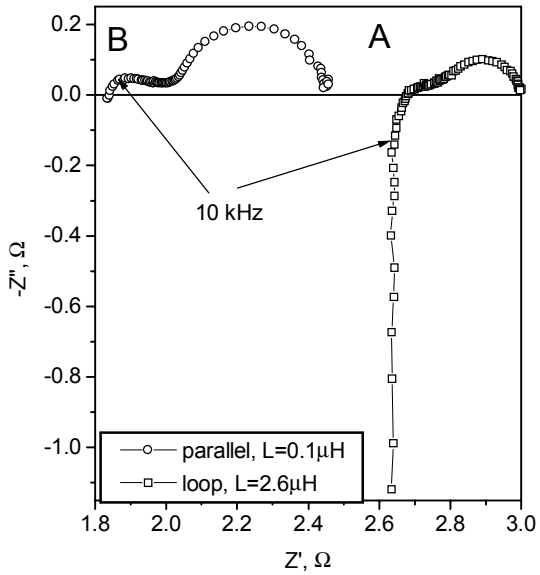

Figure 2.4 Impedance spectra measured on two similar Ni/YSZ cermet anodes with different wiring geometries, see text for details. Frequency range: 0.1 Hz to 65 kHz.

After characterising a number of similar electrodes it may be possible to anticipate the shape of the impedance spectrum (more specifically the frequency exponents of the constant phase elements).[11,13] These parameters may then be constrained, increasing the accuracy in *Rs* and thus *Rp*.

In summary, it is extremely important to be aware of the difficulty in asserting the true *Rs* in impedance spectra when the applicable frequency range is insufficient or when the inductance is high. High inductance can often be cured by appropriate design of the measurement rig. An inductive element should be allowed for in any fitting of experimental data.

2.6 Active Electrode Thickness

Using composite/cermet electrodes in an SOFC is a way of improving the electrode performance per nominal electrode area.[14] The reaction sites are often related to the triple phase boundary,[15-17] allowing the definition of a triple phase boundary length specific reaction resistance, $Rp_{spec.}$. The location of active sites extends into the volume of the composite structure where the three phases are percolating: YSZ to the electrolyte, electrode material to the current collector and pores to the gas channels above the composite.

In a well percolating composite the active electrode thickness is limited by the ohmic resistance in the YSZ, R_{YSZ}, between the active sites and the electrolyte.[8] As the apparent

activation energies of the YSZ and the overall electrode process are not identical,[8,11] the ratio $Rp_{spec.}/R_{YSZ}$ changes with temperature and so does the active thickness.

A fundamental requirement when performing activation energy studies is an invariant electrode area. Therefore the actual thickness of composite/cermet electrodes should be considered and the temperature range should be such that the physical (actual) thickness is always smaller than the potentially active thickness.

Acknowledgment

The authors are gratefully acknowledging colleagues in the SOFC-group at Risø National Laboratory for fruitful discussions and technical assistance. Special thanks are due to J. Winkler et al. for allowing us to refer to their work prior to publication, and to N. Bonanos for proof-reading. This work is supported by the Danish Energy Agency and ELSAM under the DK-SOFC project, by the European Energy Agency under contract no. JOU2-CT92-0063 and by STATOIL in a joint research project with STATOIL R&D.

References

[1] J. Divisek, L. G. J. de Haart, P. Holtappels, U. Stimming and I. C. Vinke, in *High Temperature Materials: Ceramics and Metals*, F. W. Poulsen, N. Bonanos, S. Linderoth, M. Mogensen and B. Zachau-Christiansen, Editors, 17th Risø International Symposium on Materials Science, Roskilde, DK. 235 (1996)

[2] J. Divisek, L. G. J. de Haart, P. Holtappels, T. Lennartz, W. Malléner, U. Stimming and K. Wippermann, *J. Power Sources*, **49** 257 (1994)

[3] F. P. F. van Berkel, F. H. van Heuveln and J. P. P. Huijsmans, *Solid State Ionics*, **72** 563 (1994)

[4] D. W. Dees, U. Balachandran, S. E. Dorris, J. J. Heiberger, C. C. McPheeters and J. J. Picciolo, in *SOFC I*, S. C. Singhal, Editor, **PV 89-11**, The Electrochemical Society Proceedings Series, Pennington, NJ. 317 (1989)

[5] M. Mogensen and T. Lindegaard, in *SOFC III*, S.C. Singhal and H. Iwahara, Editors. **PV 93-4**, The Electrochemical Society Proceedings Series, Pennington, NJ. 484 (1993)

[6] J. Winkler, P. V. Hendriksen, N. Bonanos and M. Mogensen, *J. Electrochem. Soc*. **145** 1184 (1998)

[7] K. Nisancioglu, in *Proceedings of natural gas fuelled solid oxide fuel cells & systems, IEA, workshop on mathematical modelling*. Office federale de l'energie, Berne, CH. 87 (1989)

[8] M. Juhl, S. Primdahl, C. Manon and M. Mogensen, *J. Power Sources* **61** 173 (1996)

[9] S. P. S. Badwal, *Solid State Ionics* **52** 23 (1992)

[10] F. T. Ciacchi, K. M. Crane and S. P. S. Badwal, *Solid State Ionics*, **73** 49 (1994)

[11] S. Primdahl and M. Mogensen, *J. Electrochem. Soc.* **144** 3409 (1997), chapter 3 in this thesis

[12] B.A. Boukamp, *Solid State Ionics,* **20** 31 (1986)

[13] M. Mogensen, S. Primdahl, J. T. Rheinländer, S. Gormsen, S. Linderoth and M. Brown, in *SOFC IV*, M. Dokiya, O. Yamamoto, H. Tagawa, S. C. Singhal, Editors, **PV 95-1**, The Electrochemical Society Proceedings Series, Pennington, NJ. 657 (1995)

[14] C. Bagger, in *1992 Fuel Cell Seminar*, Courtesy Associates, Inc. Washington D.C. 241 (1992)

[15] T. Kawada, N. Sakai, H. Yokokawa, M. Dokiya, M. Mori and T. Iwata, *J. Electrochem. Soc*. **137** 3042 (1990)

[16] N.Q. Minh and T. Takahashi, *Science and Technology of Ceramic Fuel Cells*, Elsevier Science B.V. Amsterdam. (1995)

[17] J. Mizusaki, H. Tagawa, T. Saito, K. Kamitani, T. Yamamura, K. Hirano, S. Ehara, T. Takagi, T. Hikita, M. Ippommatsu, S. Nakagawa and K. Hashimoto, *J. Electrochem. Soc*. **141** 2129 (1994)

Chapter 3

Impedance of Ni/YSZ Cermet Anodes[†]

Abstract

The oxidation of hydrogen on Ni/yttria-stabilized zirconia (YSZ) is studied by impedance spectroscopy. The active thickness obtained appears to be 20 μm or less. Conditions such as temperature, anodic overpotential, electrode potential, H_2 and H_2O partial pressure are varied.

Three distinct arcs are identified in impedance spectra, representing at least three rate limiting processes. One equivalent circuit of the type LR(RQ)(RQ)(RQ) where Q is a constant phase element with the admittance $Y^*=Y_0(j\omega)^n$ is used to describe all recorded impedance spectra in the temperature range of 850°C to 1000°C. The n-values are held constant, allowing a direct comparison of R and Y_0 values for different structures and conditions.

The high frequency arc (1kHz - 50kHz) is sensitive to the cermet structure (particle size) and relatively insensitive to the atmosphere composition and overpotential. The related imperfect capacitance is suggested to be the double layer capacitance in the Ni/YSZ interface.

The medium frequency arc (10Hz - 1kHz) and the low frequency arc (0.1Hz - 10Hz) are sensitive to atmosphere composition and overpotential. Both reaction resistances change their dependence on H_2 partial pressure around 0.5 atm. The perfect capacitance related to the low frequency arc is in the order of 0.5-2.5 F/cm^2, indicating an absorbed charged species rather than surface adsorption.

[†] This chapter has been published with minor revisions as S. Primdahl and M. Mogensen, "Oxidation of Hydrogen on Ni/YSZ-Cermet Anodes", *J. Electrochem. Soc.* **144** 3409-3419 (1997)

3.1 Introduction

The most widely studied anode for oxidation of hydrogen in solid oxide fuel cells (SOFC's) is the Ni/YSZ cermet anode. Alternative metallic anodes such as Pt, Ru and Pd have been investigated in conjunction with YSZ,[1-3] and mixed conducting oxides such as CeO_2, $(CeO_2)_{0.8}(SmO_{1.5})_{0.2}$, and PrO_2.[4,5]

Sophisticated application methods such as chemical/electrochemical vapor deposition (CVD and EVD) have been demonstrated to yield interesting structures.[6] For technological use, the Ni/YSZ cermet anode should be produced by a cost-effective process. This may be done by depositing slurries containing Ni or NiO, YSZ and organic additives by e.g. spray painting, screen printing or tape casting on the electrolyte.

This chapter is intended to i) bring forward a method of rationalizing impedance data and ii) present relevant data for the oxidation of hydrogen on Ni/YSZ cermet anodes produced by spray-painting. The impedance data are rationalized by fitting to a representative equivalent circuit, thus allowing the dependence of three processes on typical parameters to be derived. A tentative evaluation of the nature of each process is given.

3.1.1 Location of Active Reaction Sites

The use of a cermet structure is a basic requirement to obtain adhesion and stability when using nickel as the active anode.[7-9] The poor match of thermal expansion coefficients (TEC) between YSZ (10.8×10^{-6} K^{-1})[10] and Ni (17×10^{-6} K^{-1})[11] combined with extensive sintering of μm-size Ni particles at even 800°C[12] can be restrained from damaging the anode structure when NiO and later Ni is contained in a rigid YSZ-structure.

Another reason to use a cermet structure is the increase in reaction sites per nominal electrode area. In order to provide reactants and remove products of the overall anode reaction (3.1) at any reaction site it is necessary to obtain percolation of gases, oxide ions and electrons. Potential reaction sites without percolation are not considered efficient.

$$H_2(g) + O^{2-}_{electrolyte} \rightarrow H_2O(g) + 2e^-_{anode} \qquad (3.1)$$

As the electrolyte is a poor electronic[13] and protonic conductor[14] and as nickel does not conduct oxide ions, it seems reasonable to accept the active triple phase boundary (TPB) line as being closely related to the number of active reaction sites for a given cermet structure. The overall reaction consisting of several successive steps might not take place on the TPB line, but at least some of the reactants and/or products must pass an area restrained by this line. The extent and position of this area are uncertain, a band of no more than 1 μm has been suggested on both the electrolyte[15] and the nickel.[9] As a consequence of mixing Ni with YSZ to allow for extensive percolation in both phases, active TPB can be located all over the porous cermet structure.

The high resistivity towards oxide ion conduction in YSZ can be considered a limiting factor for the active electrode thickness.[16,17] Using the model presented by Juhl *et al.*,[16] a specific electrolyte resistance of 10 Ωcm at 1000°C[18] and a specific polarization resistance of 10^3 Ωcm,[19] a maximum active thickness in the order of 50 μm can be estimated. An intimate YSZ-contact in the electrolyte-electrode interface is thus essential, as the active volume must extend from this

interface into the cermet. As the apparent thermal activation of the anode reactions does not match that of the electrolyte (see below), the active volume of the cermet structure should indeed change with temperature as also suggested for cathodes.[16] Any cermet structure above the active volume is considered to act merely as a simple current collector, and Ni-felt or a porous Ni powder structure should be preferred due to the better conductivity.

Optimization of a Ni-YSZ cermet anode is thus assumed to reduce to two problems: i) increasing the TPB volume density within an electrochemically active volume adjacent to the electrolyte and ii) sustaining percolation in the three phases.

3.1.2 Structure

Microstructural features of importance when quantifying and reproducing a given cermet structure are mainly related to i) particle packing described by particle and porosity size distribution, number of neighbors and homogeneity, and ii) sintering properties described by particle size distribution, internal porosity, wetting of the other phase, availability of identical neighbors and extent of neck-formation.

The site percolation limit in close packed random mixtures of two types of uniform spheres is found to be about 30 vol%.[20] These conditions are rarely fulfilled in real cermet structures. Nevertheless, a limiting behavior around 30 vol% has been demonstrated for Ni/YSZ cermets.[8,21,22] Investigations of polarization resistance as a function of nickel particle diameter or mean nickel particle separation are reported.[8,23] These studies are indeed simplified studies of percolation in binary mixtures of complex particle size distributions.

There seems to be a tendency towards declining polarization resistance with finer particles of both YSZ and Ni/NiO.[8,23] Investigations of the importance of particle size ratio between Ni and YSZ has been reported.[8,24] In general this kind of study raises the question whether particles with a size ratio of e.g. 100 can be considered part of the same structure, or whether the fine grains are forming a microstructure of their own and the larger grains just serve to enhance the surface of either electrolyte or current collector. In other words, fundamental changes in structure and percolation are convoluted in the grain size ratio.

The complex microstructure of Ni/YSZ cermet anodes, the problem of establishing a quantitative description of such structures and the complex impedance spectra obtained have initiated a number of studies on uncomplicated geometries with the aim of avoiding structural limitations and measure purely chemical parameters. Attempts to determine the specific reaction resistance related to the TPB has been done for uncomplicated geometries using Ni-wire imprints,[19] Ni-mesh,[25] Ni-stripes,[26,27] and a Ni ball.[28,29] Unfortunately the results are not revealing a simple relationship.

We have chosen to investigate cermet anodes with varied structure to identify the nature of limitations in the combined chemical and structural system. The chemical parameters being reaction resistances for a number of rate limiting reactions should remain recognizable and comparable throughout variations in structure. It is thus expected that modifications in the production of anodes influence the rate limiting structural parameters to assist in interpreting the rate limiting steps.

3.1.3 Impedance Measurements

As the polarization resistance R_P is low on good anodes, a significant error in measurements often relates to determination of the series resistance R_S. Apart from limitations in frequency when using a potentiostat, phase errors on analyzers and induction in leads in the vicinity of electrical ovens influence the determination of R_S and R_P.[30,31]

It is essential to ensure a valid measurement geometry when using the three electrode configuration for impedance measurements. The YSZ pellet (in Figure 3.1) used in this study is designed for three electrodes to allow an accurate study of one electrode. Modeling has indicated that such studies with a reference electrode on electrolyte foils are highly sensitive to the alignment of electrodes within fractions of the electrolyte thickness.[32] An inappropriate position of a reference electrode relative to the current distribution in the electrolyte geometry severely influences even DC measurements.[33] Examples of circumstances at the counter electrode influencing measurements in a three electrode arrangement have been given on even 2 mm thick electrolyte discs.[34]

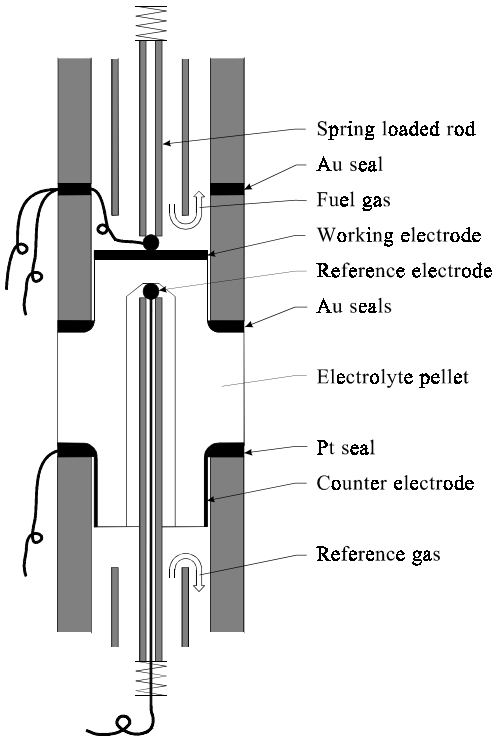

Figure 3.1 4-leads measurement rig and design of YSZ pellet for anode testing.

3.2 Experimental

3.2.1 Sample Preparation

A 40-50 µm thick "standard" anode is prepared by spray-painting. The ethanol based slurry is composed of green NiO and YSZ (Tosoh, ZrO_2 with 8 mol% Y_2O_3), suspended by a dispersant (polyvinyl pyrrilidone).[35] After deagglomeration in a ballmill, the YSZ particle size is about 0.4 µm. The NiO particle size distribution is bimodal with fractions of approximately 0.4 µm and 10 µm in a volume ratio of 6:1. The slurry is sprayed onto YSZ pellets in layers of 10-30 µm and sintered for 2 hours at 1300°C after each layer. The Ni/YSZ volume ratio is 40/60 in the reduced cermet. To investigate the importance of the structure the production parameters are varied from the "standard" according to Table 3.1. The identification codes for all anodes consisting of letters and numbers are also given.

Table 3.1 Produced and tested Ni/YSZ cermet anodes.

Identity	Anode type	Thickness	Ni/YSZ vol. ratio	Comments/pretreatment
S1-12	"standard"	40-50 μm	40/60	three layers
S13			50/50	three layers
T14-23	varied thickness	5-70 μm	40/60	
FF24-25	Fine NiO & YSZ	40-50 μm	40/60	Dry grinding of the combined powders.
FF26			50/50	
FF27-28			50/50	Combined powder made by a plasma method[¤].
FN29	Fine NiO	40-50 μm	40/60	Wet grinding of NiO, 0.4 μm[#]
CY30-31	Coarse YSZ	40-50 μm	40/60	Wet grinding of calcined YSZ (0.4 μm and 6.5 μm, 1:2 [#])
C32	Coarse Ni-rich	250 μm	67/33	Screen printed in one layer.

[¤] Produced according to ref. 48.
[#] Particle size distribution measured by laser diffraction (Malvern Mastersizer)

The YSZ pellets are provided with a Pt-paste counter electrode, a Pt-ball reference electrode and mounted in a 3-electrode setup, Figure 3.1. The working electrode is contacted with several mm of 0.3 mm Pt wire pressed against the center. Anodes are heated to 1000°C in nitrogen and reduced by gradually changing to a standard measurement atmosphere: 97% H_2 + 3% H_2O with an open circuit voltage (OCV) against Pt in air of about -1070 mV ($pO_2 \sim 2\times10^{-18}$ atm). A total of 100 ml/min (at 25°C) dry gas is passed over the ~0.44 cm^2 electrode area. Atmosphere control is performed by mixing nitrogen and hydrogen through massflow meters and saturating this mixture (or one of the gases) with water at a controlled temperature. In the following the term "wet" is used for gases saturated at room temperature (i.e. ~ 3% water). The balance of atmosphere compositions is always nitrogen.

3.2.2 Electrochemical Testing

It is important to realize how parameters are linked. Temperature, T, electrode potential, E, partial pressure of water, pH_2O, and hydrogen, pH_2, are all connected through the Nernst equation and the water formation reaction. Any experiment designed to study one parameter eventually causes changes in at least one other parameter. The H_2/H_2O compositions investigated at 1000°C are given in Figure 3.2, at the same time indicating how the electrode potential is connected to these. Measurements obtained at constant E thus reflect the dependencies of both atmosphere components.

pO_2 is determined by the Nernst expression from the OCV vs. Pt/air. The partial pressure pH_2O is determined from pO_2 and pH_2 by iterations on the following equation valid for 1000K<T<1300K:[36]

$$pH_2O = 10^{-(2.958-13022/T)} \cdot pH_2 \cdot \sqrt{pO_2} \qquad (3.2)$$

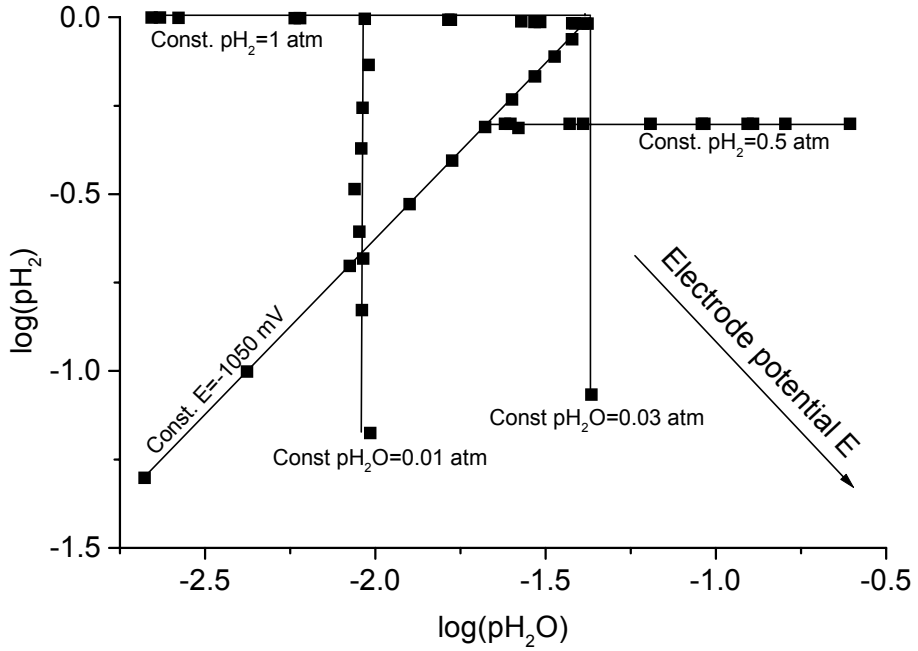

Figure 3.2 A summary of the H_2/H_2O atmosphere compositions investigated at 1000°C. Note how the dependencies of pH_2 and pH_2O are added at any given constant electrode potential E.

Electrochemical measurements are conducted in the temperature range of 850-1000°C and in a range of atmospheres. Impedance spectroscopy is conducted at OCV and at anodic overpotentials of up to 50 mV with an applied amplitude of 20-30 mV. This amplitude is verified to be well inside the linear range, and less than half the applied amplitude is perturbing the electrode due to the series resistance of the electrolyte pellet. The used frequency range is 65 kHz to 0.1 Hz. At least 20 minutes is allowed for stabilization before recording each impedance spectrum. Anode performance is expressed as the polarization resistance R_P at 1000°C at OCV in wet hydrogen.

The equipment used for impedance spectroscopy is a Solartron 1250 FRA combined with a Solartron 1286 ECI or an EG&G 273 potentiostat. The current measurement resistors used are 1 Ω for polarized and 10 Ω for unpolarized measurements. The two systems are verified on an appropriate test circuit to reproduce data within 1%.
After testing samples are cooled below 50°C in wet 9% H_2. Selected anodes are molded in epoxy, cut, ground and polished before inspection by optical and electron microscopy.

3.3 Results

3.3.1 Impedance Spectra

Recorded impedance spectra contain two or three distinct arcs, Figure 3.3. In general, data are fitted with the software EQUIVCRT by B.A. Boukamp,[37] using the equivalent circuit $LR_s(RQ)_1(RQ)_2(RQ)_3$ where L is an inductance, R a resistance and Q a constant phase element with the admittance $Y^*=Y_0(j\omega)^n$. Here Y_0 is an admittance, j the imaginary unit, ω the angular frequency and n is the frequency exponent.

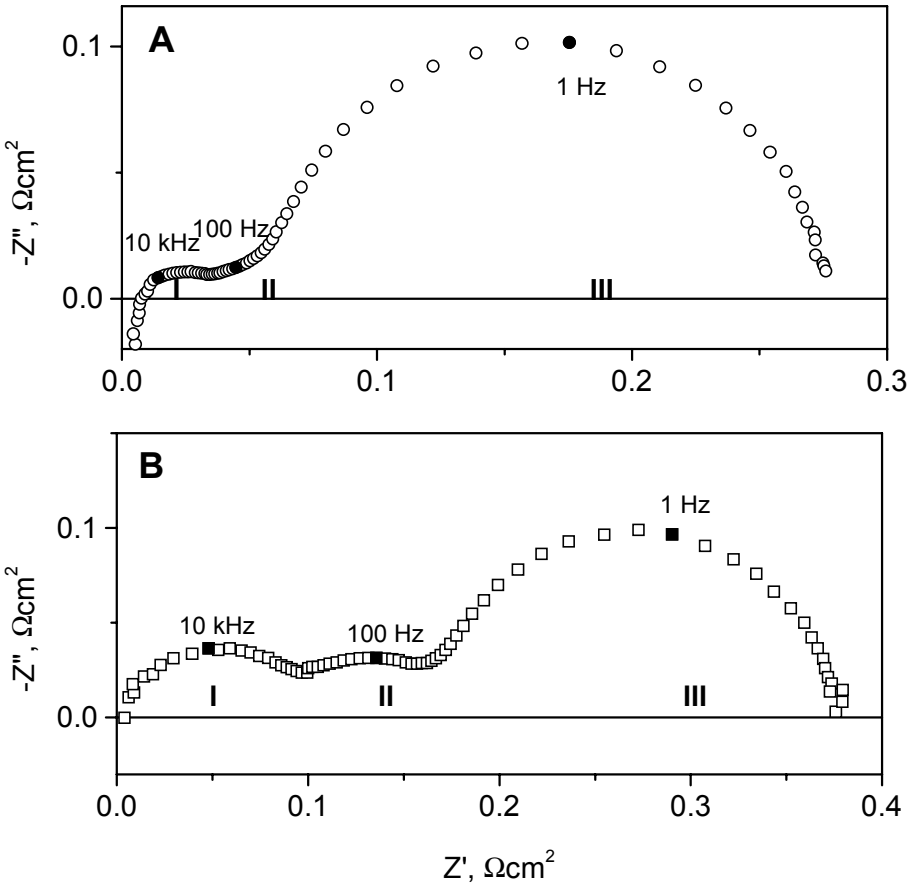

Figure 3.3 Recorded impedance spectra at 1000°C, OCV in wet hydrogen. A) Standard anode S7, B) Fine powder anode FF28. Roman numbers indicate numbering of arcs.

The inductance L is primarily ascribed to the leads, but variations are seen within measurements on the same electrode. For this reason L has not been restricted in any fits. R_s is electrolyte resistance between reference electrode and anode. Typical values at 1000°C for L and R_s are 10^{-7} H and 1-2 Ω, respectively.

The index-numbering of each arc is done by increasing time constant τ=RC, using the magnitude of Y_0 as a capacitance. In all cases the difference in parameter values makes a more refined criterion unnecessary. The processes causing each arc are denoted process I-III and the respective parameters R, Y_0 and n are given the subscript 1-3.

It is necessary to confine the nature of the constant phase elements and thus the frequency exponents n_{1-3} to obtain a consistent equivalent circuit. Only in cases where the n-values are constant, can different sets of R and Y_0 values be directly compared. The values (n_1,n_2,n_3)=(0.8, 0.75, 1.00) were selected after fitting a large number of anodes with distinct arcs under various relevant conditions[38]. The above mentioned equivalent circuit with constant n-values has proven capable of describing all impedance measurements satisfactorily with less than 2% relative error on both real and imaginary data at all frequencies. In the following sections the dependencies of the three processes on varying conditions are presented. A summary of the findings is given in Table 3.2.

Table 3.2 Summary of observed characteristics for the three rate limiting steps.

Parameter	**R_1**	**R_2**	**R_3**	**Figure**
Activation energy	0.8 eV	small, <0	small, <0	3.6
$1/R \propto pH_2^{\alpha}$, $pH_2<0.5$ atm $1/R \propto pH_2^{\alpha}$, $pH_2>0.5$ atm	$\alpha\approx0$ $\alpha\approx0$	$\alpha=0.1$-0.3 $\alpha=1$	$\alpha=0.2$ $\alpha=1$	3.9
$1/R \propto pH_2O^{\beta}$	$\beta\approx0$	$\beta=1$	$\beta=1$	3.8
Const. potential E $1/R \propto pH_2^{\alpha}pH_2O^{\beta}$, $pH_2<0.5$atm $1/R \propto pH_2^{\alpha}pH_2O^{\beta}$, $pH_2>0.5$atm	$\alpha+\beta=0.2$ $\alpha+\beta=0.5$	$\alpha+\beta=1.2$ $\alpha+\beta=2.3$	$\alpha+\beta\approx0$ $\alpha+\beta=1.3$	3.11
$\log(1/R) \propto k\eta$	$k=2.2\ V^{-1}$	$k=6.8\ V^{-1}$	$k=6\ V^{-1}$	3.7
	$Y_{0,1}$	**$Y_{0,2}$**	**$Y_{0,3}$**	
Frequency exponent	$n_1=0.8$	$n_2=0.75$	$n_3=1$	
$Y_0 \propto k/T$	$k<0$	$k=0$	$k>0$	3.13
Y_0 dep. on pH_2	slightly increasing	constant	slightly increasing	3.16
Y_0 dep. on pH_2O	decreasing	increasing	strongly increasing	3.15
Y_0 dep. on pH_2 and pH_2O (const. E)	slightly decreasing	slightly increasing	increasing	3.17
Y_0 dep. on η	linear, slightly decreasing	increasing	increasing	3.14
Nature of process	gas insensitive, depends on structure, changes on thermal ageing, $Y_{0,1}$ is factor 10^2 smaller than $Y_{0,2\text{-}3}$	gas sensitive, sens. to presence of felt current collector, dominant at low pH_2	gas sensitive, simple capacitance	
Suggested reaction	Charge transfer between YSZ and Ni, double layer capacitance	-	Bulk capacitance, possibly change of gas composition	

3.3.2 Cermet Structure

In this study, surprisingly little variation is observed in the electrochemical performance of anodes with modifications in microstructure, Figure 3.4. At the same time the spread in R_P measured on nominally identical anodes is considerable.
There is a tendency towards higher R_P for anodes with fine powders (identification code FF24-28), and even higher R_P for anodes with coarse YSZ (CY30-31). The high frequency resistance R_1 is higher by a factor of 5-8 whereas R_2 and R_3 are relatively unaffected (±25%) compared with standard reference anodes. Only the screen-printed coarse anode C32 with high Ni-loading has an R_P which is substantially higher than the standard.

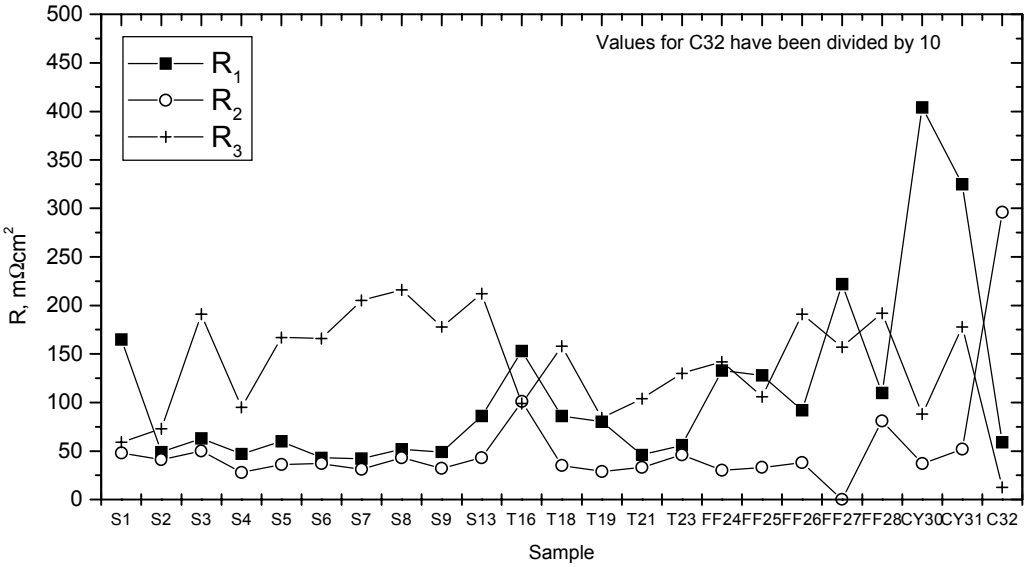

Figure 3.4 Polarization resistance for Ni/YSZ cermet anodes of varying structure, consult Table 3.1 for sample details. Impedance spectroscopy in wet hydrogen at OCV, 1000°C.

3.3.3 Cermet Thickness

No significant dependence of Rp on anode thickness has been found within the range of 20-70 μm, Figure 3.5. Impedance spectra recorded at 1000°C at OCV in wet hydrogen on anodes of 20 μm and 70 μm respectively are superimposable and indicate no differences. This observation is also taken as a verification of an efficient current collection from the full anode area to the central Pt wire.

Anodes of ~5 μm and ~10 μm have been tested, but are unable to sustain current collection over the sample surface causing an increasing and unstable R_P. A Ni-felt with insignificant electrochemical activity on YSZ (40 Ωcm^2 at 1000°C in wet hydrogen) has been applied as a current collector. This improves performance but degradation is still unacceptable for a characterization comparable to other electrodes.

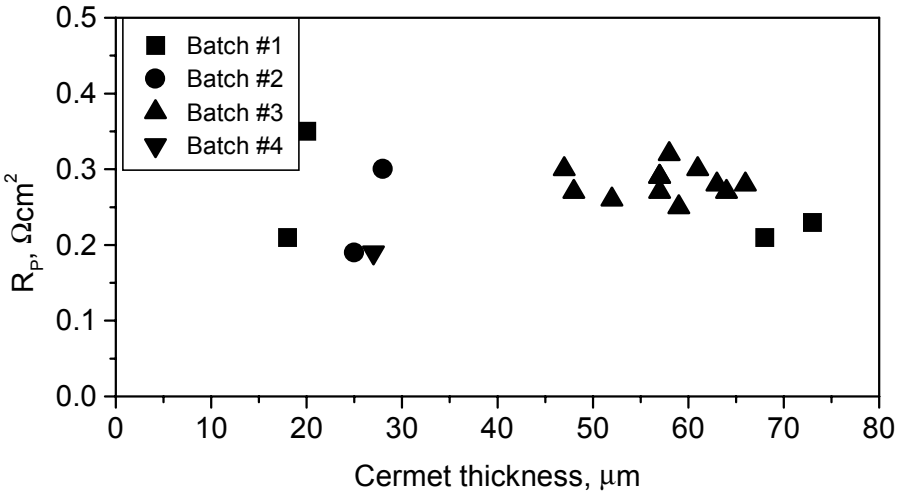

Figure 3.5 Polarization resistance as a function of cermet thickness on standard anodes in the range of 20-70 µm. Impedance spectroscopy in wet hydrogen at OCV, 1000°C.

3.3.4 Dependencies

For a standard anode the apparent activation energy of process I is close to 0.8 eV, Figure 3.6. Process II and III appears to be either unaffected or slightly deactivated by temperature. Using the total R_P of the same data the apparent anode activation energy is in the range of 0.5-0.7 eV.

The polarization resistance at 1000°C at OCV in wet hydrogen decreases with anodic polarization in the investigated range of 0-50 mV, Figure 3.7. The behavior at 850°C is similar. Process I appears to be the least sensitive to overpotential, whereas process II and III are equally sensitive.

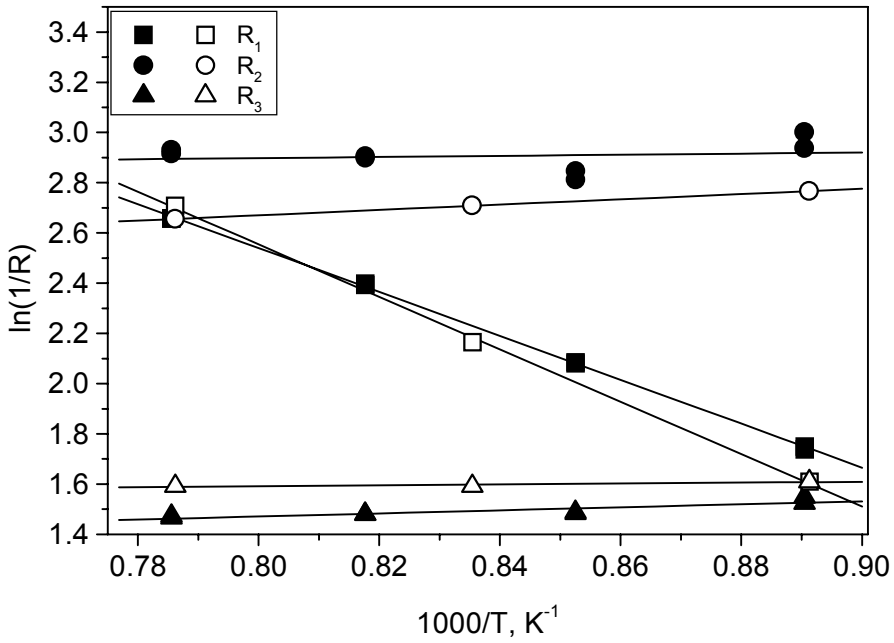

Figure 3.6 Thermal activation of rate limiting processes in the range of 850-1000°C. Impedance spectroscopy in wet hydrogen at OCV, 1000°C. R is in Ωcm^2. Anodes S3 (solid) and S5 (open).

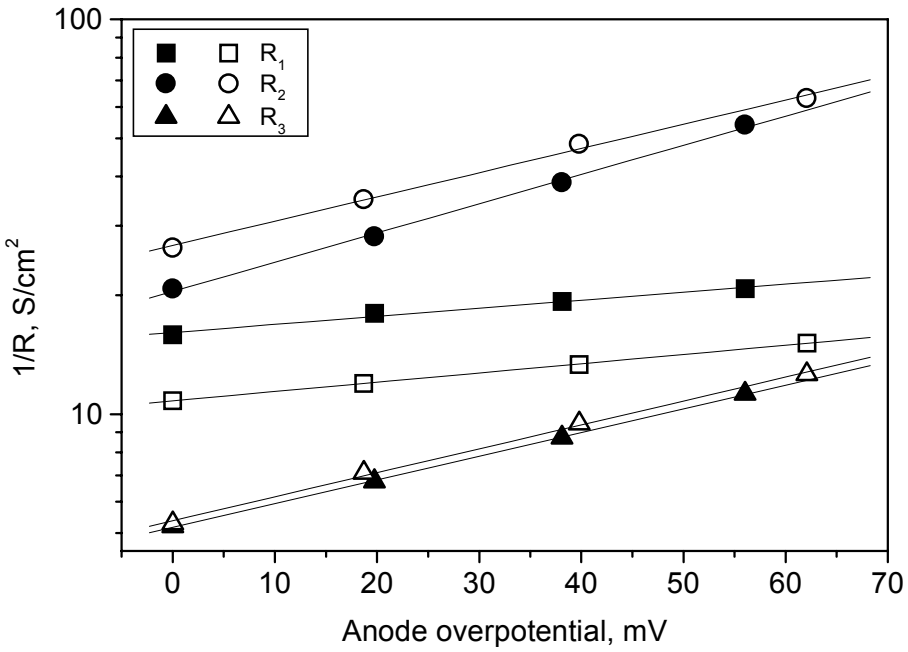

Figure 3.7 Polarization resistance depending on anodic overpotential at 1000°C in wet hydrogen. Standard anode S3 (solid) and fine powder anode FF26 (open).

Varying pH_2O in the ranges of 0.002-0.04 atm and 0.025-0.25 atm at a constant pH_2 of ~0.5 atm and ~1 atm respectively the polarization resistances for the three processes are presented in Figure 3.8. The reaction rate exponent for processes II and III is near 1, whereas process I is less sensitive to pH_2O. As a consequence of the varying pH_2/pH_2O the potential E is not constant.

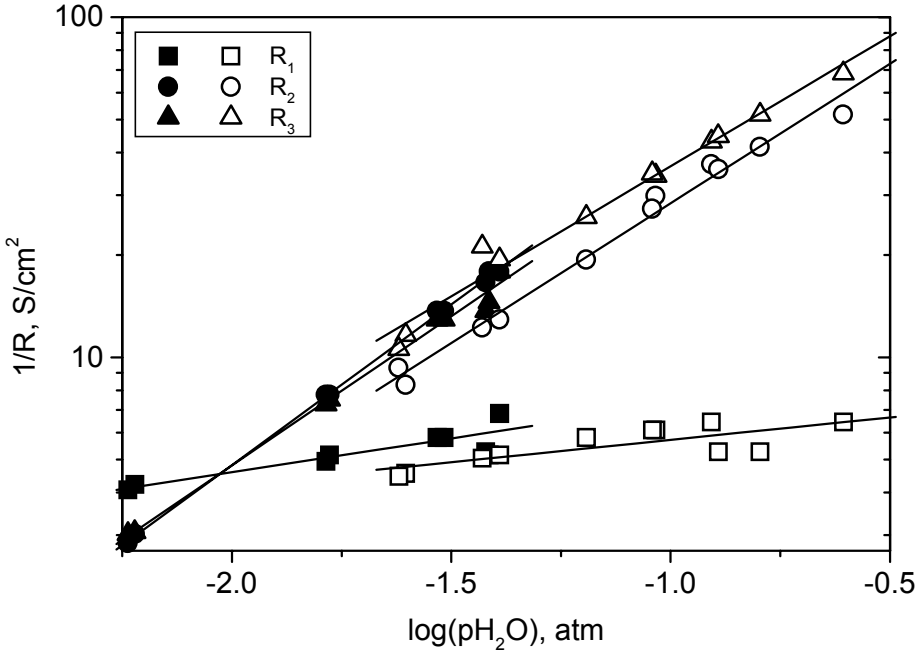

Figure 3.8 Polarization resistance as a function of steam partial pressure. Varying pH_2O from 0.2-4% in H_2 (solid) and from 2.5-25% in 50% H_2 (open). Balance is N_2. Standard anode S1 at 1000°C, OCV. The electrode potential is not constant in this plot.

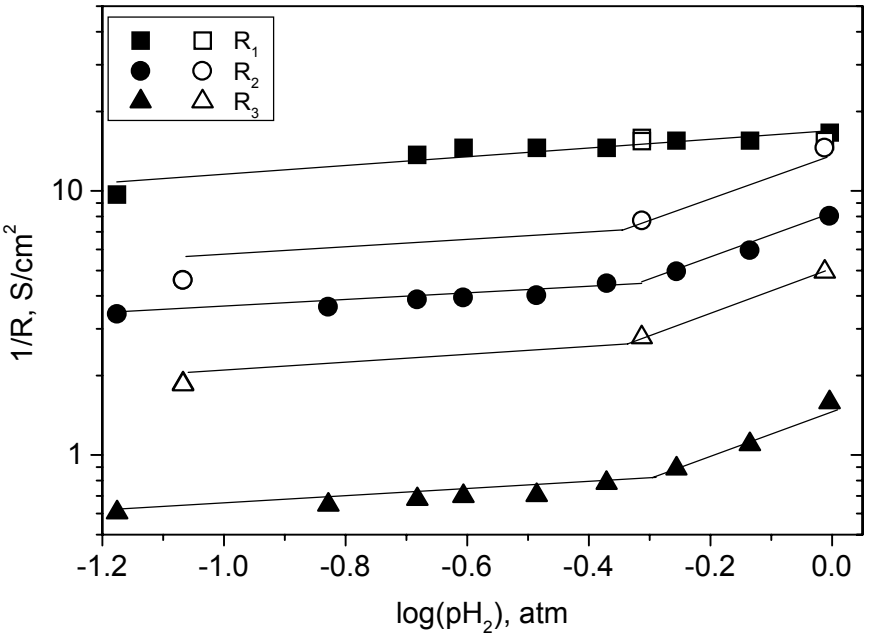

Figure 3.9 Polarization resistance at 1000°C, OCV against hydrogen partial pressure. Varying pH_2 from 5-100% in nitrogen with pH_2O constant at 1% (standard anode S9, solid) or 3% (standard anode S11, open).

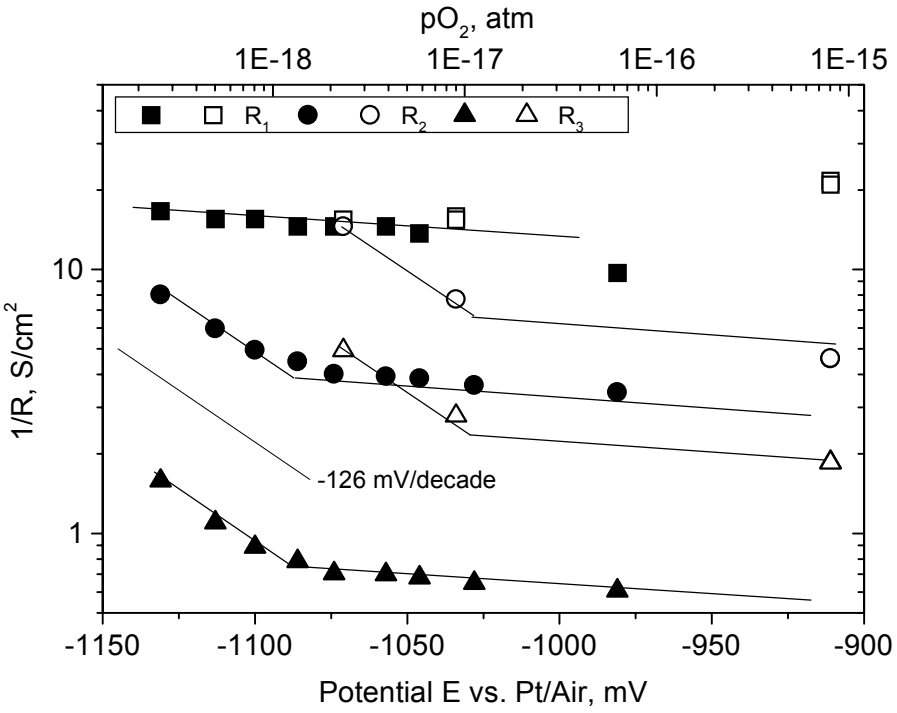

Figure 3.10 Replot of Figure 3.9 to demonstrate that E or pO_2 are not the correct parameters for describing the point of changing reaction mechanisms. Varying pH_2 from 5-100% in nitrogen with pH_2O constant at 1% (standard anode S9, solid) or 3% (standard anode S11, open).

Varying pH_2 in the range of 0.05-0.96 atm at constant pH_2O of 0.01 atm or 0.03 atm indicates a change of mechanism around pH_2~0.5 atm, Figure 3.9. At high pH_2 the reaction rate exponents for processes II and III are about 1, whereas process I is rather insensitive throughout the two regions. At low pH_2 both process II and III are less sensitive. Again the potential E is not constant. Re-plotting Figure 3.9 against E vs. Pt/Air clearly demonstrates how the change in mechanism is pH_2 dependent rather than potential dependent, Figure 3.10. The potential where the two sets of curves break is different by ~60 mV for 1% and 3% steam respectively. Figure 3.8 indicates that the change of properties is not related to pH_2O either.

Varying pH_2 in the range of 0.05-0.96 atm at a constant pH_2/pH_2O ratio of 32 (constant E) confirms the change of mechanism around pH_2~0.5 atm, Figure 3.11A. The high pH_2 range is re-plotted in Figure 3.11B. At high pH_2 the reaction rate exponent for process III is about 1.3 and about 2.3 for process II. In the low pH_2 range the reaction rate exponent for process II is about 1.2 and R_1 is less dependent on pH_2. In this range R_3 is too small (relative to R_2) to be interpreted.

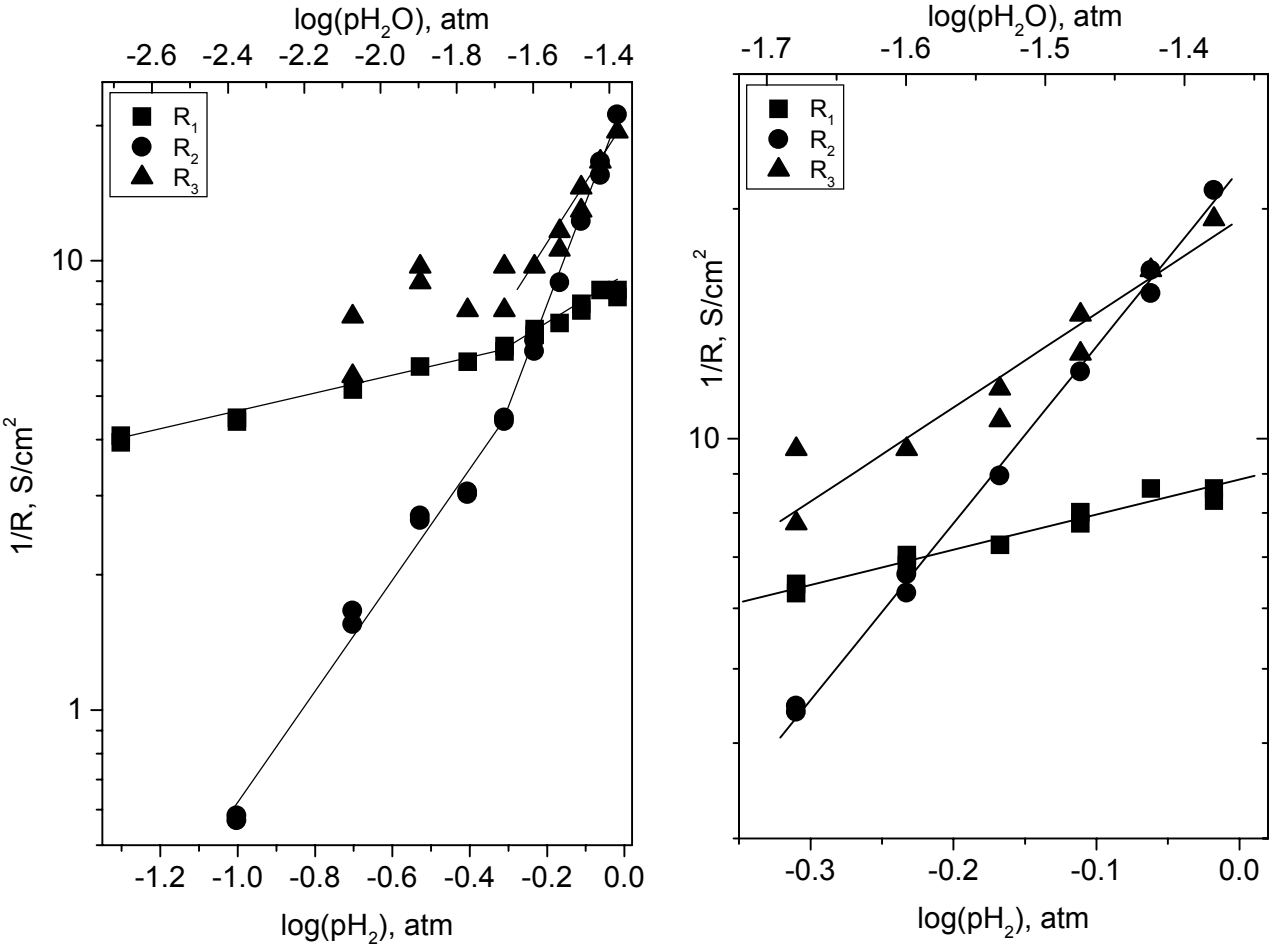

Figure 3.11 Polarization resistance against hydrogen partial pressure. A) Varying pH_2 from 0.05-0.97 atm at a constant pH_2/pH_2O ratio of 32. Standard anode S1 at OCV at 1000°C. At low pH_2 the magnitude of R_2 makes R_3 negligible. B) Replot of high pH_2 part of A).

3.3.5 Initial Performance and Aging

Standard anodes are in general quite stable as soon as the atmosphere composition has stabilized after the above given reduction procedure. However, using an alternative method and measuring the impedance shortly thereafter indicates a severe loss of activity within the first two hours. Heating the anode in air and switching to wet hydrogen at 1000°C yields an R_P of only 0.14 Ωcm^2 at OCV, half the value measured three hours later on the same sample and in general on standard samples heated in nitrogen according to standard reduction procedure, Figure 3.12. The ratios between the three reaction resistances remain fairly constant indicating a general loss of activity rather than one rate limiting process being retarded.

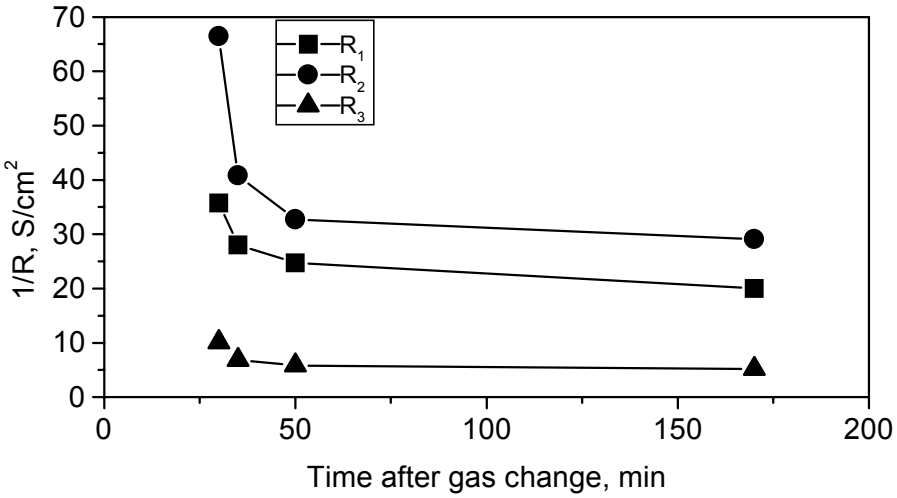

Figure 3.12 The inverse resistance as a function of time showing the initial aging of cermet anodes after heating in air and switching to wet hydrogen. Standard anode S12.

Thermal aging has a different effect on the three processes. Anodes FF24 and FF25 with fine particles were measured in wet hydrogen at 850°C before and after increasing the temperature to 1000°C for 24 hours. R_1 is increased by a factor 2, other parameters remain undisturbed (±20%). In this context further sintering of the Ni is expected to occur, whereas the already sintered YSZ is geometrically stable.

3.3.6 Capacitance and Constant Phase Elements

The constant phase elements relating to the resistances presented in Figures 3.7-3.13 are given in Figures 3.15-3.19. The dependencies of these parameters on varying conditions are summarized in Table 3.2.

$Y_{0,1}$ is an imperfect capacitance with the dimension $Ss^{0.80}$. The value of $Y_{0,1}$ is in the range of 2000-7000 $\mu Ss^{0.80}/cm^2$ nominal electrode area. $Y_{0,2}$ is in the interval of 0.05-0.9 $Ss^{0.75}/cm^2$ nominal electrode area. The ideal capacitance $Y_{0,3}$ is between 0.2 and 2.5 F/cm^2 nominal electrode area, and is very sensitive to pH_2O.

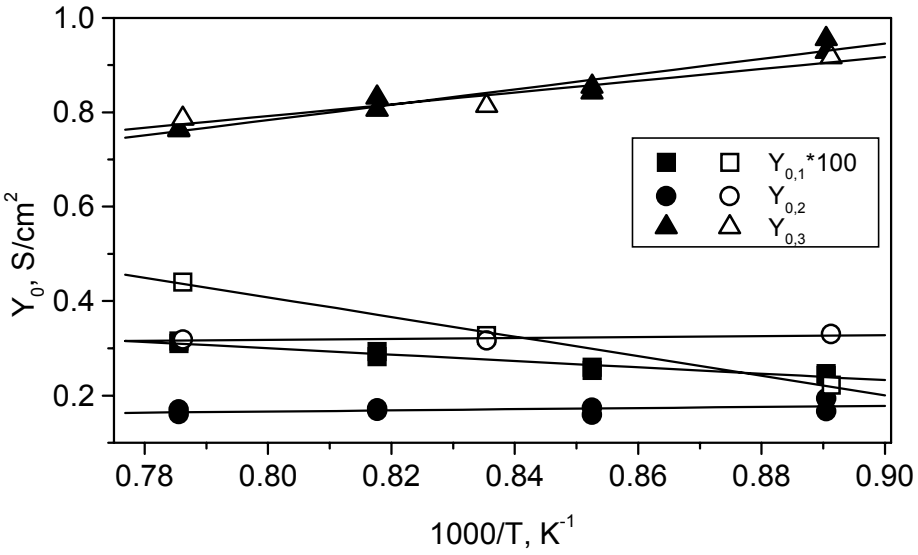

Figure 3.13 Constant phase element parameters in the range of 850-1000°C. Impedance spectroscopy in wet hydrogen at OCV, 1000°C. Anodes S3 (solid) and S5 (open).

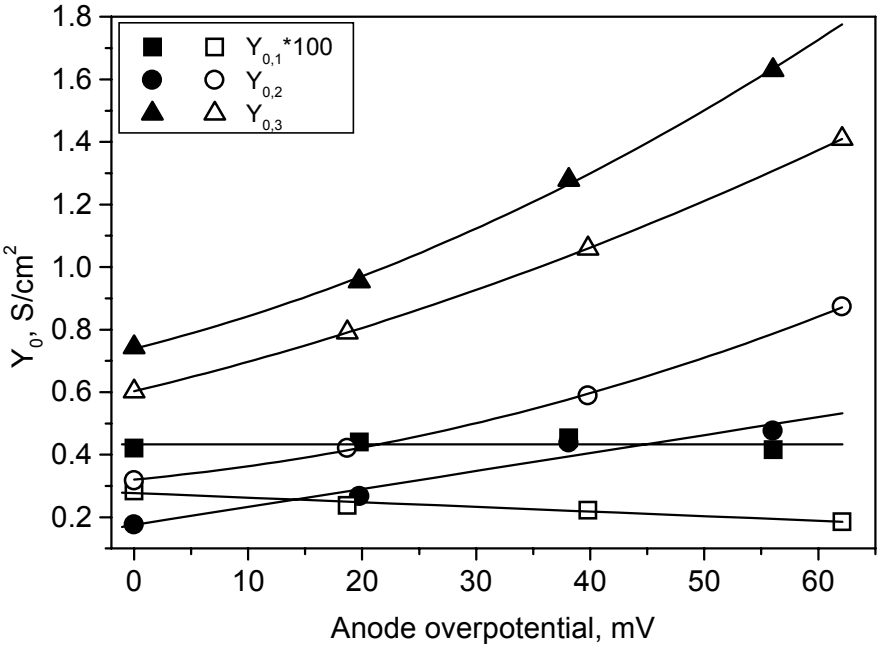

Figure 3.14 Constant phase element parameters as a function of anodic overpotential at 1000°C in wet hydrogen. Standard anode S3 (solid) and fine powder anode FF26 (open).

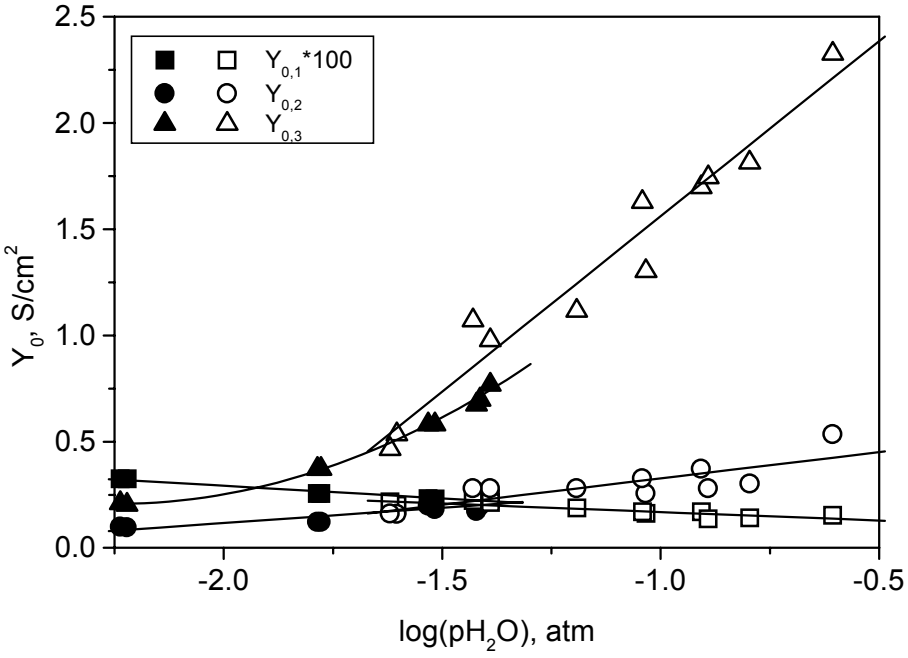

Figure 3.15 Constant phase element parameters as a function of steam partial pressure. Varying pH_2O from 0.2-4% in H_2 (solid) and from 2.5-25% in 50% H_2 (balance is N_2) (open). Standard anode S1 at 1000°C and OCV. The electrode potential is not constant in this plot.

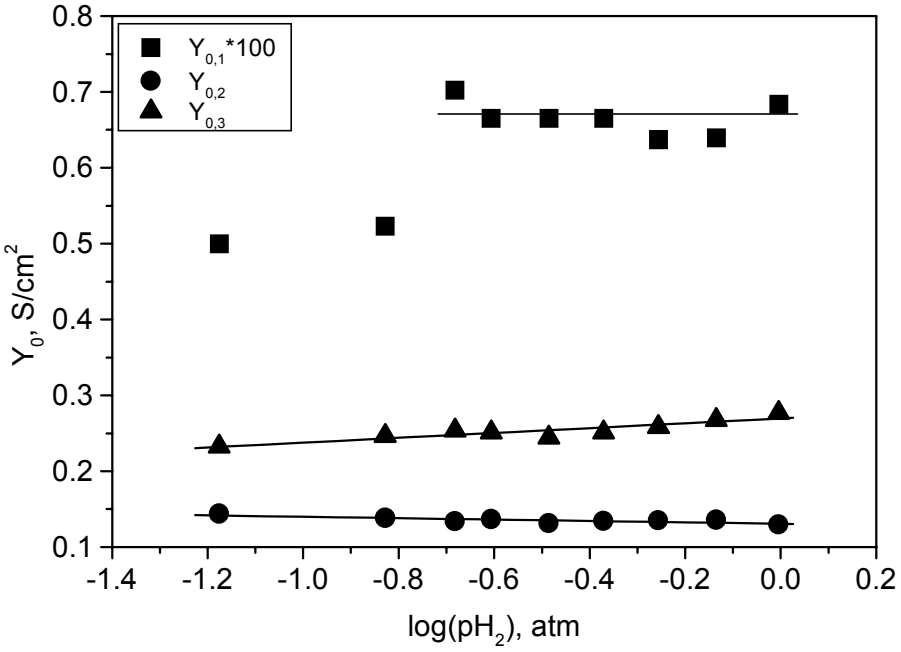

Figure 3.16 Constant phase element parameters at 1000°C, OCV as a function of hydrogen partial pressure. Varying pH_2 from 5-100% in nitrogen with pH_2O constant at 1%. Standard anode S9.

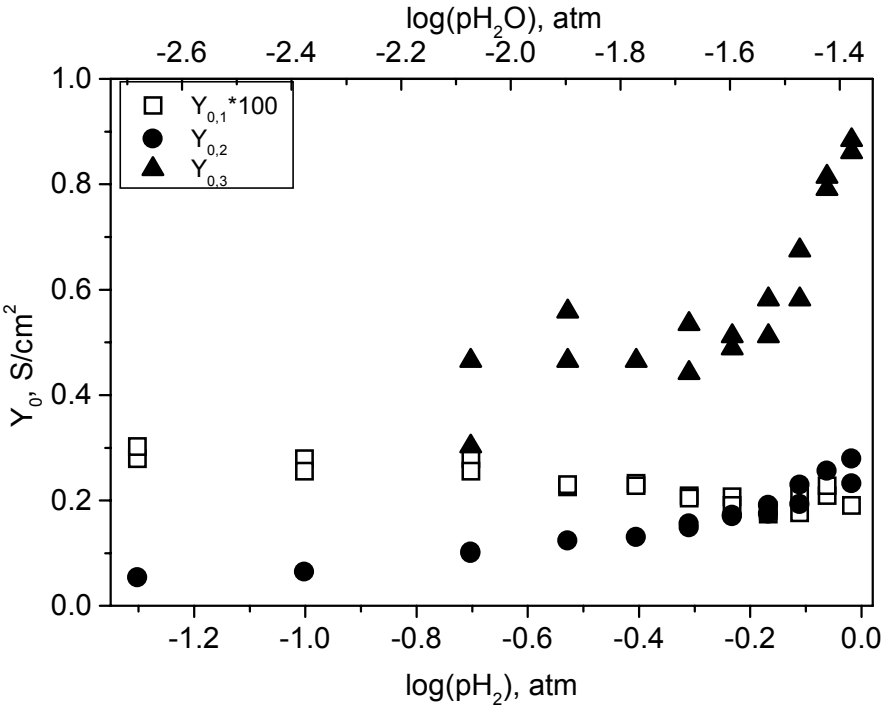

Figure 3.17 Constant phase element parameters as a function of hydrogen partial pressure. Varying pH_2 from 0.05-0.97 atm at a constant $pH_2/pH_2O = 32$. Standard anode S1 at OCV at 1000°C.

3.4 Discussion

3.4.1 Structure and Active Volume

Attempts to improve the method[35] and recipe used for standard anodes have proven to be difficult. However, further improvement of the structure is considered possible. Simple 50/50vol% cermet models such as a monolayer of 1 µm spheres using 1 µm TPB per particle contact and a specific polarization resistance of 10^3 Ωcm[19] indicate that an R_P as low as 0.04 Ωcm^2 should be achievable.

Of the three rate limiting processes, only process I seems to be significantly dependent on the cermet structure. The use of coarse YSZ grains causes an increase in R_1 only, and thermal aging of reduced anodes at 1000°C relative to measurements at 850°C also mainly affects R_1.

Neither of the resistances $R_{1\text{-}3}$ measured at 1000°C at OCV in wet hydrogen change with cermet thickness in the range of 20-70 µm. This result is taken as an indication of a less than 20 µm thick active volume of the cermet anode near the electrolyte interface at 1000°C.

More work is needed to deduce the relevant structural data from images of the cermet in order to clarify the link to electrochemical parameters. The first step in this process is to establish a series of different structures with sufficiently different electrochemical characteristics. Thereafter a comprehensive task of image analysis and modeling to relate 2-dimensional structural observations to a 3D-model remains.

In the temperature range of 850-1000°C the apparent activation energy for the full anode reaction is in the range of 0.5-0.7 eV compared with the activation energy of oxide ion conductivity in the electrolyte of 0.8-0.9 eV.[18,39] If it is then assumed that ionic resistance in YSZ is a limiting factor for the extent of the active electrode volume according to the considerations on thickness above, decreasing the temperature decreases the active part of a given cermet volume. In other words, to keep the active electrode geometry constant the full anode thickness must be small enough to be active at the minimum temperature used for deriving activation energies.

3.4.2 Number of Rate Limiting Processes

In the literature, attention to interpreting impedance spectra has been small, allowing only a limited comparison for the three rate limiting processes reported above.
Impedance spectra in wet hydrogen at 1000°C and at OCV on symmetric Ni-YSZ cermet anodes on YSZ-tape are reported by Dees *et al.*[23] Under these conditions R_P is 0.20 Ωcm^2, and results below 0.1 Ωcm^2 are indicated. At least two arcs are readily recognized at frequencies comparable with our findings, and it seems three arcs would be necessary to produce a satisfactory fit. Under the same conditions we find two dominant arcs present in impedance spectra on cermet anodes[30] and three arcs are needed during numeric fitting.[38] The same observations are valid for Ni/YSZ cermet anodes under similar conditions prepared at ECN.[40] Kawada *et al.*[21] reported only one arc in impedance spectra measured at the same conditions for cermet anodes sintered at 1500°C with a total R_P of 0.3 Ωcm^2. The summit of this arc is at 1 kHz. Identical anodes sintered at lower temperatures reveal how this one arc contains at least two arcs with similar time constants. Reported measurements on Ni/YSZ cermet anodes under other atmospheric compositions[1,31] contain more than one simple arc.

On the basis of these observations, it is suggested that at least three rate limiting processes are found in Ni/YSZ cermet anodes. These processes may be either chemical or physical. In some cases it seems that less than three arcs are present in impedance spectra. This is suggested to be an effect of the related time constants being of the same order of magnitude making the arcs difficult to separate.

3.4.3 Atmosphere Composition and Electrode Potential

In general, kinetic studies on anodes in hydrogen-water mixtures at elevated temperature are troubled by the close relationship between temperature, the partial pressures pH_2, pH_2O, pO_2 and electrode potential E. Neither of these parameters can be changed independently. The partial pressures pO_2 and pH_2O are often referred to in literature. Use of the parameter pO_2 in conjunction with SOFC anodes is suggested to be omitted in favor of the corresponding electrode potential E vs. Pt/air, as the extremely low partial pressure of oxygen molecules is considered of no direct relation to the electrochemical processes. Likewise, the tendency to focus on the controllable parameter pH_2O has led to a diminished attention to the accompanying changes in E and speculations of the product water as a catalytic reacting species.[41]

Strong evidence is given that a change is taking place in the processes II and III at pH_2~0.5 atm independently of potential E and pH_2O, Figures 3.9-3.12. A change of process at pO_2~10^{-15} atm in mixtures of H_2 and H_2O at 1000°C reported by Eguchi *et al.*[4] supports this finding as a pO_2 of 10^{-15} at 1000°C is obtained by using near by equal amounts of H_2 and H_2O.

3.4.4 Polarization and Atmosphere

Measurements at an anodic overpotential η in a gas composition with the equilibrium potential E involves a production of water molecules at the active TPB. This change of atmosphere composition is only partially suppressed by a high gas flow. Even though no evidence of diffusion limitations in the porous structure has been observed, the bulk composition of the gas may be changed. As an estimate, an anodic overpotential of η=50-60 mV on standard anodes corresponds with 250 mA/cm^2 at 1000°C. At the used flowrates (100 ml/min, 3% H_2O) the water evolved causes E to decrease by approximately 12 mV in the bulk atmosphere, leading to a probable error of +20% on η, which the above given data and Figure 3.7 are not corrected for.

Guindet *et al.* have given impedance spectra under polarization of a Ni ball on YSZ at 960°C and pH_2=0.195 atm, pH_2/pH_2O=7.15.[28,29] The decreasing resistances at increasing polarization and two dominant arcs of which the low-frequency is almost a semicircle and the high-frequency is somewhat suppressed is similar to our findings on cermets at 1000°C in wet hydrogen, Figure 3.7.

3.4.5 Capacitive Elements

Highly capacitive elements are frequently encountered in solid electrodes, but no explanation of this has been offered.

By combining the imaginary part of the admittance representation of a constant phase element (3.3) with the admittance of a capacitance (3.4), the frequency dependent capacitance C(f) of a constant phase element at any frequency f is given by (3.5).

$$Y(\omega) = Y_0\omega^n \cos(\frac{n\pi}{2}) + jY_0\omega^n \sin(\frac{n\pi}{2}) \tag{3.3}$$

$$Y(\omega) = j\omega C \tag{3.4}$$

$$C(f) = Y_0(2\pi f)^{n-1} \sin(\frac{n\pi}{2}) \tag{3.5}$$

The summit frequency for a parallel RQ is given by (3.6).[42]

$$f_{Summit} = \frac{1}{2\pi}\left(RY_0\right)^{-1/n} \tag{3.6}$$

For all three processes, f_{Summit} appears to vary systematically within one decade with pH_2 and pH_2O over the studied ranges, whereas f_{Summit} is virtually constant with temperature, Fig. 20. For each process this reciprocal time constant is taken as evidence of the parallel components (RQ) representing features of the same process. The summit frequencies are as averages represented as 10 kHz for process I, 100 Hz for process II and 10 Hz for process III.

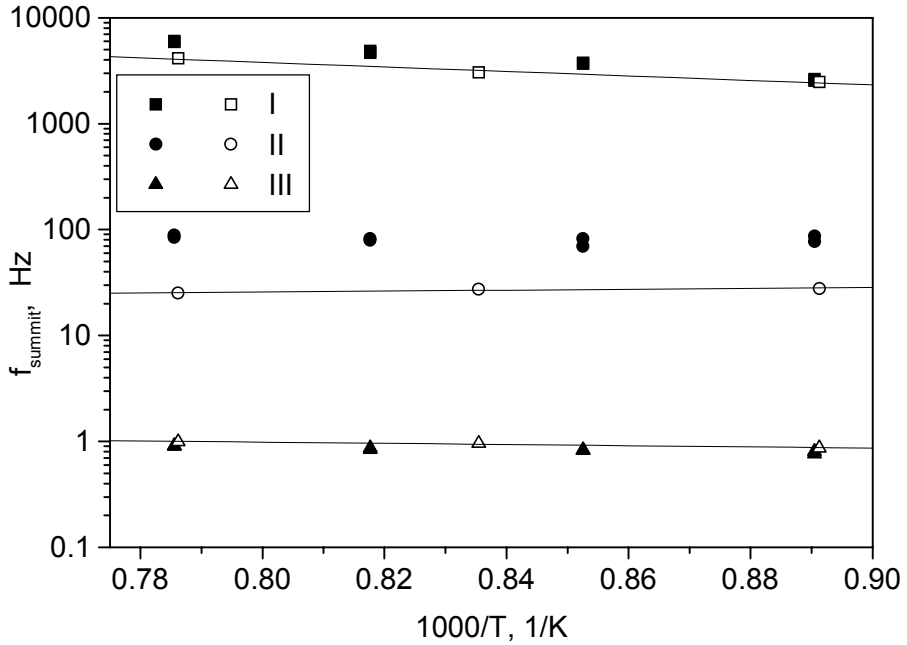

Figure 3.18 Summit frequency as calculated from equation [8] in the temperature range 850 to 1000°C. Anodes S3 (solid) and S5 (open).

$Y_{0,1}$ is in the range of 2-7 $mSs^{0.8}/cm^2$ nominal interface corresponding to 200-700 $\mu F/cm^2$ nominal electrode area at 10 kHz. $Y_{0,2}$ in the interval of 0.05-0.9 $Ss^{0.75}/cm^2$ nominal electrode area corresponds to 9-200 mF/cm^2 nominal electrode area at 100 Hz according to (3.5). The simple capacitance $Y_{0,3}$ is between 0.2 and 2.5 F/cm^2 nominal electrode area.

As an order of magnitude estimate, a simple model calculation based on anode weight loading (~11 mg/cm^2, 40 vol% Ni), Ni spheres of 2 µm and YSZ spheres of 1 µm predicts about 50 cm^2 YSZ surface, 20 cm^2 Ni surface and 10 cm^2 percolating Ni/YSZ interface per nominal cm^2 in a 50 µm thick standard cermet anode. Only the interface between Ni and YSZ grains which both percolate to respectively current collector and electrolyte should be considered, as only these interfaces experience a potential perturbation.

In the following a few estimates are presented to indicate which capacities could be expected from the anode structure.
For the double layer capacitance models predict a maximum of 30 $\mu F/cm^2$ at a minimum acceptable plate spacing of 0.3 Å, equal to 1/4 diameter of an oxide ion.[43] Accepting 10 cm^2/cm^2 Ni/YSZ interface on the anode this corresponds with 300 $\mu F/cm^2$ nominal electrode area.
The potential capacitance of adsorbed/absorbed charged species is estimated as (3.7).

$$C = k \cdot zNF / U \tag{3.7}$$

where z is the charge of a species, N the maximum number of molecules calculated from the geometric data with an equilibrium coverage θ of 1, F is the Faraday constant and U the applied perturbation voltage, in this case taken to be 10 mV. In the following only 1% of the adsorbed/absorbed species is assumed to be converted in one AC cycle, therefore k=0.01.

Adsorption of a monocharged species with an adsorption site area of 3 $Å^2$ on the 50 cm^2/cm^2 YSZ surface corresponds with a capacitance of 30 mF/cm^2 nominal electrode area. Equally adsorption on the Ni surface corresponds with 10 mF/cm^2.
Absorption of H^+ in the bulk of the porous YSZ has been considered. With a solubility of 1 $\mu mol/cm^3$ H^+ in YSZ at 1000°C[44] and $8 \cdot 10^{-4}$ cm^3 YSZ per cm^2 anode, the capacitance is 80 $\mu F/cm^2$ nominal electrode area. A similar calculation for Ni using a solubility of $1 \cdot 10^{-4}$ mol/cm^3 at 1000°C[44] and $6 \cdot 10^{-4}$ cm^3 Ni per cm^2 yields a capacitance of 6 mF/cm^2 nominal electrode area.

3.4.6 Nature of Rate Limiting Processes

At an electrode potential of -700 mV to -900 mV vs. Pt/air at 1000°C a relatively high equilibrium coverage of oxide, $\theta_{O^{2-}}$, and/or hydroxide, θ_{OH^-}, of the order of 0.1-1 may be assumed. Under these conditions it has been suggested that a probable reaction mechanism might be the full oxidation of H_2 on Ni.[1,4,26,28,41,45] At E< -950 mV vs. Pt/air at 1000°C where the oxide/hydroxide coverage on Ni is expected to be low ($\theta < 0.01$) this mechanism seems unlikely for the following reasons:[46] i) The dissociative adsorption of H_2 on Ni is fast and ii) The diffusion of H_{ads} on a nickel surface is fast. Therefore protons are considered available in excess on the Ni-YSZ contact. Furthermore the reaction on the interface is expected to involve protons moving to the YSZ rather than oxide ions moving to the Ni.

Process I is the most insensitive to atmosphere composition, electrode potential and polarization. R_1 has an activation energy of 0.8 eV, comparable with activation energies for conduction. R_1 relates significantly to structural variations induced by altering the powder particle size distribution used for producing the cermets and increases by thermal aging of reduced anodes. $Y_{0,1}$ is interpretable as the double layer capacitance of the Ni/YSZ interface. As a natural consequence of this interpretation of $Y_{0,1}$, the parallel resistance R_1 is attributed to the transfer of charged species (protons) across the Ni/YSZ interface. Presumably some of the O^{2-}-resistance through YSZ particles in the porous electrode are contributing too, due to the distributed length of transport.[47] The suppression of this arc is also qualitatively explained by this distribution of resistance.

Process II is the most sensitive to atmosphere composition at constant electrode potential and constitutes the dominant polarization resistance at low pH_2. The electrode structure has a limited influence on R_2. The dependence of R_2 on potential at high pH_2 (Figure 3.10) has been discussed previously[30] and suggests a two-electron transfer process. At present too little evidence is available for identifying this process with certainty.

Process III is in many ways similar to process II. The main difference is observed below a pH_2 of 0.5 atm at constant electrode potential, where R_3 is small and rather insensitive to pH_2. The magnitude of the perfect capacitance $Y_{0,3}$ is from 0.25 to 2.5 F/cm^2 nominal electrode area, and very sensitive to pH_2O. Considering the increase in $Y_{0,3}$ by increasing pH_2O suggests adsorption of water as the origin of this capacitance. Given the consideration on available capacitance above, the most reasonable explanation is adsorption of water on the YSZ surface. However, this explanation involves exchange of the total amount of adsorbed molecules, not only a few percent as could be expected. Alternatively, a change of the gas phase composition could be the explanation.

3.5 Conclusion

The performance of a Ni-YSZ anode is dependent on the cermet structure. The electrochemically active region of examined cermets extends no more than 20 μm from the electrolyte interface at 1000°C, and it is probably even smaller at lower temperatures.

At least three rate limiting processes contribute to the polarization resistance of Ni/YSZ cermet anodes. Measured impedance spectra for different cermet anode structures under variation of T, η and gas composition are described well by the equivalent circuit $LR(RQ)_1(RQ)_2(RQ)_3$ where Q is a constant phase element with the admittance $Y^*=Y_0(j\omega)^n$, using the constant values $(n_1,n_2,n_3)=(0.8, 0.75, 1)$ to obtain sets of R and Y_0 which can be compared directly.

The high frequency reaction I is thermally activated, E_a = 0.8 eV. The high frequency reaction resistance R_1 is comparatively insensitive to pH_2 and pH_2O in the ranges studied, and relatively insensitive to anodic overpotential. This process is the only one sensitive to the cermet structure (varied by particle size), and the associated capacitance is comparable with that expected from a double layer capacitance at the Ni/YSZ interface. Therefore R_1 is attributed to a combination of resistance of charge transfer from Ni to YSZ and O^{2-}-resistance in YSZ particles in the cermet.

The reactions II and III at medium and low frequency, respectively, exhibit no thermal activation or dependence on structure. Both processes are sensitive to pH_2 and pH_2O and anodic polarization. The dependence on atmosphere indicates a change of mechanism at $pH_2 \approx 0.5$ atm, irrespective of E and pH_2O.

The capacitance associated with R_3 is in the order of 0.5-2.5 F/cm^2 nominal electrode area and very dependent on pH_2O. The magnitude suggests changes in bulk composition rather than surface adsorption of charged species.

Acknowledgment

This work was supported in part by the European Commission under contract no. JOUE-CT92-0063 and in part by ELSAM and the Danish Energy Agency under the Danish DK-SOFC-program. Discussions with Dr. Svein Sunde, Risø National Laboratory, and Dr. Torben Jacobsen, Technical University of Denmark, are appreciated. The present data have been generated as a result of the joint effort of many members of the SOFC project group at Risø. Their contributions are gratefully acknowledged.

References

[1] T. Setoguchi, K. Okamoto, K. Eguchi and H. Arai, *J. Electrochem. Soc.* **139** 2875 (1992)
[2] M. Suzuki, H. Sasaki, S. Otoshi, A. Kajimura and M. Ippommatsu, *Solid State Ionics*, **62** 125 (1993)
[3] H. Uchida, M. Yoshida and M. Watanabe, *J. Phys. Chem.* **99** 3282 (1995)
[4] K. Eguchi, T. Setoguchi, K. Okamoto and H. Arai, In *SOFC III*, S.C. Singhal and H. Iwahara, Editors, **PV 93-4**, The Electrochemical Society Proceedings Series, Pennington, NJ. 494 (1993)
[5] M. Watanabe, H. Uchida, M. Shibata, N. Mochizuki and K. Amikura, *J. Electrochem. Soc.*, **141** 342 (1994)
[6] Z. Ogumi, T. Ioroi, Y. Uchimoto, Z. Takehara, T, Ogawa and K. Toyama, *J. Am. Ceram. Soc*. **78** 593 (1995)
[7] N.Q. Minh, *J. Am. Ceram. Soc*. **76** 563 (1993)
[8] T. Saito, in *SOFC Micromodelling, an Int. Energy Agency SOFC Task Report*, L. Dubal, Editor. Swiss Federal Office of Energy, Berne, CH (1992)
[9] N. Nakagawa, H. Sakurai, K. Kondo, T. Morimoto, K. Hatanaka and K. Kato *J. Electrochem. Soc.* **142** 3474 (1995)
[10] R. Männer, E. Ivers-Tiffée and W. Wersing, in *SOFC II*, F. Grosz, P. Zegers, S. C. Singhal and O. Yamamoto, Editors. EUR-13564-EN, 715 (1991)
[11] A. Rahmel and M. Schütze *Oxid. Met*. **38** 255 (1992)
[12] M. M. Murphy, J. Van herle, A. J. McEvoy and K. R. Thampi, *J. Electrochem. Soc.* **141** L94-96 (1994)
[13] H.L. Tuller in *Nonstoichiometric oxides*, O. T. Sørensen, Editor, Materials Science series, Academic Press. 271 (1981)
[14] C. Wagner, *Ber. Bunsenges. Physik. Chem.* **72** 778 (1968)
[15] M. Kleitz, T. Kloidt and L. Dessemond In *High Temperature Electrochemical Behaviour of Fast Ion and Mixed Conductors,* F. W. Poulsen, J. J. Bentzen, T. Jacobsen, E. Skou and M. J. L. Østergård, Editors, 14th Risø International Symposium on Materials Science, Roskilde, DK. 89 (1993)
[16] M. Juhl, S. Primdahl, C. Manon and M. Mogensen, *J. Power Sources* **61** 173 (1996)
[17] T. Kawada, N. Sakai, H. Yokokawa, M. Dokiya, M. Mori and T. Iwata, *Solid State Ionics*, **40/41** 402 (1990)
[18] F. T. Ciacchi, K. M. Crane and S. P. S. Badwal, *Solid State Ionics*, **73** 49 (1994)
[19] P. A. Osborg and T. Norby, in *7th SOFC WORKSHOP, Theory and measurement of Microscale Processes in Solid Oxide Fuel Cells*, 47 (1995). IEA report obtainable from H. Nabielek, KFA-ISR Forschungszentrum Jülich GmbH, D-52425 Jülich, Germany.
[20] M. J. Powell, *Phys. Rev. B*, **20** 4194 (1979)
[21] T. Kawada, N. Sakai, H. Yokokawa, M. Dokiya, M. Mori and T, Iwata, *J. Electrochem. Soc.* **137** 3042 (1990)
[22] D. W. Dees, T. D. Claar, T. E. Easler, D. C. Fee and F. C. Mrazek, *J. Electrochem. Soc.*, **134** 2141 (1987)
[23] D. W. Dees, U. Balachandran, S. E. Dorris, J. J. Heiberger, C. C. McPheeters and J. J. Picciolo, in *SOFC I*, S. C. Singhal, Editor, **PV 89-11** The Electrochemical Society Proceedings Series, Pennington, NJ. 317 (1989)
[24] F. P. F. van Berkel, F. H. van Heuveln and J. P. P. Huijsmans *Solid State Ionics*, **72** 240 (1994)
[25] T. Norby, O. J. Velle, H. Leth-Olsen and R. Tunold in *SOFC III*, S. C. Singhal and H. Iwahara, Editors, **PV 93-4**, The Electrochemical Society Proceedings Series, Pennington, NJ. 473 (1993)
[26] J. Mizusaki, H. Tagawa, T. Saito, T. Yamamura, K. Kamitani, K. Hirano, S. Ehara, T. Takagi, T. Hikita, M. Ippommatsu, S. Nakagawa and K. Hashimoto, *Solid State Ionics*, **70/71** 52 (1994)
[27] J. Mizusaki, H. Tagawa, T. Saito, K. Kamitani, T. Yamamura, K. Hirano, S. Ehara, T. Takagi, T. Hikita, M. Ippommatsu, S. Nakagawa and K. Hashimoto, *J. Electrochem. Soc.* **141** 2129 (1994)
[28] J. Guindet, C. Roux and A. Hammou in *SOFC II*, F. Grosz, P. Zegers, S.C. Singhal and O. Yamamoto, Editors, EUR-13564-EN, 553 (1991)
[29] J. Guindet, *Contribution a L'etude de Materiaux d'Anode pour Pile a Combustible a Oxyde Electrolyte Solide*, Thesis (in french), Institut National Polytechnique de Grenoble (1988)

[30] M. Mogensen and T. Lindegaard, in *SOFC III*, S.C. Singhal and H. Iwahara, Editors, **PV 93-4**, The Electrochemical Society Proceedings Series, Pennington, NJ. 484 (1993)
[31] J. Divisek, L. G. J. de Haart, P. Holtappels, T. Lennartz, W. Malléner, U. Stimming and K. Wippermann, *J. Power Sources*, **49** 257 (1994)
[32] J. Winkler, P. V. Hendriksen, N. Bonanos and M. Mogensen *J. Electrochem. Soc.* **145** 1184 (1998)
[33] M. Nagata, Y. Itoh and H. Iwahara, *Solid State Ionics*, **67** 215 (1994)
[34] H. Narita, J. Mizusaki and H. Tagawa, *Denki Kagaku*, **60** 756 (1993)
[35] C. Bagger, In *1992 Fuel Cell Seminar,* Courtesy Associates, INC. Washington D.C. 241 (1992)
[36] R. Hartung and H.-H. Möbius, *Chemie-Ing. Techn*., **40** 592 (1968)
[37] B. A. Boukamp, *Solid State Ionics*, **20** 31 (1986)
[38] M. Mogensen, S. Primdahl, J. T. Rheinländer, S. Gormsen, S. Linderoth and M. Brown, In *SOFC IV,* M. Dokiya, O. Yamamoto, H. Tagawa and S. C. Singhal, Editors, **PV 95-1**, The Electrochemical Society Proceedings Series, Pennington, NJ. 657 (1995)
[39] S. P. S. Badwal *Solid State Ionics* **52** 23 (1992)
[40] J. P. de Jong, ECN, Petten, Holland, *Private communication* (1996)
[41] N. Q. Minh and T. Takahashi, *Science and Technology of Ceramic Fuel Cells*, Elsevier Science B.V. (1995)
[42] T. Jacobsen, B. Zachau-Christiansen, L. Bay and S. Skaarup in *High Temperature Electrochemistry: Ceramics and Metals*. F. W. Poulsen, N. Bonanos, S. Linderoth, M. Mogensen and B. Zachau-Christiansen, Editors, 17th Risø International Symposium on Materials Science, Roskilde, DK. 29 (1996)
[43] N. L. Robertson and J. N. Michaels, *J. Electrochem. Soc.* **138** 1494 (1991)
[44] M. Mogensen, S. Sunde and S. Primdahl in *High Temperature Electrochemistry: Ceramics and Metals*. F. W. Poulsen, N. Bonanos, S. Linderoth, M. Mogensen and B. Zachau-Christiansen, Editors, 17th Risø International Symposium on Materials Science, Roskilde, DK. 77 (1996)
[45] M. Mogensen, in *High Temperature Electrochemical Behaviour of Fast Ion and Mixed Conductors,* F. W. Poulsen, J. J. Bentzen, T. Jacobsen, E. Skou and M. J. L. Østergård, Editors, 14th Risø International Symposium on Materials Science, Roskilde, DK. 117 (1993)
[46] M. Mogensen and S. Skaarup, *Solid State Ionics,* **86-88** 1151 (1996)
[47] J.R. Macdonald, *Impedance Spectroscopy*, John Wiley & Sons, Inc. New York (1978)
[48] A. Kuzjukevics, S. Linderoth and J. Grabis in *High Temperature Electrochemistry: Ceramics and Metals*. F. W. Poulsen, N. Bonanos, S. Linderoth, M. Mogensen and B. Zachau-Christiansen, Editors, 17th Risø International Symposium on Materials Science, Roskilde, DK. 319 (1996)

Chapter 4

Gas Conversion Impedance[†]

Abstract

The appearance of an extra arc in impedance spectra obtained on high performance solid oxide fuel cell (SOFC) anodes is recognized when experiments are conducted in a test setup where the working and reference electrodes are placed in separate atmospheres. A simple continuously stirred tank reactor (CSTR) model is used to illustrate how anodes measured with the reference electrode in an atmosphere separate from the working electrode is subject to an impedance contribution from gas conversion. The gas conversion impedance is split into a resistive and a capacitive part, and the dependencies of these parameters on gas composition, temperature, gas flow-rate and rig geometry is quantified. The fuel gas flow-rate per anode area is decisive for the resistivity, whereas the capacitance is proportional to the CSTR volume of gas over the anode. The model predictions are compared with actual measurements on Ni/Yttria stabilized zirconia (YSZ) cermet anodes for SOFC. The contribution of the gas conversion overpotential to DC current-voltage characteristics is deduced for H_2/H_2O and shown to have a slope of RT/2F in a Tafel plot.

[†] This chapter has been published as S. Primdahl and M. Mogensen, "Gas Conversion Impedance, a Test Geometry Effect in Characterization of Solid Oxide Fuel Cell Anodes", *J. Electrochem. Soc.* **145** 2431-2438 (1998)

4.1 Introduction

A detailed understanding of the rate limiting steps in state-of-the-art Ni/YSZ cermet SOFC anodes is highly desirable from an optimization point of view. One of the most promising ways of unraveling such complex systems is by impedance spectroscopy. Here a number of more or less well-separated arcs representing at least the same number of processes can be analyzed individually as function of the primary test conditions.

Ni/YSZ cermet anodes for SOFC have been investigated intensively and impedance spectra and interpretations of these have been offered in literature.[1-10] The findings are surprisingly inconsistent judging from the number of reported arcs in impedance spectra, even considering the different anode structures and test conditions applied. In this chapter it is demonstrated how part of the disagreement may originate in the measurement setup rather than in the examined electrodes.

Considering a single electrode on an electrolyte (i.e. a half cell), the electrode overpotential $\eta_{Electrode}$ is given as the electrode potential $E(i)$ at current density i minus the equilibrium potential $E_{Eq.}$ (Nernst potential = zero-current-potential) corrected for the potential loss in the electrolyte of series resistance R_S, Eq. (4.1).

$$\eta_{Electrode} = E(i) - E_{Eq.} - iR_S \tag{4. 1}$$

This electrode overpotential is the summation of overpotentials of k rate limiting processes in the electrode, Eq. (4.2). Processes like chemical reactions, charge transfer and diffusion in the electrode are typically to be considered.

$$\eta_{Electrode} = \sum_{\alpha=1}^{k} \eta_{\alpha} \tag{4. 2}$$

One of the important assumptions in the above definitions is a sufficiently high flow-rate of reactants to the cell to suppress concentration changes above the surface of the working electrode. It is the breakdown of this assumption which is examined below.
When a working electrode and a reference electrode are placed in different atmospheres all electrochemical measurements involve the Nernst potential E, Eq. (4.3), between the oxygen partial pressures of these atmospheres.

$$E = \frac{RT}{4F} \ln\left(\frac{x_{O_2,red}}{x_{O_2,ox}}\right) \tag{4. 3}$$

Here R, T and F have their usual meaning. x_{O_2} refers to the molar fraction of O_2 in the reducing and oxidizing atmospheres, respectively. Variations in x_{O_2} in each of the compartments is a product of the gas flow rate per anode area, conversion by passing current and gas mixing by diffusion, convection and stirring. This phenomenon has already been considered and measured for DC-loading of fuel cells.[11,12] The variation in the Nernst potential is inherent to the passage of

current, and must be anticipated also in impedance measurements. It is here suggested to use the term gas conversion impedance.

It is the aim of this chapter to i) draw attention to the presence of gas conversion impedance in SOFC research, and ii) to quantify the nature of gas conversion impedance and predict the AC and DC responses by introducing a simple CSTR model. Finally it is important to note how the presence of gas conversion impedance depends on the measurement setup.

4.2 Experimental

4.2.1 Sample Preparation

A 40 to 50 μm thick Ni/YSZ cermet anode is prepared by spray-painting. The ethanol based slurry is composed of green NiO and YSZ (Tosoh, ZrO_2 with 8 m/o Y_2O_3), suspended by a dispersant (polyvinyl pyrrilidone).[13] After deagglomeration in a ball mill, the YSZ particle size is about 0.4 μm. The NiO particle size distribution is bimodal with fractions of approximately 0.4 μm and 10 μm in the volume ratio 6:1. The slurry is sprayed onto YSZ three-electrode pellets (See Figure 4.1A) and on both sides of YSZ tapes in layers of 10 to 20 μm and sintered for 2 hours at 1300°C after each layer. The Ni/YSZ volume ratio is 40/60 in the reduced cermet.
A second type of Ni-based anode has been applied to a three-electrode pellet. Here $Ni(NO_3)_2$ is decomposed in moist 9% H_2 at 1420°C on the electrolyte[14], and afterwards a 90/10 v/o Ni/YSZ paint is deposited without sintering. A sufficient contact and anode stability is obtained. This anode is intended to have active sites only on the interface towards the electrolyte, the 10% YSZ is added to restrain Ni agglomeration by sintering and is not expected to percolate.

4.2.2 Test Setup Designs

Two different test setups are used in characterization of these anodes:
The YSZ three-electrode pellets are provided with a Pt-paste counter-electrode, a Pt-ball reference electrode and mounted in a three-electrode setup, Figure 4.1A. This setup provides a reference atmosphere and a sealed cylindrical anode compartment for exposing the anode to a reducing fuel gas. The fuel gas is feed through a concentric tube in the anode chamber. The reference electrode is placed in air (reference gas), and a Nernst potential is measured. The working electrode of ~0.44 cm^2 is contacted with several mm of 0.3 mm Pt wire pressed against the center. The height from the anode surface to the feed tube is approximately 1 cm. The cross section area of the anode compartment is 0.50 cm^2. The electrolyte geometry used here is verified by finite element analysis[15] to have a frequency stable, homogeneous current distribution, causing less than 3% error on a polarization resistance of 0.3 Ωcm^2.
The symmetric cells with two equal electrodes on each side of a 180 to 200 μm thick YSZ tape are measured in a one atmosphere setup. The samples are broken into ~5 × 5 mm^2 squares and mounted as a two-electrode cell between grids of Pt current collecting wires, Figure 4.1B. Due to the symmetric arrangement without reference electrodes the measured impedance represents the sum of the electrode responses, and interpretable data can only be obtained in the linear current-overpotential range around open circuit voltage (OCV).

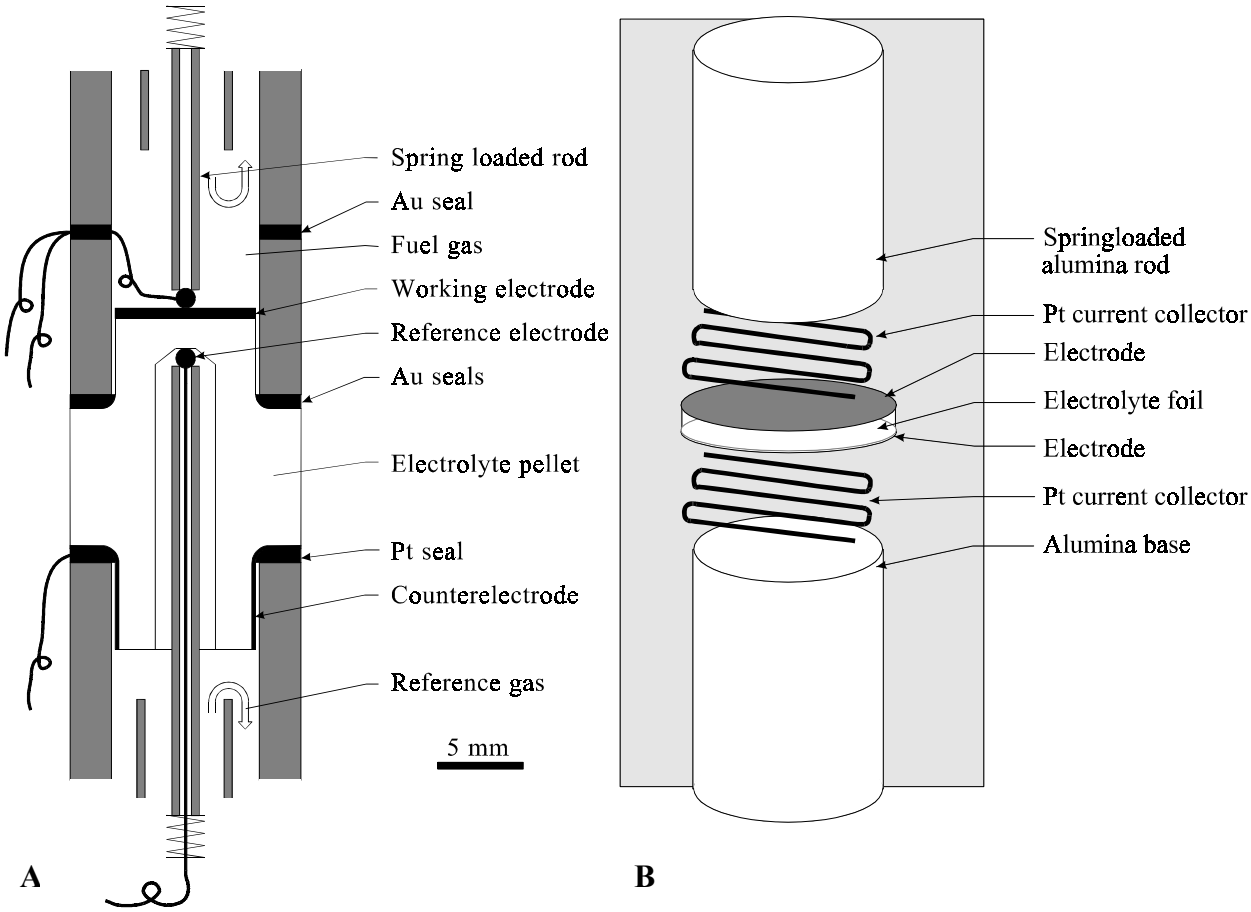

Figure 4.1 A) Three-electrode pellet (white body in center) and test setup for three-electrode measurements, where working electrode (anode) and reference electrode are in separate atmospheres. The anode area is 0.44 cm^2 and the volume of the tube enclosing the anode is 0.50 cm^3/cm. B) Test setup for symmetric electrodes in a common atmosphere. Typical sample areas are 0.25 cm^2, the Pt wires are 0.3 mm in diameter with a grid distance of 1 to 2 mm.

4.2.3 Electrochemical Testing

Anodes are heated to 1000°C in nitrogen and reduced by changing directly to a measurement atmosphere of 97% H_2 + 3% H_2O with an OCV against Pt/air of about -1070 mV ($pO_2 \sim 2 \times 10^{-18}$ atm). Gas flow-rates in the range of 10 to 200 ml/min (at 25°C) have been applied. When nothing else is indicated, a total of 100 ml/min (at 25°C) dry gas is passed over the anodes. Atmosphere control for variation of the molar fraction of each gas $x_{i,gas}$ (i = incoming) at constant gas flow-rate is performed by mixing nitrogen and hydrogen through thermal mass flowmeters and saturating this mixture with water at a controlled temperature. An experiment has been conducted where nitrogen has been substituted by argon and helium at constant gas flow-rate and molar fractions of hydrogen and water.

x_{O_2} is determined by the Nernst expression from OCV vs. Pt/air. The partial pressure x_{H_2O} is determined from x_{O_2} and x_{H_2} by the following equation valid for 1000 K<T<1300 K[16]:

$$x_{H_2O} = 10^{-(2.958-13022/T)} \cdot x_{H_2} \sqrt{x_{O_2}} \qquad (4.4)$$

Impedance spectroscopy is conducted with an applied amplitude in the range of 7 to 70 mV and in general a value of 20 mV is used. This amplitude has been verified to be well inside the linear range. The used frequency range is 500 kHz to 0.01 Hz or in some cases only 50 kHz to 0.01 Hz. At least 20 minutes is allowed for stabilization before recording each impedance spectrum.
The equipment used for impedance spectroscopy is a Solartron 1250 FRA combined with a Solartron 1286 ECI or a Solartron 1260 FRA with a Solartron 1287 ECI. The current measurement resistor used is 1 Ω for polarized and 10 Ω for unpolarized measurements. The two systems are verified on an appropriate test circuit to reproduce data within less than 1%.

4.3 Results and Discussion

4.3.1 Impedance Spectra

Impedance spectra obtained on nominally identical Ni/YSZ cermet anodes in the two presented measurement setups differ considerably, Figure 4.2. The anode on a three-electrode pellet measured in the two atmospheres setup contains at least three arcs. A small arc is located between the two dominant ones and is not clearly seen at these conditions. The symmetric sample measured in the one atmosphere setup exhibit only two well defined arcs. Comparing the highlighted frequencies it is evident how the dominant arc at low frequency measured in the two atmospheres setup is not present in the measurements performed in the one atmospheres setup.
A comparison of impedance measurements obtained on two structurally different anodes in the two atmospheres setup is given in Figure 4.3. The spectra are brought to the same scale and shifted in real part to have the same resistance at low frequency. It is seen that these two anodes measured in the same two atmospheres setup exhibit identical arcs at low frequencies.

4.3.2 Interpretation of Impedance Spectra

To elaborate further on the behavior of the low frequency arc present in measurements in the two atmospheres setup, it is necessary to apply a simple model (an equivalent circuit) to present the following results in a meaningful and representative way. The low frequency arc is observed to describe a nearly perfect semicircle, which allows a description by only two parameters; a resistor R and a capacitor C in parallel.
In the present approach we assume the impedance spectrum can be interpreted by three independent rate-limiting processes in a series arrangement. Data are thus fitted with the software EQUIVCRT,[17] using the equivalent circuit $LR_S(RQ)_1(RQ)_2(RC)_3$ where the annotation I-III is assigned to the respective processes by increasing timeconstant. Here L is an inductance, R a resistance, C a capacitance and Q a constant phase element given as $Q=Y_0(j\omega)^n$. Y_0 is an admittance, j the imaginary unit, ω the angular frequency and n is a frequency exponent. The frequency exponents $(n_1, n_2)=(0.8, 0.75)$ were derived earlier[3] for Ni/YSZ cermet anodes from a data matrix to produce consistently high fit quality under all examined conditions (<2% relative error on both real and imaginary data at all frequencies) and are applied again here. For the Ni-based anodes frequency exponent of $(n_1, n_2)=(0.9, 0.75)$ are found suitable.

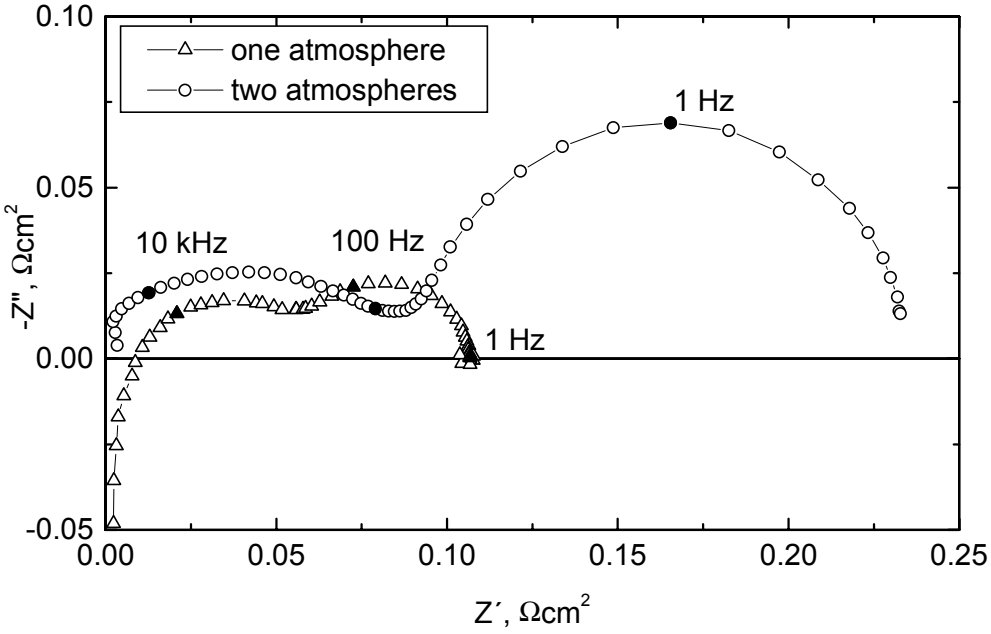

Figure 4.2 Impedance spectra obtained on nominally identical anodes in a one atmosphere setup (Δ) and in a two atmospheres setup (o). Conditions: 97% H_2 + 3% H_2O at 1000°C at OCV. Spectra are corrected for area and series resistance for presentation purposes.

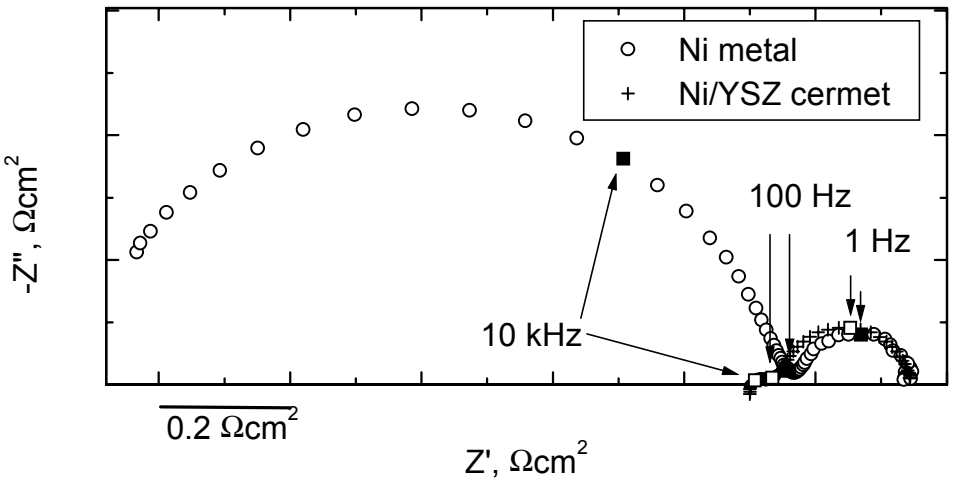

Figure 4.3 Impedance spectra obtained in setup with anode and reference electrode in separate atmospheres on a Ni/YSZ cermet anode (+) and a Ni based anode (o). Measurements in 97% H_2 + 3% H_2O at 1000°C at OCV. The spectra are corrected for anode area and to have the same real component at low frequency in order to compare the low frequency arcs.

Data obtained on symmetrical anodes with both electrodes in a common atmosphere (Figure 4.1B) only contain two arcs, Figure 4.2. Comparing the summit frequencies indicates that the low frequency arc denoted III is not present in this measurement geometry.
The parameters R_3 and C_3 for the low frequency arcs in Figure 4.3 are given in Table 4.1 as well as the summit frequency f_3 according to Eq. (4.5).

$$f_3 = \frac{1}{2\pi R_3 C_3} \tag{4. 5}$$

Table 4.1 Parameters for the low frequency semicircle in Figure 4.3. Applied parameters are: A = 0.44 cm^2, J_i = 1.62 mol/m^2s, T = 1000°C, x_{H_2O} = 0.03, x_{H_2} = 0.97.

Sample	R_3, Ωcm^2	C_3, F/cm^2	f_3, Hz
A214, Ni/YSZ cermet anode	0.20	0.74	1.1
A527, Ni-based anode	0.18	0.80	1.0

The low frequency arc is observed to have a dependence on gas flow rate in the range of 10 to 200 ml/min. In Figure 4.4 the dependence for the parameters R_3 and C_3 is presented.

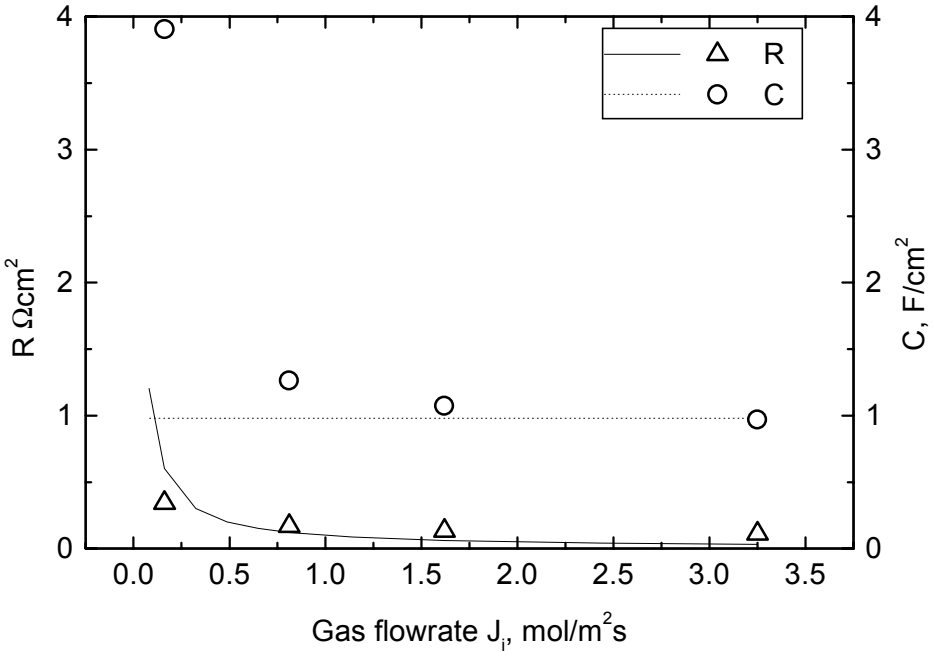

Figure 4.4 Experimental impedance data for R_3 (Δ) and C_3 (o) after fitting to the selected equivalent circuit as a function of gas flow-rate J. Temperature is 1000°C, atmosphere is 97% H_2 + 3% H_2O. The lines represent the model prediction of gas conversion impedance for V = 0.35 cm^3.

The effect of the molecular weight of the inert gas on the low frequency arc has been measured applying helium, argon and nitrogen at a constant flow-rate and temperature with x_{i,H_2} = 0.02 and x_{i,H_2O} = 0.035. R_3 is presented in Table 4.2.

Table 4.2 Resistivity of the low frequency impedance arc after a simple interpretation as a parallel RC subcircuit. Applied parameters are: J_i = 1.62 mol/m^{2}s, T = 1318 K, x_{H_2O} = 0.035, x_{H_2} = 0.02

Inert gas	Rg, Ωcm^2
He	0.12
Ar	0.21
N_2	0.20

Varying the molar fraction of water x_{H_2O} from 5×10^{-3} to 0.25 at constant flow-rate with a constant x_{H_2} of 0.5 or 0.97 to 1.00 respectively (balance being nitrogen), reveals a significant variation in the low frequency arc. In Figure 4.5 the parameters R_3 and C_3 are presented as function of x_{H_2O}. C_3 can be very high, up to several F/cm^2 at high water contents. A capacitance of this magnitude is not ascribable to interface capacitance or adsorption on surfaces, as calculated earlier[3] a bulk process is required. In combination with the dependence of both R_3 and C_3 on gas flow-rate, it is assumed that this bulk process could be gas conversion in the volume over the anode. This assumption is examined in the following model.

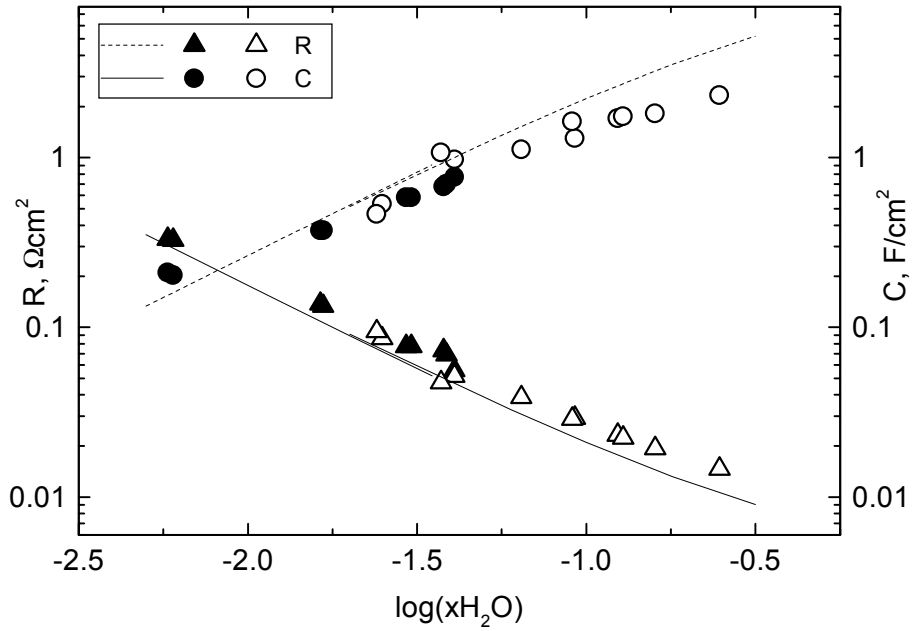

Figure 4.5 Experimental impedance data after fitting to the selected equivalent circuit, R_3 (Δ) and C_3 (o) as a function of molar fraction of water, x_{H_2O}. Solid points are at x_{H_2} = 0.97, open points at x_{H_2} = 0.50. Temperature is 1000°C, the gas flow-rate is 1.62 mol/m^{2}s. The lines represent the model predictions of R_g and C_g for V = 0.35 cm^3.

4.3.3 AC Model

The impedance relating to the change of atmosphere composition over the anode has been considered before,[18,19] and is derived analytically as follows: An anode of area A with a volume V over the anode in an atmosphere separated from the reference gas is considered, Figure 4.6. The gas flows are treated as area-specific flow-rates, J (unit of mol/m^{2}s), with subscripts i = incoming, o = outgoing and a = anode reaction. In the following the subscript is expanded to include the species (H_2, H_2O) considered. A CSTR model is applied, based on the assumption of perfect mixing of gases at 800 to 1000°C due to the fairly high diffusion rates.[20] Therefore the molar fraction of any species in the volume V are identical to the molar fractions in the outlet gas; $x = x_o$. The current is defined as positive in the anodic direction. A H_2/H_2O fuel gas containing inert gas is considered.

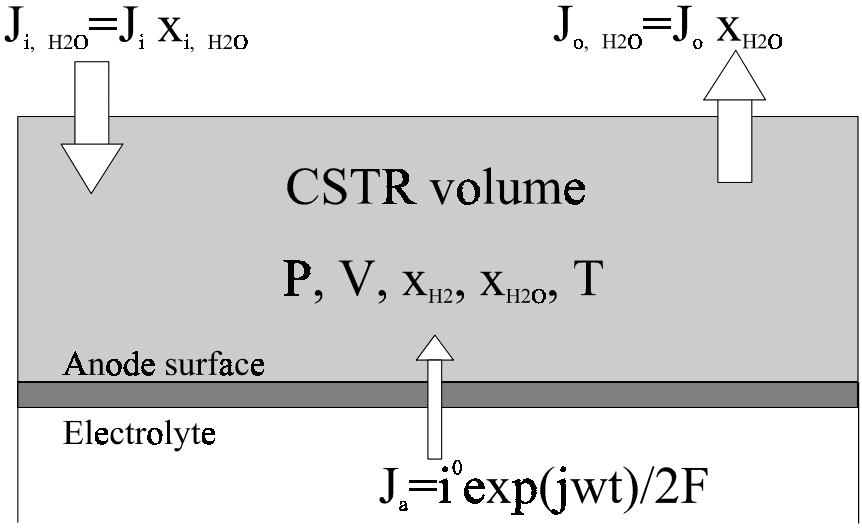

Figure 4.6 The continuously stirred tank reactor (CSTR) model. A volume V over the anode surface is assumed to have uniform gas composition. The considered gas flow-rates J are indicated.

The electrode is perturbed by an AC impressed current and the resulting variation in gas compositions Δx_{H_2O} and Δx_{H_2} in the CSTR volume are evaluated and inserted in a linearized Nernst expression to yield the area-specific impedance Z_g. Details of the calculation are given in Appendix A. The impedance is broken down into a parallel resistor R_g and capacitor C_g with the dependencies given in Eqs. (4.6) and (4.7). The criteria for linearization are $\Delta x_{H_2O} << x_{i,H_2O}$ and $\Delta x_{H_2} << x_{i,H_2}$, i.e. small perturbations compared with the inlet gas composition.

$$R_g = \frac{RT}{4F^2 J_i}\left(\frac{1}{x_{i,H_2O}} + \frac{1}{x_{i,H_2}}\right) \tag{4. 6}$$

$$C_g = \frac{4F^2 PV}{(RT)^2 A}\frac{1}{\frac{1}{x_{i,H_2O}} + \frac{1}{x_{i,H_2}}} \tag{4. 7}$$

Here x_{i,H_2} and x_{i,H_2O} are the inlet molar fractions of hydrogen and water, respectively, J_i is the inlet area-specific gas flow-rate (mol/m^{2}s), P the absolute pressure, A the anode area and V the CSTR volume of the measurement setup.
R_g and C_g are thus parameters with physical meaning and are obtainable by a simple interpretation of an arc in impedance measurements. The summit frequency of the impedance arc is given by Eq. (4.8) obtained from Eq. (4.5).

$$f_g = \frac{J_i ART}{2\pi PV} \tag{4. 8}$$

4.3.4 DC Model

Using the above described model and definition of parameters, the same type of calculation is carried out for a steady state DC case. Details of the calculation are given in Appendix B.
The general steady state expression for η_g is given in Eq. (4.9), valid for $\Delta x_{H_2} < x_{i,H_2}$ anodic and for $\Delta x_{H_2O} < x_{i,H_2O}$ cathodic. At the boundaries a limiting current density is found.

$$\eta_g = \frac{RT}{2F}\left(\ln\left(\frac{x_{i,H_2}}{x_{i,H_2O}}\right) + \ln\left(\frac{x_{i,H_2O} + i/J_i 2F}{x_{i,H_2} - i/J_i 2F}\right)\right) \tag{4. 9}$$

For the criteria $x_{i,H_2} >> \Delta x_{H_2}$ and $\Delta x_{H_2O} >> x_{i,H_2O}$ Eq. (4.10) is obtained, revealing a Tafel behavior with a limiting slope of *RT/2F* at high currents when the feed gas is rich in hydrogen and lean in water.

$$\eta_g = \frac{-RT}{2F}\ln\left(2FJ_i x_{i,H_2O}\right) + \frac{RT}{2F}\ln(i) \tag{4. 10}$$

Using instead the criterion $\Delta x_{H_2O} << x_{i,H_2O}$ and $\Delta x_{H_2} << x_{i,H_2}$, Eq. (4.11) is obtained. This linear dependence of overpotential on current is valid only for small perturbations of x_{i,H_2O} and x_{i,H_2}. Eq. (4.11) is seen to be consistent with Eq. (4.6) of the AC model.

$$\eta_g = \frac{RT}{4F^2 J_i}\left(\frac{1}{x_{i,H_2}} + \frac{1}{x_{i,H_2O}}\right) i \tag{4. 11}$$

4.3.5 Evaluation of the Model

Gas conversion is taking place on both working and counter-electrode. In the above it is assumed that the reference potential is constant, i.e. not influenced by gas conversion.
In the setup with two atmospheres used here the reference electrode is situated in the same atmosphere as the counter-electrode. If the potential at the reference electrode is not affected by gas conversion at the counter-electrode, only gas conversion on the test electrode is included in the electrochemical measurements performed in this setup. Calculating the variation in molar fraction of oxygen at the counter-electrode in air, one obtains an insignificant Δx_{O_2} of 3×10^{-8} and a gas conversion overpotential of about 4 nV. See Appendix C for details. It follows that an extremely high current density *i,* or a low flow-rate J_i is required before an appreciable gas

conversion takes place in air. In the two atmospheres setup the reference potential is stable and only gas conversion impedance on the anode is of significance in the measurements.
Measurements on a small symmetric cell in a one atmosphere setup where the two electrodes are within the same effective CSTR volume does not include gas conversion. These observations explain the main difference between the impedance spectra observed in Figure 4.2.

Equations (4.6) and (4.7) represent the model predictions for dependencies of the measurable parameters R_g and C_g in a setup where CSTR conditions are fulfilled. In the following these parameters are compared with the actual measurements of R_3 and C_3 obtained in the two atmospheres setup of Figure 4.1.
R_g is compared with the measured values in Table 4.1 by inserting the relevant parameters in Eq. (4.6). A value of 0.06 Ωcm^2 is obtained, a factor of 3 lower than the observed R_3. A capacitance C_g of 1.1 F/cm^2 is obtained according to 7, using $V = 0.5$ cm^3 as a maximum value. Deriving the volume from measured values for C_3 of 0.74 to 0.80 F/cm^2 (Table 4.1), an effective CSTR volume of 0.35 cm^3 is obtained.
The predicted f_g is 2.3 Hz according to Eq. (4.8) after inserting the relevant parameters used for data in Table 4.1, whereas the measured f_3 of the low frequency arc is about 1 Hz. Considering the separation in time constant of the arcs as evaluated from Figure 4.2 and Figure 4.3, the agreement between model and measurement is good.
Looking at the area specific gas flow-rate, relevant parameters for measurements are inserted in Equations (4.6) and (4.7) and plotted with measured data in Figure 4.4. A reasonable agreement is found at most gas flow-rates except the lowest.
Comparing R_g and C_g with experimental data as function of x_{i,H_2O} in Figure 4.5 show good agreement over the investigated range. At the lowest $x_{i,H_2O} = 5 \times 10^{-3}$ a Δx_{H_2O} of less than 8×10^{-4} is calculated, this means the model criteria from the linearization $\Delta x << x_i$ are not quite fulfilled in the lower x_{i,H_2O} range of Figure 4.5. For details of the calculation please refer to Appendix D.
Based on the temperature dependence of R_g given in Eq. (4.6) a slightly negative apparent activation energy of -0.09 eV can be calculated. This is in good agreement with earlier data[3] measured on Ni/YSZ cermet anodes in the same two atmospheres setup.
With the parameters used for measurements given in Table 4.2 the model prediction of Rg is 0.14 Ωcm^2. This is in good agreement with data for R_3 measured in He as the inert component as opposed to Ar and N_2 in which H_2 and H_2O have lower diffusion rates. In other words, the assumption of CSTR conditions seems to be quite well fulfilled in He but not using inert gases with higher a molar weight.

It is often difficult to ascertain if gas conversion impedance is contributing to results reported in literature, as insufficient information is available on details of the setup. Due to the limited magnitude of gas conversion impedance (typically <1 Ωcm^2 in $H_2 + H_2O$ at a gas flow-rate of 1.62 mol/m^2s) it is only a relevant process for high performance anodes where this contribution cannot be ignored. Point electrodes[7,8] and pattern electrodes[5,6] used for kinetic studies are typically of an impedance where gas conversion is negligible. Impedance data obtained on symmetric cells[10] measured in one common atmosphere are not expected to be affected by gas conversion impedance if the dimensions of the cell are small.

However irrelevant gas conversion might seem from an electrode kinetics point of view, it is not an artifact. In fact gas conversion overvoltage is just a kind of concentration overvoltage in analogy to diffusion overvoltage. In SOFC stack technology and modeling the inherent DC gas conversion is treated as an increasing fuel utilization in the direction of the gas flow over the electrodes.

In single-cell testing and electrode characterization using two atmospheres where a uniform gas composition is desired or assumed under DC load, gas conversion poses a problem. The gas conversion overpotential can be demonstrated in a two atmospheres setup by introducing an oxygen sensor in the anode chamber, dealing with the phenomena as a concentration polarization under DC load.[11,12] The overvoltage relating to gas conversion is not measured when the reference electrode is placed in the fuel gas near the anode.[21,22] However, gas conversion still takes place and contributes to the real i-η characteristics of the cell. The idea of having a "reference" electrode in a gas mixture with an unstable potential is in it self a problem. In practice gas conversion should be suppressed experimentally by using a sufficiently high gas flow rate.

According to the derived DC model, the gas conversion impedance exhibits a Tafel behavior with a limiting slope of $RT/2F$ at high currents in a feed gas rich in hydrogen and low in water content. The DC model anodic gas conversion overpotential according to Eq. (4.9) is given in a Tafel plot in Figure 4.7 for three hydrogen-water mixtures using relevant parameters for the setup of Figure 4.1A. The limiting slope of $RT/2F$ is seen only at the lowest water partial pressures, and at a current density of about 25,000 mA/cm^2 a limiting current is approached as the hydrogen is fully consumed by the current. Decreasing the flow rate to expand the linear Tafel slope is not successful as the limiting current decreases. Under cathodic polarization (not shown) the gas conversion rapidly reaches a limiting current due to the low water partial pressures. An experimental i-η curve is given in Figure 4.7 as well, after correction for electrode loss and diffusion overvoltage. The agreement is seen to be reasonable. The experimental data do not exceed 500 mA/cm^2 to avoid ohmic heating in the thick electrolyte pellet.[23] DC characterization aiming at interpretation of electrode kinetics from linear Tafel slopes should demonstrate linearity over at least 1½ decade.

The present model is evaluated for a H_2/H_2O containing fuel gas, and can be used directly if an inert gas component is present. The results are analogous for CO/CO_2 containing fuels, and molar fractions can be substituted directly in the derived formulae. Gas conversion in other fuel gases (e.g. CH_4 and NH_3) can be evaluated in a similar manner, but may be complicated by the number species and reactions to be considered.

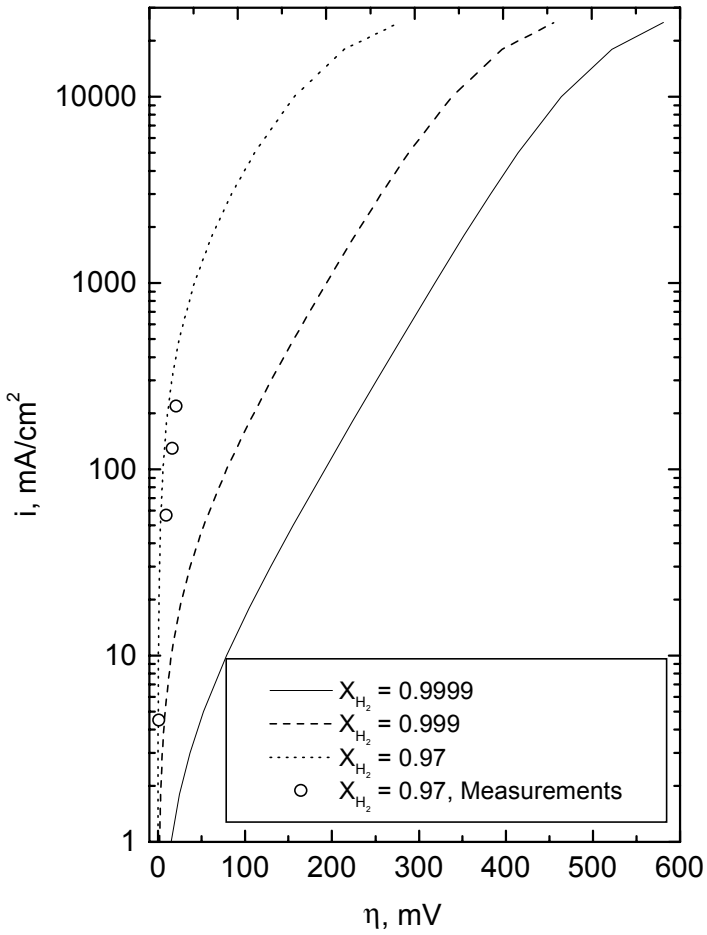

Figure 4.7 Model prediction of anodic gas conversion overpotential and experimental overpotential including gas conversion data in a Tafel type plot. Model predictions according to Eq. (4.9) with the parameters T = 1273 K, J = 1.62 mol/m^{2}s, x_{i,H_2} is given in the legend, balance is x_{i,H_2O}. The experimental curve was obtained in the setup of Figure 4.1A at identical conditions with x_{i,H_2} = 0.97. Anode A214.

4.4 Summary

Gas conversion impedance is an effect of the passage of current through an electrode in a finite gas flow-rate. Gas conversion impedance is not detectable when the reference electrode is positioned effectively in the same gas as the tested electrode, or in symmetric two electrode cells where the electrodes are placed sufficiently near each other in a common atmosphere. Gas conversion impedance is only detectable in a measurement setup where the electrode is characterized against a stable reference potential. This is shown to be the case when the reference electrode is placed in air, even when the counter-electrode is positioned in the same atmosphere.

A simple continuously stirred tank reactor (CSTR) model is proposed, and the gas conversion impedance is derived quantitatively for small AC perturbations in the linear i-η range and for steady state DC conditions.
The presented CSTR model successfully accounts for the presence of a low frequency arc in impedance spectra obtained in the used two atmospheres setup, as well as it predicts an (RC) subcircuit (a semicircle in impedance plots) in agreement with experiment.
The dependence of the resistance R_g on x_{i,H_2O}, J_i and temperature is demonstrated to be in agreement with theory. The predicted R_g may be a factor of 2 to 3 lower than measured data. The agreement is illustrated to be better in case He is used as inert gas because the higher diffusion rates of H_2 and H_2O in He than in N_2 and Ar brings the gas closer to CSTR conditions.
The predicted capacitance C_g exhibit good agreement with measurements and is able to account for the quite high capacitances measured at high x_{i,H_2O}. C_g is calculated using a specific volume of the setup of 0.35 cm^3 over the anode, this corresponds to a volume extending more than 5 mm above the anode surface.
As a result of the good agreement of R_g and C_g with measurements, a comparable time constant is found for the model and measurements.

Gas conversion impedance is now recognized to be included in anode measurements on Risø three-electrode pellets tested in the two atmospheres setup of Figure 4.1A as a low frequency semicircle with a summit frequency around 1 Hz. This semicircle has been the dominant contribution to impedance spectra in several cases.[1-3, 24]

In practice the gas conversion overpotential can be decreased considerably by establishing an effective gas exchange over the anode by a high flow-rate J_i. A reduction of the volume V decreases the capacitance and shifts the arc of gas conversion impedance towards higher frequency, making it difficult to separate it from other rate limiting processes. Recent non-linear modeling of gas conversion impedance in a plug flow geometry indicates that gas conversion is still present as a distorted semicircle in impedance plots.[25]
The DC case is calculated to exhibit an $RT/2F$ slope in a Tafel plot at high current densities.
Gas conversion impedance bears no relation to the anode performance itself, but is a function of the setup geometry, position of the reference electrode and the gas flow-rate. Therefore data used for kinetic studies should be corrected for gas conversion or analyzed in a model taking gas conversion into account, unless it can be demonstrated by impedance spectroscopy that gas conversion is playing an insignificant role compared with the true electrode losses.

4.5 Appendices

A. AC Model

An AC model based on the geometry of Figure 4.6 is derived as follows. The AC overpotential η on the anode causes an AC current density i ,Eq. (4.12), and a gas conversion according to Eq. (4.13). Here i^0 is the peak current density amplitude, t the time, ω the angular frequency and j the imaginary unit.

$$i = i^0 \exp(j\omega t) \qquad (4.12)$$

$$H_2(g) + O^{2-} \leftrightarrow H_2O(g) + 2e^- \tag{4. 13}$$

Considering the variation in molar fraction of water with time dx_{H_2O}/dt in the volume V one obtains Eq. (4.14), where P is the absolute pressure and RT has the usual meaning.

$$\frac{PV}{RT}\frac{dx_{H_2O}}{dt} = AJ_{i,H_2O} + AJ_{a,H_2O} - AJ_{o,H_2O} \tag{4. 14}$$

The flow-rate of water in and out of the volume is given as Eq. (4.15) using the relevant flow-rates and molar fractions. The flow-rate caused by the passing current density i is given as Eq. (4.16).

$$J_{H_2O} = Jx_{H_2O} \tag{4. 15}$$

$$J_{a,H_2O} = \frac{i}{2F} \tag{4. 16}$$

The variation in molar fractions is defined as $\Delta x_{H_2O} = x_{H_2O} - x_{i,H_2O}$ and $\Delta x_{H_2} = x_{H_2} - x_{i,H_2}$ for water and hydrogen, respectively. n defined by the ideal gas law $n = PV/RT$ is introduced. As the anodic reaction Eq. (4.13) involves no changes in the number of gas molecules, $J_o = J_i$ and $d\Delta x_{H_2O}/dt = dx_{H_2O}/dt$. Inserting in Eq. (4.14) and rewriting gives the simple differential equation (4.17) with the general solution (4.18) involving a constant c. Using the boundary condition of $\Delta x_{H_2O} = 0$ for $i = 0$, one obtains $c = 0$ and the specific solution of Eq. (4.19).

$$\frac{d\Delta x_{H_2O}}{dt} = \frac{Ai^0}{2Fn}\exp(j\omega t) - \frac{AJ_i}{n}\Delta x_{H_2O} \tag{4. 17}$$

$$\Delta x_{H_2O} = \frac{i^0}{2F(J_i + j\omega n/A)}\exp(j\omega t) + c\exp\left(\frac{-AJ_i}{n}t\right) \tag{4. 18}$$

$$\Delta x_{H_2O} = \frac{i}{2F(J_i + j\omega n/A)} \tag{4. 19}$$

The variation in molar fraction of hydrogen Δx_{H_2} is given as Eq. (4.20) according to Eq. (4.13).

$$\Delta x_{H_2} = \frac{-i}{2F(J_i + j\omega n/A)} \tag{4. 20}$$

The overpotential η_g relating to the change in gas composition is defined as Eq. (4.21) according to the Nernst equation. With the criteria $\Delta x_{H_2O} << x_{i,H_2O}$ and $\Delta x_{H_2} << x_{i,H_2}$ (changes in

the atmosphere composition are small compared with the inlet gas composition) this equation is linearized by the Taylor expansion ln(1+y) = y for y << 1 resulting in Eq. (4.22).

$$\eta_g = \frac{RT}{2F}\ln\left(\frac{x_{H_2O}\cdot x_{i,H_2}}{x_{i,H_2O}\cdot x_{H_2}}\right) \tag{4. 21}$$

$$\eta_g = \frac{RT}{2F}\left(\frac{\Delta x_{H_2O}}{x_{i,H_2O}} - \frac{\Delta x_{H_2}}{x_{i,H_2}}\right) \tag{4. 22}$$

Calculating now the impedance Z associated with this variation in partial pressures using Eqs. (4.19), (4.20) and (4.22) one obtains Eq. (4.23).

$$Z = \frac{\eta_g}{i} = \frac{RT}{4F^2}\left(\frac{1}{x_{i,H_2O}} + \frac{1}{x_{i,H_2}}\right)\frac{1}{\left(J_i + j\omega n/A\right)} \tag{4. 23}$$

The last term in Eq. (4.23) can be shown to describe a semicircle in a plot of ($-Z_{Imag.}$ vs. $Z_{Re.}$) for ω going from 0 to ∞. This indicates how the impedance is equivalent to that of a circuit containing a resistor R_g and a capacitor C_g in parallel. Such circuits are conveniently analyzed in the representation of admittance Y , Eq. (4.24). Rewriting Eq. (4.23) to the admittance Y=1/Z yields the expression of Eq. (4.25).

$$Y = \frac{1}{R_g} + j\omega C_g \tag{4. 24}$$

$$Y = \frac{4F^2}{RT}\frac{1}{\left(\frac{1}{x_{i,H_2O}} + \frac{1}{x_{i,H_2}}\right)}\left(J_i + j\omega n/A\right) \tag{4. 25}$$

Combining Eqs. (4.24) and (4.25) yields R_g from the real part and C_g from the imaginary, still with the restrictions of $\Delta x_{H_2O} << x_{i,H_2O}$ and $\Delta x_{H_2} << x_{i,H_2}$ from the linearization.

$$R_g = \frac{RT}{4F^2 J_i}\left(\frac{1}{x_{i,H_2O}} + \frac{1}{x_{i,H_2}}\right) \tag{4. 26}$$

$$C_g = \frac{4F^2 PV}{(RT)^2 A}\frac{1}{\frac{1}{x_{i,H_2O}} + \frac{1}{x_{i,H_2}}} \tag{4. 27}$$

B. DC Model

In the DC case the differential equation (4.17) reduces to Eq. (4.28). Steady state implies $d\Delta x_{H_2O}/dt = 0$, thus Eq. (4.29) is obtained.

$$\frac{d\Delta x_{H_2O}}{dt} = \frac{Ai}{2Fn} - \frac{AJ_i}{n}\Delta x_{H_2O} \tag{4. 28}$$

$$\Delta x_{H_2O} = \frac{i}{J_i 2F} \tag{4. 29}$$

The change in molar fraction of hydrogen Δx_{H_2} is given as Eq. (4.30) according to Eq. (4.13).

$$\Delta x_{H_2} = \frac{-i}{J_i 2F} \tag{4. 30}$$

The overpotential η_g relating to the change in gas composition is again defined according to the Nernst equation. Using now the definitions of Δx_{H_2O} and Δx_{H_2} directly in Eq. (4.21), Eq. (4.31) is obtained.

$$\eta_g = \frac{RT}{2F}\left(\ln\left(\frac{x_{i,H_2}}{x_{i,H_2O}}\right) + \ln\left(\frac{x_{i,H_2O} + \Delta x_{H_2O}}{x_{i,H_2} + \Delta x_{H_2}}\right)\right) \tag{4. 31}$$

By inserting the expressions for Δx_{H_2O} and Δx_{H_2} in Eqs. (4.29) and (4.30) the general Eq. (4.32) is obtained, valid for $\Delta x_{H_2} < x_{i,H_2}$ anodic and for $\Delta x_{H_2O} < x_{i,H_2O}$ cathodic. At the boundaries a limiting current density is found.

$$\eta_g = \frac{RT}{2F}\left(\ln\left(\frac{x_{i,H_2}}{x_{i,H_2O}}\right) + \ln\left(\frac{x_{i,H_2O} + i/J_i 2F}{x_{i,H_2} - i/J_i 2F}\right)\right) \tag{4. 32}$$

Assuming the criteria $x_{i,H_2} >> i/2FJ_i >> x_{i,H_2O}$ Eq. (4.32) reduces to a Tafel type equation (4.33), valid at low pH_2O and high pH_2, if current i and flow-rate J_i have the magnitudes to satisfy the stated criteria.

$$\eta_g = \frac{-RT}{2F}\ln\left(2FJ_i x_{i,H_2O}\right) + \frac{RT}{2F}\ln(i) \tag{4. 33}$$

When it is instead assumed that the criteria $x_{i,H_2O} >> i/2FJ_i$ and $x_{i,H_2} >> i/2FJ_i$ are fulfilled, Eq. (4.32) reduces to Eq. (4.34). This linear dependence of overpotential on current corresponds to Eq. (4.6) for the AC case in the linear i-η range and is valid only in the low current range with high x_{i,H_2O} and x_{i,H_2}.

$$\eta_g = \frac{RT}{4F^2 J_i}\left(\frac{1}{x_{i,H_2}} + \frac{1}{x_{i,H_2O}}\right) i \qquad (4.\ 34)$$

C. Gas Conversion at the Counter-electrode

The extent of oxygen gas conversion in the common reference and counter-electrode gas of the setup given in Figure 4.1 has been evaluated.
The assumption of the reference gas (air) being insensitive to gas conversion is verified as follows. The gas conversion overpotential is given according to Eq. (4.3) as

$$\eta_g = \frac{RT}{4F}\ln\left(\frac{x_{i,O_2} + \Delta x_{O_2}}{x_{i,O_2}}\right) \qquad (4.\ 35)$$

where x_{i,O_2} is the inlet reference gas and Δx_{O_2} the change of molar fraction of oxygen by the passage of current. By inspection of the water formation reaction, Eq. (4.13), it is seen that $\Delta x_{O_2} = -½\Delta x_{H_2O}$. Using the real part of Eq. (4.19) and inserting typical values for AC-characterizations in the three-electrode setup (i^0 = 20 mA/cm^2, J_i = 1.62 mol/m^{2}s and x_{i,O_2} = 0.21), one obtains an insignificant Δx_{O_2} of 3×10^{-8} and a η_g of about 4 nV.

D. Evaluation of Criteria for Linearization

The criteria $\Delta x_{H_2O} << x_{i,H_2O}$ has been evaluated for low x_{i,H_2O} (Figure 4.5). The maximum magnitude of Δx_{H_2O} introduced by passing the AC current in impedance measurements is evaluated as follows. When the voltage amplitude of the applied AC signal is U^0, the perturbing current density amplitude i^0 over the electrode resistance R is obtained by Ohms law considering also the electrolyte resistance R_S, Eq. (4.36).

$$i^0 = \frac{U^0}{R + R_S} \qquad (4.\ 36)$$

Combining Eq. (4.36) with the real part of Δx_{H_2O} in Eq. (4.19) and inserting relevant parameter values, Δx_{H_2O} can be calculated. Considering the low x_{i,H_2O} data in Figure 4.5 relevant values are U^0 = 20 mV, R_S = 2 Ω × 0.44 cm^2, R = 0.35 Ωcm^2 and J_i = 1.62 mol/m^{2}s yielding a Δx_{H_2O} of 5×10^{-4}.

Acknowledgment

This work was supported in part by the European Commission under contract no. JOE3-CT95-0005 and in part by the Danish Energy Agency and the Danish utility group ELSAM under the Danish DK-SOFC program. Thanks are due to Dr. Torben Jacobsen, Technical University of Denmark, for bringing his model approach[18] to our attention and to Dr. Peter Holtappels, Risø National Laboratory, for valuable suggestions to the manuscript. The present experimental data have been generated as a result of the joined effort of many members of the SOFC project group at Risø. Their contributions are gratefully acknowledged.

References

[1] M. Mogensen, S. Primdahl, J. T. Rheinländer, S. Gormsen, S. Linderoth and M. Brown, in *SOFC IV*, M. Dokiya, O. Yamamoto, H. Tagawa and S. C. Singhal, Editors, **PV 95-1**, The Electrochemical Society Proceedings Series, Pennington, NJ. 657 (1995)

[2] M. Mogensen and T. Lindegaard, in *SOFC III*, S. C. Singhal and H. Iwahara, Editors, **PV 93-4**, The Electrochemical Society Proceedings Series, Pennington, NJ. 484 (1993)

[3] S. Primdahl and M. Mogensen, *J. Electrochem. Soc.* **144** 3409 (1997), chapter 3 in this thesis

[4] N. Nakagawa, H. Sakurai, K. Kondo, T. Morimoto, K. Hatanaka and K. Kato, *J. Electrochem. Soc.* **142** 3474 (1995)

[5] J. Mizusaki, H. Tagawa, T. Saito, T. Yamamura, K. Kamitani, K. Hirano, S. Ehara, T. Takagi, T. Hikita, M. Ippommatsu, S. Nakagawa and K. Hashimoto, *Solid State Ionics*, **70/71** 52 (1994)

[6] J. Mizusaki, H. Tagawa, T. Saito, K. Kamitani, T. Yamamura, K. Hirano, S. Ehara, T. Takagi, T. Hikita, M. Ippommatsu, S. Nakagawa and K. Hashimoto, *J. Electrochem. Soc.* **141** 2129 (1994)

[7] P. A. Osborg and T. Norby, in *7th SOFC WORKSHOP, Theory and Measurement of Microscale Processes in Solid Oxide Fuel Cells*, 47 (1995). IEA report obtainable from H. Nabielek, KFA-ISR Forschungs Zentrum Jülich GmbH, D-52425 Jülich, Germany.

[8] J. Guindet, C. Roux and A. Hammou, in *SOFC II*, F. Grosz, P. Zegers, S. C. Singhal and O. Yamamoto, Editors, EUR-13564-EN, 553 (1991)

[9] D. W. Dees, U. Balachandran, S. E. Dorris, J. J. Heiberger, C. C. McPheeters and J. J. Picciolo, in *SOFC I*, S. C. Singhal, Editor, **PV 89-11**, The Electrochemical Society Proceedings Series, Pennington, NJ. 317 (1989)

[10] J. Geyer, H. Kohlmüller, H. Landes and R. Stübner, In *SOFC V*, U. Stimming, S. C. Singhal, H. Tagawa and W. Lehnert, Editors, **PV 97-40**, The Electrochemical Society Proceedings Series, Pennington, NJ. 585 (1997)

[11] M. Nagata and H. Iwahara, *J. Appl. Electrochem*. **42** 275 (1993)

[12] T. Kawada, B. A. van Hassel, T. Horita, N. Sakai, H. Yokokawa and M. Dokiya, *Solid State Ionics* **70/71** 65 (1994)

[13] C. Bagger, In *1992 Fuel Cell Seminar*, Courtesy Associates, Inc. Washington, DC. 241 (1992)

[14] K. R. Thampi, A. J. McEvoy and J. Van herle, *J. Electrochem. Soc.*, **142** 506 (1995)

[15] J. Winkler, P. V. Hendriksen, N. Bonanos and M. Mogensen, *J. Electrochem. Soc.,* **145** 1184 (1998)

[16] R. Hartung and H.-H. Möbius, *Chemie-Ing. Techn*. **40** 592 (1968)

[17] B. A. Boukamp, *Solid State Ionics*, **20** 31 (1986)

[18] T. Jacobsen, *Undersøgelser over højtemperaturbrændselsceller*, Thesis (in danish), Technical University of Denmark, Lyngby, DK. (1970)

[19] S. Primdahl and M. Mogensen, in *SOFC V*, U. Stimming, S. C. Singhal, H. Tagawa and W. Lehnert, Editors, **PV 97-40**, The Electrochemical Society Proceedings Series, Pennington, NJ. 530 (1997)

[20] A. Solheim, in *SOFC Micromodelling, an International Energy Agency SOFC Task Report*, L. Dubal, Editor, Swiss Federal Office of Energy, Berne, CH. 9 (1992)

[21] K. Eguchi, Y. Kunisa, K. Adachi and H. Arai, *J. Electrochem. Soc.* **143** 3699 (1996)

[22] T. Setoguchi, K. Okamoto, K. Eguchi and H. Arai, *J. Electrochem. Soc.* **139** 2875 (1992)
[23] S. Primdahl and P. V. Hendriksen, in *High Temperature Electrochemistry: Ceramics and Metals*. F. W. Poulsen, N. Bonanos, S. Linderoth, M. Mogensen and B. Zachau-Christiansen, Editors, 17th Risø International Symposium on Materials Science, Roskilde, DK. 403 (1996), chapter 2 in this thesis
[24] O. Mar'ina, S. Primdahl, C. Bagger and M. Mogensen, in *SOFC V*, U. Stimming, S. C. Singhal, H. Tagawa and W. Lehnert, Editors, **PV 97-40**, The Electrochemical Society Proceedings Series, Pennington, NJ. 540 (1997)
[25] P. V. Hendriksen, Risø National Laboratory, unpublished data (1997)

Chapter 5

Gas Diffusion Impedance[†]

Abstract

Impedance spectra obtained on high-performance (<0.1 Ωcm^2) Ni/yttria stabilized zirconia (YSZ) cermet anodes at 1000°C in H_2/H_2O/inert gas mixtures are considered. An impedance arc with a characteristic frequency of about 10 to 100 Hz is related to finite diffusion limitation by considering the dependence on water partial pressure, apparent thermal activation and effect of the inert gas component. By experiments in different test geometries the diffusion zone is demonstrated to be a stagnant gas layer outside the anode structure. The stagnant gas layer thickness is estimated to be about 1 mm. The diffusion impedance is demonstrated to be avoidable by using a setup geometry with two coupled electrodes in direct electrical contact through opposite sides of a contacting mesh.

[†] This chapter is in press as S. Primdahl and M. Mogensen, "Gas Diffusion Impedance in Characterization of Solid Oxide Fuel Cell Anodes", *J. Electrochem. Soc*. (1999)

5.1 Introduction

A detailed understanding of the rate limiting steps in state-of-the-art Ni/YSZ cermet SOFC anodes is highly desirable from an optimization point of view. In practice these processes can consist of electrochemical steps and physical or chemical transport restrictions. Equally important is the discrimination between limiting processes related to the anode structure it self, and limitations related to the surroundings, such as contact resistance and gas access.
One of the most promising ways of unraveling such complex systems is by impedance spectroscopy. Here a number of more or less well-separated arcs are taken to represent at least the same number of processes which can be separated and analyzed individually as function of the primary test conditions.

Ni/YSZ cermet anodes for SOFC have been investigated intensively. Impedance spectra and interpretations of these have been offered in literature. [1-6] The findings are surprisingly inconsistent judging from the number of reported arcs in impedance spectra. Studies of geometrically simple Ni-anodes[7-13] have added to the available information without leading to a consistent picture.
In principal, any electrochemical measurement consists of contributions from electrolyte response, electrode response, and transport limitations for supply of reactants and removal of products. The electrolyte response is readily separated out as a series resistance, in simple geometries it can even be used to indicate the magnitude of the microscopic electrode contact area.[14] For high impedance model anodes, transport restrictions are believed to be negligible in typical setups. For anodes with low impedance, transport restrictions may contribute significantly.

The electrochemical charge-transfer reactions are suggested to occur in the vicinity of the active triple phase boundary (TPB) line. The active TPB is defined as the line where the Ni network, the YSZ network and open pores meet to form percolation paths for transport of electrons, oxide ions and gas, respectively.[15,16] The reaction resistance relating to any process occurring across the active TPB is coupled in parallel to the double layer capacitance between Ni and YSZ, which would typically be of the order of 10 $\mu F/cm^2$.[17] Thus, the electrode response for low impedance anodes is expected to have a small time constant and to contribute to the impedance spectrum at high frequency (kHz). Impedance spectra with arcs at considerably lower frequencies have been reported.[1,5-7] In the following the nature of these limiting processes is considered.

A process with a large ½time constant has been related to a variation in Nernst potential vs. a stable reference electrode, caused by the passage of current at a finite fuel flow rate. Consequently, this contribution is only observed when characterizing anodes on cells with a reference electrode in another well-buffered (high pO_2) atmosphere. This process has been described as concentration polarization in DC experiments,[18,19] and as gas conversion impedance,[20,21] forming a semicircle at low frequency (1 Hz) in impedance spectra. The resistance of this arc is typically < 0.1 Ωcm^2 in hydrogen with at least 3% H_2O. Extreme values of the conversion resistance are obtained using hydrogen with low concentrations of H_2O, as the resistance is proportional to the inverse water partial pressure at high hydrogen partial pressure.

For SOFC cathodes, gas diffusion limitations have been shown experimentally to contribute to impedance spectra at low (<10%) O_2 concentrations.[22,23] Oxygen transport has been modeled, concluding that gas diffusion limitations in the porous structure and in a boundary-layer above the

cathode surface are negligible as compared with solid-state oxygen diffusion and O_2 surface exchange at low temperature (700°C).[24]

The influence of porous electrode thickness on i-V characteristics has been evaluated by modeling gas phase diffusion of H_2/H_2O and O_2/inert gas mixtures in anode and cathode structures.[25] A modest contribution has been calculated using a 30% porous 200 µm thick cathode in air. To reach the same contribution for a 40% porous anode in hydrogen with 3% water, the anode thickness can be allowed to be a factor of 10 higher. At the same time it has been shown that with an anode porosity well above 10% no significant concentration polarization should be expected. Judging from these observations, gas diffusion limitation would not be expected to be significant for a <100 µm thick, 50% porous anode.

For diffusion limitation in porous electrode structures and in the gas outside a cathode, expressions for a stagnant gas layer of finite thickness are frequently applied in literature.[24-26] However, the possible presence of a stagnant gas layer outside the porous anode has not been considered in SOFC work. For a H_2/H_2O/inert gas mixture with small changes of gas composition, a convenient form of this well-known gas diffusion resistance can be derived, Eq. (5.1). See Appendix A for details. Considering the anode process of hydrogen oxidation in which the number of gas molecules is conservative, the analysis is particularly simple as pressure driven diffusion can be disregarded. The results are analogous for CO/CO_2 containing fuels, and molar fractions can be substituted directly in the derived formula.

$$R_D = \frac{\eta_D}{i} = \left(\frac{RT}{2F}\right)^2 \frac{l}{PD_{Eff}} \left(\frac{1}{X_{H_2,B}} + \frac{1}{X_{H_2O,B}}\right) \tag{5. 1}$$

Here R_D is the diffusion resistance, η_D the diffusion overpotential, i the current, P the pressure, D_{Eff} the effective diffusion coefficient, F is the Faraday number, RT has the usual meaning and $X_{j,B}$ denotes molar fraction of species j in the bulk gas. It is clear from this type of equation that diffusion limitation is expected to be significant at low reactant concentrations.

The effective diffusion coefficient used above can be considered to be equal to the binary diffusion coefficient D_{12} for a binary gas mixture in an open volume. In ternary gas mixtures the lowest D_{12} for any of the three binary pairs can be applied. This pair would typically include water rather than hydrogen, due to the molecular weights. In porous volumes a correction for the average percolating porosity in the direction of diffusion must be made, and in pores smaller than typically a few µm Knudsen diffusion must be considered.[27]
Binary diffusion coefficients D_{12} in m^2/s for simple molecules can be obtained by applying the Fuller correlation, Eq. (5.2),[28]

$$D_{12} = \frac{10^{-7} T^{1.75} \sqrt{\frac{1}{M_1} + \frac{1}{M_2}}}{P\left(\sqrt[3]{v_1} + \sqrt[3]{v_2}\right)^2} \tag{5. 2}$$

where T is temperature in K, M is molar weight of the gases, P is pressure in atm. and v is the diffusion volumes of the species as given elsewhere.[28] Excellent agreement between the Fuller correlation and measurements at ambient temperature has been demonstrated.[27]

It is the aim of this chapter to draw attention to gas diffusion impedance in SOFC anode research by demonstrating how i) gas diffusion in a stagnant gas layer may prevail over gas diffusion in the porous anode structure, ii) gas diffusion contributes to measurements on high-performance anodes under typical test conditions, and iii) the current collector structure influences this diffusion limitation. Finally, a setup geometry is presented where stagnant layer gas diffusion can be avoided.

5.2 Experimental

5.2.1 Sample Preparation

Ni/YSZ cermet anodes of 0.44 cm^2 were deposited on YSZ three-electrode pellets, Figure 5.1, by a low cost procedure.[5] The anodes were 40 to 50 μm thick with a porosity of 40 to 60% and contained 40 v/o Ni in the reduced state. The YSZ pellets were provided with a Pt-paste counter electrode, a Pt-ball reference electrode in the center bore, and two leads in contact with the working electrode. The electrolyte geometry used here has been verified by finite element analysis to have a frequency stable, homogeneous current distribution, causing less than 3% error on an electrode polarization resistance of 0.16 Ωcm^2.[29]

Two different test setup geometries were used in characterization of these anodes, and various current collectors and measurement configurations were applied:

i) The three-electrode pellet was mounted in the two-atmospheres setup of Figure 5.1. This setup provided a reference atmosphere and a sealed cylindrical anode compartment for exposing the anode to a reducing fuel gas. The fuel gas was fed through a concentric tube in the anode chamber. The working electrode was contacted with a Pt wire point contact pressed against the center by a 2 mm diameter spring-loaded pushrod. The height from the anode surface to the feed tube was approximately 1 cm. The cross section area of the anode compartment was 0.50 cm^2.

An alternative "supported felt" current collector structure was also used: The working electrode was contacted by 1 or 3 layers of 1 mm thick Ni-felt (Ni-fiber mat, 80/20 fibers/particles, Fibrex). The pushrod was brought to press a perforated Al_2O_3 disk of 2 mm thickness and 0.45 cm^2 area with grooves cut on the lower side against the Ni-felt to ensure contact to the working electrode.

ii) In another test geometry two three-electrode pellets in one atmosphere were positioned with the two working electrodes facing each other. The working electrodes were contacting opposite sides of a Ni-mesh (0.13 mm Ni wires, 0.50 mm wire spacing, Johnson Matthey GmbH), see Figure 5.2. In this setup the measurement connections could be switched around outside the furnace, allowing a) measurement of each anode with the other pellet restricting gas access to in-plane diffusion, or b) measurement of both electrodes as "coupled electrodes" where the two working electrodes experienced the same current with opposite polarity. Thereby the two working electrodes would convert the gaseous products of each other at any time. This led to a situation with primarily one-dimensional diffusion through the Ni-mesh between the working electrodes, see inserts of Figure 5.5 and Figure 5.6 for details.

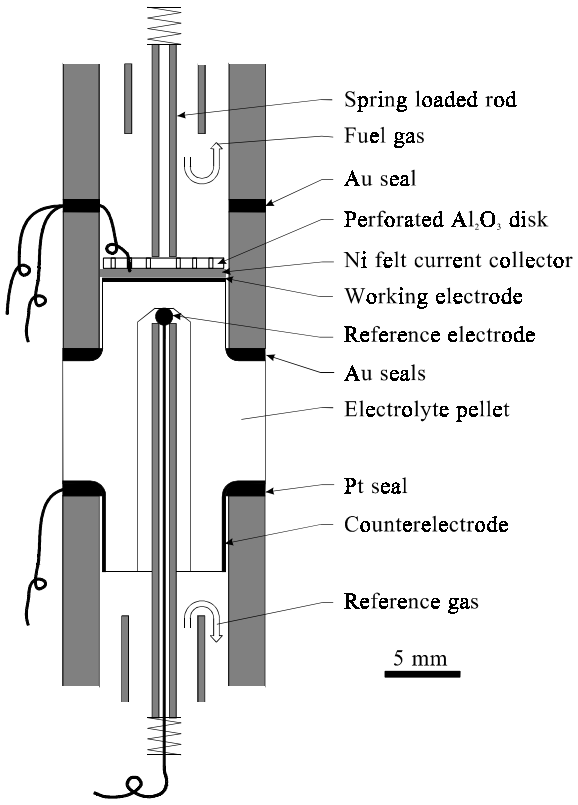

Figure 5.1 Three-electrode pellet (white body in center) and two-atmospheres test setup for three-electrode measurements. Working electrode (anode) and reference electrode are in separate atmospheres. A simpler current collector can be used, removing the perforated Al_2O_3 plate and Ni-felt, and using only a Pt wire under the pushrod.

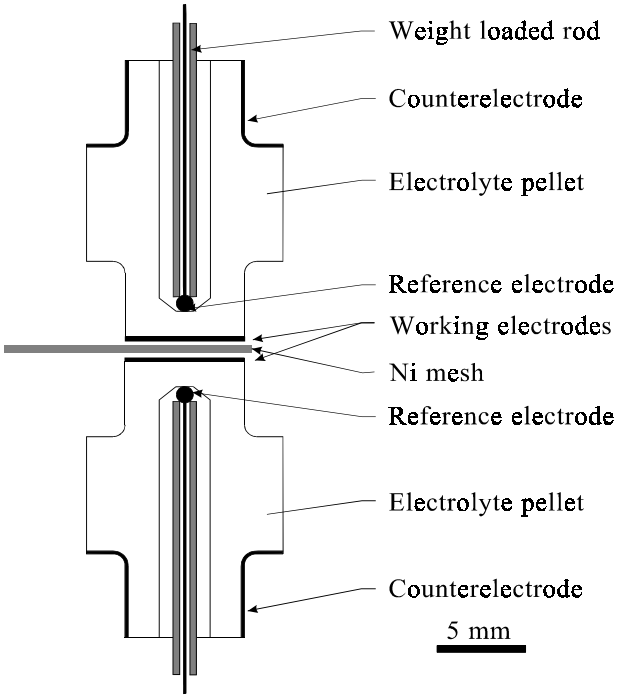

Figure 5.2 Two three-electrode pellets in one atmosphere, placed working electrode to working electrode to allow different measurement configurations. See also inserts of Figure 5.5 and Figure 5.6.

5.2.2 Electrochemical Testing

Cells were heated to 1000°C in nitrogen or 9% H_2 in nitrogen, thereafter changing directly to a measurement atmosphere of 97% H_2 + 3% H_2O with an open circuit potential (OCV) against Pt/air of about -1060 mV ($pO_2 \sim 3 \times 10^{-18}$ atm). The gas flowrate was 100 ml/min (at 25°C) in all measurements. Atmosphere control for variation of incoming (suffix *I*) molar fractions $X_{j,I}$ of species *j* at constant gas flowrate was performed by mixing hydrogen and an inert gas (N_2, Ar or He) through thermal mass flowmeters and saturating this mixture with water at a controlled temperature.

X_{O_2} was determined by the Nernst expression from OCV vs. Pt/air. The molar fraction of water $X_{H_2O,I}$ was determined from X_{O_2} and $X_{H_2,I}$ by the following equation valid for 1000 K < T < 1300 K[30]:

$$X_{\mathrm{H_2O},I} = 10^{-(2.958-13022/T)} \cdot X_{\mathrm{H_2},I}\sqrt{X_{\mathrm{O_2}}} \qquad (5.3)$$

Impedance spectroscopy was conducted with an applied amplitude of 20 to 40 mV between reference and working electrode. This amplitude was verified to be well inside the linear range. The used frequency range was 500 kHz to 0.01 Hz or in some cases only 50 kHz to 0.01 Hz. At least 20 minutes was allowed for stabilization before recording each impedance spectrum.
The equipment used for impedance spectroscopy was a Solartron 1250 FRA combined with a Solartron 1286 ECI or a Solartron 1260 FRA with a Solartron 1287 ECI. The current measurement resistor used was 10 Ω. The two systems were verified on an appropriate test circuit to reproduce measurements within less than 1%.

5.2.3 Equivalent Circuits

In the present approach it was assumed that impedance spectra could be deconvoluted through an equivalent circuit, describing a number of independent rate-limiting processes in a series arrangement. Obtained impedance spectra were fitted with a non-linear-least-squares fitting routine, EQUIVCRT,[31] using the following elements:
For unidentified processes represented as impedance arcs (a depressed semicircle), the equivalent subcircuit (RQ) with a resistance R and a constant phase element Q in parallel was applied. Q has an admittance $Y^* = Y_0(j\omega)^n$ where Y_0 is an adjustable admittance depending on the characteristics of the corresponding process, j the imaginary unit, ω the angular frequency and n is a frequency exponent.

For a diffusion limitation where perfect one-dimensional diffusion in a stagnant layer of homogeneous finite thickness could be assumed from the test conditions, the finite-length Warburg diffusion (O-element) was used. The admittance of the finite-length Warburg diffusion is $Y^* = Y_0\sqrt{j\omega}\coth\left(B\sqrt{j\omega}\right)$ with an admittance parameter $Y_0 \propto \sqrt{D_{Eff}}$ [$Ss^{1/2}$] where D_{Eff} is the effective diffusion coefficient in the given gas mixture. The variable B is given as $B = l/\sqrt{D_{Eff}}$ [$s^{1/2}$] where l is the thickness of the stagnant gas layer. The diffusion resistance is given as $R_D = B/Y_0$.[31, 32] For measurements where in-plane diffusion was expected to be significant a more general interpretation was applied in the form of an (RQ) subcircuit.
A measuring-system inductance L and a series resistance R_S of the electrolyte pellet between reference electrode and working electrode are generally accepted.

In principle, the n-value should remain constant for a given physical or chemical process. However, in case the physical conditions are changing, e.g. when changing the setup geometry, different n-values and even different dispersion elements may be applied. Where significant overlap with other arcs is encountered, a convenient parameter to follow for a given process is the time constant, or the inverse summit frequency f_S of the related subcircuit.

The summit frequency of an (RQ) subcircuit is given by Eq. (5.4),[33] and the summit frequency for the finite-length Warburg diffusion element has been demonstrated by series expansion to be given approximately by Eq. (5.5).[32]

$$f_S = \frac{1}{2\pi\sqrt[n]{RY_0}} \qquad (5.4)$$

$$f_S \approx \frac{2.53 D_{Eff}}{2\pi l^2} \qquad (5.\ 5)$$

5.3 Results

Impedance spectra obtained at OCV at 1000°C in hydrogen with 3% H_2O on nominally identical Ni/YSZ cermet anodes in the two measurement setups differ considerably. After subtraction of a series resistance R_S in the range of 1 to 3 Ω and correction for inductance and electrode area, the spectra are presented in Figure 5.3 to Figure 5.6.

Impedance spectra obtained in the two-atmospheres setup contain at least three arcs, Figure 5.3. A small arc located between two dominant arcs was substantially enlarged, Figure 5.4, when a supported felt current collector was placed in the gas above the anode.
Impedance spectra obtained in the two configurations used for two pellets in one atmosphere are shown in Figure 5.5 and Figure 5.6. Impedance spectra obtained on one of the anodes include two distinct arcs and a minor contribution at low frequency. Measurements on the two electrodes in the coupled electrodes configuration reveals only one dominant arc in the impedance spectrum, and again a minor contribution at low frequency. The dominant arc measured on one anode is missing when measuring two coupled electrodes.

Comparing the time constants indicated by frequencies in Figure 5.3 to Figure 5.6, general trends in the impedance spectra are recognized.
The arc at high frequencies (kHz) has a real part of about 0.10 Ωcm^2 and is consistently present in the obtained spectra. It is hereafter referred to as arc I. Arc I has been demonstrated to depend on the microstructure of the anode itself.[5,21,34] An $(RQ)_1$ subcircuit with an n-value of about 0.8 has been used previously for data fitting.[5,34]
The arc at 10 to 100 Hz in Figure 5.3 to Figure 5.5 is denoted II, and has so far been unidentified. Two fitting approaches are taken; an $(RQ)_2$ subcircuit is applied in general, and an O element is applied for measurements in the two-atmospheres setup with a point contact current collector where one-dimensional diffusion in a fairly homogeneous gas layer of finite thickness can be anticipated.
The arc at 1 Hz (hereafter referred to as arc III) in Figure 5.3 and Figure 5.4 is caused by gas conversion and has been described for the two-atmospheres setup.[20,21] This impedance arc should not be found in measurements on samples of limited dimensions in a one atmosphere setup.[21]
The small arc at about 0.5 Hz in Figure 5.5 and Figure 5.6 is an artifact, as elaborated in the discussion. An $(RQ)_{Artefact}$ subcircuit with an n-value of 0.90 appears to be appropriate for data fitting. For the spectrum in Figure 5.5, parameters are fixed to those obtained from Figure 5.6 on a "number of electrolyte pellets" basis.

After this rather qualitative discussion of the shape of impedance spectra and an identification of contributions, the impedance data obtained are fitted using the equivalent circuit elements given in Table 5.1 for each test geometry. In general fitting with the described equivalent circuits yields errors of less than 0.5% in both real and imaginary part. The individual arcs as found by fitting are presented as dashed lines in Figure 5.3 to Figure 5.6.

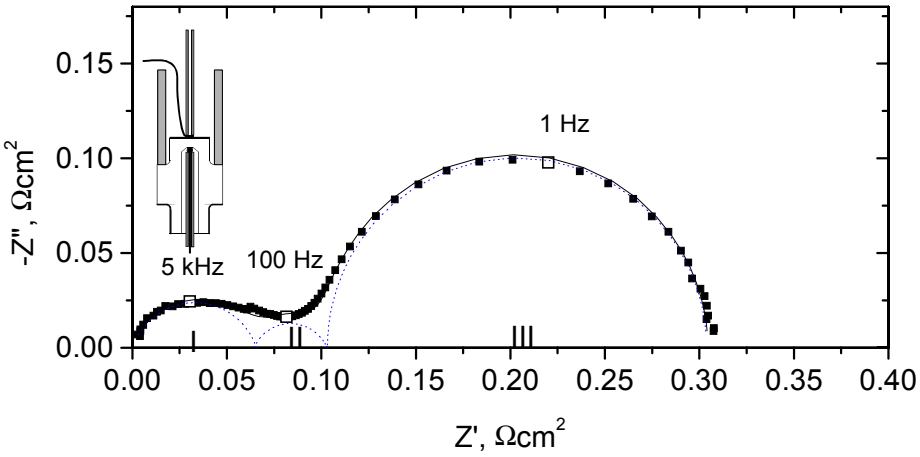

Figure 5.3 Impedance spectrum obtained in the two-atmospheres setup of Figure 5.1. Measurements in 97% H_2 + 3% H_2O at OCV at 1000°C, anode A93. Current collection as shown in the insert. The full line indicates the total equivalent circuit fit, dashed lines indicate the subcircuits.

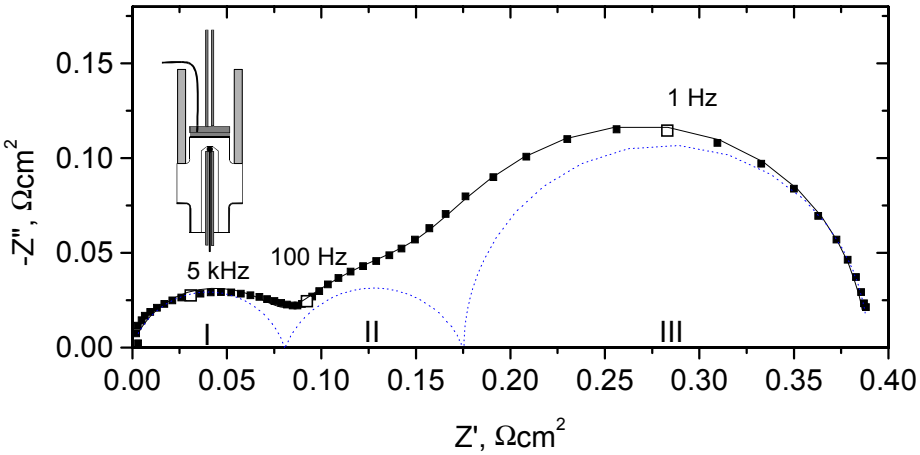

Figure 5.4 Impedance spectrum obtained in the two-atmospheres setup of Figure 5.1. Measurements in 97% H_2 + 3% H_2O at OCV at 1000°C, anode A93. Current collection as shown in the insert. The full line indicates the total equivalent circuit fit, dashed lines indicate the subcircuits.

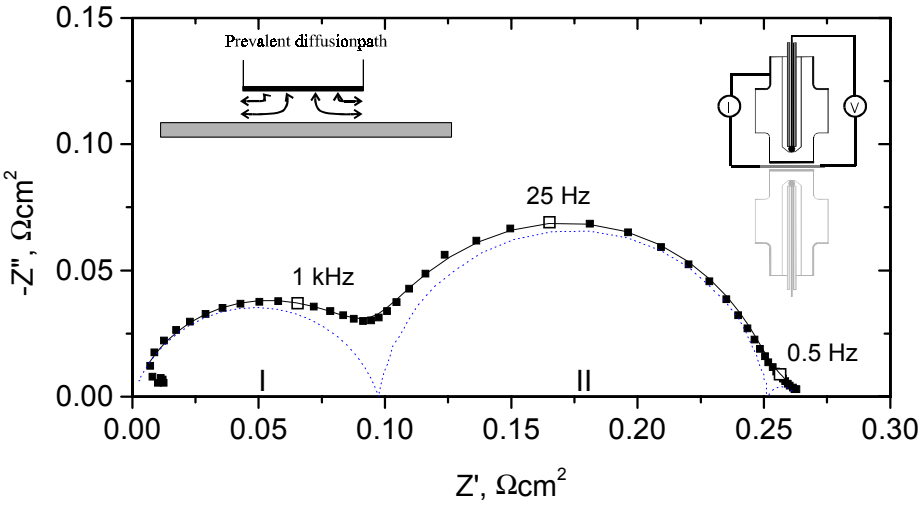

Figure 5.5 Impedance spectra obtained in the two pellets geometry of Figure 5.2. Measurements in 97% H_2 + 3% H_2O at OCV at 1000°C. Single electrode configuration as shown in the insert, anode A631. The full line indicates the total equivalent circuit fit, dashed lines indicate the subcircuits.

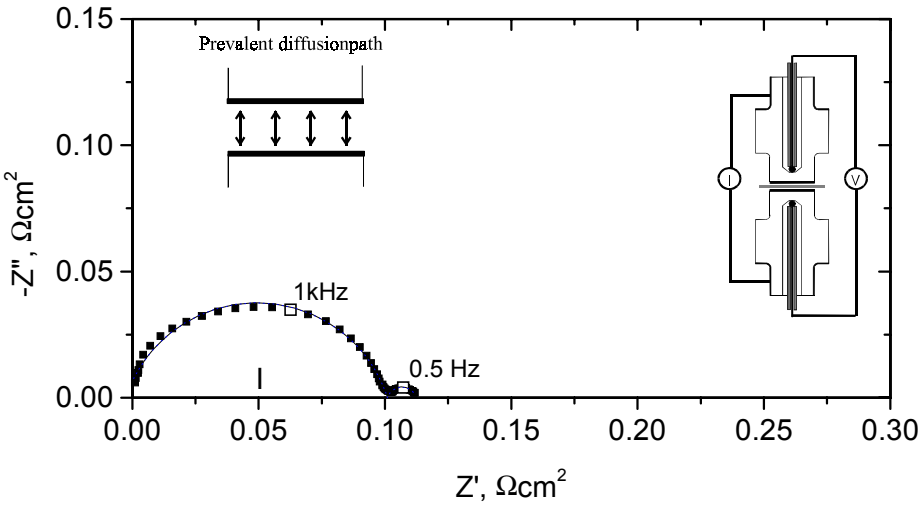

Figure 5.6 Impedance spectra obtained in the two pellets geometry of Figure 5.2. Measurements in 97% H_2 + 3% H_2O at OCV at 1000°C. Measured in coupled electrodes configuration as shown in the insert, anodes A630 and A631. The full line indicates the total equivalent circuit fit.

Table 5.1 Used equivalent circuit elements for fitting experimental data. In addition to the subcircuits for each arc an inductance L and a series resistance R_S are applied to account for inductance plus phase errors, and ohmic loss in the electrolyte, respectively.

Setup	measurement configuration	Arc I	Arc II	Arc III	Artifact arc
Two atmospheres	central current collection	$(RQ)_1$, $n_1 = 0.8$	$(RQ)_2$, $n_2 = 0.75$	$(RC)_3$	-
	central current collection	$(RQ)_1$, $n_1 = 0.7$	O	$(RC)_3$	-
	current collector inserted	$(RQ)_1$, $n_1 = 0.8$	$(RQ)_2$, $n_2 = 0.75$	$(RC)_3$	-
One atmosphere	single pellet	$(RQ)_1$, $n_1 = 0.8$	$(RC)_2$	-	(RQ), n = 0.9
	coupled electrodes	$(RQ)_1$, $n_1 = 0.8$	-	-	(RQ), n = 0.9

Arc II is examined further in the two-atmospheres setup. The molar fraction of water X_{H_2O} is varied from 0.005 to 0.04 at an X_{H_2} of 0.96 to 0.995, at constant flowrate and using a point contact current collector. In Figure 5.7 the parameters R_2 and R_O are presented, as obtained by fitting impedance spectra with equivalent circuits containing either an $(RQ)_2$ or an O-element. An almost linear dependence of both R_2 and R_O on $X_{H_2O}^{-1}$ is observed.

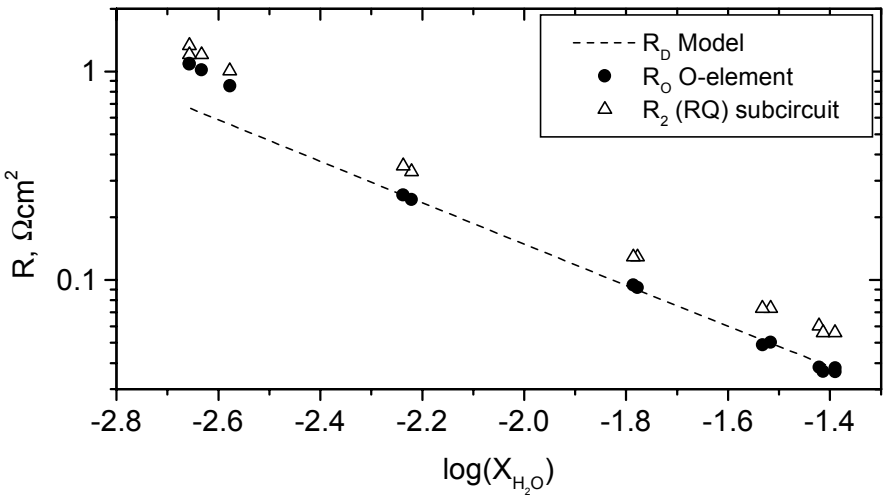

Figure 5.7 R_2 and R_O according to impedance spectra fitted to selected equivalent circuits as a function of molar fraction of water, X_{H_2O}, in an approximately constant X_{H_2} of 0.96 to 0.995. Anode A51 as measured in the setup of Figure 5.1 at 1000°C with central current collection. The dashed line indicate model prediction R_D according to Eq. (5.1) with $D_{Eff} = 11 \times 10^{-4}$ m^2/s and $l = 0.7$ mm.

The effect of different current collection methods has been evaluated. The parameters R_2 and $Y_{0,2}$ obtained by fitting impedance spectra are given in Table 5.2. A limited variation is seen in $Y_{0,2}$, whereas the change in R_2 is significant. No difference is found using a point contact or a point contact assisted by a 10-20 μm thick, porous Pt-layer. By inserting a supported felt current collector R_2 increases a factor of 2, and when 3 layers of felt are used, a further increase is noted.

Table 5.2 Equivalent circuit parameters for arc II derived by fitting the measured impedance spectra to the selected equivalent circuit (n_2 = 0.75). Different current collection geometries affecting the gas access were used. f_S is calculated according to Eq. (5.4) and l is calculated from f_S and $D_{Eff} = 1.1 \times 10^{-3}$ m^2/s using Eq. (5.5). All measurements in the geometry of Figure 5.1. T = 1273 K, 97% H_2 + 3% H_2O.

Anode	Current collector	R_2, Ωcm^2	$Y_{0,2}$, $Ss^{-0.75}/cm^2$	f_S, Hz	l, mm
A93	point	0.038	0.26	75	2
A93	point + Pt	0.038	0.28	66	3
A92	1 felt¤	0.066	0.33	27	4
A93	3 felts¤	0.094	0.30	19	5

¤ Ni-felt supported by a perforated Al_2O_3 plate.

The effect of applying different inert gases as balance in 10% H_2 with 3.5% H_2O is examined using a supported felt current collector. The parameters R_2 and $Y_{0,2}$ obtained after fitting impedance spectra are presented in Table 5.3. Again Y_0 is unaffected, whereas R_2 is substantially higher using inert gases of a higher molecular weight with lower diffusion coefficients. Little difference is observed between Ar and N_2.

Table 5.3 Equivalent circuit parameters for arc II derived by fitting the measured impedance spectra for anode A582 to the selected equivalent circuit (n_2 = 0.75). Different inert gases used in the geometry of Figure 5.1 with a supported Ni-felt current collector. f_S is calculated according to Eq. (5.4) and D_{Eff} is calculated from f_S using Eq. (5.5) and l = 4 mm. D_{12} is the binary diffusion coefficient for the couple H_2O/inert according to Eq. (5.2). T = 1318 K, 10% H_2 + 3.5% H_2O, balance is inert gas.

Inert gas	R_2, Ωcm^2	$Y_{0,2}$, $Ss^{-0.75}/cm^2$	f_S, Hz	D_{Eff}, 10^{-4} m^2/s	D_{12}, 10^{-4} m^2/s
Helium	0.25	0.12	17	7	11.3
Argon	0.46	0.12	8	3	3.47
Nitrogen	0.48	0.12	7	3	3.55

5.4 Discussion

5.4.1 Process Identification

It is assumed that arc II represents the same limiting process in both the one atmosphere setup and the simple two-atmospheres setup. The increase in R_2 by introducing a supported felt current collector (Ni-felt and perforated Al_2O_3 disk) on an anode structure in the two-atmospheres

setup is taken as a strong indication that the limiting process is related to this volume. The further increase in R_2 by 2 additional layers of 1 mm Ni-felt indicates that the volume thickness is in the mm range. This point is verified by measuring two coupled electrodes at a distance of less than 0.3 mm in the one atmosphere setup. Process II is not detected. Hereafter process II is assumed to be gas diffusion in a mm thick volume above the anode surface.
This assumption is examined by comparing the experimental findings with the predicted dependencies of DC steady state diffusion resistance as given by R_D in Eq. (5.1). This comparison between AC and DC diffusion resistance is valid, as the stagnant gas layer diffusion process is strictly in series with the reaction resistance. At infinite frequency no effective transport occurs in the stagnant layer, and at a frequency approaching zero, the AC diffusion impedance approaches the DC diffusion resistance. It follows that values of R_2 and R_O can be compared directly with the DC steady state diffusion resistance.

R_D is compared with experimental R_O values as function of X_{H_2O}, Figure 5.7, using a D_{Eff} of 11×10^{-4} m^2/s obtained as D_{12} for H_2O/H_2 at 1000°C according to Eq. (5.2). The calculated dependence $R_D \propto X_{H_2O}^{-1}$ is also found for R_O, and a good fit with experimental data is obtained using a layer thickness l of 0.7 mm. The R_2 value obtained when fitting with an $(RQ)_2$ subcircuit is slightly higher than R_O due to the overlap with arc I and the higher n_1-value used, but the dependence on gas composition is the same. Using the same D_{Eff}, a layer thickness l of 1 mm is obtained. It should be noted that the criterion $X_{H_2O,B} >> \Delta X_{H_2O}$ (see Appendix A) for Eq. (5.1) is not entirely fulfilled at low X_{H_2O} where data points deviate from the calculated curve.
Results presented in Table 5.2 for a point contact current collector yield an approximate gas layer thickness of 2 mm. This result is found by setting the summit frequency of arc II as given by Eq. (5.4) equal to f_S as given by Eq. (5.5) for a D_{Eff} of 11×10^{-4} m^2/s. When a supported felt current collector is applied, the gas layer thickness is about 4 mm.
Data in Table 5.3 obtained in different inert gases with a supported felt current collector are treated the same way to estimate values of D_{Eff}, using an l of 4 mm as found above. Good agreement with D_{12} according to Eq. (5.2) is found in nitrogen and argon. The value of D_{Eff} in helium is about 40% lower than expected. Assuming that the layer thickness could be 25% smaller for a light inert gas, the expected D_{12} value is arrived at.
A slightly negative apparent activation energy of -0.024 eV can be calculated for R_D based on Eq. (5.1), including the temperature dependence of D_{Eff} as given in Eq. (5.2). This is well in agreement with earlier data indicating a slight increase in resistance by increasing temperature for arc II, as measured on nominally identical anodes in the same two-atmospheres setup.[5]

Due to the limited magnitude of diffusion impedance (typically <0.1 Ωcm^2 in H_2 with at least 3% H_2O) it is only a relevant process for high-performance anodes where this contribution cannot be ignored. In this context high-performance can be defined as an electrode polarization resistance of 1 Ωcm^2 or less. The anodes examined in this study exhibit a polarization resistance of about 0.10 Ωcm^2 at 1000°C in hydrogen with 3% water, and no evidence in literature of less than 0.15 Ωcm^2 under these conditions has been found.[1,6] Pattern electrodes[8,9] and point electrodes[10-13] used for kinetic studies typically exhibit an impedance where the contribution from diffusion is negligible unless low concentrations of water and hydrogen are used.

A calculated l value of about 0.7 to 1 mm for the two-atmospheres setup with a point contact current collector is considered to be high. A gas jet of 100 Nml/min is introduced at a distance of 1 cm over a setup cross section of 0.5 cm^2. It may be that the volume geometry causes

a "gas cushion" of non-uniform thickness to form, rather than effective flushing of the anode surface. The increase in l to 3 to 4 mm by applying a supported felt current collector is consistent with the physical dimensions of the current collector.
In the one atmosphere setup, the coupled electrodes geometry is effectively minimizing diffusion limitation above the anode by assuring a uniform supply of a fuel gas mixture corresponding to the actual current at a distance of only 0.13 mm (½ mesh thickness) over the porous structure. Measuring only one cell against a dense surface at a distance of less than 0.3 mm, the predominant diffusion path is in-plane and R_2 is high.

At this point it may be speculated: if diffusion impedance relating to the gas above the electrode structure is observed, what is then the diffusion limitation in the anode structure? Indications of the electrochemical conversion taking place in the first 10 µm from the anode-electrolyte interface in cermet anodes has been obtained through experiments and modeling,[34-36] consequently diffusion of species through the anode structure must take place. With a lower D_{Eff} due to Knudsen diffusion in pores of about 1 µm and a 50 µm thick anode with a porosity of no more than 50%, a limitation from diffusion in the structure can be estimated. Applying a D_{Eff} for H_2/H_2O of 2.7×10^{-4} m^2/s (50% porosity, 1 µm pores and 1000°C)[27] and an l-value of 50 µm, a resistance R_D of 1.8×10^{-3} Ωcm^2 and a summit frequency of 45 kHz is arrived at using Eqs. (5.1) and (5.5) at 1000°C in 97% H_2 + 3% H_2O. R_D of this type of structure is thus negligible for the studied anodes. This impedance can probably not be resolved from the electrode response in general, due to the similar time constants.

5.4.2 Impedance Artifact

The nature of the low frequency arc of Figure 5.5 and Figure 5.6 is now considered. Typical parameters obtained in the coupled electrodes configuration (Figure 5.6) are R = 0.05 Ω, $Y_0 = 7$ $Ss^{-0.9}$, n = 0.9 and f_S = 0.5 Hz. An interpretation as a stagnant layer diffusion limitation based on f_S according to Eq. (5.5) yields a layer thickness of about 28 mm.
The effect of having a reference electrode in an atmosphere with a "weakly buffered" electrochemical potential (low pO_2) is considered. When the reference gas composition is influenced by the conversion of gas at the current bearing electrodes (counter electrodes in this case), a change of reference potential occurs. In the three-electrode pellets used the distance from counterelectrode to reference electrode is approximately 15 mm, and the volume comprises an 0.2 mm gap between the reference bore and an Al_2O_3 tube holding the reference electrode. Furthermore, the artifact arc is only observed in the one atmosphere setup using three-electrode pellets, and not found when using a two-electrode geometry on thin YSZ foils.[37] Therefore the arc at 0.5 Hz in Figure 5.5 and Figure 5.6 is interpreted as due to variations in the reference gas caused by diffusion between the counter electrode and the reference electrode.

5.4.3 Diffusion Impedance in SOFC Anode Literature

It can be difficult to assert if diffusion impedance relating to the volume outside the porous anode structure is contributing to a set of impedance data reported in literature. Also the co-existence with gas conversion impedance in setups with a reference electrode in a stable reference atmosphere outside the anode chamber can impede an identification, as the dependencies on temperature and reactant concentration in the bulk gas are similar.
Diffusion impedance has been reported in measurements on a 1 cm^2 symmetric two-electrode sample mounted in one atmosphere between gas distribution plates with a forced flow.[6] The

diffusion impedance has been found to form a nearly perfect semicircle of 0.2 Ωcm^2 at about 10 Hz (hydrogen with 2.5% H_2O, 850°C). By considering the resistance and time constant of the measurements and dimensions of the setup geometry, it has been concluded that the diffusion limitation is taking place along the gas channels, not in a stagnant layer.
A depressed arc of 0.1 Ωcm^2 below 10 Hz (hydrogen with 3% H_2O, 1000°C) has been found in measurements on large (6 to 7 cm^2) symmetrical two-electrode samples in one atmosphere, independent of the presence of H_2S.[1] Based on the above findings, it is here suggested that this arc may be caused by diffusion outside the anode. Due to the sample size, the influence of gas conversion cannot be excluded without a more thorough examination of the setup geometry.
Following deposition of a YSZ-layer of low porosity on top of a dense Ni anode, the appearance of an extra arc in impedance spectra has been observed and ascribed to diffusion in the porous YSZ layer.[10] The resistance is increasing linearly with thickness at a rate of 1 Ωcm^2 per 60 μm, demonstrated to be fairly independent of temperature and to have a linear dependence on $X_{H_2O}^{-1}$ in agreement with Eq. (5.1). Due to the low porosity, it was reasonable to assume that the high resistance was caused by a D_{Eff} orders of magnitude lower than for an open volume, yielding a very low time constant as demonstrated. The low time constant has also been troubling the authors, as an i-η curve obtained by a current interrupt technique was not in agreement with impedance spectra. It is suggested to be caused by difficulties resolving both the change from series resistance to electrode polarization resistance after 1 to 2 μs, and the gradual change to steady state obtained after about 100 s judging from impedance spectra.
A study of diffusion in a cermet anode structure has been reported.[26] In the light of the values derived above, the observed tendencies of i-η curves ascribed to diffusion in the anode structure are suggested to be caused by diffusion in a stagnant layer above the anode instead.
Also in the previously published anode results from Risø,[4,5,20,21] diffusion impedance of a stagnant gas layer above the anode contributes an arc denoted II in impedance spectra obtained by measurements in the two-atmospheres setup.

5.5 Conclusion

Gas diffusion is observed as an arc in impedance measurements on high-performance Ni/YSZ cermet anodes in different test setups. The diffusion resistance is < 0.15 Ωcm^2 at 1000°C in H_2 with 3% water. The inverse time constant of this arc is about 10 to 100 Hz.
The diffusion limitation observed is shown to relate to a volume of stagnant gas outside the porous anode structure and not to the porous anode structure itself. A diffusion length in the range of 0.7 to 4 mm, depending on the presence of current collector structures, was found.

The diffusion resistance in a typical porous anode structure is estimated to be a few mΩcm^2 at typical test conditions, and a calculated summit frequency of 45 kHz implies that diffusion impedance in an anode structure is concealed in the electrode impedance.

5.6 Appendices

A. DC Diffusion Limitation

A simple stagnant gas model based on the geometry of Figure 5.8 is derived below. Only DC steady state gas phase diffusion is considered, other electrode responses are omitted by assuming zero charge transfer resistance. A stagnant layer of thickness l is assumed over an anode of area A. Diffusion in the stagnant layer proceeds in one dimension, and we further restrict the analysis to consider only a linear gradient in gas compositions across the stagnant layer. The considered anode process of hydrogen oxidation is conservative with respect to the number of gas molecules, making the analysis particularly simple as pressure driven diffusion can be disregarded. The concentration C_j of electrochemically active species (suffix j = H_2 or H_2O) at the distance l from the anode surface are equal to that of the bulk gas outside the stagnant layer, $C_{j,B}$. The concentration of species at the anode surface is denoted $C_{j,A}$. The variation in concentration $\Delta C_{j,A}$ at the interface is defined as $C_{j,A}$-$C_{j,B}$, and when $C_{j,B}$ is constant, $d\Delta C_{j,A} = dC_{j,A}$. The linear gradient of gas compositions throughout the stagnant layer is given by Eq. (5.6) from the model.

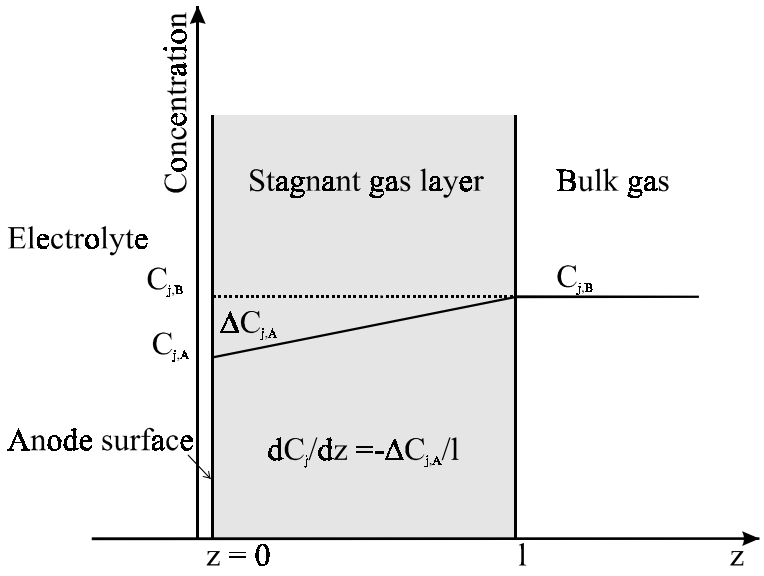

Figure 5.8 The used stagnant layer model. At a distance l over the anode surface a constant bulk gas composition is assumed. In the stagnant layer a linear concentration profile is assumed.

$$\frac{dC_j}{dz} = \frac{-\Delta C_j}{l} \tag{5. 6}$$

In the DC steady state case the diffusion of uncharged species at the anode surface is given by Fick's first law,

$$J_{j,A} = -D_{Eff} \frac{dC_{j,A}}{dz}_{z=0} \tag{5. 7}$$

where $J_{j,A}$ is the diffusion flux of species j at the anode surface, D_{Eff} is the effective diffusion coefficient of species j in a given gas mixture, and $dC_{j,A}/dz_{z=0}$ is the concentration gradient of species j at the anode surface where $z = 0$. The diffusion flux $J_{j,A}$ is controlled by the current density, i, according to Eq. (5.8)

$$J_{j,A} = \frac{i}{2F} \tag{5. 8}$$

Inserting now Eq. (5.6) in Fick's law (Eq. (5.7)) and combining with Eq. (5.8), the following expressions for variation of gas composition at the anode interface are obtained:

$$\Delta C_{\mathrm{H_2O},A} = \frac{li}{2FD_{Eff}} \tag{5. 9}$$

$$\Delta C_{\mathrm{H_2},A} = \frac{-li}{2FD_{Eff}} \tag{5. 10}$$

The overpotential η_D relating to the change in gas composition at the anode surface is given as Eq. (5.11) according to the Nernst equation.

$$\eta_D = \frac{RT}{2F}\ln\left(\frac{C_{\mathrm{H_2O},A}\cdot C_{\mathrm{H_2},B}}{C_{\mathrm{H_2O},B}\cdot C_{\mathrm{H_2},A}}\right) \tag{5. 11}$$

$$\eta_D = \frac{RT}{2F}\left(\ln\left(\frac{C_{\mathrm{H_2},B}}{C_{\mathrm{H_2O},B}}\right)+\ln\left(\frac{C_{\mathrm{H_2O},B}+\Delta C_{\mathrm{H_2O},A}}{C_{\mathrm{H_2},B}+\Delta C_{\mathrm{H_2},A}}\right)\right) \tag{5. 12}$$

By inserting Eqs. (5.9) and (5.10) and introducing molar fractions according to the ideal gas law, the general Eq. (5.13) is obtained

$$\eta_D = \frac{RT}{2F}\left(\ln\left(\frac{X_{\mathrm{H_2},B}}{X_{\mathrm{H_2O},B}}\right)+\ln\left(\frac{X_{\mathrm{H_2O},B}+RTli/2FPD_{Eff}}{X_{\mathrm{H_2},B}-RTli/2FPD_{Eff}}\right)\right) \tag{5. 13}$$

With the criterion $\Delta C_j << C_{j,B}$ (changes in the atmosphere composition are small compared with the bulk gas composition) Eq. (5.11) is linearized by the Taylor expansion ln(1+y) = y for y << 1 resulting in Eq. (5.14).

$$\eta_D = \frac{RT}{2F}\left(\frac{\Delta C_{\mathrm{H_2O},A}}{C_{\mathrm{H_2O},B}}-\frac{\Delta C_{\mathrm{H_2},A}}{C_{\mathrm{H_2},B}}\right) \tag{5. 14}$$

In this case $X_{\mathrm{H_2O},B} >> RTli/2FPD_{Eff}$ and $X_{\mathrm{H_2},B} >> RTli/2FPD_{Eff}$ must be fulfilled, and Eq. (5.14) yields Eq. (5.15) by substituting molar fractions for concentrations.

$$\eta_D = \left(\frac{RT}{2F}\right)^2 \frac{l}{PD_{Eff}} \left(\frac{1}{X_{\mathrm{H_2},B}} + \frac{1}{X_{\mathrm{H_2O},B}}\right) i \qquad (5.\ 15)$$

This linear dependence is valid only in the low current density range with high $X_{\mathrm{H_2O},B}$ and $X_{\mathrm{H_2},B}$.

Acknowledgment

This work was supported in part by the European Commission under contract no. JOE3-CT95-0005, and in part by the Danish Energy Agency under the Danish DK-SOFC program. Discussions with Dr. P. V. Hendriksen, Risø National Laboratory and Dr. H. J. M. Bouwmeester, University of Twente are appreciated. The presented experimental data have been generated as a result of the joint effort of many members of the SOFC project group at Risø. Their contributions are gratefully acknowledged.

References

[1] D. W. Dees, U. Balachandran, S. E. Dorris, J. J. Heiberger, C. C. McPheeters and J. J. Picciolo, in *Solid Oxide Fuel Cells*, S. C. Singhal, Editor, **PV 89-11**, The Electrochemical Society Proceedings Series, Pennington, NJ. 317 (1989)

[2] T. Kawada, N. Sakai, H. Yokokawa, M. Dokiya, M. Mori and T. Iwata, *J. Electrochem. Soc.* **137** 3042 (1990)

[3] M. Mogensen and T. Lindegaard, in *SOFC III*, S. C. Singhal and H. Iwahara, Editors, **PV 93-4**, The Electrochemical Society Proceedings Series, Pennington, NJ. 484 (1993)

[4] M. Mogensen, S. Primdahl, J. T. Rheinländer, S. Gormsen, S. Linderoth and M. Brown, in *SOFC IV*, M. Dokiya, O. Yamamoto, H. Tagawa and S. C. Singhal, Editors, **PV 95-1**, The Electrochemical Society Proceedings Series, Pennington, NJ. 657 (1995)

[5] S. Primdahl and M. Mogensen, *J. Electrochem. Soc.* **144** 3409 (1997), chapter 3 in this thesis

[6] J. Geyer, H. Kohlmüller, H. Landes and R. Stübner, In *SOFC V*, U. Stimming, S. C. Singhal, H. Tagawa and W. Lehnert, Editors, **PV 97-40**, The Electrochemical Society Proceedings Series, Pennington, NJ. 585 (1997)

[7] J. Guindet, C. Roux and A. Hammou, in *SOFC II*, F. Grosz, P. Zegers, S. C. Singhal and O. Yamamoto, Editors, EUR-13564-EN. 553 (1991)

[8] J. Mizusaki, H. Tagawa, T. Saito, T. Yamamura, K. Kamitani, K. Hirano, S. Ehara, T. Takagi, T. Hikita, M. Ippommatsu, S. Nakagawa and K. Hashimoto, *Solid State Ionics*, **70/71** 52 (1994)

[9] J. Mizusaki, H. Tagawa, T. Saito, K. Kamitani, T. Yamamura, K. Hirano, S. Ehara, T. Takagi, T. Hikita, M. Ippommatsu, S. Nakagawa and K. Hashimoto, *J. Electrochem. Soc.* **141** 2129 (1994)

[10] N. Nakagawa, H. Sakurai, K. Kondo, T. Morimoto, K. Hatanaka and K. Kato, *J. Electrochem. Soc.* **142** 3474 (1995)

[11] P. A. Osborg and T. Norby, in *7th SOFC WORKSHOP, Theory and measurement of Microscale Processes in Solid Oxide Fuel Cells*, 47 (1995). IEA report obtainable from H. Nabielek, KFA-ISR Forschungs Zentrum Jülich GmbH, D-52425 Jülich, Germany.

[12] F. Z. Mohamedi-Boulenouar, J. Guindet and A. Hammou, in *SOFC V*, U. Stimming, S. C. Singhal, H. Tagawa and W. Lehnert, Editors, **PV 97-40**, The Electrochemical Society Proceedings Series, Pennington, NJ. 441 (1997)

[13] R. J. Aaberg, R. Tunold, M. Mogensen, R. W. Berg and R. Ødegård, *J. Electrochem. Soc.* **145** 2244 (1998)

[14] J. Newman, *J. Electrochem. Soc.* **113** 501 (1966)
[15] T. Takahashi, H. Iwahara and Y.Suzuki, in *Third Int. Symp. on Fuel Cells*, Presses Academiques Europeennes, Bruxelles. 113 (1969)
[16] S. Pizzini, in *Fast Ion Transport in Solids, Solid State Batteries and Devices*, W. van Gool, Editor, North-Holland Publishing Company, Amsterdam. 461 (1973)
[17] N. L. Robertson and J. N. Michaels, *J. Electrochem. Soc.* **138** 1494 (1991)
[18] M. Nagata and H. Iwahara, *J. Appl. Electrochem*. **42** 275 (1993)
[19] T. Kawada, B. A. van Hassel, T. Horita, N. Sakai, H. Yokokawa and M. Dokiya, *Solid State Ionics,* **70/71** 65 (1994)
[20] S. Primdahl and M. Mogensen, in *SOFC V*, U. Stimming, S. C. Singhal, H. Tagawa and W. Lehnert, Editors, **PV 97-40**, The Electrochemical Society Proceedings Series, Pennington, NJ. 530 (1997)
[21] S. Primdahl and M. Mogensen, *J. Electrochem. Soc.* **145** 2431 (1998), chapter 4 in this thesis
[22] J. A. Lane, S. Adler, P. H. Middleton and B. C. H. Steele, in *SOFC IV*, M. Dokiya, O. Yamamoto, H. Tagawa and S. C. Singhal, Editors, **PV 95-1**, The Electrochemical Society Proceedings Series, Pennington, NJ. 584 (1995)
[23] P. Holtappels, M. J. Jørgensen, S. Primdahl, M. Mogensen and C. Bagger, in *Third European SOFC Forum*, P. Stevens, Editor, European Fuel Cell Forum, Oberrohrdorf, CH. 311 (1998)
[24] S. B. Adler, J. A. Lane and B. C. H. Steele, *J. Electrochem. Soc.* **143** 3554 (1996)
[25] K.-Z. Fung and A. V. Virkar, in *SOFC IV*, M. Dokiya, O. Yamamoto, H. Tagawa and S. C. Singhal, Editors, **PV 95-1**, The Electrochemical Society Proceedings Series, Pennington, NJ. 1105 (1995)
[26] K. Eguchi, Y. Kunisa, K. Adachi and H. Arai, *J. Electrochem. Soc.* **143** 3699 (1996)
[27] A. Solheim, in *SOFC Micromodelling, an International Energy Agency SOFC Task Report*, L. Dubal, Editor, Swiss Federal Office of Energy, Berne, CH. 9 (1992)
[28] J. R. Welty, C. E. Wicks and R. E. Wilson, *Fundamentals of Momentum, Heat and Mass Transfer*, *Third Edition*, John Wiley & Sons, Inc., New York. 490 (1984)
[29] J. Winkler, P. V. Hendriksen, N. Bonanos and M. Mogensen, *J. Electrochem. Soc.* **145** 1184 (1998)
[30] R. Hartung and H.-H. Möbius, *Chemie-Ing. Techn*. **40** 592 (1968)
[31] B. A. Boukamp, *Solid State Ionics*, **20** 31 (1986)
[32] J. R. Macdonald, *Impedance Spectroscopy*, John Wiley & Sons, Inc., New York. 88 (1987)
[33] T. Jacobsen, B. Zachau-Christiansen, L. Bay and S. Skaarup, in *High Temperature Electrochemistry: Ceramics and Metals*. F. W. Poulsen, N. Bonanos, S. Linderoth, M. Mogensen and B. Zachau-Christiansen, Editors, 17th Risø International Symposium on Materials Science, Roskilde, DK. 29 (1996)
[34] M. Brown, S. Primdahl and M. Mogensen, *J. Electrochem. Soc*. submitted (1999), chapter 6 in this thesis
[35] S. Sakamoto, H. Taira and H. Takagi, *Denki Kagaku*, **64** 609 (1996)
[36] S. Sunde, *J. Electrochem. Soc.* **143** 1930 (1997)
[37] S. Primdahl and M. Mogensen, in *SOFC VI*, accepted (1999), chapter 8 in this thesis

Chapter 6

Anode Structure/Performance Relations[†]

Abstract

The relations between morphology and electrochemical performance of Ni/yttria-stabilized zirconia (YSZ) anodes are investigated. Four types of anodes are prepared on YSZ electrolyte three electrode pellets. A fine cermet of 0.5-1 μm particles, a coarse cermet of 2-3 μm particles, a porous Ni-paste anode and a Ni-felt anode. The anodes are characterized by impedance spectroscopy at open circuit potential, and the electrode relevant part (polarization resistance, R_P) of the spectra is identified and investigated. The active thickness of the fine cermet anode is demonstrated to be about 10 μm, and is believed to relate to the conductivity of the YSZ network. In the temperature range of 850 to 1000°C the dependence of R_P exhibits an apparent activation energy which increases with coarseness of the anode. No significant dependence on pH_2 (0.01-0.97 atm) at 1000°C is observed. A dependence on pH_2O of about $R_P \propto pH_2O^{-1/2}$ is found. Physical transport limitations are suggested as possible causes for the observed anode polarization.

[†] This chapter has been submitted as M. Brown, S. Primdahl and M. Mogensen, "Structure/Performance Relations for Ni/YSZ Anodes for SOFC", *J. Electrochem. Soc.* (1999).
Earlier published in part as chapter 6 of M. Brown, Thesis, University of Waikato, New Zealand (1999)

6.1 Introduction

The performance of a solid oxide fuel cell (SOFC) anode is strongly dependent on the fabrication methods and resulting microstructure of the cermet. Since the polarization characteristics of the anode are highly dependent on its morphology, it is necessary to investigate the correlation between anodes with different structures, such as fine structured cermets, coarse cermets, porous Ni anodes and Ni-point electrodes.

A homogeneous or graded structure consisting of three phases, Ni, yttria stabilized zirconia (YSZ) and porosity should be obtained, providing percolation paths for electrons, oxide ions and gaseous hydrogen and water, respectively. This requirement originates in the poor conductivity of electrons in YSZ and oxide ions in Ni. The line where the three phases meet is referred to as the triple phase boundary (TPB) and is considered to be electrochemically active only if percolation paths for the active species are provided. The reaction rate for electrochemical oxidation of hydrogen has been demonstrated to correlate with the length of the TPB on model Ni anodes,[1,2] making extension of the TPB a technology aim.

This aim can in theory be achieved by a finer structure, or by increasing the thickness of the cermet anode. In practice, however, both solutions are limited by the requirement for low resistivity percolation of active species. As the characteristic dimensions of the structure decrease, and as the anode thickness increases, the transport resistivities increase.

6.1.1 Limitations on Performance

In general, the anodic oxidation of hydrogen can be limited by i) electrochemical and chemical reaction steps at the TPB, ii) by physical transport restrictions for electrons and oxide ions in the solid structure, iii) by surface adsorption and iv) surface diffusion of species, and v) by gas diffusion in the cermet structure. Furthermore, vi) concentration polarization in the gas outside the anode structure can contribute to actual measurements without having any relation to the anodes investigated.

A few observations regarding these contributions to the measurable overpotential are discussed in the following.

i) The hydrogen oxidation process has been proposed not to contribute, based on extrapolation of overpotentials obtained at lower temperatures to SOFC-relevant temperatures using the observed activation energy.[3]
i-iv) Due to the catalytic properties of Ni, a high sticking coefficient and surface coverage of hydrogen, the adsorption, bond-breaking and diffusion of hydrogen on Ni has been suggested not to contribute significantly.[4,5]
v) Diffusion restriction in the porous structure of anodes is a significantly smaller problem than for cathodes.[6] According to model calculations, the diffusion limitation in the porous cermet is insignificant for anodes of about 50 μm thickness and with a porosity of about 50%.[6,11] Diffusion in ceramic structures over anodes has been demonstrated to be significant when the porosity is extremely low.[7]
vi) Gas conversion, relating to the changes in the Nernst potential of the fuel gas (with respect to a stable reference electrode) by passing a current at finite fuel gas flow rate, has been shown to add significantly to the measured overpotential of state-of-the-art anodes.[8,9] Also diffusion in the gas over the anode surface has been reported.[10] A model involving a 1 mm thick layer of stagnant

gas over the anode surface has been based on illustrative experiments.[11] These types of concentration polarization outside the anode structure depend on the apparatus design, placement of reference electrode and gas exchange rates, and can vary significantly with the test geometry. It is recognized that in studies of state-of-the-art anodes, or any anode in low partial pressures of hydrogen or water, the electrochemical data can be affected by the presence of this type of concentration polarisation.[4,8,9]

Both state-of-the-art anodes with high current densities and 'model' anodes with simple geometries have been reported. The results of these studies are in general in disagreement. The number of distinct arcs in impedance spectra under apparently similar experimental conditions is inconsistent, and the apparent activation energy and dependence on gas composition of the resistances associated with these arcs are inconclusive.

When the concentration polarization effects in data reported in the literature are identified and subtracted, one is left with several indications that only one arc (or two overlapping arcs with similar time constants) at high frequency in impedance spectra is related to the Ni/YSZ cermet anode microstructure.
Impedance measurements on point electrodes, Ni films and cermets can give a number of combinations of arcs. This can vary from one arc for certain point electrodes to three or four arcs for some cermets. Microelectrodes (point shaped contacts) are reported to give one[12] or two[2,13,14] arcs. Measurements on Ni pattern electrodes are reported to yield one[1] or two[15] arcs. Measurements on cermets are reported to contain one arc,[16] one arc plus an arc from diffusion above the active anode[10,7] or one arc plus two arcs relating to diffusion over the anode and gas conversion.[9,11,17]

Studies revealing how only the high frequency arc is affected by poisoning of the Ni surface by H_2S in the fuel, is taken as evidence of a rate limiting process involving the Ni surface or a species made available from this surface.[10,18]
Furthermore, the impedance for a reaction expected to take place on or at the TPB, must be in parallel to the interface capacitance. This capacitance has been reported for Pt/YSZ to be in the order of 10 $\mu F/cm^2$ at 800 to 1000 °C.[19] The capacitance associated with the Ni/YSZ interface (high frequency arc) was about 10 $\mu F/cm^2$ for both Ni-pattern[2] and cermet[20] anodes.

On summarizing the literature, it has been suggested that Ni/YSZ anodes operated in H_2/H_2O atmospheres at 700 to 1000°C, can be thought to exhibit one arc representing one significant rate limiting process, but in several cases a second arc has appeared.[16,21] The exact nature of these arcs is unclear. However, the sintering of anodes has been demonstrated to affect the shape of the high frequency impedance for Ni/YSZ cermets,[21] making transport restrictions in the solid phases a likely contributor.[22]

In this study, four types of Ni/YSZ anodes have been characterized and compared to illustrate similarities and differences between state-of-the-art cermet anodes, coarse structured cermets, and two-dimensional Ni anodes with a significantly higher polarization resistance. The various anodes have been studied on a well characterized electrolyte geometry[23] in a setup where the gas conversion[8,9] and diffusion[11] over the anode are well understood, and can be corrected for where appropriate. The anode structure-dependent high frequency arc in the impedance spectrum has been studied.

The aim of this chapter is to:

i) Determine the electrochemically active thickness of a technological cermet anode, and to indicate the nature of the limitation to this thickness,
ii) Illustrate how the structure-dependent part of impedance spectra in some cases is composed of more than one arc, and
iii) Discuss the nature of the limitations reflected in the impedance arc(s) in terms of apparent thermal activation and dependence on partial pressures of H_2 and H_2O.

6.2 Experimental

6.2.1 Sample Preparation

All electrochemical tests were carried out on a three-electrode pellet produced from YSZ (ZrO_2 doped with 8 m/o Y_2O_3, Tosoh Corporation). The pellets, with circular working electrodes of about 0.44 cm^2 are fabricated with a Pt-paste counter electrode, a Pt-ball reference electrode in the center bore and two Pt leads in contact with the working electrode. The electrolyte geometry used here is verified by finite element analysis to have a frequency-stable, homogeneous current distribution, causing less than 4% error in a polarization resistance in the range of 0.02 to 2 Ωcm^2.[23]

Four types of anodes were prepared:

(i) A fine cermet Ni/YSZ anode was prepared by spray-painting. An ethanol-based slurry, composed of NiO (99% NiO, Johnson Matthey) and YSZ, was suspended by a dispersant.[24] The Ni/YSZ volume ratio was 40/60 in the reduced cermet. After deagglomeration in a ball mill, the YSZ particle size was observed to be 0.4 μm. The NiO particle size distribution was bimodal with fractions of approximately 0.4 μm and 10 μm in the volume ratio 6:1. The slurry was sprayed onto sintered YSZ three-electrode pellets in layers of up to 20 μm and sintered for 2 hours at 1300°C, after the application of each layer. The anodes were typically 40 to 50 μm thick after three layers were deposited.
Anodes of this type were prepared with a thickness between 3.5 μm to 50 μm. A Ni-based current-collecting layer was applied on these thin anodes, consisting of a 20 to 50 μm thick, unfired layer of a paste containing 90/10 v/o Ni/YSZ, fabricated as described below under (iii).

(ii) Coarse cermet anodes were prepared at Forschungszentrum Jülich by screen-printing. The organic based screen print paste contained 57 w/o green NiO (Baker), 38 w/o YSZ calcined at 1300°C for 2 hours and 5 w/o ethylcellulose. The samples were dried and sintered at 1500°C for 4.5 hours.

(iii) A Ni-paste anode was prepared by applying a Ni-paste without sintering before testing. To enhance adhesion of the Ni anode on the YSZ pellet a Ni solution containing 1 mmol/l $Ni(NO_3)_2$ in ethanol with 4 w/o binder, (B60H, Mowital) was painted on the electrolyte pellet and decomposed in moist 9% H_2 at 1420°C.[25]
The Ni-paste was prepared as follows: YSZ calcined at 1100°C for two hours was ball milled in ethanol with a dispersant until an average diameter of 0.4 μm was reached for the mono-modal particle size distribution. Ni (Ni #255, Inco) with a particle size of 1 to 2 μm in 10-20 μm

filamentous agglomerates was added, and the viscous paste was milled until the bimodal particle size distribution contained about 20 v/o of 0.4 μm and 80 v/o of 8 μm diameter particles and agglomerates. The paste was applied by brush in a layer of 20 to 50 μm thick. The Ni/YSZ volume ratio was 90/10 in the anode.

(iv) A Ni-felt anode was constructed as follows. A 1 mm thick Ni-felt (Ni-fibermat, 80/20 fibers/particles, Fibrex) consisting of fibers of 50 μm diameter was pressed against the surface of a three-electrode pellet using a perforated Al_2O_3 disk.

6.2.2 Electrochemical Testing

The three-electrode pellets were mounted in a four-lead three-electrode setup, Figure 6.1. This setup provided a reference atmosphere (air) and a sealed anode compartment with a controllable atmosphere.

Cells were heated to 1000°C in 9% H_2 + 3% H_2O before switching to an atmosphere of 97% H_2 + 3% H_2O with an open circuit voltage (OCV) against Pt in air of about -1070 mV ($pO_2 \sim 2 \times 10^{-18}$ atm.). A total of 100 ml/min (at 25 °C) gas was passed over the anodes. Fuel composition was controlled by mixing nitrogen and hydrogen through thermal mass flowmeters and saturating this mixture, or part of it, with water at a controlled temperature.

pO_2 was determined by the Nernst expression from OCV vs. Pt/air. The accurate partial pressure pH_2O is determined from pO_2 and pH_2 by the following equation valid for 1000 K < T < 1300 K:[26]

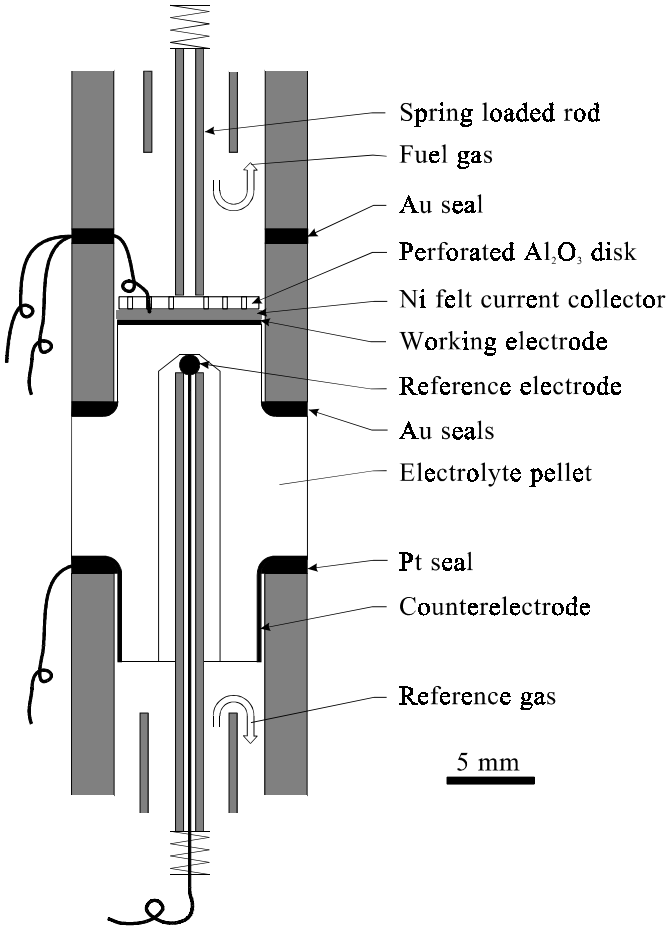

Figure 6.1 Test setup comprising a three-electrode pellet exposed to two atmospheres.

$$pH_2O = 10^{-(2.958-13022/T)} \cdot pH_2 \cdot \sqrt{pO_2} \qquad (6.1)$$

Impedance spectroscopy was conducted with an applied amplitude of 20 to 30 mV. The frequency range used was 500 kHz to 0.01 Hz, in some cases only 65 kHz to 0.1 Hz. The equipment used for impedance spectroscopy was a Solartron 1260 or 1250 frequency response analyzer with a Solartron 1287 or 1286 electrochemical interface.

A single anode of type i) was reduced at 1000°C, cooled and thereafter exposed to 20 ml of 15% hydrochloric acid in water three times, to remove the metallic Ni from the cermet structure. The edges of the electrode which were slightly higher than the central electrode were removed by a scalpel under a stereo microscope. The YSZ-structure was covered by 3 layers of leaf-gold, and an 0.3 mm gold sheet was placed on top of the leaf-gold, pressed down by an Al_2O_3 disk and a spring-load in the three-electrode setup. The electrode was characterized in air at 1000°C. Hereafter the porous YSZ structure was removed, and again the electrode surface was covered by gold and characterized in air at 1000°C.

6.2.3 Morphology Investigation

After testing anodes were cooled in 9% H_2 + 3% H_2O, vacuum-molded in epoxy, cut and polished for structural examinations of the cross sections in a Low-vacuum scanning electron microscope (LV-SEM). Using back-scattered electrons it was not possible to distinguish between Ni and YSZ due to the similar average atomic weight. Optical microscopy with the inherent limitations in resolution was used as a supplement to identify the distribution of the solid phases. The thickness of all tested anodes was determined in LV-SEM.

6.3 Results

6.3.1 Anode Structure

The microstructure of the fine cermet anodes is given in Figure 6.2A. The particles were 0.5 to 3 μm, and the porosity was in the order of 50%. Using optical microscopy, the distribution of the two phases was verified to be fairly homogeneous. Furthermore, Ni was evaluated to constitute the fraction of larger particles, with YSZ particles typically in the range of 0.5 to 1 μm. The anode thickness was evaluated from an average of 10 images obtained over a 7 mm cross section of the anode.

The structure of the coarse cermet anodes is indicated in a cross section in Figure 6.2B. The particle size was in the range of 3 to 5 μm for both phases with the Ni particles being clearly distinguishable from the YSZ particles by their morphology.

Ni-paste anodes consisting of 90/10 v/o Ni/YSZ had a porous, well percolating Ni-structure, Figure 6.2C. The low amount of fine dispersed YSZ particles was taken to indicate that all active TPB should be found on the two-dimensional interface between the bulk electrolyte and the Ni anode. The characteristic size of the Ni particles touching the electrolyte was about 10 μm, and about 20% of the electrolyte surface was contacted by the Ni anode judging from 10 SEM images. This yielded a TPB of about 800 cm/cm^2.

The Ni-felt anodes consisting of 50 μm diameter fibers left a 20 μm wide imprint of each contact on the polished electrolyte pellet surface, Figure 6.2D. The imprint was taken to represent the TPB on the two-dimensional interface, and the estimated contact surface was 8% with a TPB length of the order of 90 cm/cm^2. Along the rim of the contact area fine Ni-particles were observed on the electrolyte surface. This has also been observed and discussed by others.[27]

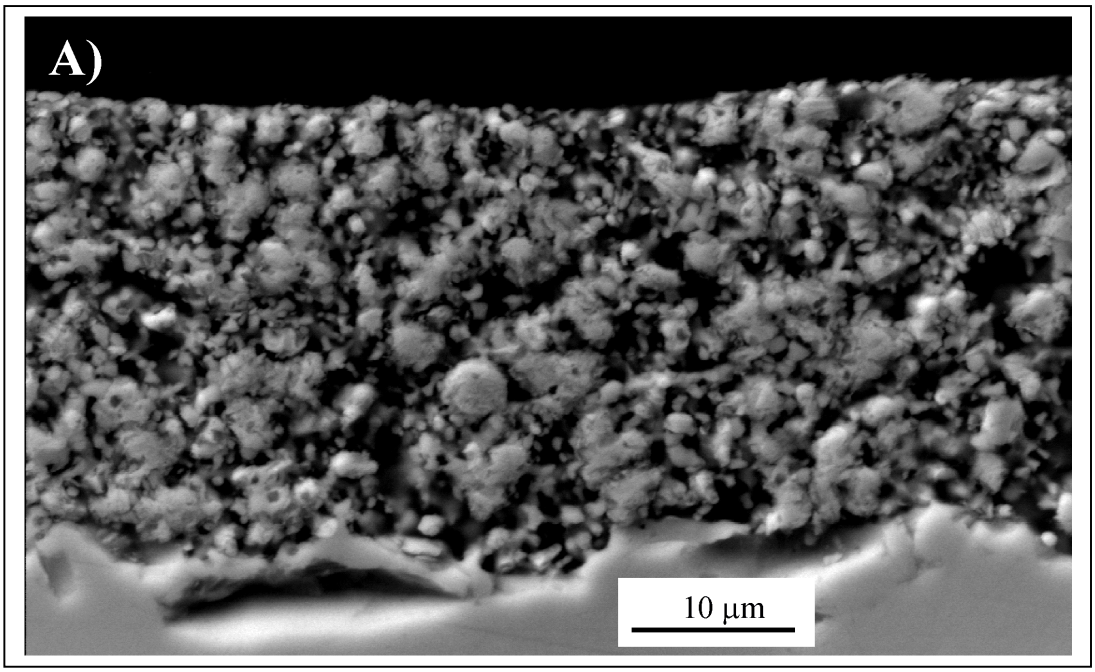

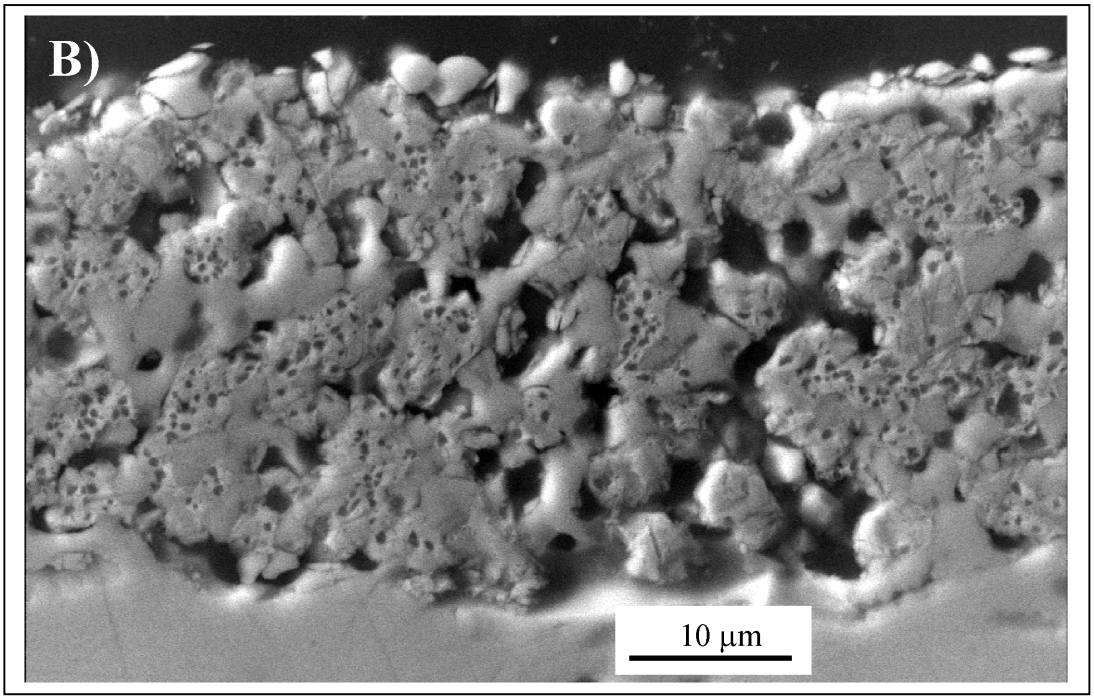

Figure 6.2 SEM micrographs showing structure of anodes as observed by back-scattered electrons on a polished cross section. A) fine cermet (larger particles are predominantly Ni), B) coarse cermet (Ni-particles appear micro-porous), C) Ni-paste anode. D) Ni-felt anode imprint on the surface of the electrolyte pellet with Ni particles deposited along the contact line. (*Cont. next page*)

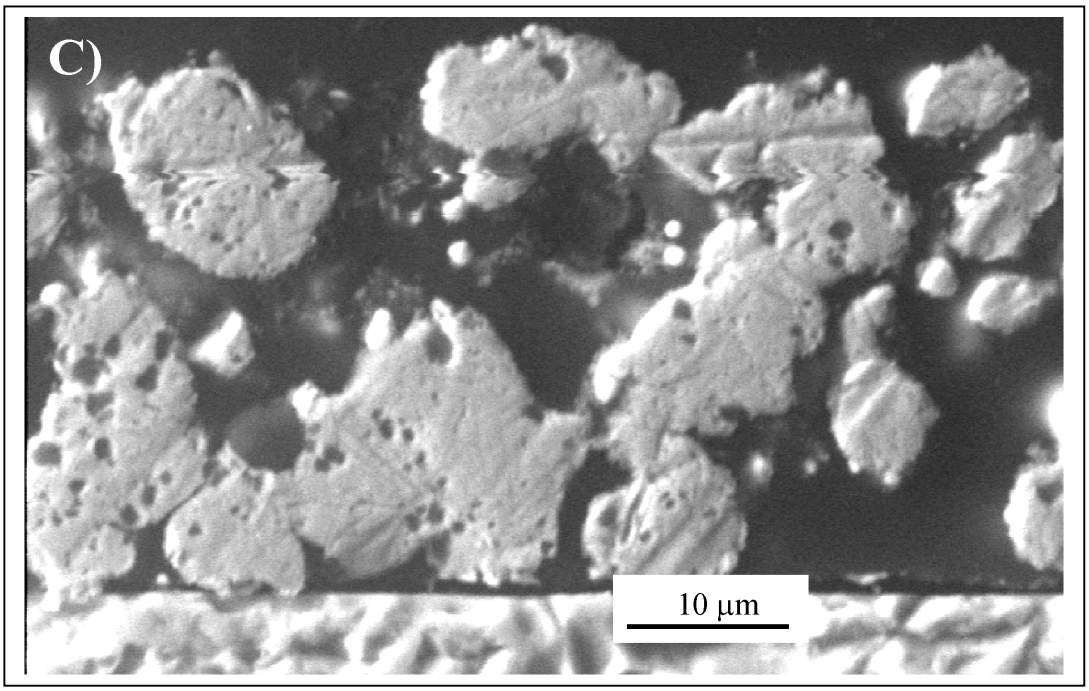

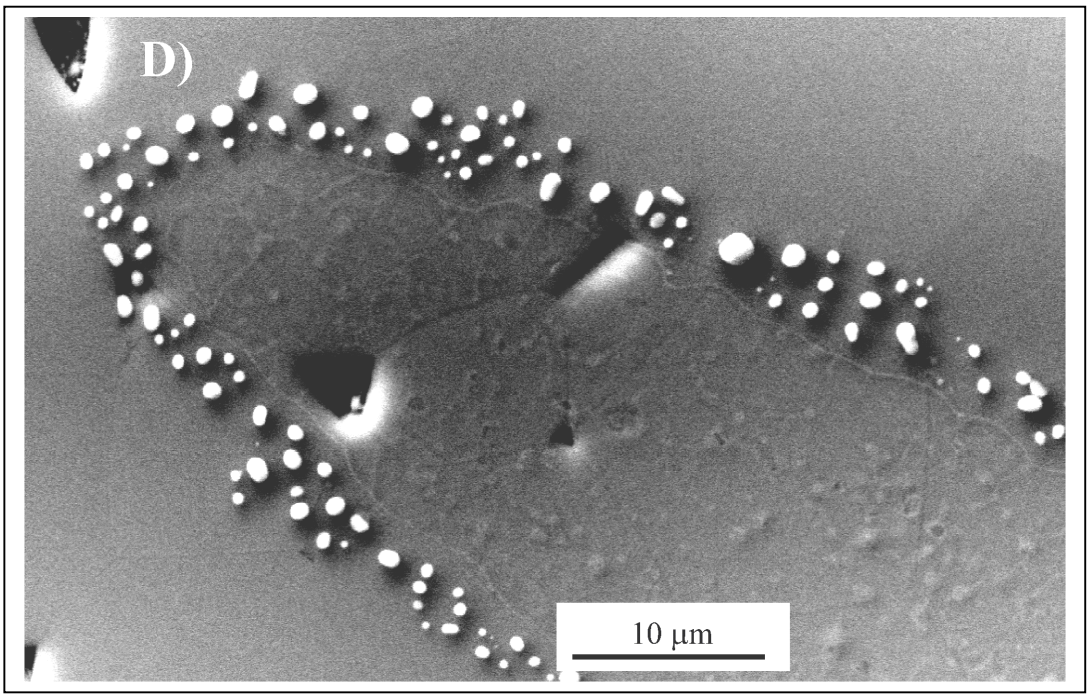

Fig 6.2. Cont.

6.3.2 Impedance Spectra

Impedance spectra obtained at the maximum temperature (1000 °C) are considered first, as the concentration overpotentials (gas conversion and diffusion) are most distinct at high temperatures. This was concluded from the fact that the size of these arcs is fairly independent on temperature, whereas the electrode response is observed to be thermally activated.[20]

Spectra obtained at OCV at 1000°C in 97% H_2 + 3% H_2O are given in Figure 6.3, after correction for a series resistance of 1 to 3 Ω, and a macroscopic anode area in the range of 0.4 to 0.45 cm^2. Characteristic frequencies are marked for ease of comparison. Firstly, gas conversion (marked III) was recognized in Figure 6.3A to Figure 6.3C, comprising of 0.12 to 0.15 Ωcm^2 at a characteristic frequency of 1 Hz.[9] The diffusion impedance relating to the gas over the anode was resolvable in Figure 6.3A and Figure 6.3C, as an arc (marked II) of about 0.025 Ωcm^2 at an intermediate characteristic frequency of 10 to 100 Hz.[11] In Figure 6.3B the diffusion impedance cannot be resolved, and in Figure 6.3D neither of the concentration polarization processes are recognized, due to the relative magnitude of the electrode impedance.

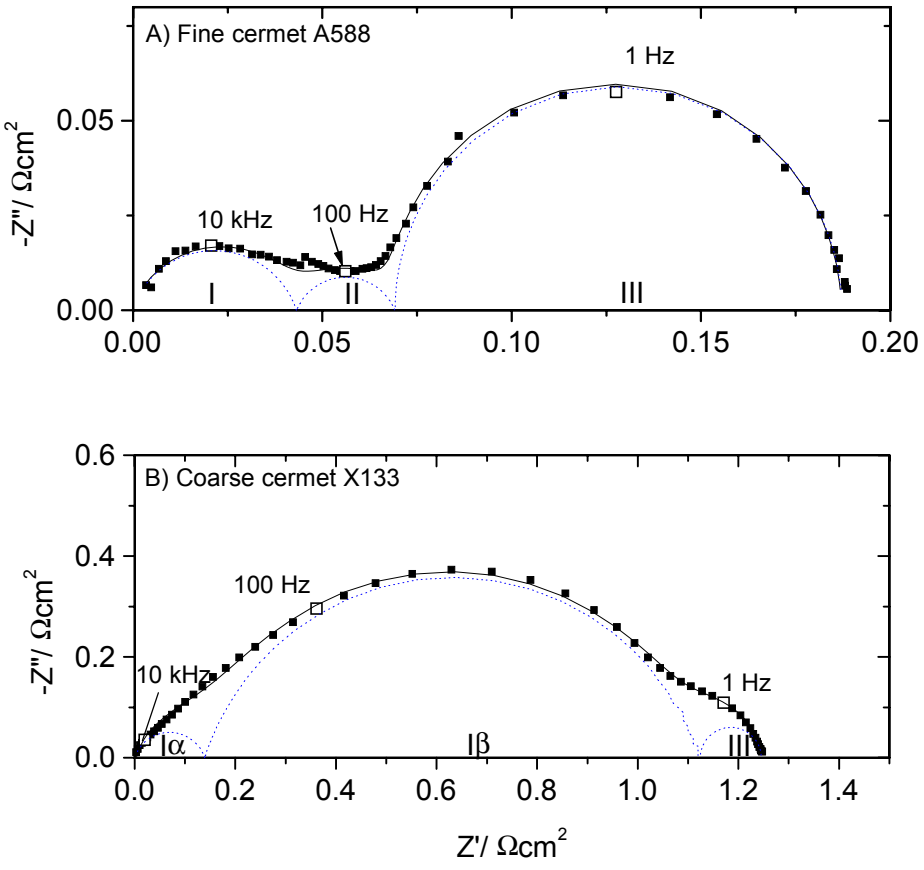

Figure 6.3 Area specific impedance spectra obtained at OCV at 1000°C in H_2 + 3% H_2O. Points are experimental data, solid lines are total fit data and dashed lines indicate each impedance arc in the fit. A) Fine cermet, B) coarse cermet, C) Ni-paste anode and D) Ni-felt anode. (*Cont. next page*)

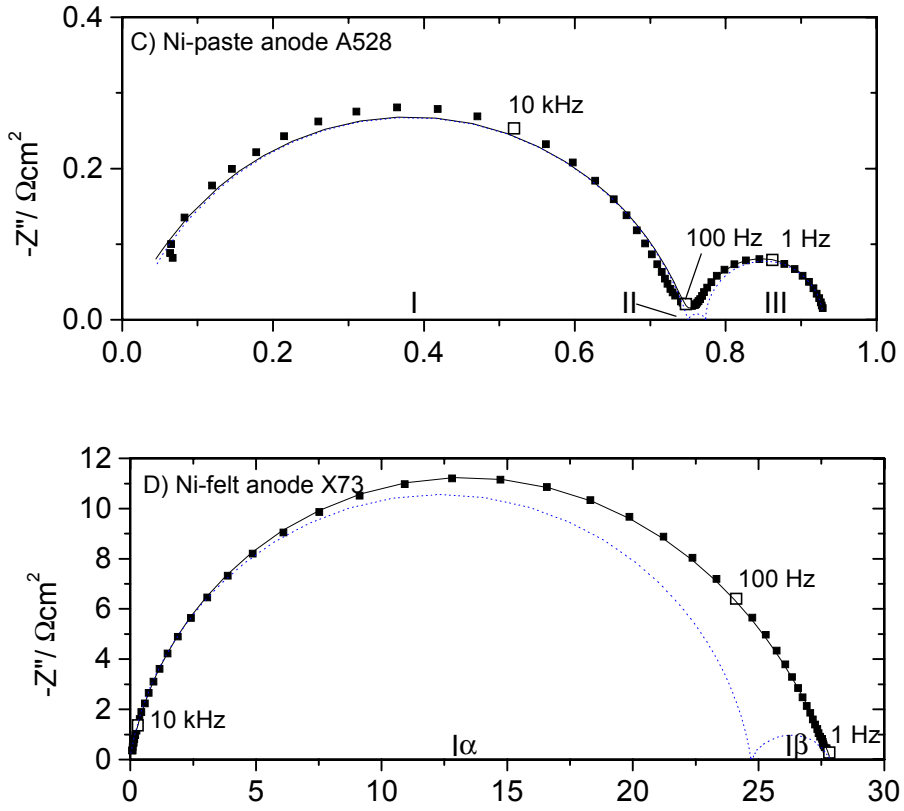

Fig. 6.3 Cont.

The structure dependent part of the impedance spectrum (marked I) could be described by one arc in Figure 6.3A and Figure 6.3C, whereas two arcs were required in Figure 6.3B and Figure 6.3D.

The processes contributing to the impedance spectra were described by an equivalent circuit. This allowed the data to be condensed and provided the basis of a meaningful and comparable presentation. The selected equivalent circuit must be complex enough to account for the characteristics of the impedance spectra.

Impedance data were fitted with the software EQUIVCRT,[28] using an equivalent circuit containing the elements L, R, C and Q, where L is an inductance, R a resistance, C a capacitance and Q a constant phase element of which the admittance Y^* is $Y_0(j\omega)^n$. Here Y_0 is an admittance factor, j the imaginary unit, ω the angular frequency and n is the frequency exponent.

The structure dependent part of the obtained impedance spectra was, in general, well described by one arc at lower temperatures, represented by an $(RQ)_1$ subcircuit with an n-value of 0.8 to 0.9. This is in agreement with reported impedance spectra on Ni/YSZ anodes for both cermet anodes[9,11,20] and for point electrodes.[12]

At higher temperature, two arcs were needed for coarse cermet anodes and Ni-felt anodes. The smaller of the two high frequency arcs was the higher frequency one for the coarse cermet anode, and the converse for the Ni-felt anode, Figure 6.3B and Figure 6.3D. Two arcs denoted $(RQ)_{1\alpha}(RQ)_{1\beta}$ were used with fixed *n*-values selected as average values of what was obtained in unrestricted fits for these anodes. α and β refer to arcs with high and low relaxation frequencies recognized in impedance spectra from a given anode type rather than a distinct process. The use of such average *n*-values for such overlapping arcs (processes with similar time constants) is debatable.[29] Nevertheless, this approach is considered to be the best option for impedance spectra where one arc is too simple for an interpretation.

Homogeneous, one-dimensional finite length diffusion impedance can generally be handled as a finite length Warburg diffusion. An $(RQ)_2$ subcircuit with an *n*-value of 0.75 was previously applied for this setup[9,11,20] and is also used here, accepting a broader time distribution of the process caused by the inhomogeneous gas flow pattern over the anode surface in the setup.[11] Gas conversion is demonstrated to contribute a perfect semicircle at lower frequencies, and modeling predicts an $(RC)_3$ subcircuit.[8,9]

In general, impedance data were interpreted from the lowest frequencies obtained, up to a vertical line at frequencies from 10 to 100 kHz. This vertical component was interpreted as a simple inductance, *L*, introduced by the measurement system. A series resistance, R_S, is primarily caused by the electrolyte resistance between the working electrode and the reference electrode.

The above considerations, in conjunction with the impedance spectra obtained, led to the overall equivalent circuit $LR_S(RQ)_{1\alpha}(RQ)_{1\beta}(RQ)_2(RC)_3$. The equivalent circuits used, and selected *n*-values for each anode type, are listed in Table 6.1. In spectra where the ratio R_1/R_2 or R_1/R_3 was too high to yield reliable data for the minor arc, appropriate data points were omitted together with the relevant part of the equivalent circuit. In the following, the resistive parameters $R_{1\alpha}$, $R_{1\beta}$ and $R_1 = R_{1\alpha}+R_{1\beta}$ are studied and discussed.

Table 6.1 Appearance of the anode structure dependent section of the impedance spectra and selected equivalent circuits and *n*-values for each arc. α denotes the high frequency arc, where two arcs are required to obtain acceptable fits.

Anode type	Electrode imp. arcs	Electrode circuit	n-values	Total equivalent circuit, incl. concentration polarization
Fine cermet	one arc	$(RQ)_1$	0.8	$LR_S(RQ)_1(RQ)_2(RC)_3$
Coarse cermet	two arcs	$(RQ)_{1\alpha}(RQ)_{1\beta}$	0.8 and 0.8	$LR_S(RQ)_{1\alpha}(RQ)_{1\beta}(RQ)_2(RC)_3$
Ni-paste	one arc	$(RQ)_1$	0.8	$LR_S(RQ)_1(RC)_3$
Ni-felt	two arcs	$(RQ)_{1\alpha}(RQ)_{1\beta}$	0.9 and 0.7	$LR_S(RQ)_{1\alpha}(RQ)_{1\beta}$

6.3.3 Thickness

Fine cermet anodes with a thickness in the range of 3.5 μm to 54 μm were measured with an overlying current collector structure. A blank sample with only the current collector deposited on an electrolyte pellet was assigned the thickness 0 μm. R_1, R_2 and R_3 are given in Figure 6.4 as function of anode thickness, after testing at 1000°C in 97% H_2 + 3% H_2O, and fitted to the selected equivalent circuit. At a thickness of about 10 μm a pronounced change in R_1 was observed. At lower thickness the values were about 0.7 Ωcm^2, at higher thickness it was an order of magnitude lower. The value of the series resistance was scattered between 0.4 and 1.3 Ωcm^2, which is expected for the electrolyte pellets at this temperature, thus indicated good in-plane conductivity in the current collector. As predicted, no variation was seen in R_2 and R_3 with thickness.

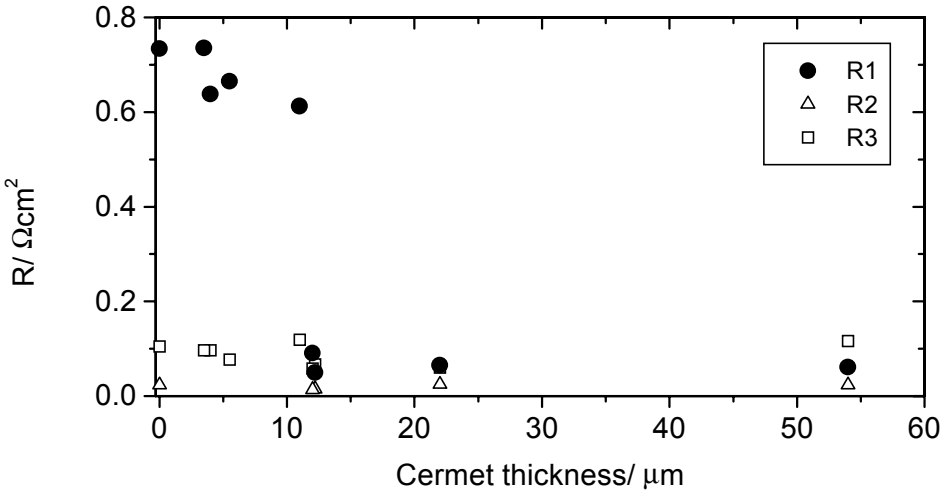

Figure 6.4 Dependence of anode polarization resistance on cermet thickness for the fine cermet anodes at 1000°C in 97% H_2 + 3% H_2O at OCV. R_1 is electrode impedance, R_2 and R_3 are gas diffusion and gas conversion outside the anode structure, respectively.

The series resistance of the YSZ component of the cermet in fine cermet anodes was evaluated after dissolution of the Ni-phase, and again after removing the porous YSZ structure to reveal the resistance of the electrolyte pellet. The R_S obtained with the porous YSZ structure was 1.40 Ωcm^2, and only 0.70 Ωcm^2 for the blank YSZ pellet. Apparently a resistance of the same order as in a 2 mm dense YSZ slab is obtained for the 70 μm thick porous YSZ structure.

6.3.4 Apparent Thermal Activation

Impedance spectra at OCV were obtained in 97% H_2 + 3% H_2O, in the temperature range of 750 to 1000°C, for the four types of anodes. After fitting with the appropriate equivalent circuits, (listed in Table 6.1) the resistances $R_{1\alpha}$, $R_{1\beta}$ and R_1 were plotted with Arrhenius type plots, given in Figure 6.5A to Figure 6.5C. Approximation to straight lines (Arrhenius behavior) was assumed and the apparent activation energies are summarized in Table 6.2. Note that when apparent activation energies are obtained by varying the temperature in a constant atmosphere, the electrode potential (oxygen partial pressure) is not kept constant.

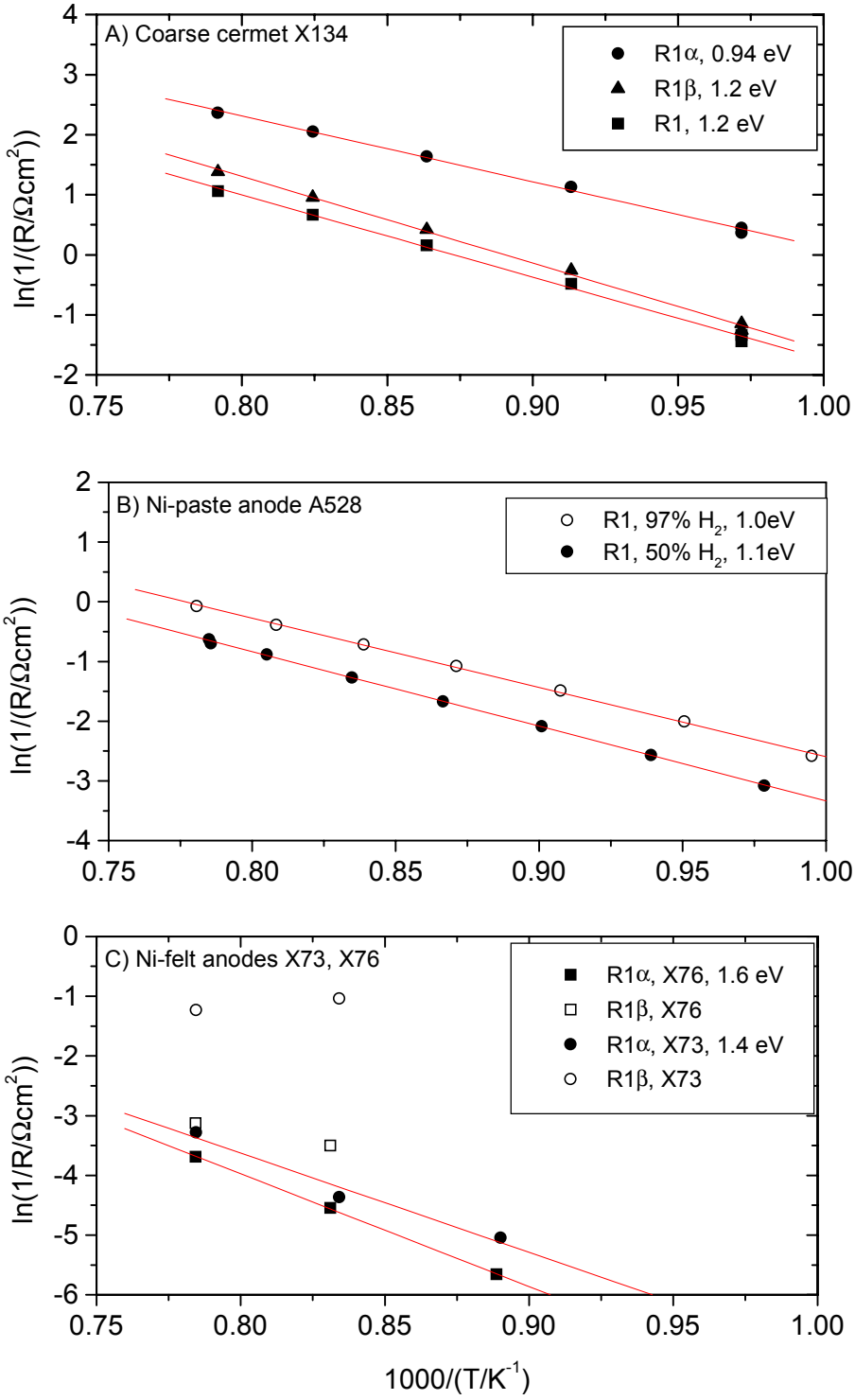

Figure 6.5 Arrhenius plot wherefrom the apparent activation energy of $R_{1\alpha}$, $R_{1\beta}$, and R_1 can be estimated. Data obtained by fitting impedance spectra recorded at 700°C to 1000°C in H_2 + 3% H_2O at OCV according to Table 1. A) Coarse cermet anode, X134. B) Ni-paste anode, A528. pH_2 = 0.97 (open) and 0.50 (solid), balance N_2. C) Ni-felt X73 (squares) and X76 (bullets).

6.3.5 Gas Composition

Impedance spectra were obtained while varying the pH_2 at constant pH_2O at 1000°C and fitted to the appropriate equivalent circuits. Reciprocal values of the resistances $R_{1\alpha}$, $R_{1\beta}$ and R_1 are given as a function of pH_2 in a double logarithmic plot, Figure 6.6A to Figure 6.6C. The curves for R_1 indicated a fairly constant resistance with changing pH_2. However, at a pH_2 of about 0.3 atm the slope appears to change somewhat for the Ni-paste anode and the Ni-felt anode. Linear slopes are summarized in Table 3.

Impedance spectra were obtained while varying the pH_2O at constant pH_2 at 1000°C and fitted to the appropriate equivalent circuits. Reciprocal values of the resistances $R_{1\alpha}$, $R_{1\beta}$ and R_1 are given as a function of pH_2O in a double logarithmic plot, Figure 6.7A to Figure 6.7C. The curves indicated a reduction in resistance with increasing pH_2O. There was a tendency for the cermet anodes to have a weaker dependence on pH_2O than the Ni-felt and Ni-paste anodes. Overall the slopes were near 0.5, the results are summarized in Table 4.

Again it is important to remember that changing the partial pressure of either gas also changes the pO_2 and the electrode potential. Consequently, the derived dependencies may be of a composite nature.

6.4 Discussion

6.4.1 Active Thickness

As observed in Figure 6.4, the active thickness of fine cermet anodes produced was about 10 μm when tested with an effective current collector.

An earlier study of nominally identical anodes indicated no change in the polarization resistance with thickness in the range of 20 μm to 70 μm.[20] For similar anodes the exchange current density at 1000°C has been demonstrated to increase for a thickness up to about 10 μm, after which the value was constant.[30] The steep change of R_1 in Figure 6.4 is suggested to be caused in part by the coarseness of the current collector, see Figure 6.2C. Because of the distance between cermet/current collector contacts an in-plane percolation problem emerges in the cermet as the thickness approaches the characteristic particle size of 1 to 3 μm, Figure 6.2A.

As the porosity is adequate (about 50% and no diffusion restriction observed), the limitation for this active thickness in a cermet could be taken to be transport resistance in the poorer solid conductor, presumably the YSZ structure.[10,31] The area-specific oxide-ion conductivity $\sigma_{o^{--}}$ of the porous YSZ structure in a fine cermet anode is calculated from the R_S contribution of 0.70 Ωcm^2. With a structure thickness of 70 μm, the conductivity is 0.01 S/cm, a factor 10 lower than $\sigma_{o^{--}}$ for the bulk YSZ of about 0.10 S/cm at 1000°C.[32] This factor agrees with the findings of others.[10]

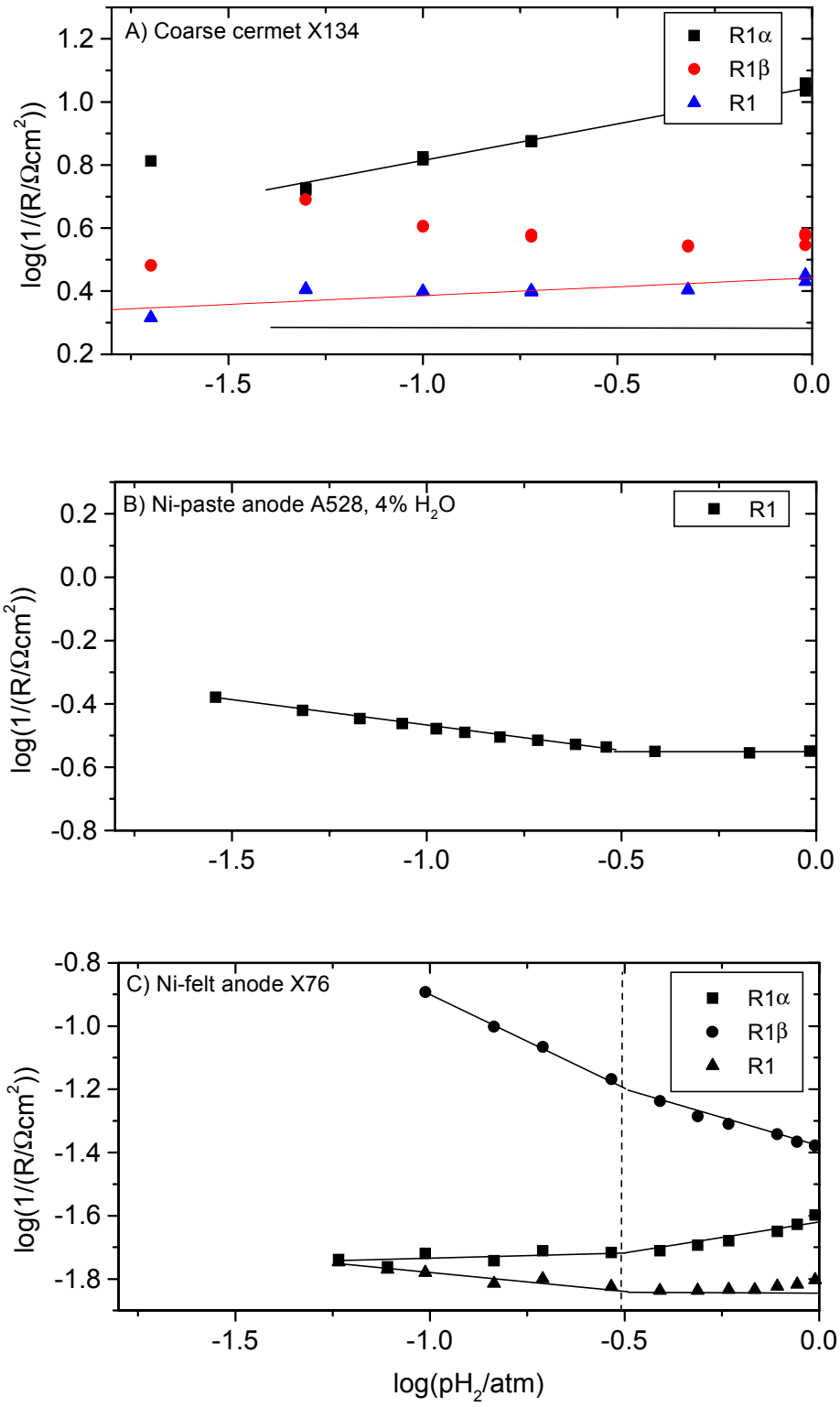

Figure 6.6 Dependence of $R_{1\alpha}$, $R_{1\beta}$ and R_1 on pH_2 at 1000°C in 3% H_2O at OCV. A) Coarse cermet X134, B) Ni-paste anode A528, C) Ni-felt anode X76.

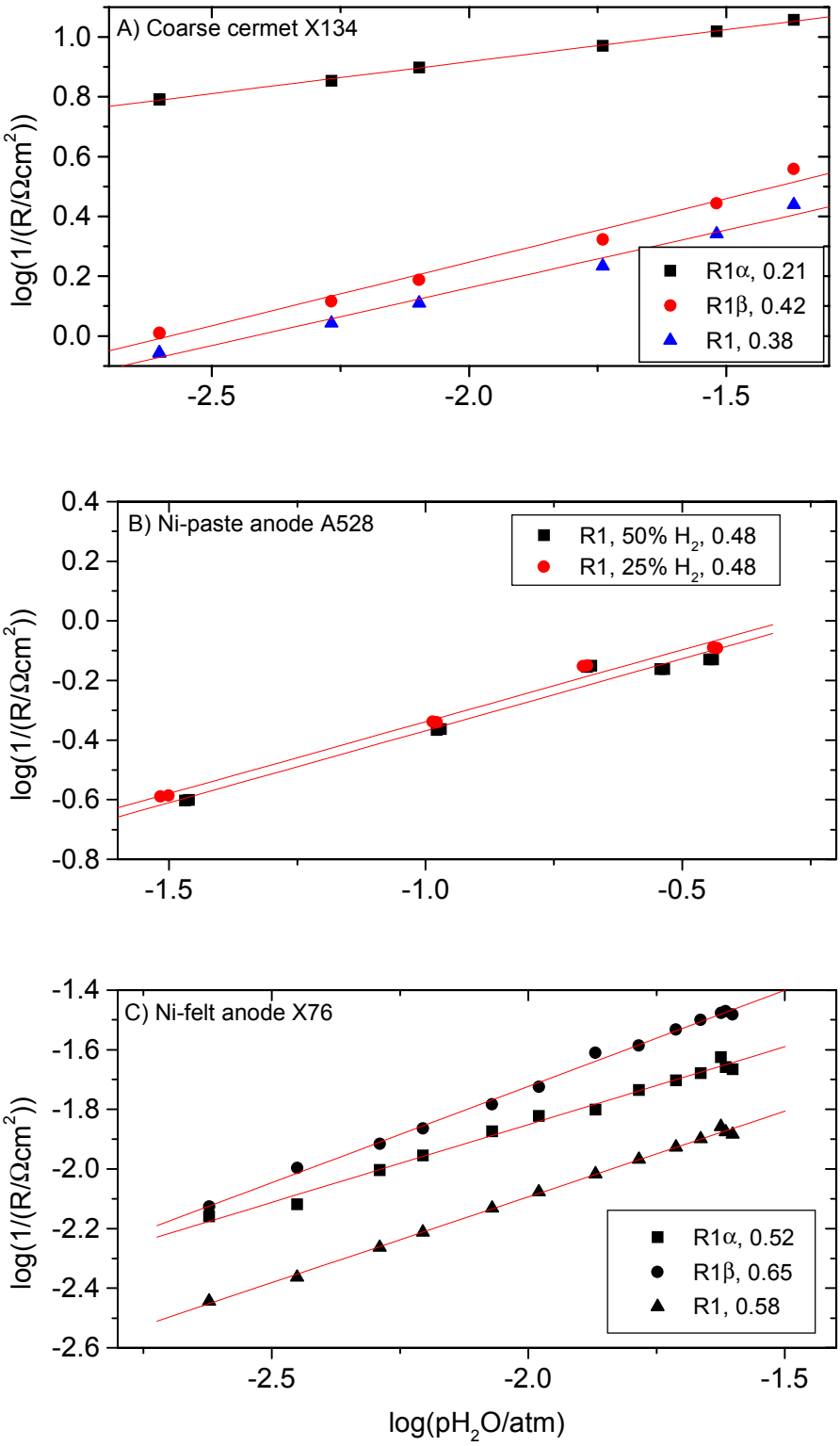

Figure 6.7 Dependence of $R_{1\alpha}$, $R_{1\beta}$ and R_1 on pH_2O at 1000°C in H_2 at OCV. A) Coarse cermet anode X134 in 96-99.9% H_2. B) Ni-paste anode A528, 50% H_2 (squares) and 25% H_2 (bullets), balance N_2. C) Ni-felt anode X76 in 96-99.9% H_2.

In the present context it is interesting to note that the area-specific resistance of the porous YSZ structure within the active thickness of about 10 μm, is identical to the area-specific polarization resistance of 0.10 Ωcm^2. As the current always favors a path of lower resistance, only minor contributions to the total current density are expected from TPB points with a specific oxide-ion transport resistance comparable with or higher than the specific electrode reaction resistance.[33]

It is of interest to determine the role and effect of the thickness-limiting electrolyte resistance in a cermet structure. YSZ grain boundary impedance, current constriction[34-36] and structural effects[22] in the porous electrolyte may probably only be seen at extreme frequencies at this temperature, and are therefore all assumed to contribute to the series resistance R_S. This is in agreement with the present results obtained by dissolution of the Ni-phase, and the relative stability of nominally identical anodes over time as compared with the known degradation rate of σ_{o--} with time.[37]

For a Ni-based anode with no internal percolation in a YSZ-phase, the active TPB is found on a 2D interface between the electrode material and the electrolyte. With a 3D extent of the position of active TPB in cermet anodes, a distribution of series resistance for the active TPB sites is obtained rather than a well defined equi-potential electrode surface.

6.4.2 Apparent Thermal Activation

The apparent activation energy of structure related processes in the four examined anodes range from 0.8 to 1.8 eV. In literature, a spread of values has also been reported, 0.5 eV for a micro-porous Ni-film electrode[7], 0.8 eV[17] and 1.0 eV[10] for cermets, 1.3 eV for a cermet,[38] 0.6 and 1.8 eV for two arcs on point electrodes[2], and 1.6 eV for one arc on a point electrode.[12] The published data suggested the presence of a high apparent activation energy for point contacts and coarse cermets, and lower values in anodes with a fine structure. In this context the Ni-film electrode exhibiting 0.5 eV is considered a fine structure, as the Ni-film has been re-oxidized during the sample preparation and consequently is expected to be micro-porous. The only relevant process known to exhibit an apparent activation energy comparable with the observed 1.8 eV, is n-type electron conduction in the electrolyte under reducing conditions. This apparent activation energy can range from 1.3 to about 3.9 eV,[39] depending on whether the formation energy of electron/hole formation has to be included.

Another possible explanation of variations in apparent activation energy is the effect of contaminants on a range of potential limiting processes. Both raw material source and the electrode sintering temperature could be of importance in this respect, but no consistent trends are found in the reported data of Table 6.2.

Table 6.2 Apparent activation energy of the structure related impedance arc as evaluated from linear regression in Arrhenius type plots, E_1 corresponds to R_1 whereas E_α and E_β corresponds to the α and β arc, respectively. All in H_2 with about 3% H_2O.

Anode Type	Anode	No. of electrode arcs	E_1, eV	Temperature, °C
Fine cermet[20]	A86,	1	E_1= 0.7	850-1000
	A92	1	E_1= 0.9	850-1000
Ni-paste	A527,	1	E_1= 0.9	700-900
	A528	1	E_1= 1.1	750-1000
Coarse cermet	X132,	2	E_1=1.6 E_α= 1.8 E_β= 1.1	750-1000
	X134	2	E_1=1.2 E_α= 1.2 E_β= 0.9	770-1000
Ni-felt	X73	2	E_1=1.6 E_α= 1.6 E_β=1.05	850-1000
Ni-point[40]		2	E_1= 1.41	620-800
Ni-point[12]		1	E_1= 1.6	700-1000
Ni-wire[2]		2	E_α= 0.6 E_β=1.8	550-900
Cermet[10]		1	E_1= 1.01	700-1000
Ni-film[7]		1	E_1= 0.5	700-1000
Ni-pattern[15]		1	E_1= 1.6	700-950
Cermet[38]		1	E_1= 1.3	750-1000

The thermally activated oxide-ion transport resistance in the YSZ of a cermet is partially determining the active thickness. A consequence of this is, that the active electrode examined with varying temperature may not be geometrically constant.[41] If this effect is of major importance, different active thicknesses should be obtained at different temperatures for cermets with apparent activation energies deviating from that of the electrolyte.

A reappearing feature of Ni/YSZ anodes, regardless of morphology, is a non-linearity in reported Arrhenius plots indicating higher activation energy at lower temperatures. This could be caused by a change in ratio of limiting processes for Ni-based anodes with temperature.[42,43]

6.4.3 Gas Composition

The results indicate an almost constant resistance when increasing pH_2 from 0.03 atm. to 0.97 atm, Table 6.3. The Ni-paste anodes exhibit a very slight increase in resistance up to approximately 0.3 atm pH_2. This was also observed for the Ni-felt anode with a very shallow minimum at a pH_2 of approximately 0.3 atm, whereas the coarse structured anode resistance was virtually constant over the pH_2 range of 0.01 atm. to 0.97 atm. This lack of dependence on pH_2 at 1000°C was also observed for Ni-film anodes[7], and is consistent with a high coverage of H_{ads} on the Ni-surface.[4,5] In disagreement with this, a rather well defined minimum in electrode conductivity has been reported at a pH_2 of 0.2 atm. at 975°C and fixed pH_2O for a Ni micro-electrode.[12] In general it is surprising that at the highest pH_2 where the hydrogen surface coverage on Ni is expected to be highest, the most pronounced dependence on pH_2 is observed.

Table 6.3 Apparent hydrogen partial pressure dependence as evaluated from linear regression in log-log plots, Figure 6.6. a_1 corresponds to R_1 whereas a_α and a_β corresponds to the α and β arc, respectively. All at a temperature of about 1000°C.

Anode type	Anode	$1/R_1 \propto pH_2$[a]	Range of pH_2, atm.	Constant pH_2O, atm.
Fine cermet[20]	A228	a_1=0.15	$10^{-1.2}$-10^{0}	0.03
Ni-paste	A528	$a_{1=}$-0.15	$10^{-1.6}$-$10^{-0.5}$	0.03
		a_1=0	$10^{-0.5}$-10^{0}	0.03
Coarse cermet	X134	a_1=0.05 a_α=0.25 a_β=0	$10^{-2.0}$-10^{0}	0.035
Ni-felt	X76	a_1=-0.15 a_α=0 a_β=-0.6	$10^{-1.3}$-$10^{-0.5}$	0.035
		a_1=0 a_α=0.3 a_β=-0.3	$10^{-0.5}$-10^{0}	0.035
Ni-film[7]		a_1=0	10^{-2}-10^{0}	pH_2O= 0.02
Ni-point[12]		a_1=-0.5	$10^{-1.5}$-$10^{-0.66}$	pH_2O= 0.055 [#]
		a_1=0.5	$10^{-0.66}$-10^{0}	

[#] at 975°C.

The results consistently indicate a decrease in resistance with increasing pH_2O, Table 6.4. A slope of approximately 0.5 for the Ni-paste and Ni-felt was observed, and a tendency of the cermet anodes to have a smaller dependence on pH_2O is observed. This is in good agreement with findings in literature, Table 6.4. This apparent contradiction to water as a reaction product has caused some authors to suggest an "auto-catalytic" effect of water on hydrogen oxidation.[10] Another explanation for the observed dependence is the cathodic reaction, which contributes equally to R_P at OCV and can be assumed to be significant up to anodic overpotentials of ~3RT/F, i.e. about 300 mV. An alternative interpretation is a rate limiting physical transport restriction in a solid material, where solubility or mobility depends on pH_2O. In general the observed dependencies on gas composition may also include dependencies on electrode potential, as the pO_2 is also (inherently) varying with the variation of pH_2 or pH_2O.

Table 6.4 Apparent steam partial pressure dependence as evaluated from linear regression in log-log plots, Figure 6.7. a_1 corresponds to R_1 whereas a_α and a_β corresponds to the α and β arc, respectively. All at a temperature of about 1000°C.

Anode Type	Anode	$1/R_1 \propto pH_2O$[a]	pH_2O, atm.	Constant pH_2, atm.
Fine cermet[20]	A51	a_1=0.3	$10^{-2.2}$-$10^{-1.4}$	0.97-0.99
		a_1=0.2	$10^{-1.6}$-$10^{-0.5}$	0.50
Ni-paste	A528	a_1=0.6	$10^{-2.2}$-$10^{-0.5}$	0.965-0.99
		a_1=0.5	$10^{-1.5}$-$10^{-0.4}$	0.25 and 0.50
Coarse cermet	X134	a_1=0.4 a_α=0.2 a_β=0.4	$10^{-2.6}$-$10^{-1.4}$	0-965-0.99
Ni-felt	X76	a_1=0.6 a_α=0.5 a_β=0.65	$10^{-2.7}$-$10^{-1.5}$	0.97-0.99
Ni-film[7]		a_1=0.5	10^{-2}-$10^{-0.5}$	0.7-0.99[¤]
Ni-cone[12]		a_1=0.5	$10^{-1.3}$-$10^{-0.3}$	0.7 [#]
Ni-wire[15]		a_1=0.5	about $10^{-2.2}$	about 0.0012
Ni-pattern[15]		a_1 positive	about $10^{-2.2}$	about $10^{-2.9}$

[#] at 975°C,

[¤] considered constant as the pH_2 dependence is insignificant, Table 6.3.

6.4.4 Limiting Processes

As indicated in the introduction, both chemical and physical transport limitations may contribute to the observed electrode impedance. For both types of processes the sensitivity towards contaminants in the bulk materials, on surfaces and on interfaces can be expected to cause variations between types of electrodes. Identification of limiting processes is further complicated by the possibility of parallel reaction paths being active, and by the relation between electrode potential, partial pressures of H_2 and H_2O and temperature, making independent single variations impossible.

Although it is questionable that the basic chemical limitation is hydrogen oxidation, the possibility remains. Chemical reaction mechanisms for hydrogen oxidation on the Ni/YSZ electrode have been proposed in literature by several authors, and are so far based on qualified guesses and the capability of explaining selected observations.

On the μm scale there is evidence for physical transport restrictions from the finite 10 μm active thickness of the fine cermet. Transport limitations in such structures have been modeled to cause distortions of a simple impedance arc at higher frequencies.[31,44] No particular significance is assigned to the minor arc for coarse cermet anodes and Ni-felt anodes due to the strong correlation with the dominant arc. The arc 1α for the coarse cermet anode is small compared with arc 1β, and mostly $R_{1\alpha}$ show dependencies in agreement with $R_{1\beta}$. Arc 1α could be a transport limitation induced distortion of arc 1β for the coarse cermet. In principle a similar arc could be present in impedance spectra for fine cermet anodes and Ni-paste anodes (Figure 6.3). If this arc exists, the available frequencies in combination with leads inductance and system phase error prevents detection. Also the minor arc 1β for the Ni-felt anodes is small or show dependencies in fairly good agreement with arc 1α. It is at present unknown whether transport limitations can be expected to contribute at the lower frequency side of the dominant arc.

If it is assumed that the electrochemical reaction cannot occur directly on the TPB within a distance of an atomic dimension, then finite reaction zones exist along the TPB line.
The width of the reaction zone at any TPB is thought to be a consequence of the electrode overpotential determining how far from the TPB the limiting physical transport can be driven. A possible consequence of a significant extent on either two-phase interface is that reaction zones of adjacent TPB's may overlap if the electrode structure becomes fine enough. This has been investigated without finding proof of such extent. However, results indicate the reaction zone width to be less than 1 μm on the Ni phase in a micro-porous Ni-film anode,[7] and less than 1 μm on the electrolyte[45] based on another study of etched Ni-patterns.[15] Also the width is indicated to be less than 2.5 μm on the electrolyte and less than 12.5 μm on the Ni from Ni-stripe electrodes at about 700°C.[46]

Figure 6.8 shows the electrolyte/electrode interface with two potentially parallel active reaction paths. Based on the availability of H_{ads} on the Ni surface, the dominant process could be suggested to involve a "spillover" of protons from the Ni-surface to the YSZ surface as the charge transfer step. Several possibilities exist for the subsequent water formation within the active zone on the electrolyte. A competing reaction could be due to the electronic conductivity in the YSZ electrolyte. Molecular hydrogen could react with oxide ions in the YSZ surface, possibly catalyzed by dissolved Ni in the YSZ surface,[47,48] and the released electrons could travel through the YSZ to the TPB to pass into the nickel.

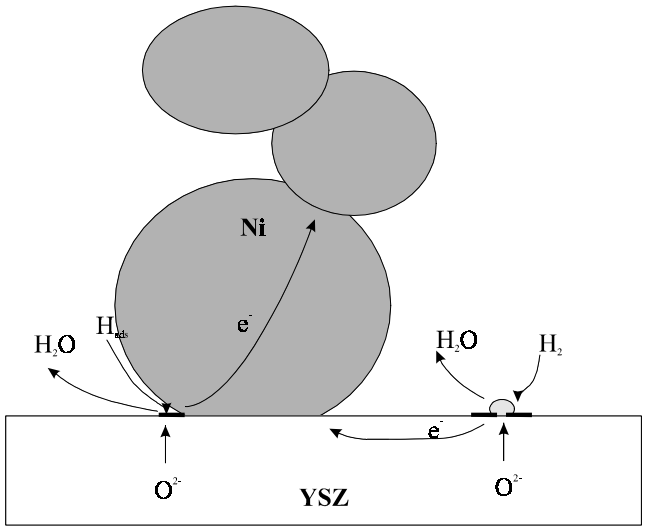

Figure 6.8 Schematic illustrating two possible reaction paths for hydrogen oxidation on Ni/YSZ cermet anodes. The effect of microstructure is illustrated.

6.5 Conclusion

In a fine cermet anode at 1000°C, an active thickness of the cermet of about 10 μm has been demonstrated, the limitation in thickness is ascribed to the ionic resistance in the electrolyte phase of the cermet structure.

Fine and coarse Ni/YSZ cermets, and Ni-electrodes with high and low coverage of the electrolyte surface were examined electrochemically. After identifying the contributions from concentration polarization in impedance spectra, one dominant impedance arc was recognized for a range of electrode structures. For some structures secondary arcs at lower or higher frequency were observed, but these were very minor or showed similar behavior as the dominant arc, indicating that they could be distortions of the primary arcs due to the microstructure.

Dependencies of R_P on partial pressure was found to be of the type $1/R_P \propto pX^a$, with exponent values of ≈0 for hydrogen and ≈0.5 for water at 1000°C. Apparent activation energies in the range of 0.8 to 1.8 eV has been observed, with a distinct tendency towards lower activation energy for fine cermets and Ni-anodes covering a high percentage of the electrolyte surface, and higher values for coarse cermets and Ni-anodes covering a lower percentage of the electrolyte surface. Two reaction paths are suggested to occur in parallel with different extent of reaction zone from the TPB. n-type conductivity in the electrolyte surface is suggested to be the limiting process with high activation energy at 1000°C.

Acknowledgments

This work has been supported by the Danish Energy Agency under the national DK-SOFC program. Dr. F. Tietz, Forschungszentrum Jülich is acknowledged for kindly supplying the coarse cermet electrodes in a Round-Robin evaluation. Discussions with Dr. P. V. Hendriksen, Risø, are

appreciated. The technical assistance of several members of the SOFC project group at Risø is gratefully acknowledged.

References

[1] J. Mizusaki, H. Tagawa, T. Saito, K. Kamitani, T. Yamamura, K. Hirano, S. Ehara, T. Takagi, T. Hikita, M. Ippommatsu, S. Nakagawa and K. Hashimoto, *J. Electrochem. Soc.* **141** 2129 (1994)

[2] P. A. Osborg and T. Norby, in *7th SOFC WORKSHOP*, *Theory and measurement of Microscale Processes in Solid Oxide Fuel Cells*, 47 (1995), IEA report obtainable from H. Nabielek, KFA-ISR Forschungszentrum Jülich GmbH, D-52425 Jülich, Germany.

[3] M. Mogensen, S. Sunde and S. Primdahl. in *High Temperature Electrochemistry: Ceramics and Metals* F. W. Poulsen, N. Bonanos, S. Linderoth, M. Mogensen, B. Zachau-Christiansen, Editors. 17th Risø International Symposium on Material Science, Roskilde, DK. 77 (1996)

[4] M. Mogensen and S. Skaarup. *Solid State Ionics*. **86-88** 1151 (1996)

[5] S. Skaarup, B. Zachau-Christiansen and T. Jacobsen, in *High Temperature Electrochemistry: Ceramics and Metals.* F. W. Poulsen, N. Bonanos, S. Linderoth, M. Mogensen, B. Zachau-Christiansen, Editors. 17th Risø International Symposium on Material Science, Roskilde, DK. 423 (1996)

[6] K.-Z. Fung and A. V. Virkar, in *SOFC IV*, M. Dokiya, O. Yamamoto, H. Tagawa and S. C. Singhal, Editors, **PV 95-1**, The Electrochemical Society Proceedings Series, Pennington, NJ. 1105 (1995)

[7] N. Nakagawa, H. Sakurai, K. Kondo, T. Morimoto, K. Hatanaka and K. Kato, *J. Electrochem. Soc.* **142** 3474 (1995)

[8] S. Primdahl and M. Mogensen, in *SOFC V*, U. Stimming, S. C. Singhal, H. Tagawa and W. Lehnert, Editors, **PV 97-40**, The Electrochemical Society Proceedings Series, Pennington, NJ. 530 (1997)

[9] S. Primdahl and M. Mogensen, *J. Electrochem. Soc.* **145** 2431 (1998), chapter 4 in this thesis

[10] J. Geyer, H. Kohlmüller, H. Landes and R. Stübner, in *SOFC V*, U. Stimming, S. C. Singhal, H. Tagawa and W. Lehnert, Editors, **PV 97-40**, The Electrochemical Society Proceedings Series, Pennington, NJ. 585 (1997)

[11] S. Primdahl and M. Mogensen. *J. Electrochem. Soc.* in press (1999), chapter 5 in this thesis

[12] F.Z. Mohamedi-Boulenouar, J. Guindet and A. Hammou, in *SOFC V*, U. Stimming, S. C. Singhal, H. Tagawa and W. Lehnert, Editors, **PV 97-40**, The Electrochemical Society Proceedings Series, Pennington, NJ. 441 (1997)

[13] J. Guindet, C. Roux and A. Hammou, in *SOFC II*, F. Grosz, P. Zegers, S.C. Singhal and O. Yamamoto, Editors, EUR-13564-EN. 553 (1991)

[14] J. Guindet, *Contribution a L'etude de Materiaux d'Anode pour Pile a Combustible a Oxyde Electrlyte Solide,* Thesis (in french), Institut National Polytechnique de Grenoble (1988)

[15] T. Norby, O. J. Velle, H. Leth-Olsen and R. Tunold, in *SOFC III*, S.C. Singhal and H. Iwahara, Editors, **PV 93-4**, The Electrochemical Society Proceedings Series, Pennington, NJ. 473 (1993)

[16] T. Kawada, N. Sakai, H. Yokokawa, M. Dokiya, M. Mori, T. Iwata, *J. Electrochem. Soc*. **137** 3042 (1990)

[17] M. Mogensen, S. Primdahl, J. T. Rheinländer, S. Gormsen, S. Linderoth and M. Brown, in *SOFC IV*, M. Dokiya, O. Yamamoto, H. Tagawa and S. C. Singhal, Editors, **PV 95-1**, The Electrochemical Society Proceedings Series, Pennington, NJ. 657 (1995)

[18] D. W. Dees, U. Balachandran, S. E. Dorris, J. J. Heiberger, C. C. McPheeters and J. J. Picciolo, in *SOFC I*, S. C. Singhal, Editor, **PV 89-11**, The Electrochemical Society Proceedings Series, Pennington, NJ. 317 (1989)

[19] N. Robertson and J. Michaels, *J. Electrochem. Soc.* **138** 1494 (1991)

[20] S. Primdahl and M. Mogensen, *J. Electrochem. Soc.* **144** 3409 (1997), chapter 3 in this thesis

[21] S. Primdahl, B. F. Sørensen and M. Mogensen, *J. Am Ceram. Soc*. submitted (1998), chapter 7 in this thesis

[22] E. M. Skou and T. Jacobsen, *Appl. Phys. A*, **49** 117 (1989)

[23] J. Winkler, P. V. Hendriksen, N. Bonanos and M. Mogensen. *J. Electrochem. Soc.* **145** 1184 (1998)
[24] C. Bagger, in *1992 Fuel Cell Seminar,* Courtesy Associates Inc., Washington DC. 241 (1992)
[25] K. R. Thampi, A. J. McEvoy and J. Van herle, *J. Electrochem. Soc*. **142** 506 (1995)
[26] R. Hartung and H.-H. Möbius, *Chemie-Ing. Techn*., **40** 592 (1968)
[27] R. J. Aaberg, R. Tunold, M. Mogensen, R. W. Berg and R. Ødegård, *J. Electrochem. Soc.* **145** 2244 (1997)
[28] B. A. Boukamp, *Solid State Ionics*, **20** 31 (1986)
[29] M. Mogensen, S. Primdahl and M. Juhl, in *SOFC V*, U. Stimming, S. C. Singhal, H. Tagawa and W. Lehnert, Editors, **PV 97-40**, The Electrochemical Society Proceedings Series, Pennington, NJ. 385 (1997)
[30] S. Sakamoto, H. Taria and H. Takagi, *Denki Kagaku*, **64** 609 (1996)
[31] T. Kawada, N. Sakai, H. Yokokawa, M. Dokiya, M. Mori and T. Iwata, *Solid State Ionics*, **40/41** 402 (1990)
[32] F. T. Ciacchi, K. M. Crane and S. P. S. Badwal, *Solid State Ionics*, **73** 49 (1994)
[33] M. Juhl, S. Primdahl, C. Manon and M. Mogensen, *J. Power Sources*, **61** 173 (1996)
[34] M. Kleitz, L. Dessemond and M. C. Steil, in *SOFC Materials, Process Engineering and Electrochemistry*, P. Biedermann and B. Krahl-Urban, Editors, 5th IEA Workshop, Forschungszentrum Jülich, D. 147 (1993)
[35] J. Fleig and J. Maier, *J. Electrochem. Soc*. **145** 2081 (1998)
[36] F. van Heuveln, *Characterisation of Porous Cathodes for Application in Solid Oxide Fuel Cells*, Thesis, University of Twente, Holland, 102-112 (1997)
[37] S. Primdahl and M. Mogensen, *J. Appl. Electrochem*. submitted (1999), chapter 9 in this thesis
[38] K. Okumura, Y. Yamamoto, T. Fukui, S. Hanyu, Y. Kubo, Y. Esaki, M. Hattori, A. Kusonoki and S. Takeuchi, in *SOFC III*, S.C. Singhal and H. Iwahara, Editors, **PV 93-4**, The Electrochemical Society Proceedings Series, Pennington, NJ. 444 (1993)
[39] J. H. Park, R. N. Blumenthal, *J. Electrochem. Soc.* **136** 2867 (1989)
[40] R. Baker, J. Guindet and M. Kleitz. *J. Electrochem. Soc.* **144** 2427 (1997)
[41] S. Primdahl and P. V. Hendriksen, in *High Temperature Electrochemistry: Ceramics and Metals*, F. W. Poulsen, N. Bonanos, S. Linderoth, M. Mogensen, B. Zachau-Christiansen, Editors, 17th Risø International Symposium on Material Science, Roskilde, DK. 403 (1996), chapter 2 in this thesis
[42] P. Holtappels, *Die Elektrokatalyse an Nickel-Cermet Elektroden*, Thesis (in german), University of Bonn, D (1997)
[43] S. Primdahl and M. Mogensen, in *SOFC VI*, accepted (1999), chapter 8 in this thesis
[44] S. Sunde, *Electrochimica Acta,* **42** 2637 (1997)
[45] M. Kleitz, T. Kloidt and L. Dessemond. in *High Temperature Electrochemical Behaviour of Fast Ion and Mixed Conductors,* F. W. Poulsen, J. J. Bentzen, T. Jacobsen, E. Skou and M. J. L. Østergård, Editors, 13th Risø International Symposium, Roskilde, DK 89 (1993)
[46] J. Mizusaki, T. Yamamura, N. Mori, H. Tagawa, K. Hirano, S. Ehara, T. Tagaki, M. Hishinuma, H. Sasaki, T. Sogi, Y. Nakamura and K. Hishimoto, *High Temperature Electrochemistry: Ceramics and Metals*, F.W. Poulsen, N. Bonanos, S. Linderoth, M. Mogensen and B. Zachau-Christiansen, Editors, 17th Risø International Symposium on Materials Science, Roskilde, DK. 363 (1996)
[47] S. Linderoth and A. Kuzjukevics, in *SOFC V*, U. Stimming, S. C. Singhal, H. Tagawa and W. Lehnert, Editors **PV 97-40**, The Electrochemical Society Proceedings Series, Pennington NJ. 1076 **(**1997)
[48] A. Kuzjukevics, S. Linderoth and J. Grabis, in *High Temperature Electrochemistry: Ceramics and Metals*, F.W. Poulsen, N. Bonanos, S. Linderoth, M. Mogensen and B. Zachau-Christiansen, Editors, 17th Risø International Symposium on Materials Science, Roskilde, DK. 319 (1996)

Chapter 7

Effect of Sintering Temperature on Anode Performance and Cell Strength[†]

Abstract

A NiO/yttria stabilized zirconia (YSZ) layer sintered at temperatures between 1100°C and 1500°C onto dense YSZ electrolyte foils forms the precursor structure for a porous Ni/YSZ cermet anode for solid oxide fuel cells (SOFC). Conflicting requirements for electrochemical performance and mechanical strength of such cells were investigated. A minimum polarization resistance of 0.09 Ωcm^2 at 1000°C in moist hydrogen was obtained for sintering temperatures of 1300°C to 1400°C. The mechanical strength of cells decreased with increasing sintering temperature due to formation of channel cracks in the electrode layers, originating in thermal expansion coefficient mismatch between the layers.

[†] This chapter has been submitted in a slightly shorter version as S. Primdahl, B. F. Sørensen and M. Mogensen, "Effect of NiO/YSZ Anode Precursor Sintering Temperature on the Properties of Solid Oxide Fuel Cells" *J. Am. Ceram. Soc*. (1998)

7.1 Introduction

In the worldwide efforts for commercialization of SOFC, a number of stacking principles as well as cell designs are being investigated. Complete cells for SOFC stacks are typically produced by one of the following two principles; i) electrolyte supported cells, where a 50 to 200 μm thick electrolyte foil carries an anode and a cathode on opposite sides,[1-3] and ii) electrode supported cells, where a 100 μm to mm thick porous current collector structure carries an active electrode, an electrolyte of 5 to 50 μm and the opposite electrode.[4-6] The issue of these cell designs is to create a "backbone" element for SOFC stacks containing a sintered cell with sufficient strength for handling and mounting the element in the final stack.
Both types of cells are applicable for high temperature SOFC stacks operating at about 1000°C. For low temperature operation (700°C to 850°C) the resistance of a thick electrolyte renders the electrolyte supported design unattractive due to an activation energy of about 0.8 eV for oxide ion conductivity in the preferred electrolyte material, yttria stabilized zirconia (YSZ).[7]

In the following study we focus on cells for the flat bipolar plate stack. The cells have to exhibit a number of features, mainly a fairly high mechanical strength for handling and mounting, sufficient in-plane conductivity, a low polarization resistance and good durability. The Ni/YSZ cermet anode used by most SOFC developers is commonly produced by reducing a NiO/YSZ anode precursor structure *in situ* in a stack prior to operation.

The polarization resistance, R_P, is generally accepted to be associated with the active triple phase boundary (TPB) line between Ni, YSZ and pores providing unbroken percolation paths for electrons, oxide ions and gaseous species, respectively.[8,9] One of the reasons for using a cermet anode is thus expansion of the TPB into part of the electrode volume rather than limiting it to the electrolyte contact interface. With a fine electrode microstructure the volume of the active anode has been demonstrated to extend about 10 μm from the electrolyte,[10,11] in reasonable agreement with model predictions.[12] To sustain electronic percolation in the anode a minimum of 30 v/o Ni must be present after reduction.[13,14,15] The amount of active TPB obtained is a consequence of sintering the anode precursor structure at sufficiently high temperature. This allows for densification and neck formation between particles, to form the necessary percolation paths. NiO diffuses out over a YSZ surface at 1300°C as can be observed by the presence of a grey color after subsequent reduction. NiO acts as a sintering aid for YSZ in quantities of less than 1 m/o.[16] The extent of solubility of NiO in YSZ depends on both sintering temperature and yttria content. A maximum solubility of 2.5 m/o in YSZ with 8 m/o Y_2O_3 has been demonstrated to exist at 1200°C.[16,17] The situation is different after reduction of NiO to Ni. The NiO phase contracts 25 v/o and with a wetting angle of about 120° Ni does not wet YSZ very well.[18] The solubility of Ni in YSZ is expected to be significantly lower than for NiO. Furthermore, Ni exhibits a high surface mobility at elevated temperature with a strong tendency to agglomerate.[19] A less than ideal performance and durability has been demonstrated for both electronic in-plane conductivity and anode performance.[20,21] Consequently the achievement of a high performance durable anode is suggested to depend on sintering of a well packed green structure to obtain a fine and rigid YSZ network capable of constraining the Ni phase from agglomeration.

The fracture strength of electrolyte supported cells has been observed to decrease with increasing sintering temperature of the deposited NiO/YSZ anode precursor. It is the aim of this study to i) examine this decrease in fracture strength with temperature, ii) determine the effect of sintering temperature on polarization resistance for a selected anode slurry, and iii) to determine if

a reasonable balance can be found between these qualities. Finally the impact of the revealed mechanisms on production of anode supported cells is considered.

7.2 Experimental Procedure

Electrolyte foils were prepared by tape casting TZ8Y (Tosoh Corporation, ZrO_2 stabilized with 8 m/o Y_2O_3) and sintering for 8 hours at 1350°C to produce sheets of 45 × 45 mm^2 with a thickness of about 160 µm and a density in excess of 98%.

So called two-electrode symmetrical cells were produced as follows: An ethanol based anode slurry containing 53 w/o green NiO (Johnson Matthey, 99% NiO) and 47 w/o TZ8Y,[22] was prepared and deposited in layers of 10 to 20 µm on both sides of the electrolyte foils by spray painting and drying in open air. This composition corresponds to 40 v/o Ni in the reduced anode structure. Following spraying of both sides, the foils were sintered for two hours at temperatures in the range of 1100°C to 1300°C. After three rounds of spraying and sintering, anode structures of about 50 µm were obtained on both sides of the electrolyte foils. Some foils were sintered a fourth time at a higher temperature.

Furthermore, a set of reference electrolyte foils was prepared. A blank electrolyte and an electrolyte painted with a saturated solution of $Ni(NO_3)_2 \cdot 6H_2O$ in ethanol were decomposed in air at 1300°C for two hours. The purpose of the latter production method was to form a very thin NiO coating.

7.2.1 Characterization

The fracture strength of all sintered, unreduced cells was evaluated on a qualitative basis by bending cells to fracture by hand. The fracture surfaces were examined in an environmental scanning electron microscope (ESEM, Model E3, Electroscan Corp., Wilmington, MA).

Other cells were fragmented by bending into small cells of about 4 × 4 mm^2 and characterized electrochemically in a controlled atmosphere in a simple two-electrode setup. Contacts to the electrodes were established by a Pt wire loop on one side of the cell, and a weight-loaded Pt bead on the opposing side. Selected cells were also characterized with a porous 20 µm painted layer of Pt paste (Demetron 308A) on top of both electrodes. No curing of the Pt paste was performed. The cells were heated to 1000°C in N_2, reduced in H_2 with 3% H_2O and characterized within 8 hours from reduction by impedance spectroscopy (Frequency Response Analyzer 1260, Solartron Instruments, Farnborough, UK) at no polarization with a 20 mV amplitude and under decreasing frequency from 1 MHz to 1 Hz. Cells were finally cooled in 9% H_2 with 3% H_2O. A two-point in-plane resistance of the electrodes was measured at ambient temperature by placing two 0.3 mm gold wire ends at a distance of 3 to 4 mm on cells with no Pt. Hereafter the cells were molded in epoxy, cut and polished.

The electrolyte foil painted with $Ni(NO_3)_2$ was examined after sintering. It had a crack-free NiO layer of less than 1 µm. The reference foils were not characterized electrochemically, and served only as references for evaluation of mechanical strength and fracture characteristics.

7.2.2 Impedance Evaluation

Impedance data were evaluated by real part only. A series resistance R_S, equal to the infinite-frequency intercept with the real axis in a complex plane (Argand) diagram, was applied to account for the purely ohmic drop caused mainly by the electrolyte foil. The polarization resistance R_P was identified as the difference in real part impedance between the infinite-frequency intercept and the intercept at frequencies approaching zero. Gas diffusion limitation in the atmosphere over the electrode surface has been demonstrated to be of the order of 0.01 to 0.03 Ωcm^2 for this type of setup under the given circumstances.[23] This contribution was identified by a nonlinear least squares fitting routine[24] and corrected for in those cases where the total impedance was below 1 Ωcm^2.

7.3 Results

7.3.1 Fracture Mode

The determination of bending strength was qualitative in method (bending by hand), but a significant trend was observed following the sintering temperature of anode precursor layers, see Table 7.1. The reference foils exhibited fairly high mechanical strength; no significant difference of properties was found for the blank YSZ foil and the foil with less than 1 μm NiO sintered at 1300°C. Cells with anodes sintered at 1100°C to 1200°C exhibited also high strength, comparable to that of the reference foils. After sintering at 1250°C the fracture occurred at a lower load than for the reference foils. Cells sintered at 1300°C and higher exhibited decreasing strength with sintering temperature, and the cells sintered at 1500°C were very weak.

Table 7.1 Mechanical properties of symmetrical cells prior to reduction. The cells are sintered up to 4 times at different temperatures, T_{Sinter}.

YSZ foil id.	T_{Sinter}	Assessment of mechanical properties
blank YSZ	1x1300°C	high strength
YSZ + $Ni(NO_3)_2$	1x1300°C	high strength
325-9	3x1100°C	high strength, weak interface
325-7	3x1200°C	high strength, weak interface
325-7’	3x1200°C + 1250°C	moderate strength
325-6	3x1300°C	low strength, channel cracks, strong interface
325-6’	3x1300°C + 1350°C	low strength, channel cracks, strong interface
325-6”	3x1300°C + 1400°C	low strength, channel cracks, strong interface
325-5	3x1300°C + 1500°C	very low strength, channel cracks, strong interface

Typical drying and sintering contraction pores (“mud-cracks”) on the surface of unreduced electrodes are seen to increase in number by increasing sintering temperature, Figure 7.1. Cells sintered at 1100°C exhibit a fairly homogeneous structure with “mud-cracks”, Figure 7.1A. Both “mud-cracks” and fine cracks are observed on the electrode surface of cells sintered at 1300°C to 1500°C (Figure 7.1B), the density of cracks increasing with sintering temperature. The edges of the fine cracks are sharp and well defined, and opposing sides match perfectly. This is taken to indicate that the cracks have formed after sintering. The cracks extend widely across the width of

the cells, but extend only to a certain depth into the electrolyte as observed elsewhere on the same specimens by fracture studies.[25] This cracking mode is denoted "channel cracking".[26] Since these channel cracks have sharp crack tips they are more detrimental to the mechanical strength of the cells than "mud-cracks" with tips smoothened by sintering.

Fracture surfaces of unreduced cells as observed by ESEM are given in Figure 7.2. The planar fracture surface of the electrolyte seen in Figure 7.2A is typical for the reference electrolyte foils and for electrolytes with sintered electrodes up to a sintering temperature of 1200°C. Delamination is observed at the interface between electrolyte and electrode layers. The electrode layers are observed to fracture at a position not coinciding with the fracture of the electrolyte. Figure 7.2B shows the fracture surface of a cell sintered at 1300°C. The serrate fracture surface of the electrolyte and the coinciding fracture of the electrode layers and the electrolyte are observed for cells sintered at 1300°C to 1500°C.

The fact that channel cracks were found on cells with a 50 μm thick coating sintered at 1300°C but not on foils having a coating of less than 1 μm is consistent with model predictions; channel cracking can be suppressed by reducing the coating thickness.[26] In general, the electrolyte fracture surface show only transgranular fracture, no significant amount of intergranular fractures were observed.

7.3.2 Microstructure

The reduced anode structure was inspected by low-vacuum SEM (LV-SEM, Model JSM-5310LV, JEOL, Tokyo, Japan) using back-scattered electrons on polished cross-sections in epoxy, as given in Figure 7.3. The contrast difference between Ni and YSZ is very low due to the limited difference in average atomic weight. Optical microscopy with a lower resolution than SEM was used to verify the distribution of the phases as stated below. Porosity is difficult to evaluate from these images, as the penetration depth of electrons in epoxy amounts to several microns whereby particles in the underlying structure contributes to the obtained image.

Anodes sintered at 1100°C to 1250°C and reduced at 1000°C (Figure 7.3A) exhibit a network of submicron YSZ particles and discrete Ni particles of about 1 to 2 μm. For anodes sintered at 1300°C to 1350°C (Figure 7.3B), the YSZ particle size was larger, about 0.5 to 1 μm, and the nickel had redistributed to form clusters of 2 to 5 μm, contacting a number of YSZ particles. This structure developed further by increasing sintering temperature to 1500°C (Figure 7.3C), where the YSZ particle size was about 1 to 3 μm and Ni agglomerates of 5 to 20 μm were found to encapsulate a number of YSZ particles. The interface towards the electrolyte was generally well defined with only slight indications of YSZ sintering necks at the highest sintering temperatures.

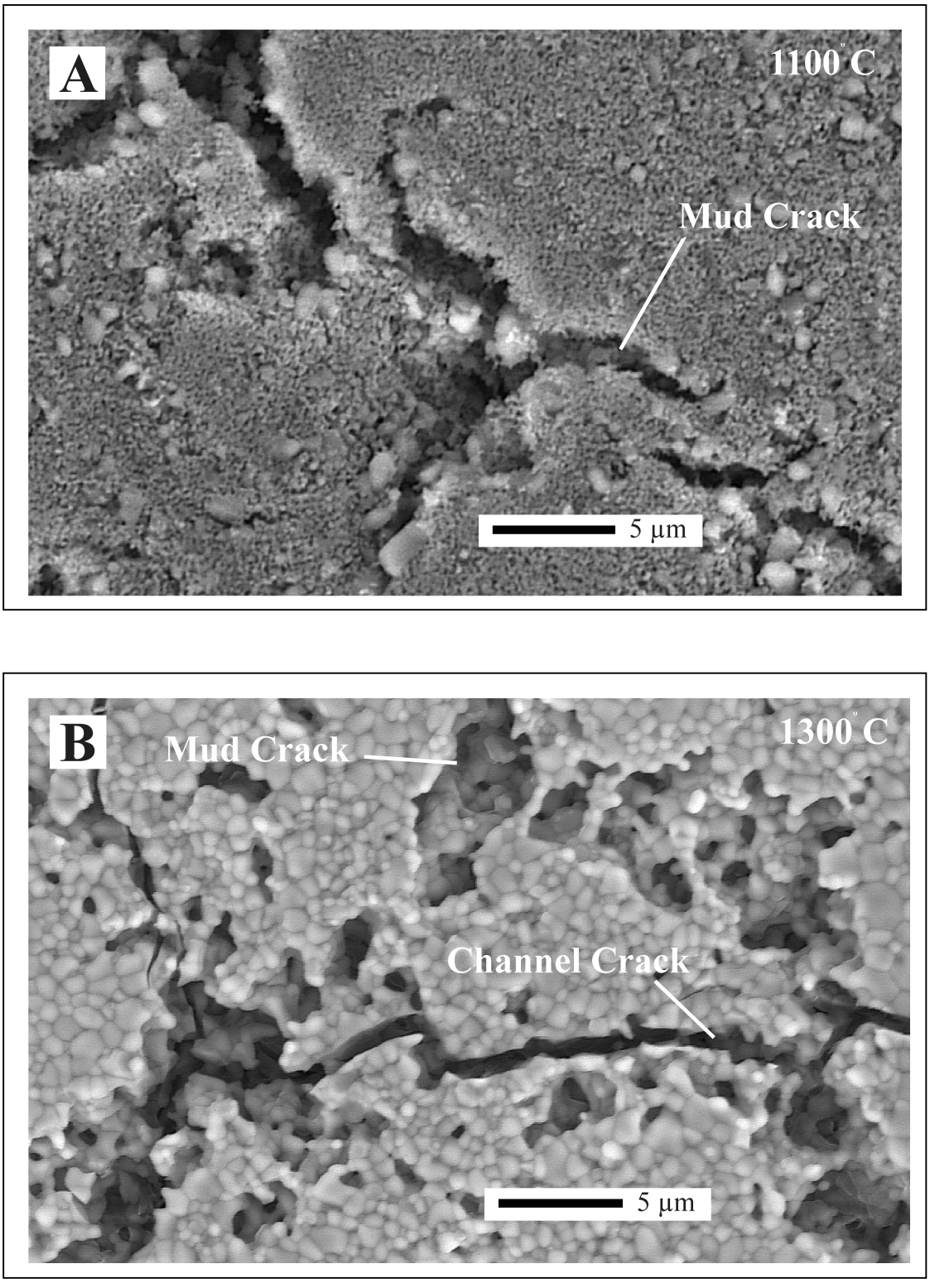

Figure 7.1 Surface of a sintered NiO/YSZ anode precursor layer as observed in ESEM. Cells sintered at A) 1100°C with "mud-cracks" from drying and sintering contraction and B) 1300°C showing "mud-cracks" and sharp channel cracks formed during cooling.

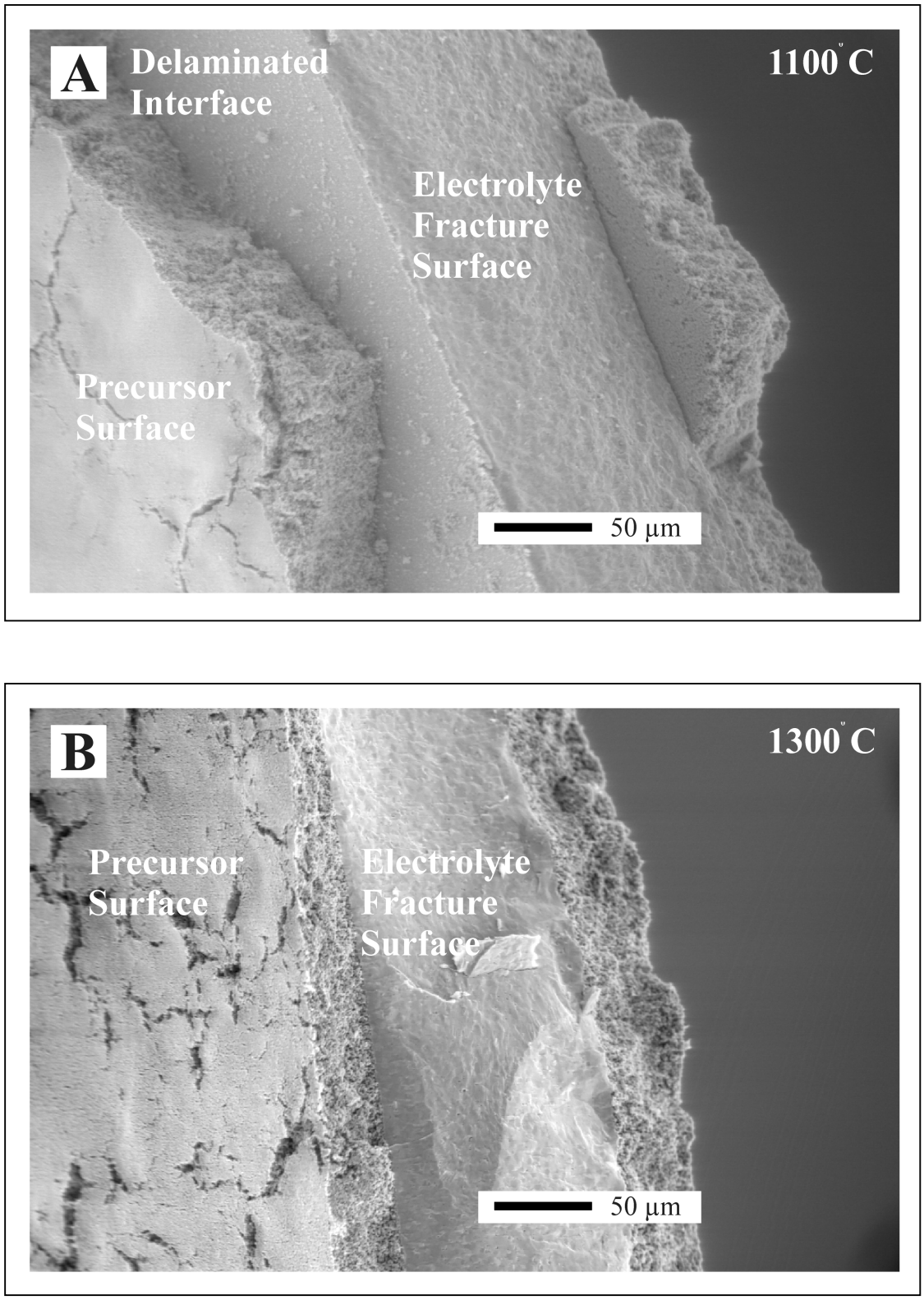

Figure 7.2 Fracture surface of unreduced cells as observed in ESEM. Cells sintered at A) 1100°C exhibiting delamination and a planar electrolyte fracture surface, and B) 1300°C exhibiting strong adherence and serrate fracture surfaces of electrodes and electrolyte following each other.

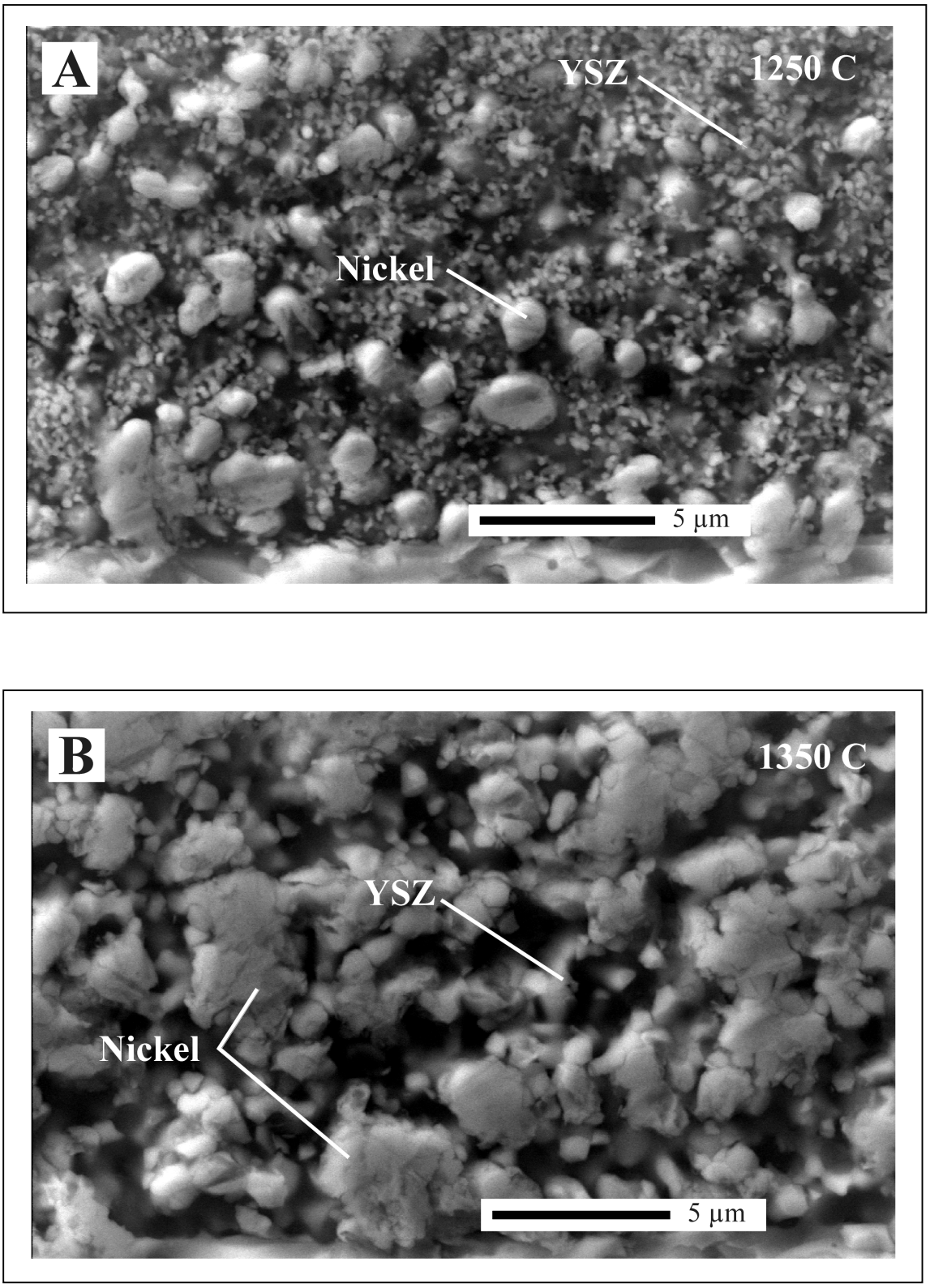

Figure 7.3 Polished cross-sections of reduced cells sintered at A) 1250°C, B) 1350°C and C) 1500°C as observed in LV-SEM. Both Ni and YSZ particles are seen to grow by increasing sintering temperature of the anode precursor. (*Cont. next page*)

Fig. 7.3 Cont.

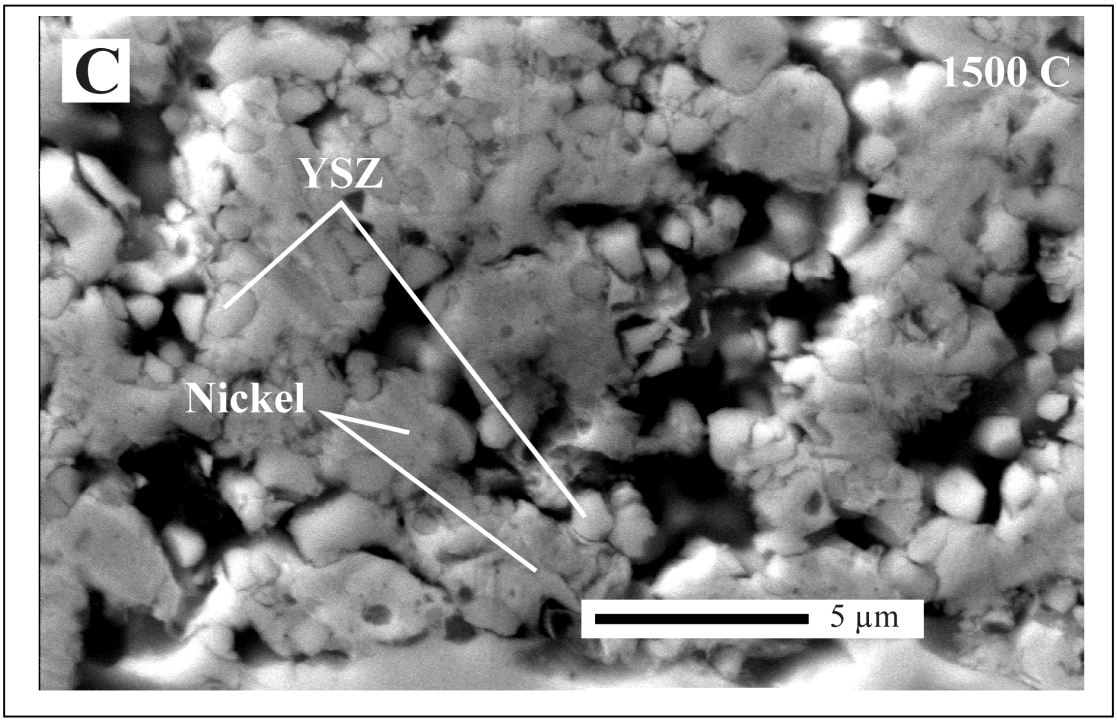

7.3.3 Electrochemical Performance

Representative impedance spectra were obtained at no polarization at 1000°C in 97% H_2 + 3% H_2O for cells sintered at 1100°C to 1500°C, Figure 7.4. The spectra were evaluated as described above and corrected for gas diffusion over the electrodes and for electrode area. R_S and R_P for cells measured without and with a Pt current collector are given in Table 7.2 and Table 7.3, respectively.

R_S and R_P are plotted against sintering temperature in Figure 7.5. R_S, as obtained without Pt current collection, was reduced by one order of magnitude by increasing the sintering temperature from 1100°C to 1250°C, and again by increasing the sintering temperature to 1300°C. A broad minimum is found at sintering temperatures of 1300°C to 1400°C, see Figure 7.5, and at 1500°C a slight increase is seen. The same trend is observed for the in-plane resistance as measured at ambient temperature, Table 7.2.
By applying a Pt current collector both R_S and R_P are reduced more than one order of magnitude for cells sintered at 1100 and 1250°C. For cells sintered at 1300 and 1350°C, R_S is decreased slightly to a value of 0.12 Ωcm^2, whereas R_P is unaffected, Table 7.3.

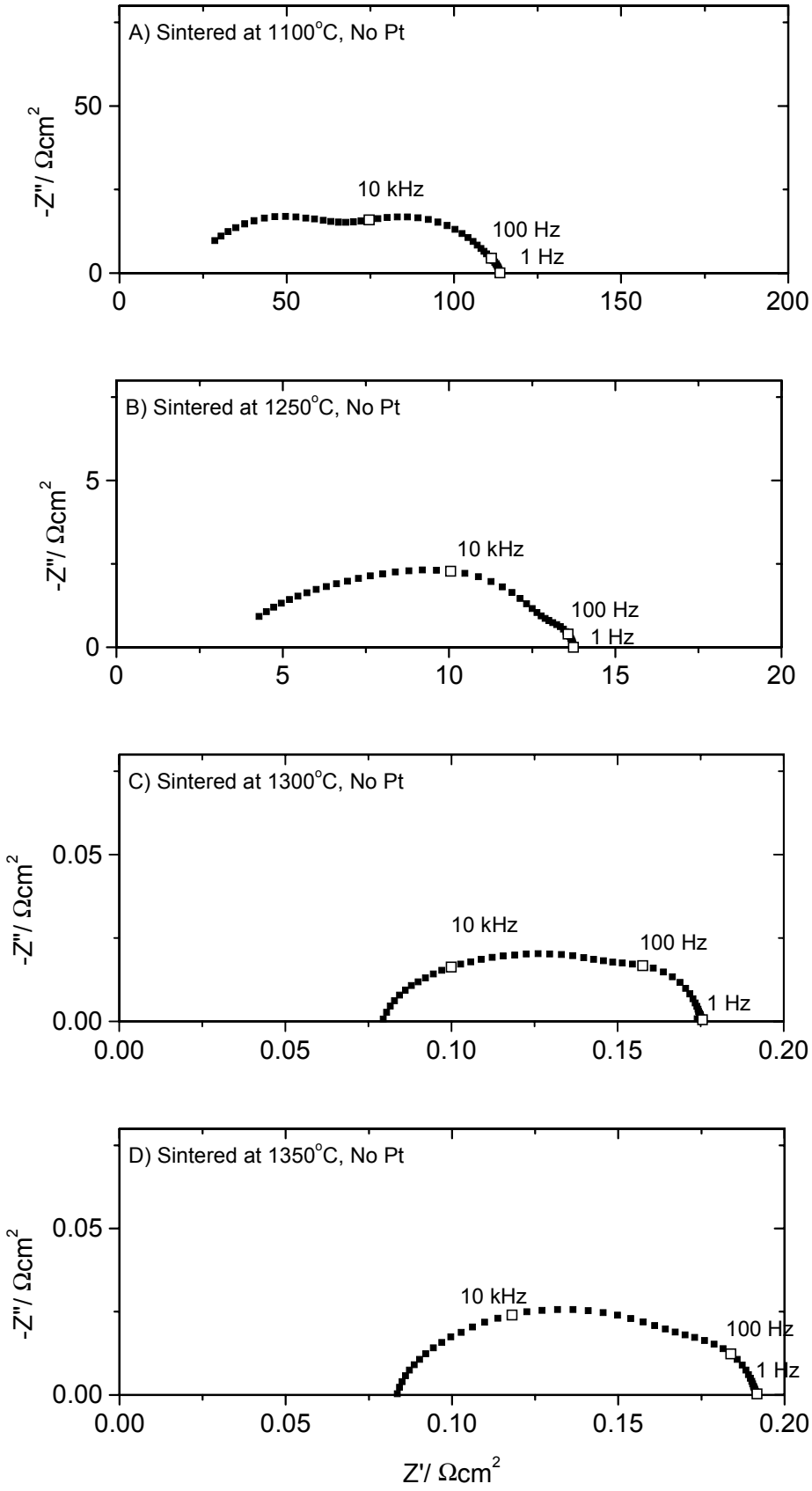

Figure 7.4 Area-specific impedance spectra (1000°C, H_2+ 3% H_2O). Sintering temperatures and additional current collector (Pt) are indicated. Gas diffusion impedance at about 100 Hz is known to contribute about 25 mΩcm^2, see C) and H). (*Cont. next page*)

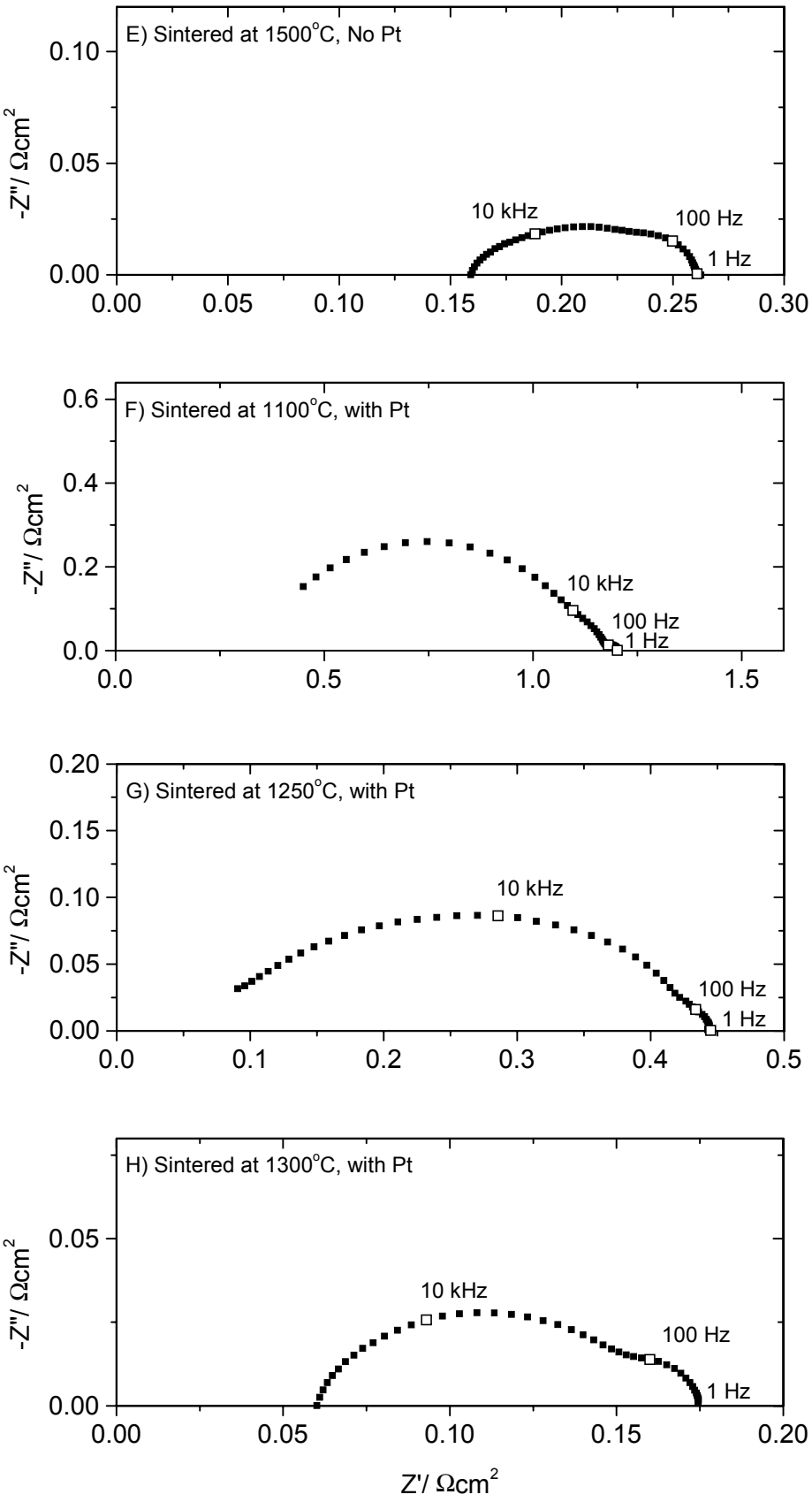
E) Sintered at 1500°C, No Pt
10 kHz
100 Hz
1 Hz
F) Sintered at 1100°C, with Pt
10 kHz
100 Hz
1 Hz
G) Sintered at 1250°C, with Pt
10 kHz
100 Hz
1 Hz
H) Sintered at 1300°C, with Pt
10 kHz
100 Hz
1 Hz
-Z''/ Ωcm2
Z'/ Ωcm2

Fig. 7.4 cont.

Table 7.2 Electrochemical properties of symmetric cells sintered at different temperatures, T_{Sinter}. No additional current collector applied.

YSZ foil id.	T_{Sinter}	Area, (cm^2)	$R_{Inplane}$, [¤] (Ω)	R_S,[§] (Ωcm^2)	R_P,[§#] (Ωcm^2)
325-9	3x1100°C	0.135	$>10^6$	41	45+48
325-7	3x1200°C	-	$>10^6$	-	-
325-7'	3x1200°C + 1250°C	0.090	5-10	5.8	5.5+4.8+0.53
325-6	3x1300°C	0.136	0.6	0.41	0.11
325-6'	3x1300°C + 1350°C	0.090	0.6	0.16	0.10
325-6"	3x1300°C + 1400°C	0.150	0.5	0.15	0.09
325-5	3x1300°C + 1500°C	0.156	0.2-2	0.42	0.06+0.07

[§] Obtained by impedance spectroscopy in 97% H_2 + 3% H_2O at no polarization at 1000°C.
[¤] Two point measurement at 25°C between 0.3 mm gold wire tips at a distance of 3 mm.
[#] Summations indicate more than one distinct arc in impedance spectra.

Table 7.3 Electrochemical properties of symmetrical cells sintered at different temperatures, T_{Sinter}, and provided with a Pt paste current collector on each electrode.

YSZ foil id.	T_{Sinter}	Area, (cm^2)	R_S,[§] (Ωcm^2)	R_P,[§#] (Ωcm^2)
325-9	3x1100°C	0.237	0.64	0.82+0.03
325-7'	3x1200°C + 1250°C	0.138	0.12	0.37
325-6	3x1300°C	0.132	0.11	0.11
325-6'	3x1300°C + 1350°C	0.204	0.12	0.04+0.07

[§] Obtained by impedance spectroscopy in 97% H_2 + 3% H_2O at no polarization at 1000°C.
[#] Summations indicate more than one distinct arc in impedance spectra.

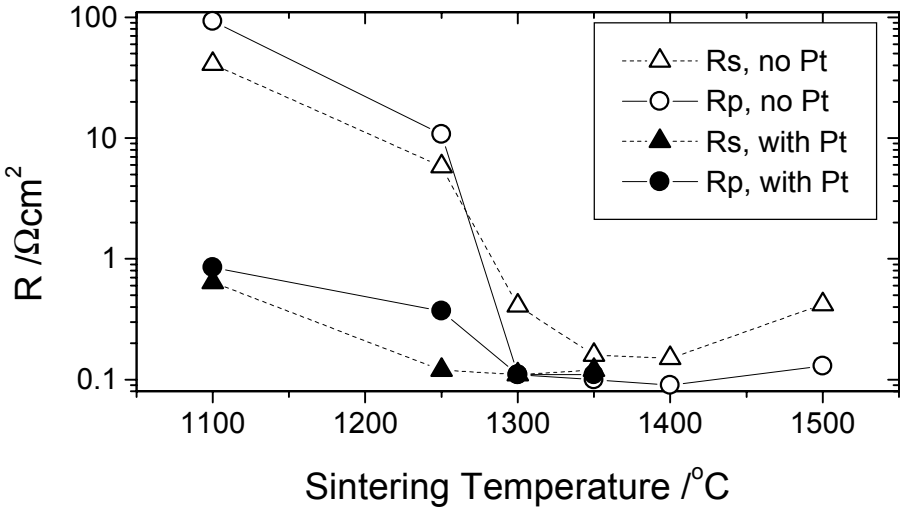

Figure 7.5 Area specific series resistance R_S (triangles) and polarization resistance R_P (bullets) as function of sintering temperature. With (solid symbols) and without (open symbols) a Pt current collector. All cells measured by impedance spectroscopy in 97% H_2 + 3% H_2O at no polarization at 1000°C.

7.4 Discussion

7.4.1 Fracture Mode

The reference electrolyte with a less than 1 μm thick film of NiO sintered at 1300°C exhibits a strength comparable to that of blank YSZ. The examined fracture surfaces for cells sintered at any temperature in the range of 1100°C to 1500°C show only transgranular fracture and few if any intergranular fractures. Both observations indicate that YSZ grain boundary weakening in the presence of NiO is not responsible for the observed change in fracture properties with sintering temperature. However, it is noted that the applied method of fracturing may influence somewhat on the fracture mechanism.

The dense and thick YSZ electrolyte is in general taken to be the stronger component in the cell. The NiO/YSZ composite is both highly porous and contains more defects. The nature of these defects is considered in the following.
"Mud-crack" pores in the electrode layers, originating in contraction due to drying and sintering of the electrode layers, in general reduce the strength of these layers as they localize stress by pinning during further densification and under external load. However, these cracks, including channel cracks relieve the strain and thus reduce the tendency to delaminate.
The difference in thermal expansion coefficient (TEC) between electrolyte and electrode layers and the resulting stress buildup must also be considered. The TEC of TZ8Y is about 10.6-11 $\times$ 10^{-6} K^{-1}.[27] A TEC of 14 $\times$ 10^{-6} K^{-1} can be found for NiO, and a TEC of 12.3 $\times$ 10^{-6} K^{-1} can be calculated and measured for a NiO/YSZ composite with 53 v/o NiO.[28] Considering the cells to be stress free at the maximum sintering temperature and to be free of cracks and delamination, the TEC difference causes the electrolyte to experience in-plane compressive stress at room temperature. This compressive stress is not critical with respect to cracking. However, the NiO/YSZ composite layer is subject to tensile stress. This type of stress can cause channel cracks in the electrode layer, as observed for cells sintered at 1300°C and higher, Figure 7.1B. The penetration depth of these cracks is expected to increase by increasing sintering temperature, as the temperature span to room temperature and thus the residual stress increases.

As observed in Figure 7.2A the interface between electrolyte and electrode layers is fairly weak for cells sintered at temperatures of 1250°C and below, and delamination can occur. Apparently, the TEC induced residual stress for these cells is not capable of causing the electrode layers to spall off during cooling. Consequently delamination only occurs in connection with channel cracking caused by external loads. At sintering temperatures of 1300°C or more no delamination occurs under external load, indicating that the interface bonding is stronger.
These observations allow us to describe the fracture patterns in Figure 7.2 by two different fracture events. The planar fracture surface of the electrolyte in Figure 7.2A indicates how the fracture of the electrolyte originates in the propagation of a single crack. This crack can propagate straight through the electrolyte once it has been initiated by the external load. The weak interface against the electrode layers causes delamination and independent fracture of the electrode layers. Flaws and cracks starting in the weaker electrode layers are deflecting at the interface, leaving the electrolyte properties to govern the cell strength.
The serrate fracture surface of the electrolyte in cells sintered at 1300°C and higher (Figure 7.2B) indicates a fracture developed by combination of several individual cracks. Furthermore, the coinciding fracture of the electrodes with the electrolyte suggest that the cracks have propagated across the interface before or under load to fracture. The origin of these cracks is suggested to be

TEC induced channel cracks in the electrode layers, as observed in Figure 7.1B. During external loading these sharp cracks cause the electrolyte to fracture at a far lower external load than is required for fracture of the blank electrolyte.

The interpretation of the fracture surfaces suggests that a change occur in the fracture mode with sintering temperature. For cells sintered at 1250°C and below, fracture appears to be controlled by the electrolyte properties. For cells sintered at 1300°C and above, fracture appears to be initiated by fine channel cracks growing from the electrodes into the electrolyte. The transition between the two regimes is suggested to relate to the adhesion of the electrodes to the electrolyte and the occurrence of delamination and crack deflection at the interface.

The described fracture events are supported by inspection of the fracture surfaces and model work on the very same cells elsewhere.[25] The distribution of stress is generic for layers of different TEC sintered together, and related mechanical problems have been discussed elsewhere.[28,29] The fracture mode for electrolyte supported cells sintered at temperatures at or above 1300°C is considered fatal and prohibitive for increasing the sintering temperature beyond 1300°C.
However, in anode supported cells the electrode is the thick component, dominating both TEC and strength. Thereby the thin and weak electrolyte experiences compressive in-plane stress at room temperature, whereas the thick electrode layer should be able to withstand the tensile stress. Consequently a sintering temperature of 1300°C or more is not expected to be disadvantageous for mechanical strength of cells in the anode supported cell design.

7.4.2 Performance and Microstructure

A number of transport steps may in principle limit the anode reaction: i) gas diffusion in the pores, ii) ionic resistance in the electrolyte network, and iii) electronic resistance in the Ni-network. All of these processes are directly related to the anode microstructure.

More than 98% densification of the electrolyte is obtained at a sintering temperature of only 1350°C. Even after sintering at 1500°C the density of the anode structure is low enough to cause no detectable diffusion limitation. Impedance contributions from gas diffusion in the structure have been estimated to be in the order of few $m\Omega cm^2$ under the given circumstances in anodes with an open porosity of about 50%.[23] This evidence of maintaining sufficient porosity in the anode is attributed to a low packing density in the green anode precursor structure compared with the tapecast electrolyte.

The apparent activation energy of R_S is about 0.8 eV as expected for YSZ,[7] whereas electronic conductivity in metals decreases slightly with increasing temperature. The dominant part of the series resistance R_S is usually considered to be electrolyte resistance. However, a low electronic conductivity in the electrodes may be very important.
In case of insufficient in-plane conductivity in the electrodes, a part of the full electrode area at the periphery of the cell is contacted through an extra metallic type resistance contribution to R_S, and contributes with reduced efficiency to the electrode processes. It is not so much the extra contribution to R_S that is measured, as it is the resistance of the reduced "effective" area of the electrolyte. In other words, a significant part of the geometric cell area is electrically inefficient but is still considered in the geometric area used for normalization of the measured impedance. Therefore, limitations in the in-plane resistance of the porous Ni and the ionic resistance of the

electrolyte cannot be distinguished between by activation energy. At the same time, the reduced "effective" cell area compared with the geometric area influence the area correction of the measured R_P in the same way as for R_S. This leads to higher R_P values than could be obtained on the same cells with a better current collector.
Detailed models for calculating R_S for various cell designs with electrodes of finite in-plane conductivity exist.[30] A convenient parameter for determining whether the in-plane conductivity is sufficient on thin symmetric cells, is the measured series resistance R_S compared with the calculated minimum value for the given electrolyte material, thickness and temperature.

The minimum series resistance attainable on these cells is calculated as follows: Assuming infinite in-plane conductivity of the electrodes (or the Pt layer where applied) and a maximum YSZ conductivity of about 0.18 S/cm at 1000°C,[7] a limiting R_S of 0.09 Ωcm^2 can be calculated for 160 μm thick TZ8Y foils.
R_S for a cell with infinite in-plane conductivity in the applied Pt layer and no Ni-percolation in the 50 μm thick anode structures can also be estimated. Previously the resistivity of a porous network of YSZ sintered at 1200°C to 1300°C has been demonstrated to be approximately 10 times higher than for dense YSZ, after etching away the Ni-substructure.[11,31] Consequently, the expected series resistance for a cell with 50 μm thick electrodes sintered at these temperatures is about 0.65 Ωcm^2 at 1000°C.
In case the in-plane conductivity of the anode (and Pt layer where applied) is finite, the series resistance may vary upwards from 0.09 Ωcm^2.

Looking now at cells tested without Pt current collection (Table 7.2), the R_S values indicate that the Ni-percolation provides reasonable current collection on cells of this size sintered at temperatures of 1300°C and higher. After sintering at 1300°C, R_S is a factor of 4 higher than estimated by the calculation above, and after sintering at 1350°C to 1400°C R_S is a factor of 2 higher than the calculated minimum. The increase in R_S after sintering at 1500°C is ascribed to loss of effective area due to the channel cracks. Cells sintered below 1300°C suffer in-plane limitation on a "cell radius" scale (1 to 2 mm). Consequently the apparent R_P cannot be taken to represent the geometric cell area; a current collector should be applied.
These findings of the in-plane conductivity are in good agreement with the development in microstructure with sintering temperature as seen in Figure 7.3. The trend in in-plane resistance $R_{Inplane}$ reflects the development in R_S remarkably well (Table 7.2), and may be considered as a "first approximation" development tool for this type of electrode.

Providing cells sintered at 1250°C or higher with a Pt current collector, an R_S value is attained which is in reasonable agreement with the calculated minimum value, Table 7.3. Cells sintered at 1100°C and tested in this way yield R_S values of about 0.64 Ωcm^2, close to the estimated 0.65 Ωcm^2 for YSZ structures sintered at 1200°C to 1300°C with no percolation in the Ni-phase. Considering the very fine YSZ structure at this sintering temperature compared with anodes sintered at 1200°C and 1300°C, Figure 7.3, this is taken as evidence of substantial percolation in the Ni-phase on an electrode-thickness scale (50 μm) after sintering at 1100°C, despite the very open Ni structure shown in Figure 7.3A.

The best obtainable polarization resistance R_P for anodes produced from this slurry appears to be about 0.10 Ωcm^2 after sintering at 1300°C or more. The optimum is shallow, a fairly constant R_P is obtained in the sintering temperature range of 1300 to 1500°C, disregarding the effect of the channel cracks. The minimum sintering temperature for optimum electrochemical

performance coincides with the sintering temperature where significant in-plane conductivity on a 1 to 2 mm scale in the Ni-structure is obtained as evaluated from R_S.
The range of sintering temperatures yielding optimum performance does not include 1250°C by addition of a Pt current collector, although R_P is lowered a factor of 25 from 10.8 Ωcm^2 to 0.37 Ωcm^2 for these cells (Table 7.3). This indicates, that even with good current collection (R_S matches the calculated minimum), the anode structure contains less active TPB, than what is obtained by raising the sintering temperature. For anodes sintered at 1100°C the performance is only enhanced a factor of 10 by adding a Pt current collector, indicating poor Ni-percolation on a 50 μm scale (anode thickness). The applied porous Pt current collector cannot be excluded to contribute significantly to the electrode process for inefficient Ni/YSZ cermet anodes sintered at 1100°C to 1250°C.

Apparently, there is no further improvement in electrochemical performance of this Ni/YSZ anode to be obtained by sintering at temperatures above 1300°C, provided an adequate current collector contacts the 50 μm thick anode on a 1 to 2 mm scale. Transferring this observation tentatively to anode-supported cells where the thick anode structure provides contacting and in-plane conductivity, the dense supported electrolyte can be sintered at any temperature in the range of 1300°C to 1500°C.

7.5 Conclusion

The mechanical strength of YSZ electrolyte foils with NiO/YSZ anode precursor layers is severely degraded by increasing the sintering temperature above 1250°C due to channel crack formation in the anode precursor layers. The channel cracks originate in TEC mismatch between the electrolyte and the sintered anode precursor layer. The strength of reference foils and the predominant occurrence of transgranular fracture in the electrolyte are taken as supporting evidence that chemical reactions with and dissolution of NiO in YSZ does not cause a significant degree of decrease in the strength of YSZ grain boundaries.

A minimum polarization resistance of about 0.1 Ωcm^2 in 97% H_2 + 3% H_2O at 1000°C is obtained after sintering at temperatures in the range of 1300°C to 1500°C. For anodes sintered at 1250°C it appears that performance is limited both by in-plane conductivity in the Ni phase on a 1 to 2 mm scale (test cell radius), and by the amount of active TPB generated in the microstructure at this sintering temperature.

For the electrolyte supported Ni/YSZ cermet anodes, a maximum sintering temperature of about 1300°C is dictated by the requirement for handling strength. Optimum anode performance requires a minimum sintering temperature of about 1300°C, leaving little room for a compromise.

This particular conflict of interests is predicted to be less severe in the case of an anode supported cell, where the thick anode structure dominates both thermal expansion and mechanical strength. Channel cracks in the electrode structures are not expected in this cell geometry and strong cells with a dense membrane should be achievable without compromising anode performance.

Acknowledgment

This work has been supported by ELSAM and the Danish Energy Agency under the DK-SOFC program. The presented experimental data have been generated as a conclusion of the joint effort of several members of the SOFC project group at Risø. Their contributions are gratefully acknowledged.

References

[1] C. Bagger, M. Juhl, P. V. Hendriksen, P. H. Larsen, M. Mogensen, J. G. Larsen and S. Pehrson, in *Second European SOFC Forum*, B. Thorstensen, Editor. European SOFC Forum, Oberrohrdorf, CH. 175 (1996)

[2] G. M. Christie, R. C. Huiberts, E. J. Siewers and J. P. P. Huijsmans, in *Third European SOFC Forum*, P. Stevens, Editor. European SOFC Forum, Oberrohrdorf, CH. 133 (1998)

[3] S. P. S. Badwal and K. Föger, in *Third European SOFC Forum*, P. Stevens, Editor. European SOFC Forum, Oberrohrdorf, CH. 95 (1998)

[4] H. J. Beie, L. Blum, W. Drenckhanh, H. Greiner and H. Schichl, in *Third European SOFC Forum*, P. Stevens, Editor. European SOFC Forum, Oberrohrdorf, CH. 3 (1998)

[5] S. C. Singhal, in *SOFC V*, U. Stimming, S. C. Singhal, H. Tagawa and W. Lehnert, Editors. **PV 97-40**, The Electrochemical Society Proceedings Series, Pennington, NJ. 37 (1997)

[6] H. Sasaki, S. Otoshi, M. Suzuki, T. Sogi, A. Kajimura, N. Sugiura and M. Ippommatsu, *Solid State Ionics*, **72** 253 (1994)

[7] F. T. Ciacchi, K. M. Crane and S. P. S. Badwal, *Solid State Ionics*, **73** 49 (1994)

[8] N. Q. Minh and T. Takahashi, *Science and Technology of Ceramic Fuel Cells*, chapter 8, Elsevier Science B. V., Amsterdam. 198 (1995)

[9] S. P. S. Badwal and K. Foger, *Materials Forum*, **21** 187 (1997)

[10] S. Sakamoto, H. Taira and H. Takagi, *Denki Kagaku*, **64** 609 (1996)

[11] M. Brown, S. Primdahl and M. Mogensen, *J. Electrochem. Soc*. submitted (1999), chapter 6 in this thesis

[12] S. Sunde, *J. Electrochem. Soc*. **143** 1930 (1996)

[13] T. Kawada, N. Sakai, H. Yokokawa, M. Dokiya, M. Mori and T. Iwata, *J. Electrochem. Soc*. **137** 3042 (1990)

[14] D. W. Dees, T. D. Claar, T. E. Easler, D. C. Fee and F. C. Mrazek, *J. Electrochem. Soc*. **134** 2141 (1990)

[15] M. J. Powel, *Phys. Rev. B*, **20** 4194 (1979)

[16] S. Linderoth and A. Kuzjukevics, in *SOFC V*, U. Stimming, S. C. Singhal, H. Tagawa and W. Lehnert, Editors. **PV 97-40**, The Electrochemical Society Proceedings Series, Pennington, NJ. 1076 (1997)

[17] A. Kuzjukevics, S. Linderoth and J. Grabis, in *High Temperature Electrochemistry: Ceramics and Metals,* F. W. Poulsen, N. Bonanos, S. Linderoth, M. Mogensen and B. Zachau-Christiansen, Editors. 17th Risø International Symposium on Materials Science, Roskilde DK. 319 (1996)

[18] P. Nikolopoulos and D. Sotiropoulou, *J. Mat. Sci. Let*. **6** 1429 (1996)

[19] M. M. Murphy, J. Van herle, A. J. McEvoy and K. R. Thampi, *J. Electrochem. Soc*. **141** L94-96 (1994)

[20] P. H. Middleton, M. E. Seiersten and B. C. H. Steele, in *SOFC I*, S. C. Singhal, Editor. **PV 89-11**, The Electrochemical Society Proceedings Series, Pennington, NJ. 90 (1989)

[21] A. C. Khandkar, S. Elangovan, M. Liu and M. Timper, in *High Temperature Electrode Materials and Characterization*, D. D. Macdonald and A. C. Khandkar, Editors. **PV 91-6**, The Electrochemical Society Proceedings Series, Pennington, NJ. 175 (1991)

[22] C. Bagger, in *1992 Fuel Cell Seminar*, Courtesy Associates, INC., Washington DC. 241 (1992)

[23] S. Primdahl and M. Mogensen, *J. Electrochem. Soc.* in press (1999), chapter 5 in this thesis

[24] B. A. Boukamp, *Solid State Ionics*, **20** 31 (1986)

[25] B. F. Sørensen and S. Primdahl, *J. Mat. Sci.* **33** 5291 (1998)
[26] J. L. Beuth, *Int. J. Solid. Structures*, **29** 1657 (1992)
[27] R. Männer, E. Ivers-Tiffée and W. Wersing, in *SOFC II*, F. Grosz, P. Zegers, S.C. Singhal and O. Yamamoto, Editors. Commission of the European Communities, Luxemburg, L. EUR-13564-EN, 715 (1991)
[28] M. Mori, T. Yamamoto, H. Itoh, H. Inaba and H. Tagawa, *J. Electrochem. Soc.* **145** 1374 (1998)
[29] R. Vassen, R. W. Steinbrech, F. Tietz and D. Stöver, in *Third European SOFC Forum*, P. Stevens, Editor. European SOFC Forum, Oberrohrdorf, CH. 557 (1998)
[30] K. Nisancioglu, in *Natural Gas Fuelled Solid Oxide Fuel Cells & Systems*, IEA Task Report, Office Federal De L'Energi, Berne, CH. 87 (1989)
[31] J. Geyer, H. Kohlmüller, H. Landes and R. Stübner, in *SOFC V*, U. Stimming, S. C. Singhal, H. Tagawa and W. Lehnert, Editor. **PV 97-40**, The Electrochemical Society Proceedings Series, Pennington, NJ. 585 (1997)

Chapter 8

Indications of the Electrode Reaction Limitations[†]

Abstract

The impedance of Ni and Ni/YSZ cermet anodes in H_2/H_2O on YSZ electrolyte pellets was examined by impedance spectroscopy in a three electrode setup where concentration polarization was prevented. The polarization resistance R_P was found to depend on $pH_2O^{-0.25}$ at 850°C, and to decrease with increasing pH_2 at high pH_2. An H/D isotope effect was found to be negligible at 1000°C, and to increase with decreasing temperature. Poisoning of the Ni surface by 35 ppm H_2S caused a 60% increase in R_P, irrespective of temperature, anode type and passage of current. Addition of small amounts of Mn to the anode appeared to be able to reduce R_P by a factor of 2 at 850 and 1000°C. The dominant limiting process is suggested to change gradually from surface or bulk transport of protons at lower temperatures to an unidentified process at higher temperatures.

[†] This chapter has been accepted as S. Primdahl and M. Mogensen, "Limitations in the Hydrogen Oxidation Rate on Ni/YSZ Anodes" in *SOFC VI*, (1999)

8.1 Introduction

The Ni/YSZ cermet anode in H_2/H_2O has been the subject of numerous electrochemical studies by dc- and impedance techniques. However, the presented data and interpretations have failed to form a consistent picture. Recently the cause for low frequency arcs appearing in some impedance studies has become evident. Concentration impedance in the form of gas conversion[1] and gas diffusion outside the electrode[2] both depend on the test setup rather than on the electrode. Diffusion inside a porous structure covering the anode has been demonstrated at moderate frequency.[3] Diffusion inside the porous electrode is found to be relevant only for very dense electrodes, in dilute gases and for thick, supporting structures.[4,5] Taking these effects in consideration, the remainder of most reported impedance spectra have relaxation frequencies in the kHz range. This is in agreement with the expectations for a limiting process parallel to a double-layer capacitance at the Ni/YSZ interface.

In order to reveal the nature of this limiting process, considerable effort has been spent worldwide. Up to this point theories have been raised and mechanisms have been proposed, but definitive experimental evidence is scarce. The triple phase boundary (TPB) line where electrode, electrolyte and gas meet is generally agreed to relate to the amount of the electrochemically active reaction sites. However, whether the reaction proceeds on the TPB or on one or more of the three adjacent two-phase interfaces is unknown. Indicative measurements excluding possibilities or verify others are in great need to help understand the limitations in Ni/YSZ anodes.

In the following it is attempted to add to and verify existing indicative measurements of the limiting process or processes on porous Ni anodes. Ni anodes and Ni/YSZ cermet anodes are investigated in a setup where concentration impedance has been demonstrated to be negligible, and in the temperature range of 700 to 1000°C the effect of H/D isotope exchange and sulfur contamination is evaluated. Furthermore, a significant reduction of R_P on quite good Ni/YSZ cermet anodes is achieved by addition of Mn.

8.2 Experimental

8.2.1 Sample Preparation

Porous Ni-anodes: YSZ particles (TZ8Y, Tosoh) of 0.4 μm after calcination (1100°C/2h) and ball-milling were mixed with Ni particles of 1 to 2 μm in 10 to 20 μm agglomerates (Ni #255, Inco) in the volume ratio 90/10. The viscous slurry was milled until the bimodal particle size distribution contained about 20 v/o of 0.4 μm and 80 v/o of 8 μm diameter particles. The slurry was applied to sintered YSZ three-electrode pellets, Figure 8.1, by brush in a layer of 20 to 30 μm and was not sintered before testing.

Ni/YSZ cermet anodes: The YSZ particles (TZ8Y, Tosoh) and 85% of the NiO particles (green NiO, Johnson Matthey) were 0.4 μm, the remaining NiO particles were 10 μm. The Ni/YSZ volume ratio after reduction was 40/60. The ethanol-based slurry was spray-painted in three layers onto sintered YSZ three-electrode pellets and sintered for 2 hours at 1300°C after application of each layer to form a 45 μm thick anode.

Similar anodes were deposited on both faces of a 180 μm thick sintered YSZ foil, and thereafter cut with diamond tools to form 4×4 mm^2 symmetrical cells. On some of the cells Mn was added to the electrode in the amount of 2-5 metal-atom% (a/o).

8.2.2 Electrochemical Testing

For electrochemical testing two three-electrode pellets carrying nominally identical electrodes as working electrode and auxiliary electrode were positioned with the two electrodes facing each other, Figure 8.1. The working electrode and the auxiliary electrode were contacting opposite sides of a Ni-mesh (0.13 mm Ni wires, 0.50 mm wire spacing, Johnson Matthey). One of the working electrodes was characterized using the other as an auxiliary electrode. This was done by passing current between the two counter electrodes and measuring the potential between the Ni-mesh and one of the reference electrodes, Figure 8.1. In this way concentration impedance was limited to one-dimensional diffusion through the Ni-mesh between the working electrode and the auxiliary electrode. This concentration impedance has been demonstrated to be negligible.[2]

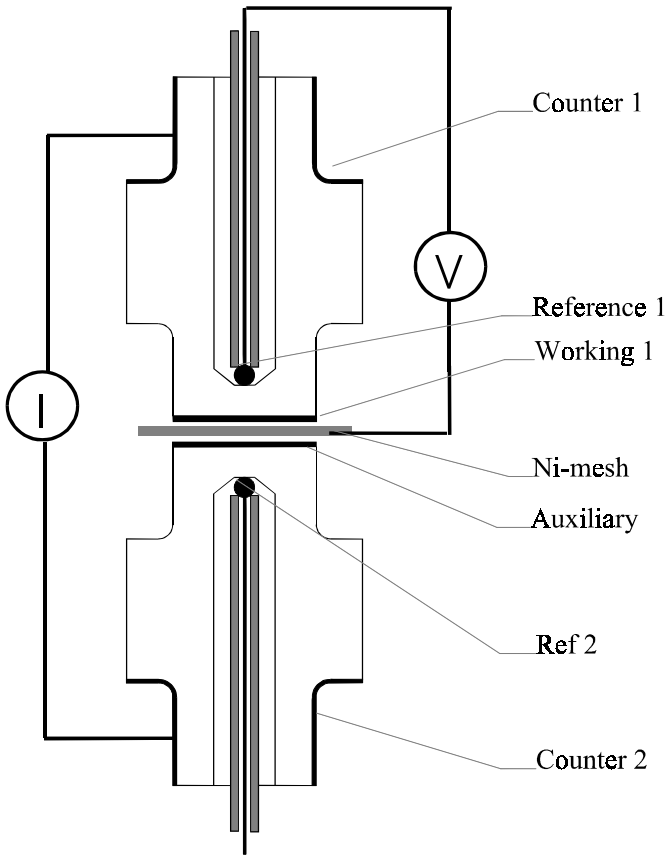

Figure 8.1 Electrochemical test geometry involving two three-electrode pellets in one atmosphere with the distance of gas transport being only between the working electrode and the auxiliary electrode over the mesh-thickness.

Cells were heated in a one-atmosphere set-up to 1000°C in $H_2/H_2O/N_2$=0.09/0.03/0.88 before changing to an atmosphere of H_2/H_2O=0.97/0.03 with an open circuit voltage (OCV) against Pt/air of about -1070 mV ($pO_2 \sim 2 \times 10^{-18}$ atm). The fuel composition was controlled by thermal mass flowmeters, mixing H_2 and He, and passing the gas or part thereof through H_2O at a given saturation temperature. For isotope studies H_2 was replaced by D_2 and H_2O by D_2O in a parallel gas supply system. For studies of sulfur contamination, 1/500 of the H_2 was passed through $(CH_3)_2S_2$ (DMDS) kept on an ice-bath at 0 to 0.2°C yielding a DMDS vapor pressure of 0.009 atm.[6] The two H_2-streams saturated with DMDS and water, respectively, were mixed at the setup-inlet where DMDS decomposed on heating to form approximately 35 ppm H_2S.
Impedance spectroscopy was conducted with an applied amplitude of 20 mV using a Solartron 1260 FRA over the frequency range of 1 MHz to 0.1 Hz.

8.3 Results

8.3.1 Impedance Interpretation

The impedance spectra obtained for the two types of anodes on three-electrode pellets were different, but in both cases the impedance spectra retained their respective shape under all test conditions, Figure 8.2.

The Ni-anodes exhibited a nearly perfect arc, interpretable as an *(RQ)* equivalent circuit with n=0.9, using the notation given elsewhere.[7] The impedance spectra obtained on cermet anodes were slightly more complex. The low frequency range formed a nearly perfect half-arc, whereas the high-frequency part was distorted towards lower real part rather than completing the arc. Both electrodes exhibited a very small arc below 10 Hz, which has earlier been identified as an artifact caused by gas diffusion between reference and counter electrode.[2] Impedance points dominated by this minor artifact were removed in the following. The reported electrode polarization resistance, R_P, was found as the arc width after data-fitting[7] for the Ni-anodes, and for cermet anodes as the difference between the vertical tangent at high frequencies and the real-part intercept with the axis at low frequency, Figure 8.2. The series resistance R_S of the electrolyte was about 2 Ω for the 0.42 cm^2 cross-section. Data were corrected for an equipment related "negative inductance" L of about -5×10^{-8} H.

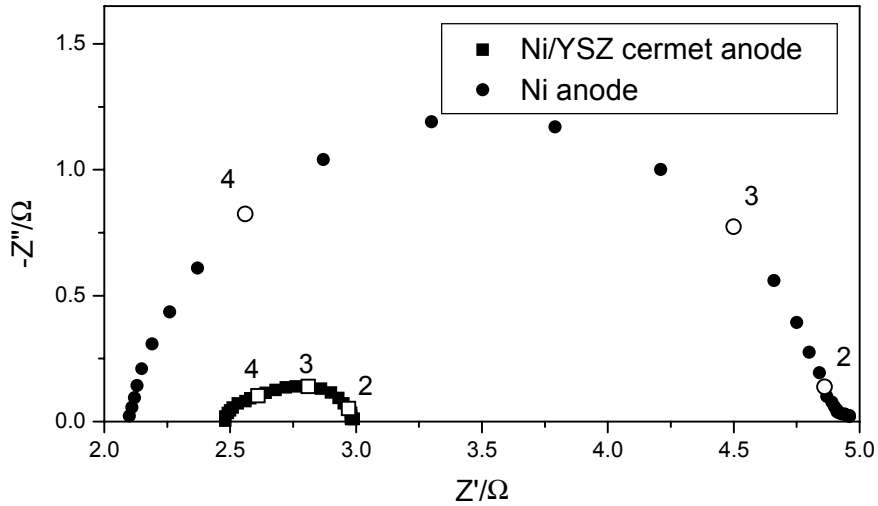

Figure 8.2 Measured by impedance spectra after correction for an inductance of about -5×10^{-8} H. Selected data-points are marked with log(frequency). pH_2/pH_2O=0.97/0.03, OCV at 1000°C. The electrode area is 0.42 cm^2.

8.3.2 Steam and Hydrogen Partial Pressure

The R_P dependence on gas composition at 850°C was investigated for the cermet anodes. The dependence on pH_2 at pH_2O=0.03 atm was found by diluting with He, Figure 8.3. Over the range of 0.03 to 0.2 atm little variation in R_P was observed in agreement with reported observations at 1000°C.[8,9] At higher pH_2 R_P decreases with increasing pH_2.

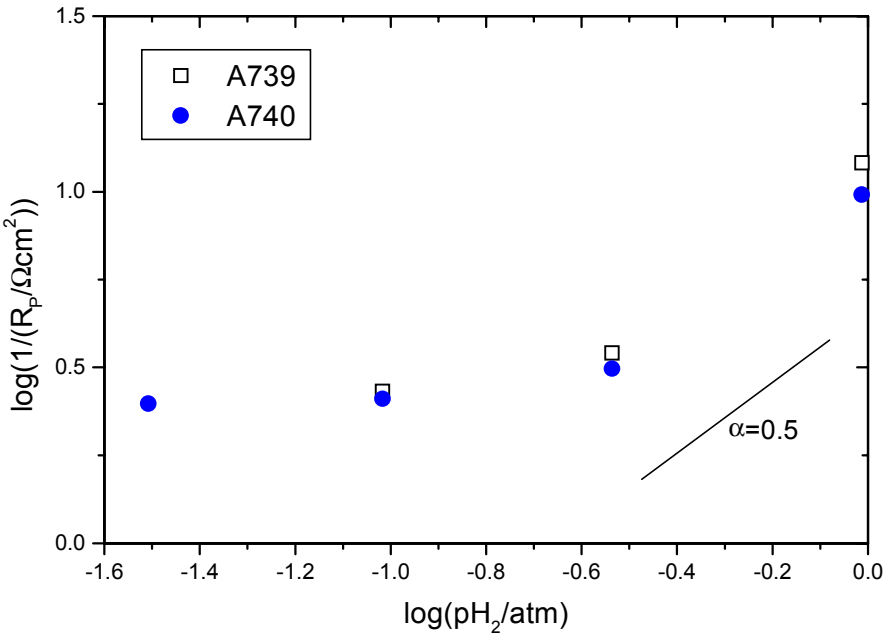

Figure 8.3 $\log(1/R_P)$ vs. $\log(pH_2)$ for cermet anodes at 850°C, OCV at pH_2O=0.03 atm. Balance is He. Here α is the slope of the solid line.

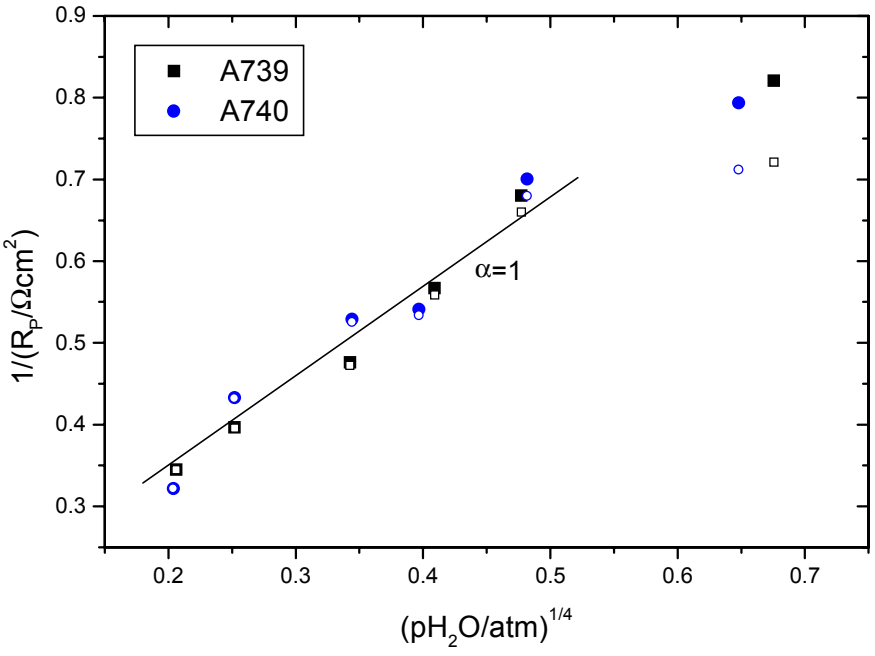

Figure 8.4 $1/R_P$ vs. $pH_2O^{-1/4}$ for cermet anodes at 850°C, OCV. Balance is H_2. Open points are corrected for the effect of varying pH_2 according to Figure 8.3. Here α is the slope of the solid line.

The observed dependence on pH_2O in pure H_2 (pH_2 not constant), is given in Figure 8.4. Over the range of 0.002 to 0.06 atm a dependence on $pH_2O^{-1/4}$ is observed. The disturbing effect of the varying pH_2 is estimated based an interpolation of the data given in Figure 8.3, and corrected (open) data points are given in Figure 8.4.

8.3.3 Isotope Effect

D_2/D_2O was applied instead of H_2/H_2O at the temperatures 1000°C, 850°C and 700°C. The ratios of the observed R_P value in the two atmospheres are given in Figure 8.5 for two cermet electrodes and two Ni-electrodes. At 1000°C no isotope effect is seen. At 850°C the effect is significant for both types of anode, and substantially larger for the porous Ni-anodes. At 700°C the effect is significant and about equal for the two types of anodes.

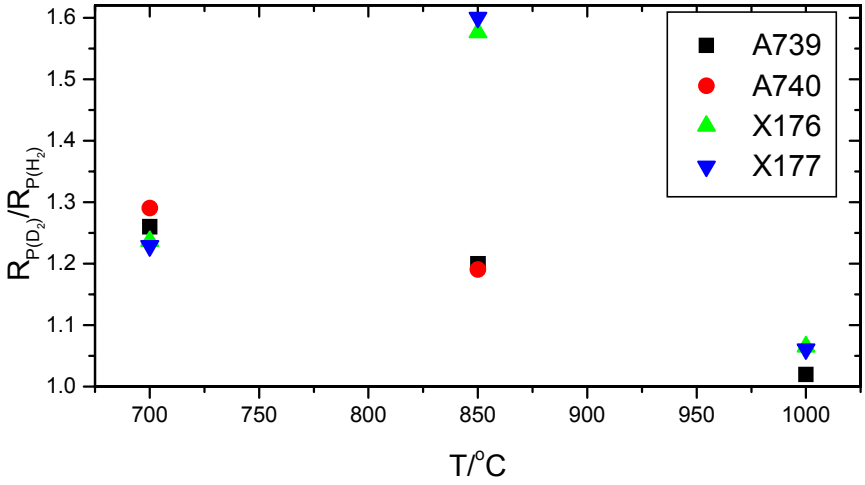

Figure 8.5 The isotope effect calculated as the ratio of R_P in the two atmospheres as a function of temperature. $pH_2/pH_2O=pD_2/pD_2O=0.97/0.03$, OCV.

8.3.4 Sulfur Poisoning

The effect of adding 35 ppm sulfur to the $H_2/H_2O=0.97/0.03$ gas at 850 and 1000°C is given in an Arrhenius type plot as R_P with and without S in Figure 8.6. Note that R_P for the Ni-anode is very high as these electrodes presumably suffered partial detachment from the electrolyte before the sulfur experiments were started. A scaling factor of 1/250 is used for the Ni-anode data (X176) in Figure 8.6. A constant increase of about 60% on R_P is found irrespective of the anode type, the temperature and an anodic current of 0 or 100 mA/cm^2. Contamination with 35 ppm of H_2S is found to be totally reversible. The time-constant of sulfur saturation and removal cannot be estimated due to a high retention time in the used set-up.

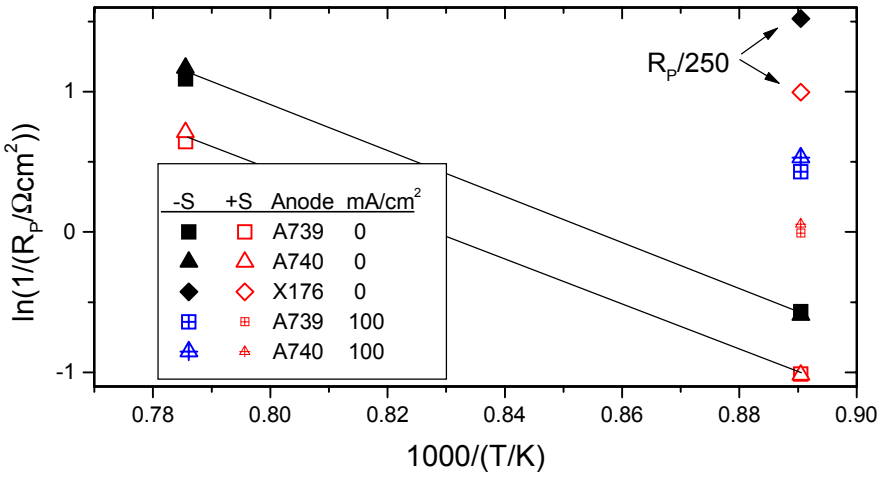

Figure 8.6 Arrhenius type plot of R_P values for cermet and Ni anodes with and without 35 ppm H_2S. pH_2/pH_2O=0.97/0.03, OCV.

8.3.5 Mn as additive

Ni/YSZ cermet anodes with and without Mn as an additive on symmetrical cells of 4×4 mm^2 were characterized by impedance spectroscopy. This cell geometry has been shown to exhibit a gas diffusion impedance outside the electrode structure of about 30 $m\Omega cm^2$ in H_2/H_2O=0.97/0.03, with a summit frequency of about 50-100 Hz. Impedance spectra were fitted to the circuit $LR_S(RQ)_P(RQ)_D$, where $(RQ)_D$ was diffusion impedance outside the anode structure,[2] and R_P was the polarization resistance.
The lowest R_P values obtained are given in Table 8.1, the scatter in measured values lies within a factor of 2 from the reported values. Examples of impedance spectra obtained at 850°C are presented in Figure 8.7.

Table 8.1 R_P in H_2/H_2O=0.97/0.03 at OCV for anodes produced with and without Mn.

Anode type	R_P at 850°C	R_P at 1000°C
Ni/YSZ	110 $m\Omega cm^2$	80 $m\Omega cm^2$
Ni/YSZ with 2-5 a/o Mn	60 $m\Omega cm^2$	30 $m\Omega cm^2$

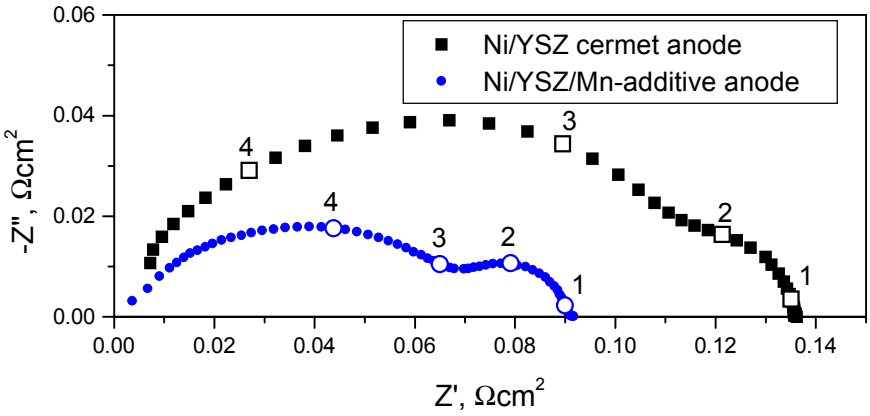

Figure 8.7 Impedance spectra obtained on symmetrical cells with Ni/YSZ cermet anode with and without Mn. pH_2/pH_2O=0.97/0.03, OCV at 850°C. Selected data points are marked by log(frequency).

8.4 Discussion

The test geometry selected was proven successful in avoiding concentration polarization in impedance measurements.[2] The simple impedance arc observed under all experimental conditions for a porous Ni anode would often be taken as evidence of one rate limiting step. However, one apparent arc may cover more parallel or consecutive rate limiting processes with similar time constants. Furthermore the dependencies on pH_2 and the isotope effect point to more than one rate-limiting process (see below). The impedance spectra for Ni/YSZ cermet anodes are more complex but still invariant in shape with test conditions. This is interpreted as transport restrictions in the cermet microstructure distorting a simple impedance arc. Distortions can be caused by the distributed nature of the reaction sites in the cermet structure indicating more than one relaxation frequency as demonstrated by modeling.[10,11] Similar distortions have been demonstrated to depend on anode microstructure by e.g. varying the sintering temperature.[9,12,13]

8.4.1 Gas Composition

Characteristic Ni-properties include excellent bond-breaking capabilities for H_2 and a high surface sticking coefficient for H_2.[14,15] In general the surface coverage on any Ni-surface increases with hydrogen partial pressure and by decreasing temperature. It is thus surprising that at the highest surface coverage a positive effect of pH_2 is observed, Figure 8.3. However, this might be taken as an indication of different types of surface sites on the Ni, where some sites contributing to the H_2/H_2O process are not occupied before a high overall surface coverage is obtained.

In this study a dependence on $pH_2O^{-0.25}$ is observed at 850°C, whereas an approximate dependence on $pH_2O^{-0.5}$ has been observed at 1000°C.[8,9] One explanation for the dependence on steam partial pressure is the cathodic reaction, which contributes equally to R_P at OCV and is assumed to be significant up to anodic overpotentials of ~3RT/F, i.e. about 300 mV. An alternative interpretation is a rate limiting physical transport restriction in a solid material, where solubility or mobility depends on pH_2O. In general the observed dependencies on gas composition

may also include dependencies on electrode potential, as the pO_2 is also (inherently) varying with the variation of pH_2 or pH_2O.

8.4.2 Isotope Effect

The trend in observed H_2/D_2 isotope effect is towards an increase with decreasing temperature. This is consistent with the findings of others,[16] where a small isotope effect has been observed for a Ni point electrode and a Ni/YSZ cermet anode at 1000°C. The quantitative effect was not obtainable due to performance fluctuations of 5%. At 600°C the isotope effect was more pronounced on the cermet, but a degradation prevented quantification.

The classical isotope effect predicts that the shift in pure diffusion resistance should be proportional to the change in the square root of the mass, for D_2/H_2 or D^+/H^+ a factor of 1.41 and for e.g. OD^-/OH^- a factor of 1.03. Furthermore evidence exist for gas phase diffusion in the structure not being limiting as the electrode process is thermally activated.[2] The observed value ranges from about 1 at 1000°C to about 1.25 at 700°C (1.6 at 850°C for porous Ni-anodes). It can be concluded that transport and/or reaction of hydrogen species are involved in the limiting process at 700 and 850°C, but not at 1000°C. These hydrogen species are taken to be protons for a number of reasons.[15] This change in isotope effect indicates a shift in the nature of the limiting process with temperature.

8.4.3 Poisoning by Sulfur

The poisoning effect of sulfur by chemisorbtion on Ni-catalysts is well known,[17] and has been investigated on Ni/YSZ cermet anodes by several groups. Two impedance arcs have been reported for a cermet anode, where the high frequency arc was increased a factor of 2 by addition of 105 ppm H_2S at 1000°C in H_2 with 3% H_2O.[18] The poisoning effect was observed not to be reversible. Geyer *et al*.[19] also reported two impedance arcs with similar behavior, and identified the low frequency arc as due to diffusion outside the electrodes. For the high frequency arc the resistance was increased a factor of 2 by addition of only 5 ppm of H_2S at 950°C in H_2 with 3% H_2O. No comments were made regarding reversibility.

Assuming that sulfur chemisorbs exclusively on the Ni-surface, the data indicate that the Ni-surface is either the location of rate limiting reaction sites, or that it provides a species to the rate-limiting reaction. It is furthermore surprising that in this study the increase in R_P is invariant with respect to electrode microstructure, temperature and anodic current. It would appear that the role of the Ni-surface is constant with these parameters under the given circumstances. This would be the case if adsorbed H_2S blocks one type of two or more types of adsorption sites on Ni, which take part in the H_2/H_2O process. The observed reversibility is in accordance with the general behavior of chemisorbed H_2S.[17]

8.4.4 Chemical Additive

Functional additives for improvement of the performance of Ni/YSZ cermet anodes have been reported. Addition of 20 a/o Mn to the cermet has been demonstrated to cause a factor 5 reduction of R_P for a cermet anode.[20] Here a factor of 2 is attained with considerably less Mn.[21] YSZ containing 5 m/o of Ti, Cr and Mn in solid solution have been applied for cermet anode production, but no lasting improvement over the basic YSZ/Ni cermet was observed.[22] Such

additives may affect both electrode morphology, physical properties of the phases and the chemical and electrochemical activities of the surfaces.

8.5 Conclusion

The polarization resistance, R_P, has been obtained by impedance spectroscopy on Ni/YSZ cermet anodes and Ni-anodes in a setup where concentration polarization is prevented. At 850°C R_P for the cermet anode shows a dependence on pH_2 only at higher pH_2, whereas a dependence on $pH_2O^{-0.25}$ is found over more than a decade in pH_2O.
An insignificant H/D isotope effect is found on both types of anodes at 1000°C, the effect increases by lowering the temperature to 850°C and 700°C.
Poisoning of the nickel surface by sulfur is demonstrated to cause a constant 60% increase in R_P for both types of anodes, both at OCV and at 100 mA/cm^2, at 850 and 1000°C. The observed effect was fully reversible.

Addition of 2-5 a/o Mn is demonstrated to reduce R_P by a factor of about 2 for Ni/YSZ cermet anodes in H_2/H_2O at 850 and 1000°C to 60 and 30 mΩcm^2, respectively.
The limiting process for hydrogen oxidation on Ni anodes is suggested to undergo a gradual transition from surface or bulk diffusion of protons at lower temperatures to an unidentified process at higher temperatures. Furthermore the morphology of the cermet structure is suggested to cause distortions of an otherwise simple impedance arc.

Acknowledgment

This work has been supported by ELSAM and the Danish Energy Agency under the DK-SOFC program. The presented experimental data have been generated in the context of the joint effort of a number of members of the SOFC project group at Risø. Their contributions are gratefully acknowledged.

References

[1] S. Primdahl and M. Mogensen, *J Electrochem. Soc.* **145** 2431 (1998), chapter 4 in this thesis
[2] S. Primdahl and M. Mogensen, *J Electrochem. Soc.* in press (1999), chapter 5 in this thesis
[3] N. Nakagawa, H. Sakurai, K. Kondo, T. Morimoto, K. Hatanaka and K. Kato, *J. Electrochem. Soc.* **142** 3474 (1995)
[4] K.-Z. Fung and A. V. Virkar, in *SOFC IV*, M. Dokiya, O. Yamamoto, H. Tagawa and S. C. Singhal, Editors, **PV 95-1**, The Electrochemical Society Proceedings Series, Pennington, NJ. 1105 (1995)
[5] J.-W. Kim, A. V. Virkar, K.-Z. Fung, K. Metha and S. C. Singhal, *J. Electrochem. Soc.* **146** 69 (1999)
[6] D. W. Scott, H. L. Finke, M. E. Gross, G. B. Guthrie and H. M. Huffman, *J. Am. Chem. Soc.* **72** 2424 (1950)
[7] B. A. Boukamp, *Solid State Ionics*, **20** 31 (1986)
[8] S. Primdahl and M. Mogensen, *J. Electrochem. Soc.* **144** 3409 (1997), chapter 3 in this thesis
[9] M. Brown, S. Primdahl and M. Mogensen, *J. Electrochem. Soc*. submitted (1999), chapter 6 in this thesis
[10] T. Kawada, N. Sakai, H. Yokokawa, M. Dokiya, M. Mori and T. Iwata, *Solid State Ionics*, **40/41** 402 (1990)
[11] S. Sunde, *Electrochimica Acta,* **42** 2637 (1997)
[12] T. Kawada, N. Sakai, H. Yokokawa, M. Dokiya, M. Mori and T. Iwata, *J. Electrochem. Soc*. **137** 3042 (1990)
[13] S. Primdahl, B. F. Sørensen and M. Mogensen, *J. Am. Ceram. Soc*. submitted (1998), chapter 7 in this thesis
[14] S. Skaarup, B. Zachau-Chistiansen and T. Jacobsen, in *High Temperature Electrochemistry: Ceramics and Metals*. F. W. Poulsen, N. Bonanos, S. Linderoth, M. Mogensen and B. Zachau-Christiansen, Editors, 17th Risø International Symposium on Materials Science, Risø, DK. 423 (1996)
[15] M. Mogensen, S. Sunde and S. Primdahl, in *High Temperature Electrochemistry: Ceramics and Metals,* F.W. Poulsen, N. Bonanos, S. Linderoth, M. Mogensen and B. Zachau-Christiansen, Editors, 17th Risø International Symposium on Materials Science, Roskilde, DK. 77 (1996)
[16] T. Norby and P. Kofstad, In *High Temperature Electrochemistry: Ceramics and Metals*. F.W. Poulsen, N. Bonanos, S. Linderoth, M. Mogensen and B. Zachau-Christiansen, Editors, 17th Risø International Symposium on Materials Science, Roskilde, DK. 381 (1996)
[17] M.V. Twigg, *Catalyst Handbook, 2nd Ed*., Manson Publishing, Ltd., London. 196 (1996)
[18] D. W. Dees, U. Balachandran, S. E. Dorris, J. J. Heiberger, C. C. McPheeters and J. J. Picciolo, in *SOFC I*, S. C. Singhal, Editor, PV **89-11**, The Electrochemical Society Proceedings Series, Pennington, NJ. 317 (1989)
[19] J. Geyer, H. Kohlmüller, H. Landes and R. Stübner, in *SOFC V*, U. Stimming, S. C. Singhal, H. Tagawa and W. Lehnert, Editors. **PV 97-40**, The Electrochemical Society Proceedings Series, Pennington, NJ. 585 (1997)
[20] S. Kawasaki, JP 5-190183 (in Japanese). (1992)
[21] S. Primdahl, M. J. Jørgensen, C. Bagger, M. Mogensen and O. Marina, (patent pending). (1998)
[22] A. Tsoga, P. Nikolopoulos, A. Kontogeorgakos, F. Tietz and A. Naoumidis, in *SOFC V*, U. Stimming, S. C. Singhal, H. Tagawa and W. Lehnert, Editors. **PV 97-40**, The Electrochemical Society Proceedings Series, Pennington, NJ. 823 (1997)

Chapter 9

Durability and Thermal Cycling[†]

Abstract

The long-term properties of Ni/yttria stabilized zirconia (YSZ) cermet anodes for solid oxide fuel cells (SOFC) were evaluated experimentally. A total of 13 anodes of three types based on two commercial NiO powders were examined. The durability was evaluated at the temperatures 850°C, 1000°C and 1050°C over 1300 to 2000 h at an anodic dc load of 300 mA cm^{-2} in hydrogen with 1 to 3% water. The anode-related polarization resistance (range of 0.05 to 0.7 Ωcm^2) was measured by impedance spectroscopy. After an initial stabilization period of up to 300 h the polarization resistance varied linearly with time within the experimental uncertainty. At 1050°C no degradation (increase in polarization resistance) was observed. At 1000°C a degradation rate of 10 $m\Omega cm^2$ per 1000 hrs was found. The degradation rate was possibly higher at 850°C. A single anode was exposed to 9 thermal cycles from 1000°C to 100°C at 100°C h^{-1}. An increase in polarization resistance of about 30 $m\Omega cm^2$ was observed over the first two cycles. For the following thermal cycles the polarization resistance was stable within the experimental uncertainty.

[†] This chapter has been submitted in a shortened version as S. Primdahl and M.Mogensen, " Durability and Thermal Cycling of Ni/YSZ Cermet Anodes for SOFC", *J. Appl. Electrochem*. (1999)

9.1 Introduction

The technology of SOFC is at present approaching the economic requirements set by analysis of the consumer market, and two essential aspects are in focus; cost of production,[1,2] and demonstration of durability. The commercial requirements for SOFC systems include a cell and stack life in the order of 40-50,000 h.[3] Considering this life expectancy it is obvious that only very small degradation rates can be accepted for a commercial product.

All components in an SOFC stack exerting resistive limitations can be expected to exhibit some degree of degradation over time. Demonstration of total stack durability is of primary interest, but a breakdown in component contributions is desirable. Such contributions could be polarization resistance of the electrodes, resistance of the electrode-, the electrolyte- and the interconnect-structures as well as contact resistance at every interface.

One of the most convenient ways of obtaining specific anode performance data is by impedance spectroscopy, using a three-electrode setup. The selection of electrolyte geometry and the placement of the reference electrode is not trivial on thin electrolytes.[4-6] Three-electrode geometries based on thick (mm) electrolytes are less prone to frequency dependent errors in determining the electrode performance. However, thick electrolytes can cause significant ohmic heating during DC measurements,[7] and the series resistance of the electrolyte material between reference electrode and working electrode cause low phase angles in impedance measurements.[8]

Electrochemical impedance measurements on three-electrode cells inevitably include resistance in the bulk electrolyte material between reference and working electrode. This is well known, and corrected for by disregarding the series resistance, determined as the real part impedance at high frequency.

Mass transport restrictions in the gas phase above the anode structure have been observed to contribute to electrochemical measurements. pO_2 variations in a volume of fuel gas with a finite exchange rate have been demonstrated to contribute to measurements vs. a stable reference electrode in another gas.[9-12] Diffusion limitation in a stagnant gas layer over the anode structure has been shown in impedance measurements, and a special setup design has been suggested to avoid contributions from mass transport.[13] Also artifact contributions related to mass transfer have been observed using reference electrodes in weakly buffered fuel gas compositions (low pO_2). A common feature of these processes is a typically resistance contribution of the order of 0.1 Ωcm^2 in hydrogen with at least 3% water. Therefore these processes are of particular importance for the evaluation of high-performance anodes.

Gas diffusion limitation inside the anode structure has been demonstrated to require either very low porosity (<10%), high anode thickness (mm scale) or very low concentrations of either H_2 or H_2O to be of importance. [13-15]

It is well established that a key to better anode performance is optimization of the cermet structure. By increasing the active three-phase boundary (TPB) line where the three percolating phases Ni, YSZ and pores meet, better performance is achieved.[16,17] The durability of the anodes can be expected, in part, to depend on the constancy of this TPB length. Examples of structures yielding poor in-plane conductivity, initial electrochemical performance and durability have been given.[18,19] It is thus not necessarily the case that a coarse structure with poor performance is more stable than a fine one. An explanation for this can be found in the mobility of Ni. Ni has a high

self-diffusion coefficient at elevated temperature,[20,21] causing agglomeration and coarsening of the Ni-structure followed by loss of electrode conductivity and TPB in the structure. A rigid, fine framework of YSZ particles is generally thought effective in restraining the Ni-sintering. Poor wetting of Ni on YSZ as demonstrated by a contact angle of about 120° is believed to help stabilize the porous binary structure.[22,23]

Detrimental depletion of Ni at high pH_2O has been demonstrated for anode structures and related to a high partial pressure of $Ni(OH)_2$ combined with the anode fuel gas sweeping the $Ni(OH)_2$ away.[24] Redistribution of Ni out on the electrolyte surface on a μm scale under anodic current has been demonstrated for a point shaped electrode.[25]

The electrochemically active TPB in the cermet has been demonstrated to be located within a distance of about 10 μm from the electrolyte at 1000°C.[26,27] The conductivity of the porous YSZ framework in the anode structure is believed to cause this limitation in the active anode thickness. Therefore the well known decrease in conductivity of YSZ electrolytes with time might be expected to contribute to cermet anode degradation.[17,28]

Suggested means for restraining the Ni rearrangement include covering the internal surface of the electrode metal structure by finely dispersed YSZ,[29] or another mixed conductor oxide with low volatility.[30]

Long-term durability of cells and stacks has been demonstrated by several groups.[31-33] Studies of electrode conductivity over time have also been reported.[19,34] In this context adequate anode thickness is an important issue. High stability of a Ni/YSZ cermet anode with a polarization resistance of 0.27 Ωcm^2 at 300 mA cm^{-2} in hydrogen with 3% water at 1000°C has been demonstrated by current interrupt over 5500 h.[29] A degradation rate of about 47 $m\Omega cm^2$ per 1000 hrs has been observed for Ni/YSZ cermet anodes on cells at 1008°C and 300 $mAcm^{-2}$.[35]

Cooling cycles must be foreseen in stack life due to e.g. failure in a support system component. The major concern about thermal cycling is thermal expansion and contraction. The mechanical integrity of the anode/electrolyte interface is affected by the relative match of thermal expansion coefficients (TEC), which is again structure dependent in porous composites. The TEC of TZ8Y is about 10.6-11 $\times 10^{-6}$ K^{-1}.[36] A TEC of 12.3 $\times 10^{-6}$ K^{-1} has been calculated and measured for a NiO/YSZ composite with 53 v/o NiO.[37] This difference has been demonstrated to be acceptable during cooling of the sintered anode precursor structure from about 1300°C.[38]
For a reduced cermet based on 53 v/o NiO, a TEC of about 11.3 $\times 10^{-6}$ K^{-1} has been obtained,[37] in better agreement with the electrolyte material despite a TEC of about 17.1 $\times 10^{-6}$ K^{-1} for metallic Ni.[39] The low cermet TEC is caused by the low hardness of the metal as compared with the ceramic.[37] As the Ni-fraction is increased towards a percolating Ni-structure with dispersed YSZ particles, the cermet approaches the TEC of the metal.
A gradual increase in anode impedance of a factor of 2 has been demonstrated over 12 thermal cycles from 1000°C to room temperature.[18]

It is the aim of this chapter to demonstrate the durability and thermal cycle behavior of Ni/YSZ cermet anodes as produced at Risø.

9.2 Experimental

9.2.1 Anode Preparation

Three-electrode electrolyte pellets, Figure 9.1, were produced by pressing, machining and sintering TZ8Y (ZrO_2 with 8 m/o Y_2O_3, Tosoh Corp.) at 1350°C for 8 h.

A 40 to 50 μm thick anode (Type "Matthey") was prepared by spray-painting. The ethanol based slurry was composed of green NiO (Johnson Matthey, 99% NiO) and TZ8Y, dispersed by polyvinyl pyrrilidone.[40] The NiO/YSZ weight ratio was 56/44. After deagglomeration in a ball mill, the YSZ particle size was about 0.4 μm. The combined particle size distribution of the prepared slurry was bimodal with fractions of approximately 0.4 μm and 10 μm in the volume ratio 9:1. The slurry was sprayed onto YSZ three-electrode pellets in layers of 10 to 20 μm and sintered for 2 hours at 1300°C after each layer. The Ni/YSZ volume ratio is 40/60 in the reduced cermet.

A number of anodes (type "Matthey graded") were prepared as given above for the first 10 μm layer. After sintering of the first anode layer, a graded current collector structure was deposited by spray painting. A layer containing NiO and YSZ in the weight ratio 64/36 was deposited. A second layer was deposited, containing NiO and YSZ in the weight ratio 70/30 and subsequently sintered at 1300°C for 2 hours. Each current collector layer was about 25 μm thick after sintering.

A third type of anode (Type "Baker") was produced according to the specifications for "Matthey" anodes, except for the use of another green NiO powder (J. T. Baker BV). The combined particle size distribution of the prepared slurry was narrow with an average particle size of 0.35 μm.

9.2.2 Setup

The YSZ three-electrode pellets were provided with a Pt-paste counter electrode and a Pt-ball reference electrode in the central bore.

A number of three-electrode pellets were mounted one at a time in a two-atmospheres setup, Figure 9.1A. This setup provided a reference atmosphere and a sealed cylindrical anode compartment for exposing the anode to a reducing fuel gas. The fuel gas was fed through a concentric tube in the anode chamber. The reference electrode was placed in air, and a Nernst potential was measured. The working electrode of ~0.4 cm^2 was contacted by a Ni-mesh (0.13 mm Ni wires with 0.50 mm wire spacing, Alfa/Johnson Matthey GmbH) pressed down by a 2 mm pushrod and a perforated Al_2O_3 disk of 2 mm thickness and 0.45 cm^2 area. The height from the anode surface to the feed tube was approximately 1 cm. The cross section area of the anode compartment was 0.50 cm^2. The temperature was measured 1 mm above the perforated Al_2O_3 disk.

A one-atmosphere setup holding 4 anodes at a time was used to increase the number of tested samples. 4 three-electrode pellets were placed together in a symmetric arrangement in a sealed Al_2O_3 tube in a furnace. The working electrode was contacted by 3 layers of a woven Ni-mesh. The mesh was supported by a dense Al_2O_3 plate of several cm^2, see Figure 9.1B. A Nernst

potential was measured against Pt/air by an immersed MgO-stabilized ZrO_2 sensor tube placed 15 mm from the samples. The temperature was measured at a distance of 5 mm from an anode, and additionally in contact with the ZrO_2 sensor tube.

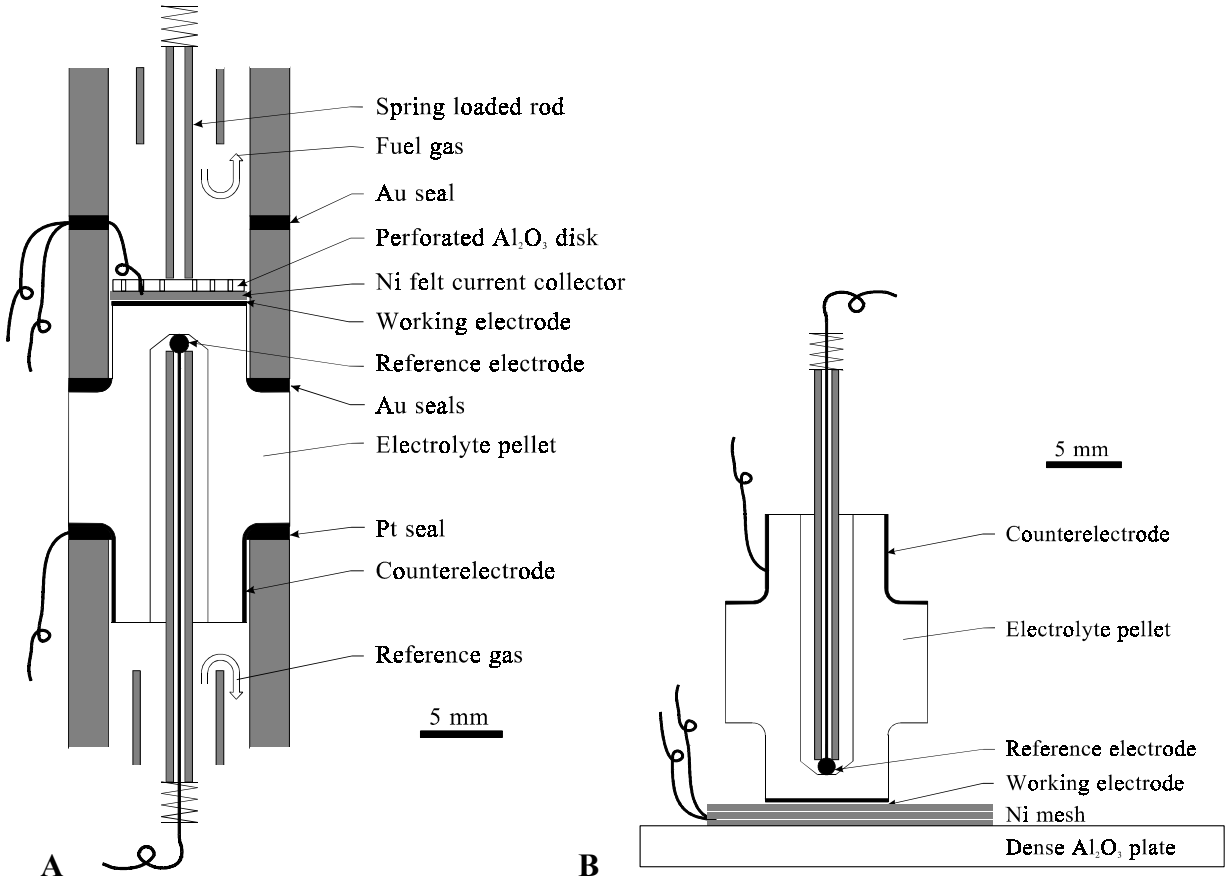

Figure 9.1 Two types of setup used for characterizing anodes. The three-electrode electrolyte pellet (white body) is placed in either A) a two atmospheres-setup where the working electrode (anode) is in the fuel gas and the reference electrode and counterelectrode are in air, or B) a one-atmosphere setup with all electrodes in the fuel gas.

9.2.3 Electrochemical Characterization

The electrolyte geometry used has been verified by finite element analysis to have a frequency stable, homogeneous current distribution, causing from 4 down to 2% error on a polarization resistance in the range of 0.02 to 2 Ωcm^2.[5]

Impedance spectroscopy was conducted with an applied amplitude of 20 mV. This amplitude was verified to be inside the linear range. The frequency range was 500 kHz to 0.01 Hz, or in some cases 50 kHz to 0.01 Hz. Measured impedance was normalized by geometric working electrode area.

The equipment for impedance spectroscopy was a Solartron 1250 FRA combined with a Solartron 1286 ECI, a Solartron 1260 FRA with a Solartron 1287 ECI or a Solartron 1250 FRA combined with an EG&G 273 potentiostat. The three systems were verified on an appropriate test circuit to reproduce measurements within less than 1%.

The durability test of anodes was initiated by heating to operation temperature in 9% hydrogen in nitrogen saturated with water at 25°C, then changing to a measurement atmosphere

of hydrogen with either 1 or 3% of water. This atmosphere was maintained throughout the experiment with a total flowrate of 100 ml min^{-1} (at 25°C) dry gas.

The pO_2 was determined by the Nernst expression from OCV vs. Pt/air. The partial pressure of water pH_2O was determined from pO_2 and pH_2 by the following equation,[41] valid for 1000 K < T < 1300 K:

$$pH_2O = 10^{-(2.958-13022/T)} \cdot pH_2\sqrt{pO_2} \qquad (9.1)$$

For safety reasons, an automatic safety system has terminated the H_2 supply when any potentially dangerous situations occurred during the test. Simultaneously a 9% H_2 in nitrogen protection gas was provided to prevent oxidation of the anodes. The duration of such interruptions was not established.

An anodic current of 300 mA cm^{-2} was applied to each anode by an external galvanostatic current source. The DC load was interrupted shortly once every one to three days, to reconnect and perform two consecutive impedance measurements. All anodes were characterized in a galvanostatic mode with the AC signal superimposed on a DC potential driving a current of 300 mA cm^{-2}. A summary of tested anodes and conditions is given in Table 9.1.

Table 9.1 List of anodes tested in hydrogen with 3 or 1% of water, including the temperature, duration and oxygen partial pressure of the test as well as conditions for the impedance measurements.

Anode	Type	Test temperature	Duration of test	pO_2, atm	Impedance measured at
A729-732	Baker	851±1°C	1800 h	$5\text{-}7 \times 10^{-22}$	300 mA cm^{-2}
A733-736	Matthey	851±2°C	1500 h	$2\text{-}6 \times 10^{-21}$	300 mA cm^{-2}
A627-628	Matthey	1004±1°C	1300 h	$3\text{-}5 \times 10^{-18}$	300 mA cm^{-2}
A648-649	Matthey Graded	1004±1°C	1300 h	$3\text{-}5 \times 10^{-18}$	300 mA cm^{-2}
A582	Matthey	1050±2°C	2000 h	1×10^{-16}/# $4\text{-}5 \times 10^{-17}$	300 mA cm^{-2}
A581	Matthey	1000±2°C	9 cycles	$5\text{-}6 \times 10^{-18}$	OCV

pO_2 changes after 1080 h due to a leak being sealed.

A thermal cycle test was conducted as follows: A Matthey anode was heated in 9% hydrogen with 3% water as described above, and allowed to stabilize for one week in hydrogen with 3% water. Thereafter impedance spectroscopy at OCV was performed. Thermal cycling was conducted by cooling from 1000°C in 40 steps of no more than 25°C. Within 10 hours a minimum temperature of 90 to 95°C was reached. Re-heating was done at a rate of 100°C h^{-1}. During cooling the hydrogen content of the fuel gas was changed from 97% to 9% in nitrogen at 600°C for safety reasons. This atmosphere was maintained until the temperature was again 1000°C. The test atmosphere was reestablished after reaching 1000°C and a stabilizing period of one hour was allowed before impedance spectroscopy at OCV was performed. After 9 thermal cycles the test was terminated.

All anodes were cooled in 9% hydrogen with 1 or 3% water. The in-plane resistance of the anode structures was qualitatively examined by measuring the dc resistance between two 0.3 mm Pt wire-ends at a distance of 0.4 and 0.7 mm. Selected cells were mounted in epoxy, cut and polished for structural characterization by low-vacuum SEM.

9.2.4 Interpretation of Impedance Data

In the present approach it was assumed that obtained impedance spectra could be deconvoluted through an equivalent circuit, containing a number of time constants corresponding to a number of rate-limiting processes in a series arrangement. Obtained impedance spectra were fitted by a non-linear-least-squares fitting routine, EQUIVCRT,[42] using the following elements: R, L, C and Q, representing resistance, inductance, capacitance and a constant phase element with an admittance $Y^* = Y_0(j\omega)^n$, respectively. Here Y_0 is an admittance factor, j the imaginary unit, ω the angular frequency and n is the frequency exponent.
The combination of phase errors at high frequency in both frequency analyzer and potentiostat as well as inductance in the leads was handled as an inductance L, of the system. A series resistance R_S was introduced to account primarily for electrolyte resistance between reference electrode and anode. Subcircuits of the type *(RC)* or *(RQ)* were applied to describe arcs in Nyquist plots of impedance spectra.

A number of processes were expected to contribute to electrochemical measurements on low-impedance anodes in the setups. These processes are identified in the following. Appropriate subcircuits are suggested and expected resistive values are given. The notation I-III for arcs of increasing time constant used elsewhere [43] is applied.
An arc III at a summit frequency of 0.1 to 10 Hz can be expected due to gas conversion in the fuel gas of a two-atmospheres setup.[12] In the identical setup this semicircle has been well described by an $(RC)_3$ subcircuit, the expected resistance is about 0.2 Ωcm^2 in hydrogen with 3% water and fairly independent of temperature. This contribution should not be observed in a one-atmosphere setup with cells of limited dimensions.
In the one atmosphere setup an artifact arc at a frequency of about 0.5 Hz can be expected, due to diffusion between the counter-electrode and the reference electrode through the central bore of the electrolyte geometry.[13] This arc has been fitted by an $(RQ)_A$ subcircuit ($n_A = 0.9$), and in hydrogen with 3% water the resistive value is about 0.01 Ωcm^2.
An arc II at a summit frequency of 10 to 100 Hz can be expected due to diffusion limitation in a stagnant gas layer above the anode structure.[13] This arc is well described by an $(RQ)_2$ subcircuit where $n_2 = 0.75$ in the two atmospheres setup, and $n_2 = 0.9$ to 1.0 in the one atmospheres setup. The variation originates in the different gas access conditions to the volume right above the anode structure. The resistances are of the order of 0.03 to 0.15 Ωcm^2 (depending on the setup) in hydrogen with 3% water and fairly independent of temperature.
An arc I at a summit frequency of 1 to 10 kHz has been demonstrated to depend on the structure of the anode cermet.[11,43] The real part of this arc is considered to be the anode resistance, R_P, and thus the topic of the present study. This semicircle has been described by an *(RQ)* subcircuit where $n_1 = 0.80$ for cermet anodes. [11,43] and values up to 0.9 for point anodes and anodes with a coarse structure.[26,44] In several cases this arc has been demonstrated to consist of two more or less well resolved arcs.[26,38] Where two arcs could be resolved, they were referred to as arc Iα and arc Iβ by increasing time constant, and fitted to each an *(RQ)* subcircuit. The polarization resistance, R_P, was then found as the sum of $R_{1\alpha}$ and $R_{1\beta}$.

Obtained impedance spectra are "pre-processed" before fitting. Spectra obtained at 850°C exhibit erratic inductive loops at low frequency, and are cut short of impedance points with positive imaginary part (below the real axis in a $-Z_{Imag}$ vs. Z_{Real} plot). This approach is taken to provide a "worst case" R_P, as the nature and interpretation of the loop is not known. At high frequency all obtained spectra are cut short of data points at frequencies higher than the vertical tangent.

A priori a series type equivalent circuit is selected to describe the electrode response (arcs Iα and Iβ). Whether the series arrangement is correct is unknown, in principle a redundant branched circuit may be more correct. For the present study this is unimportant as only the variation over time of ($R_{1\alpha}$+$R_{1\beta}$) is considered.

9.3 Results

9.3.1 Impedance Spectra

Examples of obtained impedance spectra for the three types of anodes and at the three test temperatures are presented in Figure 9.2 to Figure 9.6. To illustrate the development in shape over the test duration, several spectra are given after normalization to electrode area and correction for inductance L and series resistance R_S, which were determined by curve fitting. The arcs are identified as I (or Iα and Iβ), II and III by time constant and resistive value according to the expected contributions.

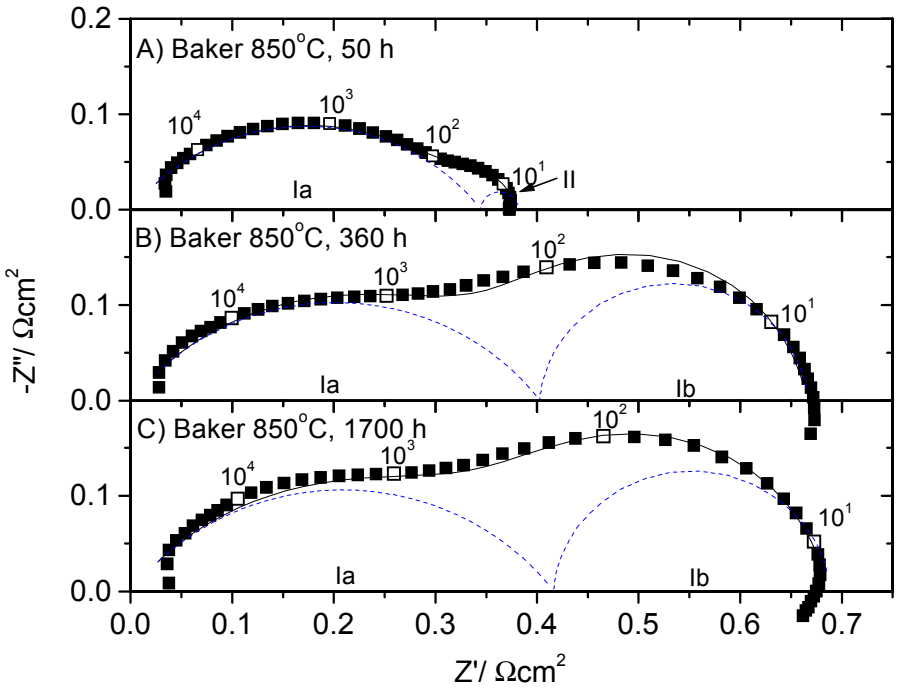

Figure 9.2 Impedance spectra obtained on Baker anode A729 as characterized in the one-atmosphere setup. At 850°C in H_2 + 1% H_2O, 300 mA cm^{-2}. Area: 0.42 cm^2. Normalization for anode area and correction for series resistance and high frequency induction has been performed. After A) 50 h, R_S=2.7 Ωcm^2, L=-8e-7 H, B) 350 h, R_S=3.5 Ωcm^2, L=-9e-7 H, and C) after 1700 h, R_S=4.1 Ωcm^2, L=-1e-6 H.

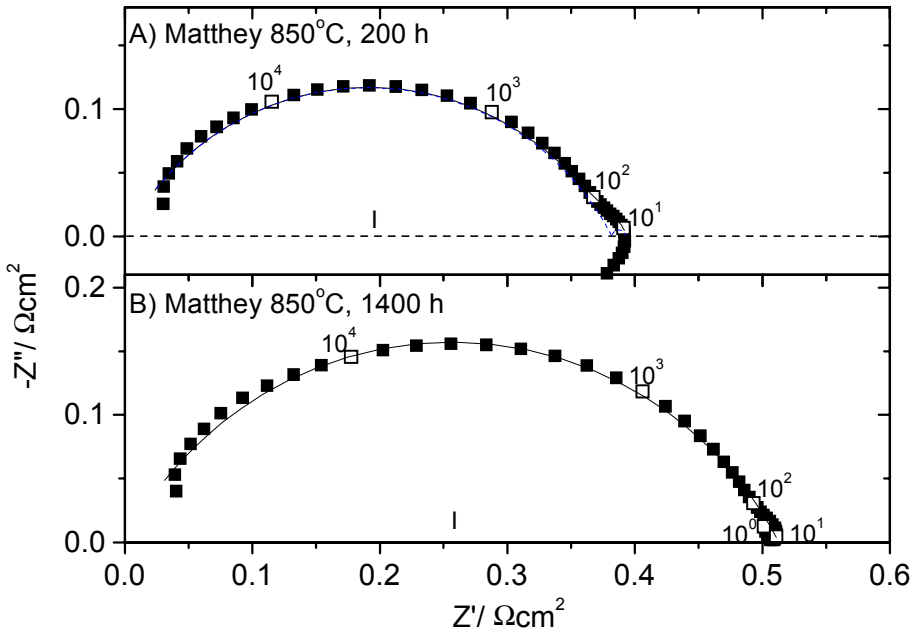

Figure 9.3 Impedance spectra obtained on Matthey anode A733 as characterized in the one-atmosphere setup. At 850°C in H_2 + 3% H_2O, 300 mA cm^{-2}. Area: 0.42 cm^2. Normalization for anode area and correction for series resistance and high frequency induction has been performed. After A) 200 h, R_S=2.4 Ωcm², L=-5e-7 H, and B) after 1400 h, R_S=1.2 Ωcm², L=-2e-7 H.

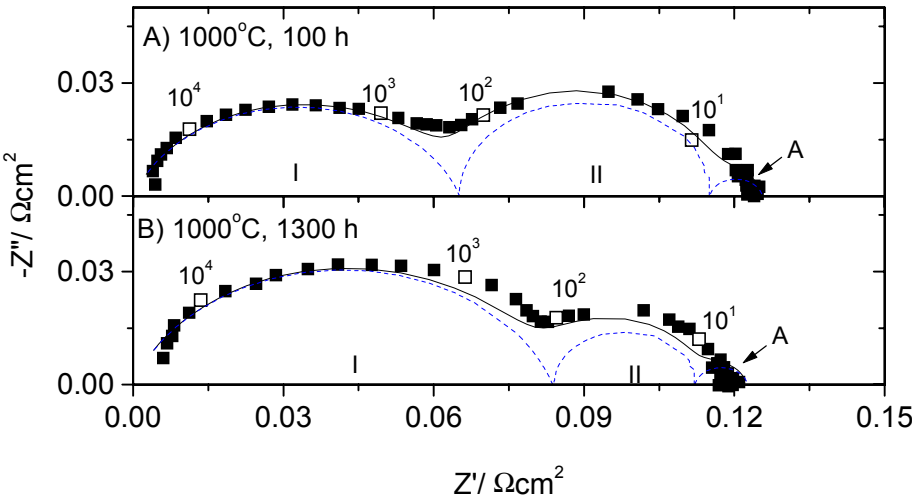

Figure 9.4 Impedance spectra obtained on Matthey anode A628 as characterized in the one-atmosphere setup. At 1000°C in H_2 + 3% H_2O, 300 mA cm^{-2}. Area: 0.42 cm^2. Normalization for anode area and correction for series resistance and high frequency

induction has been performed. After A) 100 h, R_S=0.9 Ωcm^2, L=-3e-8 H, and B) after 1300 h, R_S=1.3 Ωcm^2, L=-6e-8 H.

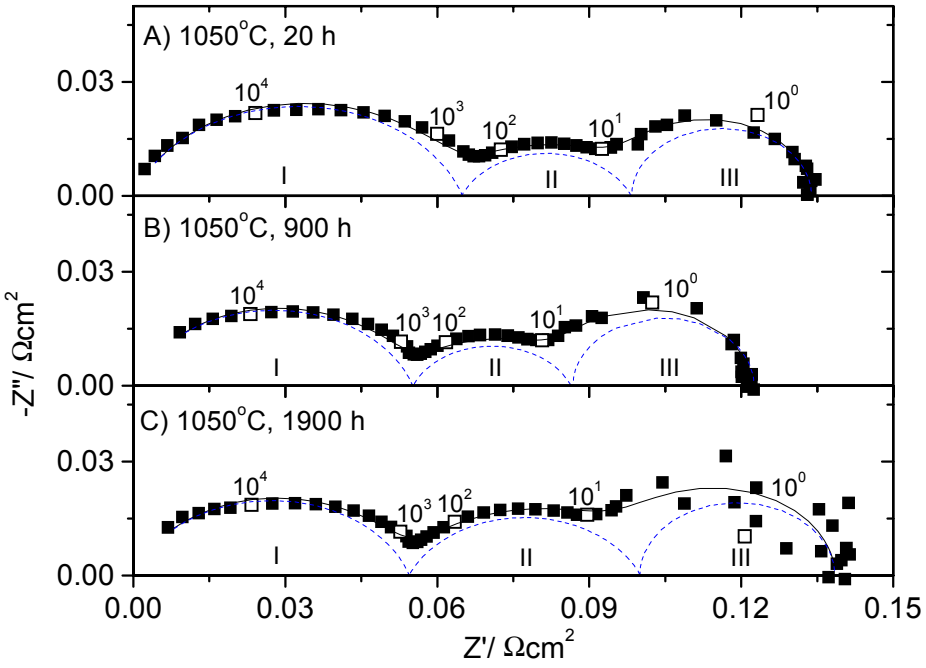

Figure 9.5 Impedance spectra obtained on Matthey anode A582 as characterized in the two-atmospheres setup. At 1050°C in H_2 + 3% H_2O, 300 mA cm^{-2}. Area: 0.40 cm^2. Normalization for anode area and correction for series resistance and high frequency induction has been performed. After A) 20 h, R_S=0.7 Ωcm^2, L=1e-7 H, B) 900 h, R_S=0.9 Ωcm^2, L=1e-7 H, and C) after 1900 h, R_S=1.0 Ωcm^2, L=1e-7 H.

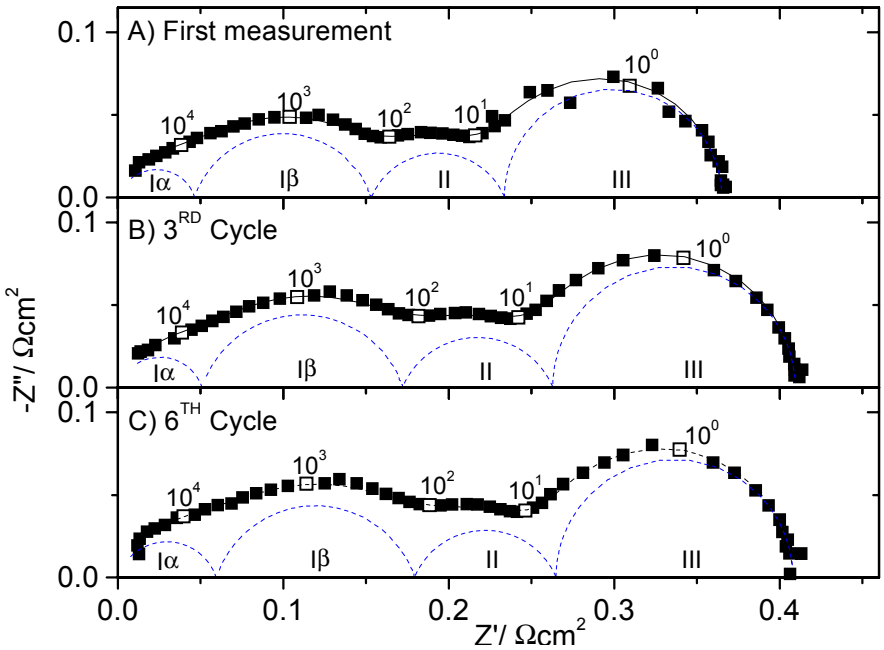

Figure 9.6 Impedance spectra obtained on Matthey anode A581 as characterized in the two-atmospheres setup. At 1000°C in H_2 + 3% H_2O at OCV. Area: 0.40 cm^2. Normalization for anode area and correction for series resistance and high frequency

induction has been performed. A) first run, R_S=0.9 Ωcm^2, L=-4e-8 H, B) after 3 cycles, R_S=0.9 Ωcm^2, L=-7e-8 H, and C) after 6 cycles, R_S=0.9 Ωcm^2, L=-2e-8 H.

Baker anodes tested at 850°C, Figure 9.2, start out with one dominant arc I with a summit frequency, f_S, of a few kHz, and a distinct arc II at f_S≈10 Hz. After a few hundred hours the arcs are no longer readily separated. After 400 h and up to 1700 h two dominant arcs are seen with f_S in the kHz range (Iα) and at about 50 Hz (Iβ). An inductive tail is noted below 10 Hz, the real part size of the tail varies erratically from 10% to about 50% of $R_{1\alpha}$+$R_{1\beta}$ and is different for the four anodes. The overall shift in shape of impedance spectra is the same for the four tested anodes, but does not occur the same day. In some spectra obtained after more than 400 h, the arc II at about 10 Hz is vaguely recognized.
The possibility of the arc denoted Iβ for Baker anodes actually being diffusion impedance outside the anode structure has been considered as follows. A gas diffusion resistance outside the anode structure of no more than 0.08 Ωcm^2 can be estimated from other measurements at 1000°C in 97% H_2 + 3% H_2O.[13] Gas diffusion limitation is slightly deactivated by temperature, ($R_D \propto T^2$). Therefore a value of 0.06 Ωcm^2 can be expected at 850°C in 97% H_2 + 3% H_2O. For the 1% H_2O gas used here, the diffusion resistance can at the most be expected to increase to 0.12 Ωcm^2. The observed magnitude of arc Iβ is 0.10 to 0.30 Ωcm^2. It is thus considered unlikely that the arc denoted Iβ is caused by diffusion impedance outside the electrode structure. This evaluation is supported by data on Matthey anodes in the same test configuration at 850°C where no such arc Iβ is observed, see below.

Matthey anodes at 850°C, Figure 9.3, start out with one dominant arc I with f_S in the kHz range, and a well-defined arc II with an f_S of about 10 Hz. After a few hundred hours the low frequency arc II is transferred into a low frequency inductive tail for a period, thereafter arc II is again present.
Matthey anodes at 1000°C, Figure 9.4, maintain two dominant arcs, one with f_S in the kHz range (I) and one with f_S below 100 Hz (II). This is a consistent feature of all impedance spectra, irrespective of the type of current collector structure (Matthey and Matthey graded). Very little change is observed in the shape of spectra over time.
The Matthey anode tested at 1050°C exhibits three distinct arcs, Figure 9.5. Again an arc I with f_S in the kHz range, a mid-frequency arc II with f_S at 10-100 Hz and a dominant arc III with f_S at about 1 Hz is observed. Again the shape of spectra is fairly constant.
In the impedance spectra of the thermally cycled Matthey anode, Figure 9.6, four arcs are recognized. Two poorly resolved arcs Iα and Iβ with f_S in the kHz range, and again arc II with f_S at about 10-100 Hz and arc III with f_S at 1 Hz. The overall shape of the spectra is constant.

For all anodes impedance data are fitted to the equivalent circuits given in Table 9.2 to the extent where the respective arc could be distinguished visually. In a first evaluation all the n-values are allowed to vary. In a second evaluation the n-values for diffusion (II), conversion (III), and artifact arcs are fixed to average values from the first evaluation. The n-values for the anode related arcs are running free. In a third evaluation all n-values are fixed at average values obtained in the second evaluation. The final n-values are given in Table 9.2. The use of these fixed average n-values is based on a need for a systematic interpretation of the high-frequency end of all impedance spectra, as elaborated in the discussion.

Table 9.2 List of tested anodes with information of setup geometry (see Figure 9.1), selected equivalent circuit in the notation of ref [42], and n-values in the final data fitting procedure for each anode. The given values of n_1 (or $n_{1\alpha}$, $n_{1\beta}$), n_2, n_3 and n_A are found as average values over the test period, and applied as fixed parameters in the third and last impedance fitting evaluation.

Anode	Setup	Equivalent Circuit	n_1, $n_{1\alpha}$, $n_{1\beta}$	n_2	n_3	n_A
A729	One-atm.	$LR_S(RQ)_{1\alpha}(RQ)_{1\beta} + (RQ)_2$ [#]	0.60, 0.95	0.90 [#]	-	-
A730		-"-	0.50, 0.95	0.90 [#]		
A731		-"-	0.75, 0.95	0.90 [#]		
A732		-"-	0.70, 0.95	0.90 [#]		
A733	One-atm.	$LR_S(RQ)_1 + (RQ)_2$ [#]	0.70	0.90 [#]	-	-
A734		-"-	0.65	0.90 [#]		
A735		-"-	0.75	0.90 [#]		
A736		-"-	0.70	0.90 [#]		
A627	One-atm.	$LR_S(RQ)_1(RC)_2(RQ)_A$	0.80	1.00	-	0.90
A628			0.80	1.00		0.90
A648	One-atm.	$LR_S(RQ)_1(RC)_2(RQ)_A$	0.75	1.00	-	0.90
A649			0.90	1.00		0.90
A582	Two-atm.	$LR_S(RQ)_1(RQ)_2(RC)_3$	0.80	0.75	1	-
A581	Two-atm.	$LR_S(RQ)_{1\alpha}(RQ)_{1\beta}(RQ)_2(RC)_3$	0.80, 0.80	0.75	1	-

[#] This subcircuit /value is only applied where the related arc is visually distinct.

The real part values for all anode related arcs (R_1 or $R_{1\alpha}$+$R_{1\beta}$) in durability tests are plotted against time after applying current in Figure 9.7 to Figure 9.10. The real part values for the two anode response arcs ($R_{1\alpha}$ and $R_{1\beta}$) in the thermal cycle test are plotted against cycle number in Figure 9.11. The ordinate scale in each figure is chosen to be the double of the average R_P value, in order to represent the anode stability in a comparable form. Events during test that might have affected anode performance are marked by dashed lines in the relevant figures. In general a small but systematic development in R_P is observed, and after some inconsistencies in the behavior during the first few hundred hours after applying current, the electrodes behave in a similar manner. Scatter of the order of 10 to 25% is observed in R_P for most tested anodes. For Matthey anode A735 at 850°C, Figure 9.8C, the scatter is 50%.

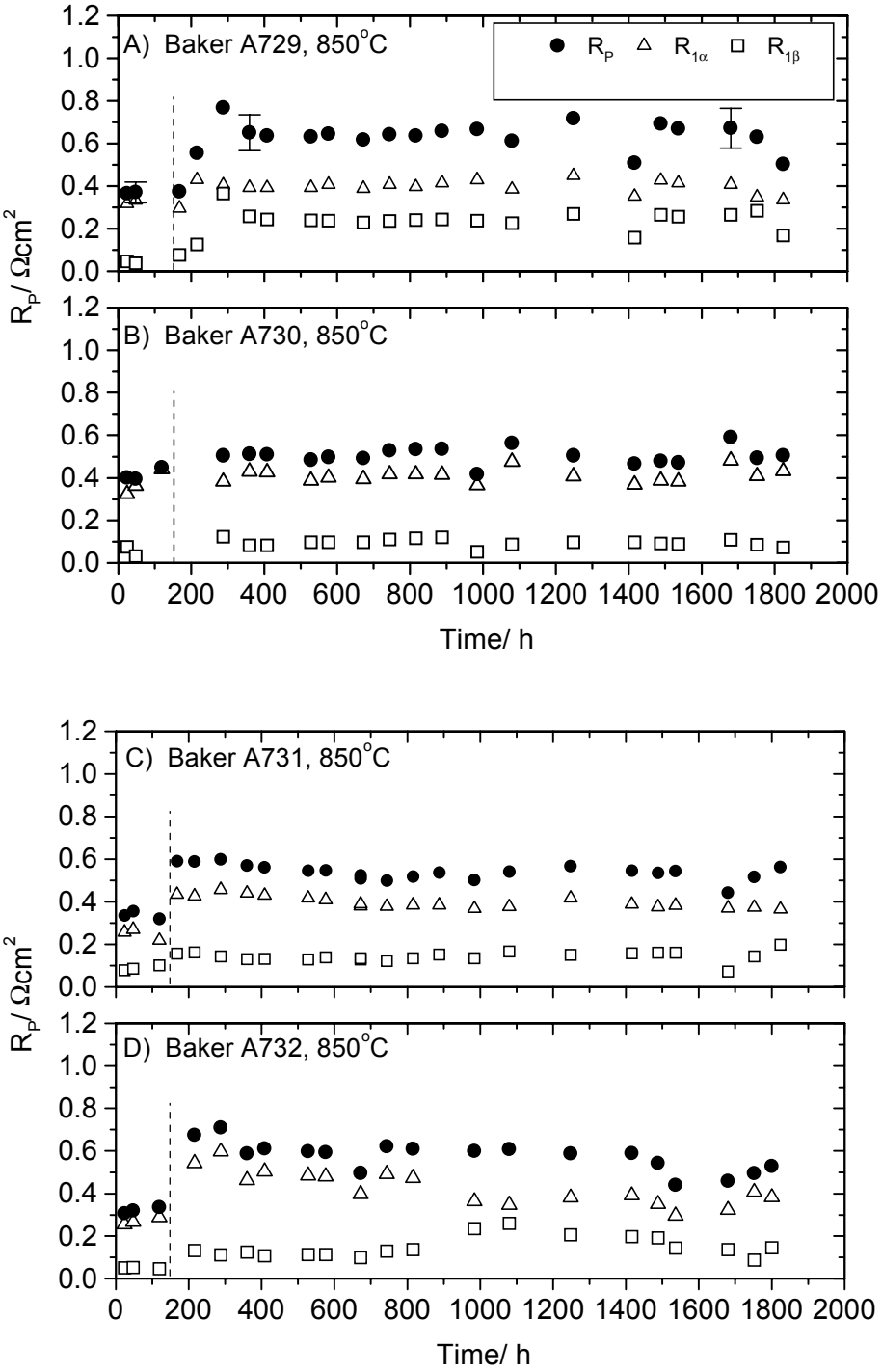

Figure 9.7 R_P for Baker anodes over time at 850°C and 300 mA cm^{-2} in hydrogen with 1% water. A) A729, B) A730, C) A731 and D) A732. $R_P = R_{1\alpha} + R_{1\beta}$ as obtained by fitting obtained impedance spectra to the selected equivalent circuit given in Table 9.2. The dashed line indicates a temporary shift to 9% H_2.

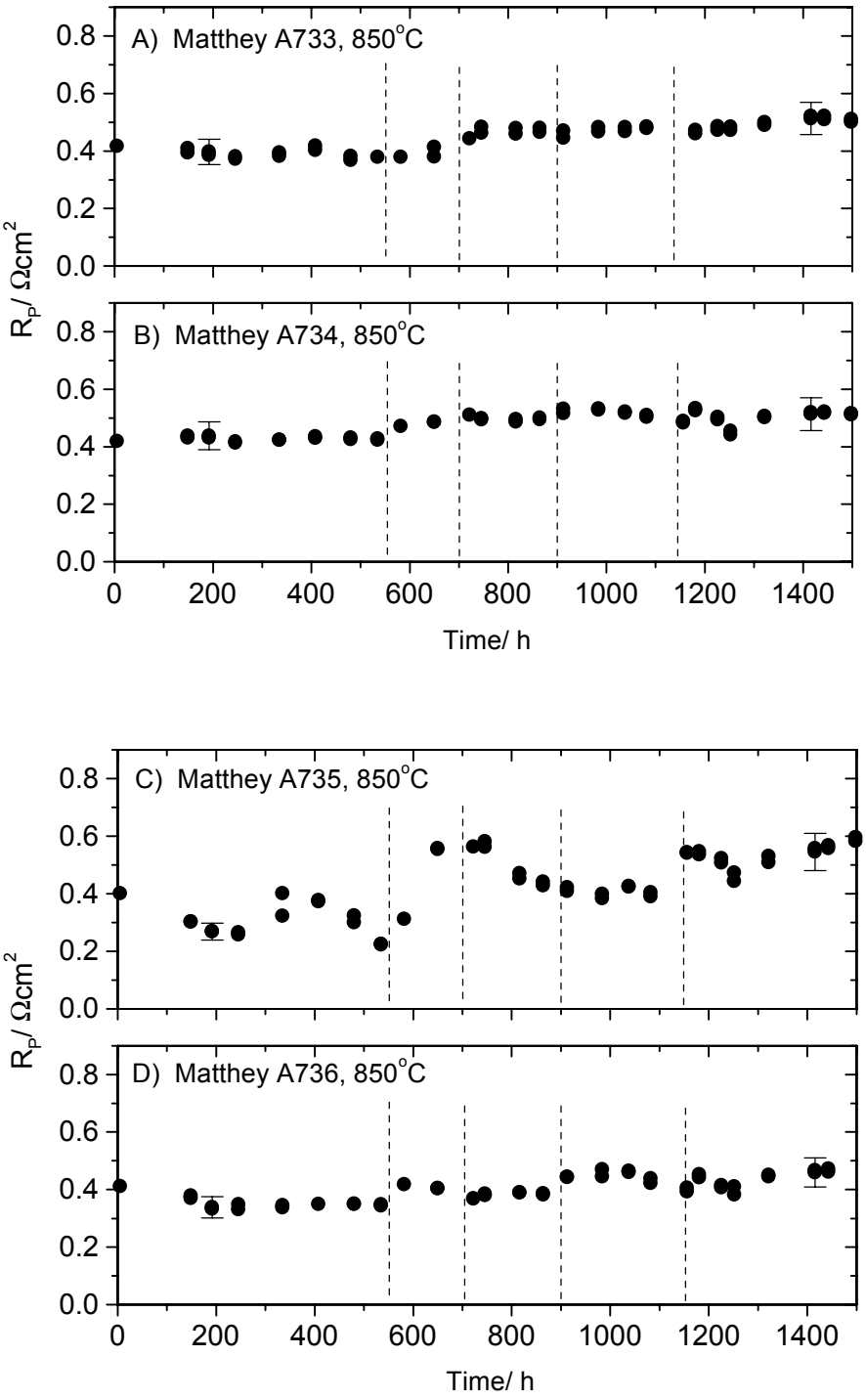

Figure 9.8 R_P for Matthey anodes over time at 850°C and 300 mA cm^{-2} in hydrogen with 3% water. A) A733, B) A734, C) A735 and D) A736. $R_P = R_1$ as obtained by fitting obtained impedance spectra to the selected equivalent circuit given in Table 9.2. The dashed lines indicate several temporary shifts to 9% H_2.

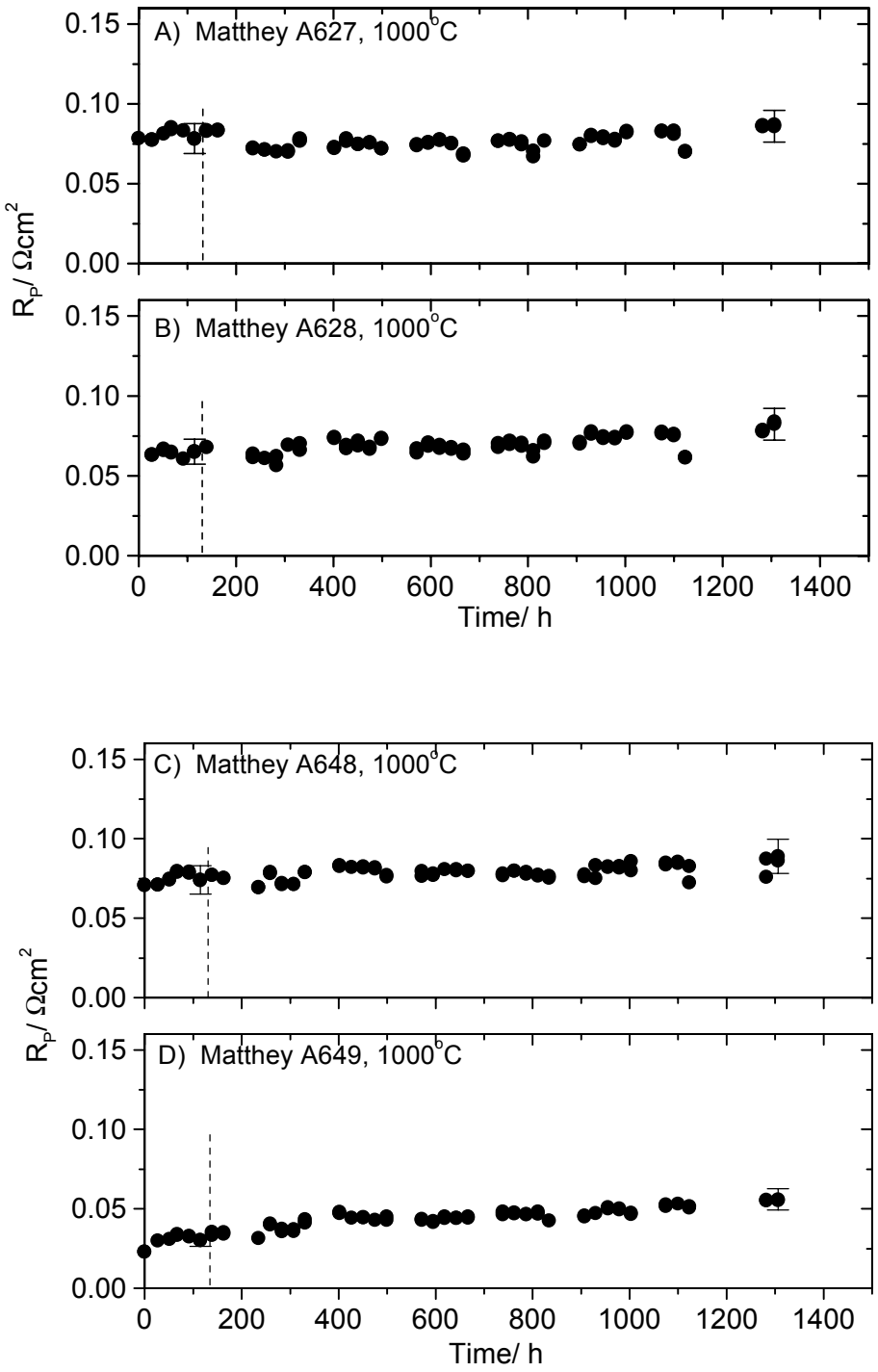

Figure 9.9 R_P for Matthey and Matthey graded anodes over time at 1000°C and 300 mA cm^{-2} in hydrogen with 3% water. A) A627 , B) A628, C) A648 (graded) and D) A649 (graded). $R_P = R_1$ as obtained by fitting obtained impedance spectra to the selected equivalent circuit given in Table 9.2. The dashed line indicates a temporary shift to 9% H_2.

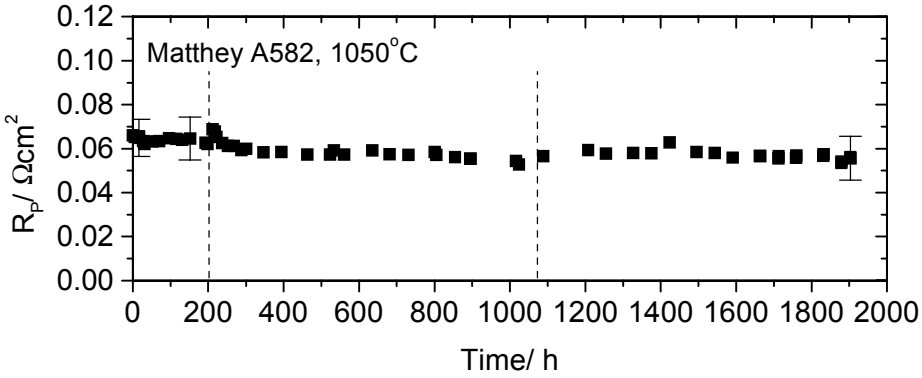

Figure 9.10 R_P for Matthey anode A582 over time at 1050°C and 300 mA cm^{-2} in hydrogen with 3% water. $R_P = R_1$ as obtained by fitting obtained impedance spectra to the selected equivalent circuit given in Table 9.2. The first dashed line indicates a temporary shift to 750°C, the second line indicates a permanent shift of pO_2, see Table 9.1.

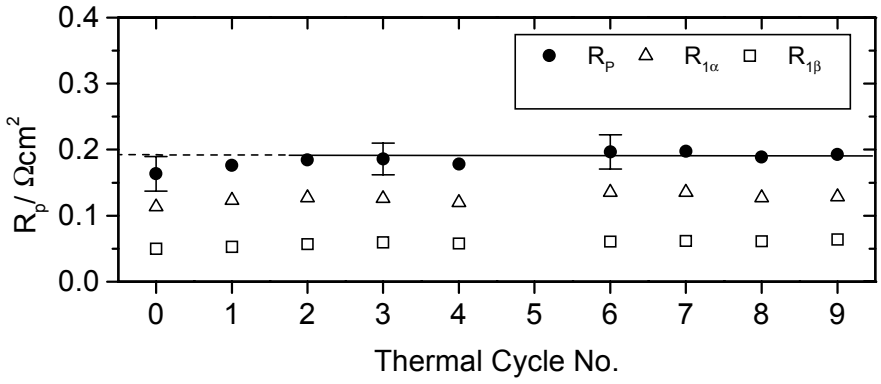

Figure 9.11 R_P by number of thermal cycles to 100°C for Matthey anode A581 as measured at OCV at 1000°C in hydrogen with 3% water. $R_P = R_{1\alpha} + R_{1\beta}$ as obtained by fitting obtained impedance spectra to the selected equivalent circuit given in Table 9.2.

Anodes were inspected after testing. The Matthey anodes appeared homogeneous when looking at the electrode surface, and the two-point in-plane resistance was about 1 to 1.5 Ω over 4 to 7 mm. The Baker anodes, however, appeared to have a well-defined central region with a slightly darker color covering about 1/3 of the working electrode area. The in-plane resistance was homogeneous over the working electrode surface and 50% lower than for Matthey anodes. Polished cross-sections of selected anodes and of reference anodes that were reduced for a short period (48 h) at 850°C and 1000°C were investigated using back-scattered electrons in LV-SEM. Although insufficient contrast was found between Ni and YSZ for digital separation of the substances, a difference in morphology was observed together with a small edge contrast that allowed the phases to be distinguished when observing the recorded images on screen. The Ni phase formed larger agglomerates encapsulating a number of YSZ particles when viewed in cross-section. This morphology was verified in optical microscopy. Typical structures are given in

Figure 9.12. The Matthey anodes exhibit larger Ni-agglomerates, whereas the Ni in Baker anodes is better distributed among the YSZ particles. This is consistent with the particle size distributions measured prior to electrode deposition. Furthermore the porosity in Baker anodes appears to be slightly lower than in Matthey anodes. No development in structure of the tested anodes is observed as compared with reduced (<48 h) reference anodes. For Baker anodes, a change in the electrolyte contacting the anode in the central part of the working electrode is observed, Figure 9.13. The first 5 μm of the electrolyte under the electrode contains fine pores and in some regions a brighter (denser) substance is concentrated in cracks. This region of the electrolyte is well defined against the underlying bulk electrolyte. No evidence of the Ni-mesh having collapsed to cause an increased diffusion limitation outside the anode structure was observed.

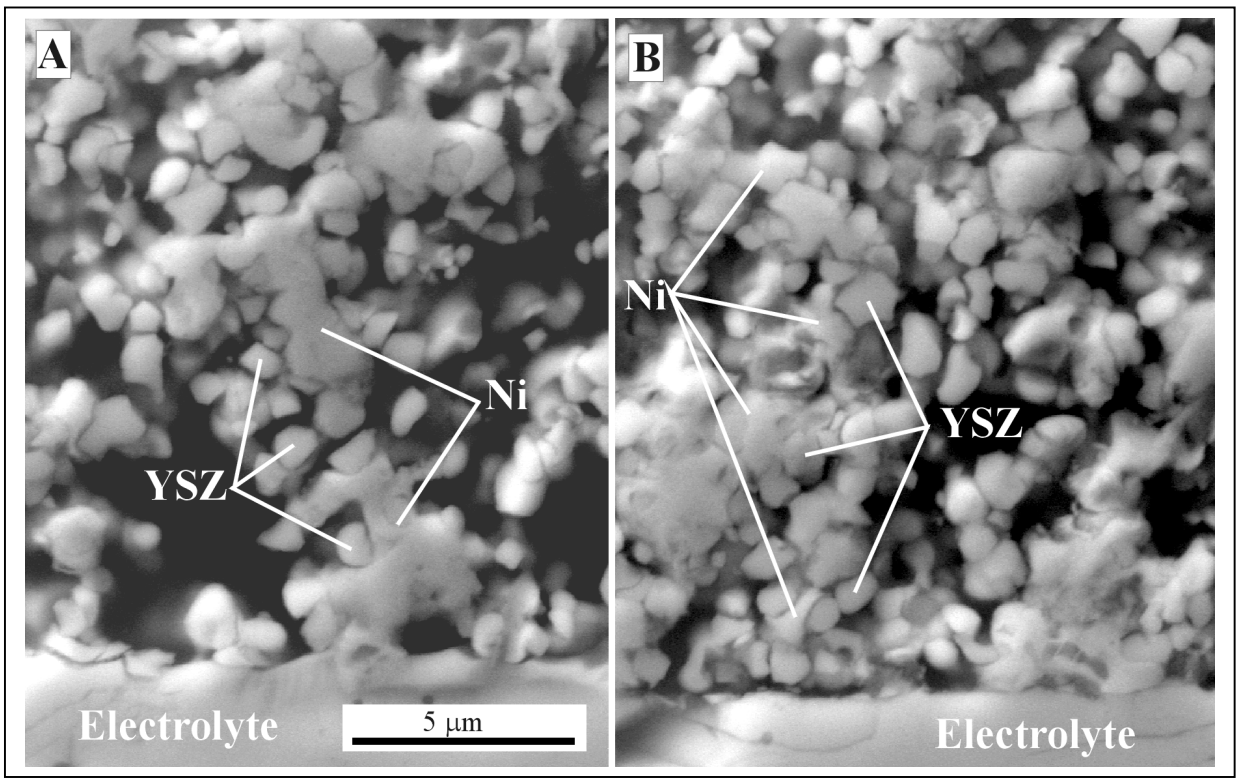

Figure 9.12 SEM images of polished cross-sections of anodes tested at 850°C. A) Matthey A736 and B) Baker A729. Images taken 1-2 mm from the edge of the electrode.

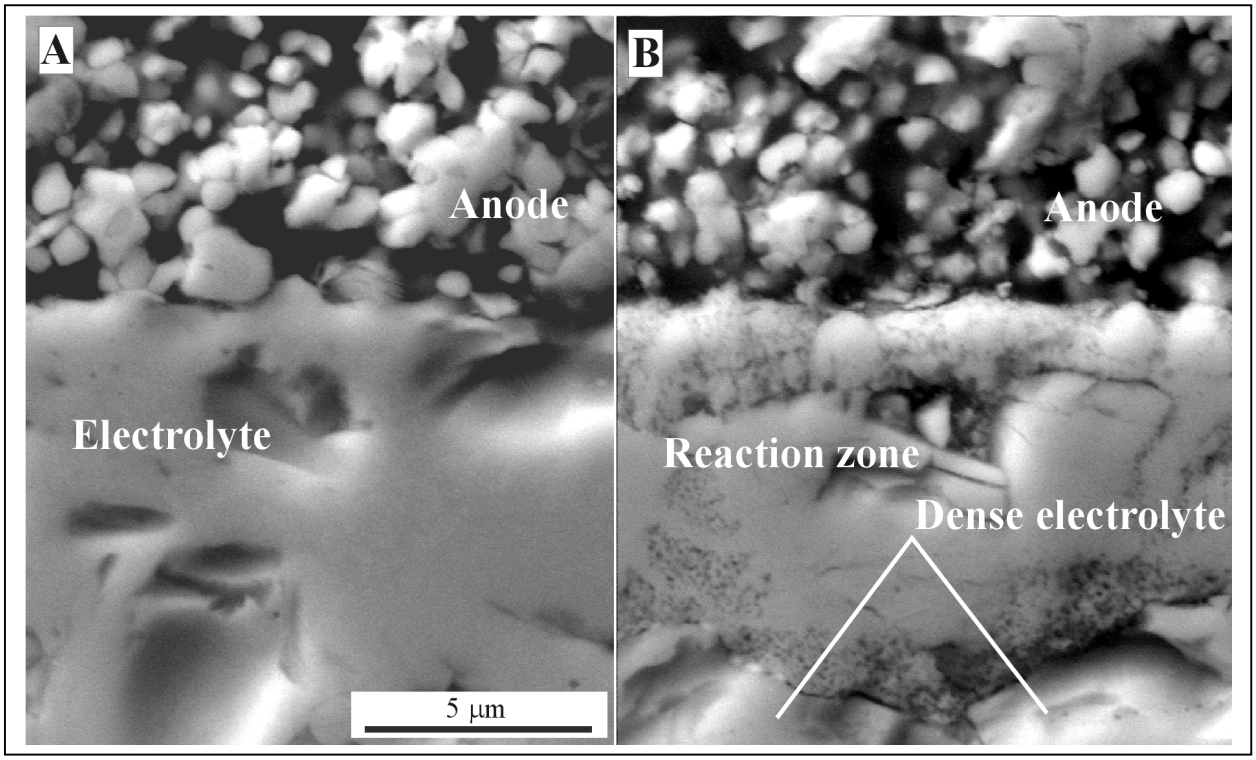

Figure 9.13 SEM images of polished cross-sections of Baker anode A729 showing the electrolyte in contact with the anode. A) Undamaged electrolyte 1-2 mm from the edge of the electrode, and B) damaged electrolyte in the central part of the electrode.

9.4 Discussion

9.4.1 Error Estimate

In the following the scatter in obtained R_P values is compared with an estimate of the uncertainty of determination.

Experimental conditions and limitations in the measurement technology influencing the determination of R_P comprises gas composition, temperature, level of quasi-equilibrium after interruption in the DC load, test cell geometry, instrument precision, quality of obtained impedance spectra and quality of the fit describing the spectra.

R_P of these anodes is known to be fairly insensitive to small changes in pH_2 and pH_2O.[43] No systematic shift in R_P is observed with the fluctuations in pO_2, Table 9.1, or the pO_2 shift in Figure 9.10. Fluctuations in test temperature as indicated in Table 9.1 will at the most cause a variation of 1.5% in R_P considering an activation energy of 0.8 eV.[43] Measurements showed that the variation in measured R_P after reconnecting cells when switching between current sources was less than 1%. The error introduced by the position of the reference electrode was taken to be 4% for R_P values below 0.2 Ωcm^2 and 3% above.[5]

The quality of obtained impedance spectra appears acceptable with respect to the signal/noise ratio, except at low frequencies above 850°C. This part of relevant impedance spectra is dominated by known mass transport processes rather than R_P.

The instrument precision is set by the potentiostat rather than by the impedance analyzer, and amounts to about 3% and 3° above 10 kHz for the real part and imaginary part, respectively.[45-48]

The absolute real part error on R_P is further enhanced by the rather high ratio of R_S/R_P for the used

electrolyte geometry as discussed elsewhere.[8] However, for repetitive measurements on an electrochemical cell with a fairly constant response, only the apparatus drift is relevant. The uncertainty on the imaginary part of high frequency impedance points is believed to reduce drastically by introduction of an unrestrained inductance L in the equivalent circuit. Furthermore, fitting data to an equivalent circuit with fixed n-values allows a majority of data-points with limited phase errors to "force" the shape of the high frequency part of the spectrum due to the unrestrained inductance. The possibility of impedance spectra having a shape at very high frequencies different from what is assumed here cannot be excluded, but no indications of such behavior is observed. In conclusion a combined instrument precision of about 5% with respect to R_P is estimated.

Based on the non-linear-least-squares fit made to the experimental data, an error estimate is offered by the fitting program for each parameter. The error on R_P is taken to be the combined errors on $R_{1\alpha}$ and $R_{1\beta}$ divided by 2, as they are strongly correlated in the relevant spectra. This error is determined for selected representative spectra, including the spectra of Figure 9.2 to Figure 9.6. For anodes tested at 850°C the error is less than 1% for Matthey anodes, and 2-3% for Baker anodes. For Matthey anodes tested at 1000°C the error amounts to 1-3%, at 1050°C 1-5% and for the thermal cycle test errors of 2-4% are found.

As an estimate of the overall uncertainty on the reported R_P values, the above contributions are combined to yield an error range of 12 to 17% for the examined spectra. These values are plotted as error-bars on the respective data-points in Figure 9.7 to Figure 9.11. Due to the 50% scatter observed in Figure 9.8C which exceeds the estimated uncertainty by a factor of 3, data on the Matthey anode A735 are not considered in the following.

9.4.2 Degradation Rates

In general a fairly linear development in R_P is observed over time in Figure 9.7 to Figure 9.10. Apparently, test circumstances such as small (factor of 2 to 3) permanent changes in pO_2 and temporary shift to 9% hydrogen does not inflict on R_P beyond the uncertainty on data. The temporary decrease of temperature to 750°C during the test at 1050°C, Figure 9.10, has a significant but temporary effect on R_P. For Baker anodes at 850°C, Figure 9.7A and B, the significant increase in R_P is seen not to coincide with the temporary shift to 9% hydrogen.
A linear fit is applied to R_P vs. time to provide an estimate of the degradation rate. Data for the first 200 h on Baker anodes and for the first 300 h on the Matthey anode tested at 1050°C are not included in the linear fit, as the behavior deviates from the otherwise linear variation with time. For a consistent and comparable estimate of the absolute and relative variation with time, the linear slopes are compared with the linear fit value extrapolated to 0 h, $R_{P(0h)}$, as given in Table 9.3. The Matthey anode tested at 1050°C indicate a slightly decreasing R_P over time, whereas Matthey anodes tested at 1000°C indicate an increase of about 10 mΩcm^2 per 1000 hrs. For the Matthey anodes tested at 850°C the increase is about 100 Ωcm^2 1000 hrs. However, these data are potentially affected by the four temporary shifts in the hydrogen partial pressure. Apparently the stability of Matthey anodes improve with increasing temperature.
There appears to be no effect on durability of applying a graded current collection on Matthey anodes. The Baker anodes exhibit decreasing R_P with time at 850°C. It should be noted that R_P is considerably higher for Baker anodes than for Matthey anodes at this temperature.

Table 9.3 Performance and durability of tested anodes as evaluated from impedance data corrected for concentration polarization outside the anode structure. The given data are obtained at 300 mA cm^{-2} and based on a linear fit over the indicated period of time. The change in polarization resistance, ΔR_P, is given absolute and relative to the linearly extrapolated R_P at 0 h, $R_{P(0\ h)}$.

Anode	Test temperature	Time range considered, h	$R_{P(0\ h)}$, $m\Omega cm^2$	ΔR_P, $m\Omega cm^2$/1000 h	ΔR_P, %/1000 h
A729	851±1°C	200-1800	690	-50±30	-7±4%
A730	-"-	-"-	500	0±20	0±4%
A731	-"-	-"-	570	-30±10	-5±2%
A732	-"-	-"-	670	-90±20	-13±3%
A733	851±2°C	0-1500	350	+110±10	+31±3%
A734	-"-	-"-	410	+80±10	+20±2%
A735[#]	-"-	-"-	-	-	-
A736	-"-	-"-	320	+100±10	+31±3%
A627	1004±1°C	0-1300	75	+3±2	+4±3%
A628	-"-	-"-	62	+11±2	+18±3%
A648	1004±1°C	-"-	74	+7±1	+9±1%
A649	-"-	-"-	34	+16±1	+47±3%
A582	1050±2°C	300-2000	59	-1±1	-2±2%

[#] Not evaluated due to poor data quality

Over the first two cycles of the thermal cycle test a degradation of 15 $m\Omega cm^2$ per cycle or 9% per cycle is observed. Still this is within the uncertainty of the data. A linear fit to the data-points from cycle 3 to cycle 9 of Figure 9.11 yields a constant performance within the experimental uncertainty. More cycles and samples are required to obtain conclusive data.

9.4.3 Degradation Mechanisms

The observed changes in the central part of an electrolyte under a Baker anode are presumably due to a solid state reaction which has not been identified. Under anodic load the atmosphere may contain substantial amounts of water in the central part of the electrode. The radial position of the electrolyte surface affected is suggested to relate to limitations in gas exchange caused by the method of electrode contacting. The gas access to and from the central part of the working electrode is restricted by diffusion in the approximately 3/4 mm wide gap defined by the Ni-mesh between the working electrode and the supporting Al_2O_3 plate. Furthermore the porosity of the Baker anode appears to be lower than that of the Matthey anode. Another important issue in this context is purity of the technical NiO powders. The effect of contaminants and additives on Ni/YSZ cermet anode performance and durability is unknown.

The influence of $Ni(OH)_2$ vapor transport is expected to be insignificant in the reported tests. At the given conditions (H_2/H_2O = 0.97/0.03) an $Ni(OH)_2$ vapor pressure of less than 10^{-12} atm at 850°C and about 10^{-9} atm at 1050°C is predicted.[24] At the same time the gas flow over the anode surface is limited in the present study, especially for the one-atmosphere setup.

The conductivity of sintered YSZ electrolyte exhibits a general degradation with time due to ordering of the oxide vacancies. Over a period of 2000 h in air this degradation amounts to about 30% at 1000°C, and 20% at 850°C, without reaching a stable value.[49] A comparable degradation of the bulk electrolyte conductivity can be observed from the R_S values indicated in the captions of Figure 9.2 to Figure 9.6. The fairly stable R_P values measured in the present work indicate that ionic resistance in the electrolyte phase of the cermet is not contributing significantly to R_P.

Ni rearrangement by surface diffusion has an activation energy of about 1 eV, causing the diffusion coefficient to be a factor of 4.5 higher at 1050°C than at 850°C. It is considered unlikely that the higher diffusion rate at 1050°C should cause the formation of a stable cermet structure in less that 100 h at 1050°C, and at the same time cause continuous changes over 1500 h at 850°C.

9.4.4 Recommendations

There appears to be significant variation in the durability of nominally identical anodes tested simultaneously. It is recommended that better statistics are obtained by testing several identical samples, preferably in a multi-cell setup.
With the inherent uncertainty on R_P, extrapolations in time are highly unreliable. Tests as performed in the present work are suggested to serve only as a qualification for starting anode durability tests of the order of 10.000 hours.

The selected test geometries are not considered ideal, and for future tests the following approach is recommended.
The low-frequency accuracy can be improved by avoiding concentration polarization (mass transport) outside the anode structure. In practice this is obtained by using an auxiliary electrode face-to-face in contact with the working electrode through a thin mesh, so that this electrode experiences the same current with opposite polarity.[13] Hereby the electrodes furnish reactants and removal of products for each other at a distance of the mesh thickness, provided the electrode reactions are reversible. This setup would also ensure a homogeneous gas access and current distribution for the working electrode. The conditions would then represent the expected conditions for an anode under a porous current collector rib or layer in a fuel cell stack. To establish representative conditions for the effect of $Ni(OH)_2$ vapor transport from "uncovered" anodes between contact ribs of a fuel cell stack, the gas transport conditions would have to be reproduced carefully in a cell setup.
To obtain better accuracy on the high-frequency impedance it is necessary to reduce the R_S/R_P ratio. No practical method has been convincingly demonstrated which does not involve increased errors due to a frequency-dependent current distribution.[5]
For the vapor transport both diffusion through stagnant gas and gas convection over the electrode are of importance. The latter is severely dependent on the final stack design, whereas the auxiliary electrode is dominated by short-distance diffusive flow.

Corroborative characterization methods are desirable. Of the suggested mechanisms contributing to a change of performance of Ni/YSZ cermet anodes over time, only Ni rearrangement and evaporation over extended time are expected to yield visible evidence. As the electrochemically active sites are within a distance of 10 μm from the electrolyte surface, a cross-section of the anode structure is needed for inspecting the geometry. The destructive inspection calls for comparison to a reference structure. This approach is considered prohibitive for examining small quantitative changes, whereas it may be suitable for qualitative characterization.

The characteristic distance of such anodes is of the order of 0.5 to 1 μm, but for two particles to loose electrical contact, a gap of a few Å is sufficient. No suitable imaging technique with this kind of resolution is available. The best option appears to be back-scattered electrons in a scanning electron microscope (SEM), where the practical 2-dimensional resolution is of the order of 0.1 μm. The penetration depth of electrons into the substances depend on the acceleration voltage and the materials density, but is often higher. However, the focal depth is much higher, leading to unrepresentative images for a porous electrode. Furthermore separation of the phases is complicated by the low contrast between Ni and YSZ due to the similar average atomic weights.

9.5 Summary

The durability of three types of Ni/YSZ cermet anodes based on two green NiO powders, denoted Baker and Matthey after the vendor, are investigated. The polarization resistance, R_P, of Ni/YSZ cermet anodes at 300 mA cm^{-2} in hydrogen with 1 or 3% water has been monitored over periods of 1300 to 2000 h in the temperature range 850°C to 1050°C. After an initial period of 0 to 300 h R_P is established to vary linearly with time.

Matthey anodes tested at temperatures from 850 to 1050°C exhibit no significant degradation at 1050°C, whereas degradation rates of 10 mΩcm^2 per 1000 hrs are noted for anodes tested at 1000°C. Data for anodes tested at 850°C indicate even higher degradation rates. However, data at 850°C are encumbered with uncertainty due to several unintended temporary changes of atmosphere, as a safety system has switched from hydrogen to 9% hydrogen in nitrogen.

A Matthey anode tested in 9 thermal cycles from 1000°C to below 100°C exhibit a degradation of about 15 mΩcm^2 per cycle or 9% per cycle over the first 2 cycles, hereafter R_P is constant within the experimental uncertainty.

Baker anodes exhibit decreasing R_P over time, but the values of R_P are a factor of 2 higher than for Matthey anodes. A reaction zone is detected in the underlying electrolyte in the central region of the working electrode where the gas access is limited. The possible reaction product and the cause of reaction have not been established.

Acknowledgment

This work was supported by the European Commission under contract no. JOE3-CT95-0005. Discussions with Dr. N. Bonanos and Dr. P. V. Hendriksen, Risø, are appreciated. The presented experimental data were generated as a result of the joint effort of many members of the SOFC project group at Risø. Their contributions are gratefully acknowledged.

References

[1] M. Ippommatsu, H. Sasaki and S. Otoshi, *Int. J. Hydrogen Energy*, **21** 129 (1996)

[2] C. Bagger, N. Christiansen, P. V. Hendriksen, E. J. Jensen, S. S. Larsen and M. Mogensen, in *High Temperature Electrochemistry: Ceramics and Metals*, F. W. Poulsen, N. Bonanos, S. Linderoth, M. Mogensen and B. Zachau-Chistiansen, Editors, 17th Risø International Symposium on Materials Science, Roskilde, DK. 167 (1996)

[3] S. P. S. Badwal and K. Foger, *Materials Forum* **21** 187 (1997)

[4] M. Nagata, Y. Ito and H. Iwahara, *Solid State Ionics* **67** 215 (1997)

[5] J. Winkler, P.V. Hendriksen, N. Bonanos and M. Mogensen, *J. Electrochem Soc*. **145** 1184 (1998)

[6] G. Reinhardt and W. Göpel, in *Third Int. Symp. on Ionic and Mixed Conducting Ceramics*, **PV 97-24**, The Electrochemical Society Proceedings Series, Pennington, NJ. 610 (1998)

[7] S. Primdahl and P. V. Hendriksen, in *High Temperature Electrochemistry: Ceramics and Metals*, F. W. Poulsen, N. Bonanos, S. Linderoth, M. Mogensen and B. Zachau-Chistiansen, Editors, 17th Risø International Symposium on Materials Science, Roskilde, DK. 403 (1996), chapter 2 in this thesis

[8] M. J. Jørgensen, S. Primdahl and M. Mogensen, *Electrochim. Acta*, in press (1999)

[9] M. Nagata and H. Iwahara, *J. Appl. Electrochem*. **42** 275 (1993)

[10] T. Kawada, B. A. van Hassel, T. Horita, N. Sakai, H. Yokokawa and M. Dokiya, *Solid State Ionics* **70/71** 65 (1994)

[11] S. Primdahl and M. Mogensen, in *SOFC V*, U. Stimming, S.C. Singhal, H. Tagawa and W. Lehnert, Editors, **PV 97-40**, The Electrochemical Society Proceedings Series, Pennington, NJ. 530 (1997)

[12] S. Primdahl and M. Mogensen, *J. Electrochem. Soc.* **145** 2431 (1998), chapter 4 in this thesis

[13] S. Primdahl and M. Mogensen, *J. Electrochem. Soc.* in press (1999), chapter 5 in this thesis

[14] N. Nakagawa, H. Sakurai, K. Kondo, T. Morimoto, K. Hatanaka and K. Kato, *J. Electrochem. Soc.* **142** 3474 (1995)

[15] K.-Z. Fung and A. V. Virkar, in *SOFC IV*, M. Dokiya, O. Yamamoto, H. Tagawa and S. C. Singhal, Editors, **PV 95-1**, The Electrochemical Society Proceedings Series, Pennington, NJ. 1105 (1995)

[16] J. Mizusaki, H. Tagawa, T. Saito, K. Kamitani, T. Yamamura, K. Hirano, S. Ehara, T. Takagi, T. Hikita, M. Ippommatsu, S. Nakagawa and K. Hashimoto, *J. Electrochem. Soc.* **141** 2129 (1994)

[17] T. Norby, P. A. Osborg and H. Ræder, in *First European SOFC Forum*, U. Bossel, Editor, European SOFC Forum, Oberrohrdorf, CH. 671 (1994)

[18] A. C. Khandkar, S. Elangovan, M. Liu and M. Timper, in *High Temperature Electrode Materials and Characterization*, D. D. Macdonald and A. C. Khandkar, Editors, **PV 91-6**, The Electrochemical Society Proceedings Series, Pennington, NJ. 175 (1991)

[19] P. H. Middleton, M. E. Seiersten and B. C. H. Steele, in *SOFC I*, S. C. Singhal, Editor, **PV 89-11**, The Electrochemical Society Proceedings Series, Pennington, NJ. 90 (1989)

[20] M. Mogensen and S. Skaarup, *Solid State Ionics,* **86-88** 1151 (1996)

[21] M. M. Murphy, J. Van herle, A. J. McEvoy and K. R. Thampi, *J. Electrochem. Soc.* **141** L94 (1994)

[22] P. Nikolopoulos and D. Sotiropoulou, *J. Mat. Sci. Let*. **6** 1429 (1996)

[23] A. Tsoga, A. Naoumidis and P. Nikolopoulos, *Acta Mater*. **44** 3679 (1996)

[24] A. Gubner, H. Landes, J. Metzger, H. Seeg and R. Stübner, in *SOFC V*, U. Stimming, S. C. Singhal, H. Tagawa and W. Lehnert, Editors, **PV 97-40**, The Electrochemical Society Proceedings Series, Pennington, NJ. 844 (1997)

[25] R. J. Aaberg, R. Tunold, M. Mogensen, R. W. Berg and R. Ødegård, *J. Electrochem. Soc.* **145** 2245 (1997)

[26] M. Brown, S. Primdahl and M. Mogensen, *J. Electrochem. Soc*. submitted (1999), chapter 6 in this thesis

[27] S. Sakamoto, H. Taria and H. Takagi, *Denki Kagaku*, **64** 609 (1996)

[28] S. P. S. Badwal, *Solid State Ionics*, **52** 23 (1992)

[29] T. Fukui, S. Ohara and K. Mukai, *Electrochem. Solid-State Let.* **1** 120 (1998)

[30] C. J. Spengler and R. J. Urka, US patent 4,849,254 (1989)

[31] S. C. Singhal, In *SOFC V*, U. Stimming, S. C. Singhal, H. Tagawa and W. Lehnert, Editors, **PV 97-40**, The Electrochemical Society Proceedings Series, Pennington, NJ. 37 (1997)
[32] H. J. Beie, L. Blum, W. Drenckhahn, H. Greiner and H. Schisschl, in Proceedings of the *Third European SOFC Forum*, P. Stevens, Editor, European SOFC Forum, Oberrohrdorf, CH. 3 (1998)
[33] W. Schäfer, H. Geier, G. Lindemann and D. Stolten, in *High Temperature Electrochemical Behaviour of Fast Ion and Mixed Conductors*, F. W. Poulsen, J. J. Bentzen, T. Jacobsen , E. Skou and M. J. L. Østergård, Editors, 14th Risø International Symposium on Materials Science, Roskilde, DK. 409 (1993)
[34] L. Kinderman, F. W. Poulsen and C. Bagger, in *Proceedings of the Third European SOFC Forum, Poster section*, P. Stevens, Editor, European SOFC Forum, Oberrohrdorf, CH. 133 (1998)
[35] T. Iwata, *J. Electrochem. Soc*. **143** 1521 (1996)
[36] R. Männer, E. Ivers-Tiffée and W. Wersing, in *SOFC II*, F. Grosz, P. Zegers, S. C. Singhal and O. Yamamoto, Editors, Commission of the European Communities, Luxemburg, L. EUR-13564-EN. 715 (1991)
[37] M. Mori, T. Yamamoto, H. Itoh, H. Inaba and H. Tagawa, *J. Electrochem. Soc.* **145** 1374 (1998)
[38] S. Primdahl, B. F. Sørensen and M. Mogensen, *J. Am. Ceram. Soc.* submitted (1998), chapter 7 in this thesis
[39] O. H. Krikorian, UCRL-6132 (1960)
[40] C. Bagger, In *1992 Fuel Cell Seminar*, Courtesy Associates, Inc. Washington, DC. 241 (1992)
[41] R. Hartung and H.-H. Möbius, *Chemie-Ing. Techn*. **40** 592 (1968)
[42] B. A. Boukamp, *Solid State Ionics*, **20** 31 (1986)
[43] S. Primdahl and M. Mogensen, *J. Electrochem. Soc.* **144** 3409 (1997), chapter 3 in this thesis
[44] F. Z. Mohamedi-Boulenouar, J. Guindet and A. Hammou, in *SOFC V*, U. Stimming, S. C. Singhal, H. Tagawa and W. Lehnert, Editors, **PV 97-40**, The Electrochemical Society Proceedings Series, Pennington, NJ. 441 (1997)
[45] 1286 Electrochemical Interface Operating Manual, Issue 3, Solartron, Farnborough, UK. (1985)
[46] SI1287 Electrochemical Interface User Guide, Issue AC, Solartron, Farnborough, UK. (1994)
[47] 1250 Frequency Response Analyser Operating Manual, Issue 6, Solartron, Farnborough, UK. (1985)
[48] 1260 Impedance Gain-Phase Analyzer Operating Manual, Issue CB, Solartron, Farnborough, UK. (1996)
[49] C.C. Appel, N. Bonanos, A. Horsewell and S. Linderoth, in preparation

Chapter 10

A Review on the H_2/H_2O/Ni/YSZ Electrode

Abstract

The properties and limitations of Ni/yttria doped zirconia (YSZ) cermets for use as anode in solid oxide fuel cells (SOFC) are discussed. The possibility of the electrode reaction to occur on surfaces along the triple phase boundary (TPB) line is discussed with respect to attainable current densities by diffusion of species in and on the solid materials. Experimental data indicate that the Ni-surface is host to formation of protons, and that at 700 to 850°C these protons are participating in the rate limiting reaction. The YSZ surface provides oxide ions from the bulk electrolyte. The site of water formation is still unknown. Besides the simple TPB line with adjacent surfaces, the limitations introduced by two physical modifications of the system are discussed. One is the presence of discrete Ni-particles on the YSZ surface along the TPB, the other is segregation of an Y_2O_3-rich phase to the surface of the YSZ.

The technical aspects of making Ni/YSZ cermet are discussed with focus on structures fabricated by sintering of layers produced by wet-ceramic processes. High performance and low degradation rates have been observed.

10.1 Introduction

A Ni/yttria-stabilized zirconia (YSZ) cermet is considered as the anode for solid oxide fuel cells (SOFC) in a number of development programs.[1-4] The advantages of using Ni include low cost, low reactivity towards YSZ, excellent catalytic capabilities, and high attainable performance.
This choice of material must be seen in spite of a number of important drawbacks related to the use of the metal Ni. Ni has a higher thermal expansion coefficient (TEC) than the electrolyte material, causing stress in sintered components, and a large volume expansion associated with oxidation. Ni also reacts to form a volatile hydroxide in water rich atmospheres at SOFC operation temperatures, and has a limited compatibility with operation in CH_4 due to excessive catalytic properties for endothermic steam reforming and carbon deposition.

Despite these weaknesses of Ni in the SOFC anode, no other material with better overall properties has been identified. The metals considered are often less efficient and more expensive, and only noble metals do not react with oxygen to cause a volume change on reduction and oxidation (redox) cycles. Ceramics such as doped ceria and chromites with mixed conductivity have been investigated as an alternative. The redox volume stability is acceptable, but stability, reactivity and performance typically need further development.

The purpose of this chapter is to review the available information on i) the electrode reaction limitations in Ni/YSZ electrodes operated in H_2/H_2O at 700 to 1000°C, ii) relevant properties of the involved materials, iii) trends in reported electrochemical studies and finally iv) technical aspects of Ni/YSZ cermet fabrication with an emphasis on anode production involving sintering in air before operation.

10.2 The Reaction Sites

In the following section the possible location and nature of the hydrogen oxidation reaction on Ni/YSZ anodes is discussed on the basis of Eq. (10.1).

$$H_{2\,(g)} + O^{2-}_{\text{(electrolyte)}} \Leftrightarrow H_2O_{\text{(gas)}} + 2e^-_{\text{(electrode)}} \qquad (10.1)$$

A simple Ni-grain contact on a yttria-stabilized zirconia electrolyte surface under an atmosphere of H_2/H_2O is considered, constituting a solid interface (Ni/YSZ) and two surfaces (Ni and YSZ), meeting at a triple phase boundary (TPB) line, Figure 10.1. On the basis of literature probable reaction paths and mechanisms are discussed.

Looking at Figure 10.1, it is clear that water formation can occur within, say, an atomic distance from the TPB line, where oxide ions are available from the electrolyte surface, electrons can escape through the Ni, and hydrogen and water have direct access from and to the gas. This simple model is based on the primary charge carriers or molecular species in each of the three phases defining the reaction site.

It is, however, unlikely that the water formation reaction in practice is restricted to this one-dimensional line. If transport of reactants, intermediates or products occur at any rate on surfaces or in bulk, a broadening of the reaction line to a reaction zone on one or both surfaces is possible.

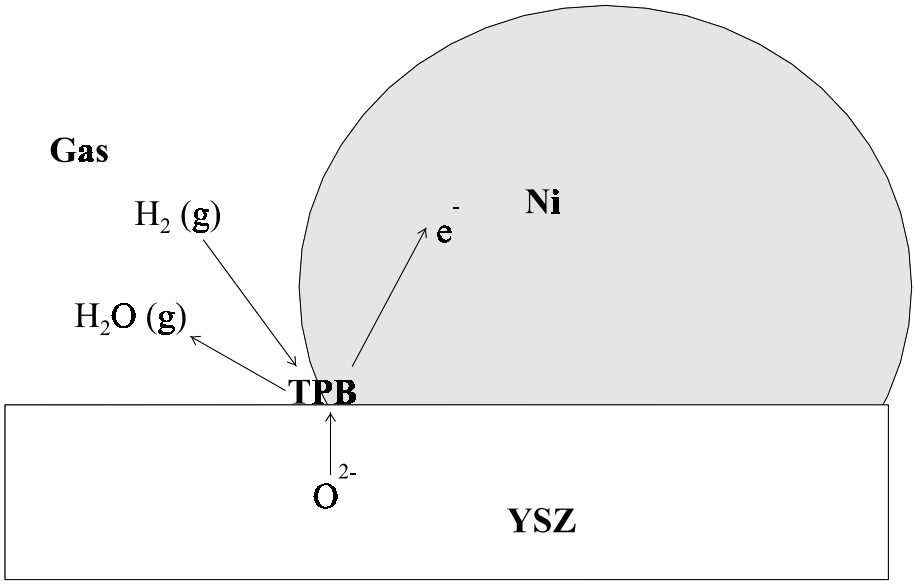

Figure 10.1 Simple Contact of Ni on YSZ forming a solid interface, two surfaces and a triple phase boundary (TPB) line.

A number of reaction schemes for the hydrogen oxidation reaction may be suggested. Taking on the general discussion of these reaction paths, a division into Ni and YSZ as the material on or in which the water formation reaction takes place is convenient. Only the species H_2, H^+, O^{2-}, OH^-, and H_2O are considered.
The transport properties of these known species are compared in the following paragraphs on the basis of limiting current for a simple transport geometry at selected temperatures. Reported solubility c, diffusion coefficient D and conductivity σ for the considered species are listed in Table 10.1 and Table 10.2. Where parameters are not directly obtainable, the Nernst-Einstein relation, (10.2), is applied. Here z_j is the species charge, e is the elementary charge, N_A the Avogadro constant and R and T retain their usual meaning.

$$\sigma = \frac{Dc(zeN_A)^2}{RT} \tag{10.2}$$

The limiting current i expected for diffusion transport in a linear gradient Δc of each species can be estimated,[5] using Eq. (10.3). Here F is the Faraday number and δ the distance of diffusion set to 0.5 µm. When bulk transport is considered Δc is set equal to 10% of the saturation concentration. In the case of limiting transport on nickel and YSZ surfaces each Ni or O atom in the surface is considered as a site. Again 10% is used as the surface concentration gradient. The assumption of a linear diffusion gradient is applied under the criterion $10(Dt)^{1/2}>\delta$. With the given δ and $t = 10^{-3}$ s equal to the typical relaxation time for limiting processes measured by impedance spectroscopy (see Table 10.3 later), this criterion equals $D>2.5\times10^{-8}$ cm^2/s.

$$i = \frac{zFD\Delta c}{\delta} \tag{10.3}$$

10.2.1 Ni as Site for Water Formation

Here only pure Ni is considered, as the solubility of ZrO_2 and Y_2O_3 in Ni has been found to be below the detection limit.[6] For the Ni-surface a number of transport steps and reactions are suggested to apply, Figure 10.2.[7]

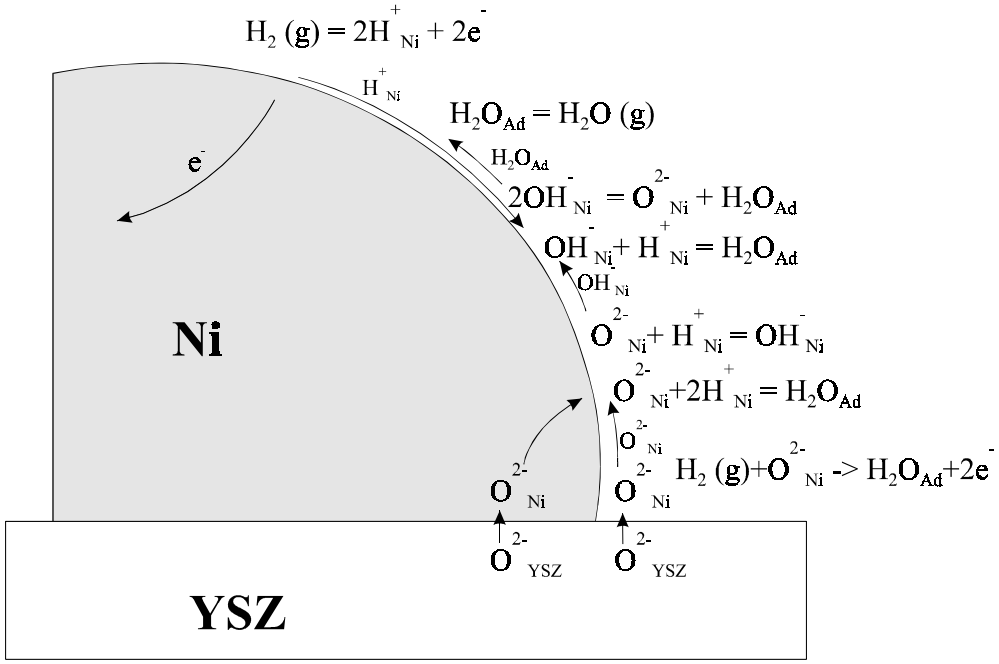

Figure 10.2 Reactions expected to be able to occur in competition on the Ni surface or possibly in the Ni bulk.

The criterion of a linear concentration gradient in the diffusion zone is fulfilled for all considered species in and on Ni. As the electronic conductivity of metallic Ni is much larger than the charge transport by any other charge carrier, it is not considered a relevant limitation in the following.

Ni is an important catalyst for a number of chemical processes involving bond breaking.[8] Hydrogen is assumed to adsorb dissociatively on the Ni surface, the process is known to be non-activated.[14] Here the adsorbed and absorbed hydrogen is taken to be present as "free" protons at and inside the electron cloud. By "free" is meant "with high mobility", not in any way a nuclei without a countercharge (electron) in the vicinity. This perception is justified by the following arguments. Even though there is a substantial overlap between the H 1s orbital and the Ni conduction band (a characteristic feature of a strong covalent bond), the mobility of hydrogen is very high as evidenced by the surface diffusion coefficient (see Table 10.1). Hydrogen absorbed (dissolved) in Ni releases its electron to the Ni conduction band, which is modified somewhat due to the presence of H.[9] Thus, after the dissociative adsorption of hydrogen molecules, the electrons of the H atoms are more or less incorporated in the Ni electron band, *and this is the final destination of electrons from the hydrogen oxidation reaction.*

Protons are available in great numbers on the multifaceted Ni-surface at SOFC relevant temperatures.[14,10] The surface coverage θ on a selected crystal surface of Ni is given in Figure 10.3. The obtainable current densities by proton transport as indicated in Table 10.1 are very

large, and thus not expected to constitute a limitation. Surface transport of protons is orders of magnitude higher than bulk diffusion.

Table 10.1 Transport of species by diffusion in or on metallic Ni

Species	Data	*i* at 850°C, #	*i* at 1000°C, #
H^+	$[c]=4.7\times10^{-4}(\text{mol/cm}^3\text{atm}^{1/2})\times \exp(-0.18\text{eV/kT})p\text{H}_2^{1/2}$. [11] $[c]=3.9\times10^{-4}(\text{mol/cm}^3\text{atm}^{1/2})\times \exp(-0.16\text{eV/kT})p\text{H}_2^{1/2}$. [12] $D=6.9\times10^{-3}(\text{cm}^2/\text{s})\exp(-0.42\text{eV/kT})$. [13] $\sigma=3.6\times10^{3}(\text{SK/cmatm}^{1/2})\times \exp(-0.6\text{eV/kT})p\text{H}_2^{1/2}/\text{T}$ ¤	1×10^0A/cm^2	2×10^0 A/cm^2
H^+,surface	$D=0.0025(\text{cm}^2/\text{s})\exp(-0.15\text{eV/kT})$. [14] $[c_{sites}]=0.284$ mol/cm^2 & θ, see Figure 10.3	1×10^4A/cm	8×10^3A/cm
e^-	$\sigma=2.59\times10^8$ S/cm @ 900K. [15] *weak temp. coeff.* *equal* to 0.06±0.001eV. [16] $\sigma=1.2\times10^8(\text{S/cm})\exp(0.06\text{eV/kT})$ ¤	4×10^{10} A/cm^2	4×10^{10}A/cm^2
O^{2-}	$[c]=0.021(\text{a/o})\exp(0.1\text{eV/kT})$. [22] *D,* σ has not been found	?	?
O^{2-}, surface	?	?	?
Ni,surface	$D=0.014(\text{cm}^2/\text{s})\exp(-0.97\text{eV/kT})$. [14] $[c]=0.284$ mol/cm^2 &	3×10^1 A/cm	1×10^2 A/cm

pH_2=0.97 atm, pH_2O=0.03 atm.
¤ Calculated on the basis of data quoted
& Ni-surface, 8.90 g/cm^3, 58.69 g/mol, cubic lattice

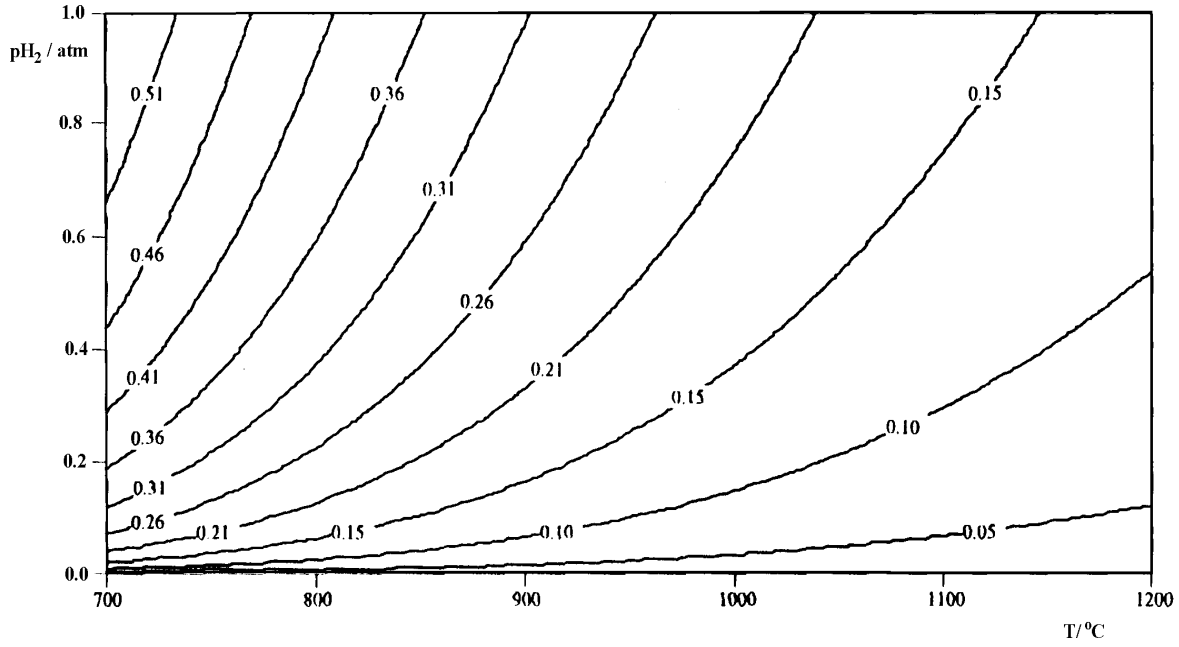

Figure 10.3 Surface coverage θ of protons on Ni(110) as function of T and pH_2.[14]

The surface self-diffusion coefficient for Ni is quite high, and the "current density" obtained by assigning one elemental charge to mobile Ni atoms of the surface is found to be comparable with that of the surface protons. These values are suggested to indicate that the Ni-surface consists of highly mobile Ni atoms and protons behaving as a two-dimensional, reactive gas.

Formation of water on the Ni surface requires oxide ions or hydroxide groups from the electrolyte to transfer onto the Ni surface, or to be transported through the Ni-lattice. Data on the transport of oxide ions in and in particular on Ni have not been found. This kind of data could directly indicate whether the water-formation reaction can at all occur on the Ni-surface at any distance from the TPB.

The relevant operation conditions for SOFC anodes are at a pO_2 lower than the equilibrium pO_2 of the Ni $+½O_2$=NiO reaction (about 10^{-10} atm. at 1000°C, and about 10^{-13} atm. at 850°C).[17] A direct anodic reaction on the Ni-surface between molecular hydrogen gas and adsorbed oxide ions has been suggested.[18] Oxide ions on Ni would probably be a short-life reactive species, as it has been demonstrated that no NiO film on the Ni-surface below the equilibrium potential can be demonstrated.[19] These observations are taken to indicate that if the water formation reaction occurs on Ni, then the transfer and transport of O^{2-} or OH^- might be rate limiting. At higher pO_2 approaching that of the Ni-NiO equilibrium NiO as an intermediate has been suggested.[20,21]

Bonding between hydroxide ions and Ni is evaluated to have an adsorption energy of about 3.8 eV, and makes dissociative water adsorption on Ni an exothermic process.[23] The considered temperature range is not stated, but it is believed to be below 100°C. If oxide ions are assumed to be able to transfer from the electrolyte to the Ni-phase, then diffusive transport of oxide ions or hydroxide groups may be relevant to consider.

Assisting transport of oxide ions from the YSZ to the Ni may occur over the solids interface where the succeeding transport steps occur in the Ni bulk. However, oxide ions are assumed not to be very mobile in bulk Ni, no references on this have been found. The oxide ion is too large for interstitial and lattice movement in metallic Ni, however, a solubility of 0.05 to 0.07 a/o O in Ni has been reported.[22] The concentration of hydroxide ions and water in the Ni lattice is assumed to constitute part of the reported oxygen solubility. Transport properties of hydroxide or water in Ni have not been found.

Water adsorption/desorption on Ni has an activation energy of 0.43-0.52 eV below room temperature.[23,24] A dependence of anodic current on water partial pressure, pH_2O^1, should be observed if the desorption step is rate limiting, this is not the case (see later).

All of the reactions indicated in Figure 10.2 could occur in the bulk material as well as on the surface. However, the high obtainable currents suggest the protons on the surface to prevail.

Extrapolation of low-temperature data on the hydrogen oxidation to SOFC relevant temperatures has been suggested in general to indicate that chemical steps are not an important limitation and therefore should hardly be detectable.[5]

10.2.2 YSZ as Site for Water Formation

A likely site for water formation is on the surface of the electrolyte near the TPB. Using a simple argument of atomic mass in relation to mobility, it has been suggested that the dominant charge transport across the TPB occurs by protons rather than by oxide ions.[5] A number of potential reaction paths and steps as suggested and discussed previously by others are given in Figure 10.4.[5,25-28]

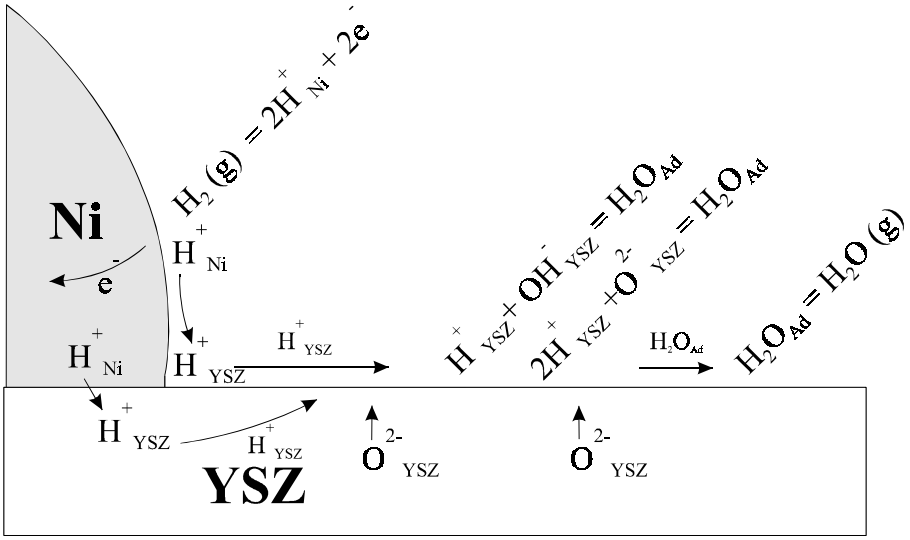

Figure 10.4 Reactions expected to be able to occur in competition on the YSZ surface.

The cubic YSZ surface is predominantly formed by oxide ions, and the bulk conductivity is fairly well known, the value at 1000°C is about 0.12-0.20 S/cm.[29-34] Impurities are expected to affect both transport by diffusion and catalytic properties in general.
The oxide ion conductivity of YSZ increases with yttria doping and exhibits a maximum at about 8-10 mol% Y_2O_3. The observed decline at higher concentrations has been suggested to be related to segregation of Y_2O_3 to the grain boundaries and trapping of oxide vacancies at Y-enriched grain boundaries in addition to the generally increased dopant-vacancy interaction.[35,33]
Trapping of vacancies at impurities has been observed to lower the oxide ion conductivity, especially by species such as Ce and Ti having ionic radii that deviate substantially from that of the host.[36] Typical levels of impurities in commercial YSZ have been summarized.[30] Segregation of Si^{4+} and di- and trivalent contaminants to the grain boundaries occurs in tetragonal and cubic YSZ. [6,37-40] Grain boundary cleansing by segregation of Si-rich phases to the bulk surface has been reported, causing yttria redistribution and enhanced YSZ grain growth in the surface.[41]

During sintering of NiO/YSZ anode precursor structures a solubility of NiO in YSZ of about 2 a/o has been observed. [6,42-45] Under SOFC anode operation conditions this NiO forms metallic Ni, as evidenced by a gray coloring of the electrolyte.

YSZ grain boundaries in contact with the TPB are not expected to be significant, as the oxide ion conductivity in grain boundaries of even pure YSZ is normally found to be inferior to that of the bulk.[35] An exception is pure ZrO_2 with no oxide ion conductivity in the grain bulk, where modeling has indicated that formation of Schottky defects on selected grain boundaries may allow for some level of oxide ion transport on the grain boundaries.[35]
No reference to surface transport of oxide ions on YSZ has been found.

Table 10.2 Transport of species by diffusion in pure YSZ with 8 mol% yttria.

Species	Data	*i* at 850°C [#]	*i* at 1000°C [#]
H^+	*[c]* $=6.5\times10^{-6}(mol/cm^3atm^{1/2})\times pH_2O^{1/2}$ @ 986°C.[$ 46] *[c]* $=6\times10^{-6}(mol/cm^3atm^{1/2})\times pH_2O^{1/2}$ @ 887°C in N_2. [47] $D=1.8\times10^{-3}(cm^2/s)\times exp(-0.8\pm0.1eV/kT)$. [46] $\sigma=13(SK/cmatm^{1/2})\times exp(-0.8eV/kT)pH_2O^{1/2}/T$. [¤]	1×10^{-4} A/cm^2	3×10^{-4} A/cm^2
H^+,surface	?	?	?
e′	$\sigma=1.31\times10^{7}(Satm^{1/4}/cm)\times exp(-3.88eV/kT)pO_2^{-1/4}$. [34] *[c]* $=7.8\times10^{-3}(molatm^{1/4}/cm^3)\times exp(-1.99eV/RT)pO_2^{-1/4}$. [34] $D=230(cm^2/s)exp(-2.00eV/kT)$. [34]	5×10^{-5} A/cm^2	1×10^{-3} A/cm^2
e′, surface	?	?	?
$h^{\cdot}$	$\sigma=235(S/cmatm^{1/4})\times exp(-1.67eV/kT)pO_2^{1/4}$. [34] *[c]* $=1.3\times10^{-4}(mol/cm^3atm^{1/4})\times exp(-0.62eV/RT)pO_2^{1/4}$. [34] $D=0.23(cm^2/s)exp(-1.15eV/kT)$. [34]	6×10^{-10} A/cm^2	2×10^{-8} A/cm^2
$h^{\cdot}$, surface	?	?	?
O^{2-}	$\sigma=163(S/cm)exp(-0.79eV/kT)$. [34] $E_A=0.85\pm0.05$ eV (850-1000°C) [32,33] $[V_O^{\cdot\cdot}]=6.7\times10^{-3}(mol/cm^3)$ $D=5.4\times10^{-6}(cm^2/Ks)\times exp(-0.79eV/kT)T$ [¤]	4×10^{0} A/cm^2	1×10^{1} A/cm^2
O^{2-},surface	?	?	?

[$] 10YSZ
[#] $pH_2=0.97$ atm, $pH_2O=0.03$ atm, pO_2 calculated according to Ref.[48]
[&] Based on 8 mol% Y_2O_3 in a ZrO_2 lattice, 5.95 g/cm^3
[¤] Calculated on the basis of data quoted.

Protons are available in great numbers from the adjacent Ni-surface, and are envisaged to spill over on the electrolyte surface by concentration driven diffusion.
Protonic conductivity in oxides can in principle occur by a "hopping" mechanism from oxygen to oxygen, or attached to an oxide ion as a hydroxide group by a "vehicle" mechanism. Based on the trend in other ceramic proton conductors, the hopping mechanism is assumed to be dominant in YSZ.[49] Based on this assumption H^+ and not OH^- is considered as a the moving species in and on YSZ. Transport at or on the surface may occur by another mechanism, this is highly uncertain.
Protons on the YSZ surface are assumed to be mobile, and to site on lattice oxide ions to form hydroxide ions on the surface. The surface coverage of such mobile protons on YSZ is unknown. Two competing steps are envisaged for formation of adsorbed water, either a proton jumps

towards a hydroxide ion to form water, or two protons simultaneously jump towards an oxide ion, Figure 10.4.

Assisting transport of protons from the Ni to the YSZ may occur over the solids interface, where the succeeding transport occurs in the YSZ bulk towards the surface. Based on the assumption of the hopping mechanism for proton conduction, concentration driven diffusion of hydroxide groups or water in the YSZ is expected to be comparable to the oxide ion transport.

10.2.3 Dynamic TPB

Based on experimental observations a complication to the simple TPB approach is discussed. It comprises the possible effects of having isolated clusters or particles of Ni on the YSZ surface at a close proximity of the TPB.

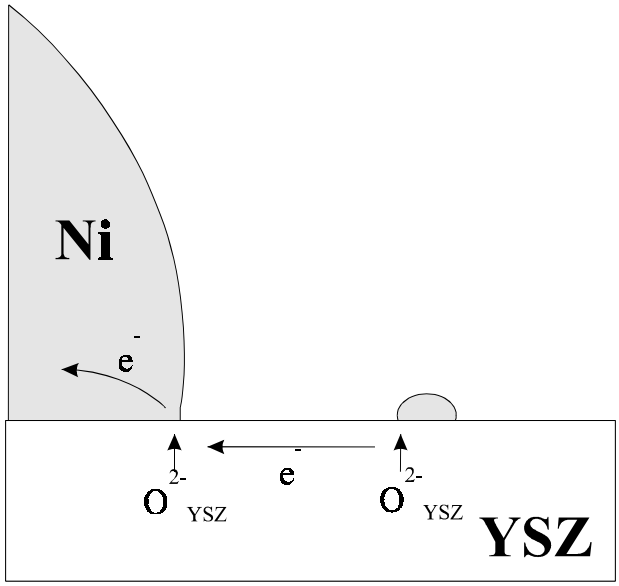

Figure 10.5 The potential role of small clusters of Ni on the electrolyte surface near a functional TPB.

Formation of clusters and particles of Ni on the electrolyte surface next to well-defined Ni/YSZ contacts has been observed.[50,51] A fine "necklace" of Ni-particles is observed within a 10 µm distance of the TPB, where the Ni tip or wire with a large radius has been within few µm over the electrolyte surface. The Ni has been assumed to be transported from the bulk Ni by a process related to passing an anodic current, which was observed to increase a factor 2 over time.[50] Such slow performance improvements with time of fine (submicron) cermets has not been reported, indicating that this effect is distinct for coarse structures.

Redistribution of Ni in a cermet has been observed after prolonged operation at high pH_2O under current load.[52] This has been explained by formation of $Ni(OH)_2$ (g) with a considerable vapor pressure under anodic operation in the presence of high water vapor pressures. It is not unlikely that large local concentrations of water and following concentration gradients may be able to remove Ni from the TPB and deposit it on a nearby surface as the pH_2O decreases.

NiO is also known to diffuse out on a YSZ surface under oxidizing conditions,[53] and the aforementioned solubility of NiO in YSZ may contribute to the formation of Ni clusters on the YSZ surface in reducing atmosphere.

Furthermore the Ni-YSZ contact has been shown to be dynamic under current load, with bulk rearrangement of the electrolyte material along the TPB, where a small "ridge" is formed.[50] A similar effect has been observed for the Pt/YSZ interface where a clear dependence on the flow of current is established.[54,55]

The presence of Ni clusters or particles that are orders of magnitude smaller than the normally considered 1 μm Ni-grains, Figure 10.5, constitutes a considerable Ni-surface and "unconnected TPB" along the connected TPB considered above. The water formation reactions on or at such particles are covered in the above treatise of the two materials. However, if the reaction takes place at these sites, a potential rate-limiting step is electronic transport through the electrolyte between Ni cluster and current collector.

Electronic conductivity in YSZ is dependent on pO_2, Figure 10.6. The transition between dominant n- and p-type conduction occurs at a pO_2 in between the operation conditions for the SOFC anode and cathode. The observed activation energies are high, Table 10.2.

Electronic conductivity in YSZ is of general interest for cermet anodes near the Ni percolation threshold (see later), if the overall percolation is limited by small blocking YSZ grains.

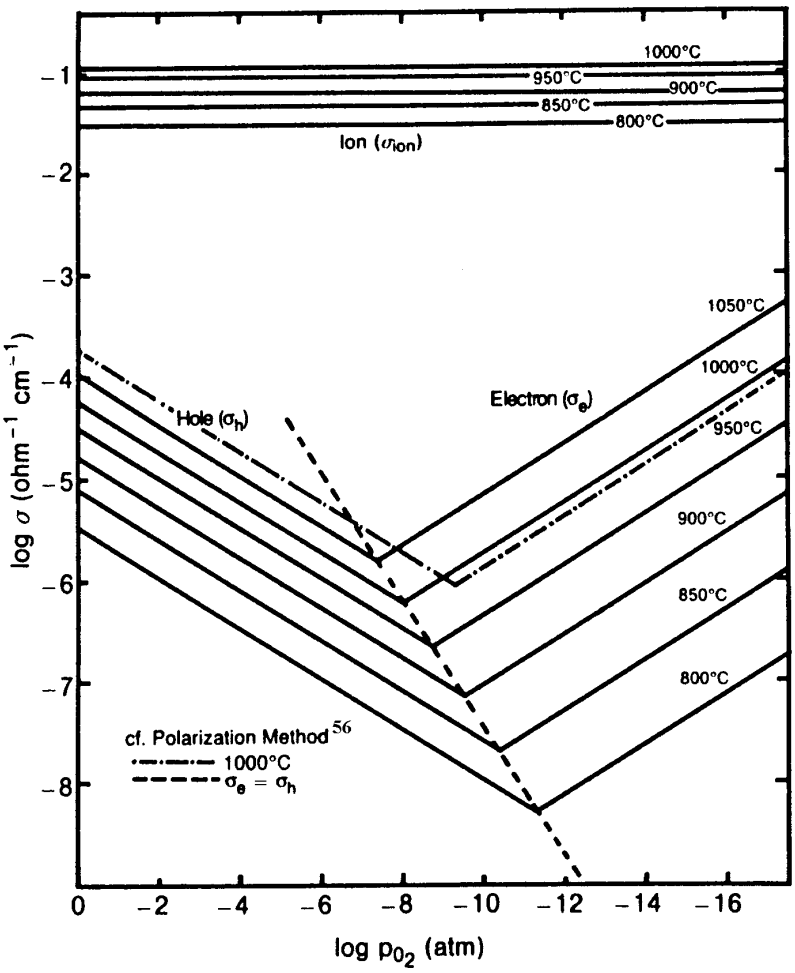

Figure 10.6 Conductivity isotherms of oxide ions, electrons and holes in YSZ with 8 mol% Y_2O_3.[34]

10.2.4 Yttria Segregation on YSZ at the TPB

An enrichment of the YSZ surface with the dopant is likely to influence the transport properties for the considered species. A segregated monolayer with an Y_2O_3 enrichment factor of 2 or more has been observed by SIMS on YSZ with 7 to 9% Y_2O_3 after a heat treatment at 1000°C.[39,40]
A segregation layer of a few atomic layers, the presence of which is depending on impurity levels and processing, might well affect the oxide ion transport to the TPB significantly. Such a thin layer of limited oxide ion conductivity constitutes a plate capacitor, whereby the associated resistance could be associated with the electrode rather than the electrolyte. Differences in current density and durability has been observed for Pt-YSZ point contacts in air, depending on whether the sintered oxide surface has been polished or not, to remove any surface segregation.[55]

Furthermore, kinetic demixing driven by the applied electrical field at a temperature of 1375°C has been demonstrated to cause Y^{3+} enrichment and Zr^{4+} depletion at the negative electrode.[57]

10.3 Electrochemical Evidence

10.3.1 Characterization of Electrodes and Related Problems

A number of general experimental considerations apply for SOFC electrode research. In particular for investigations of technological anodes characterized by low overpotentials and high attainable current densities, extra care must be taken in the design and interpretation of experiments.

Test Geometry The design of the test cell geometry and the test facility geometry has important consequences for the quality of data that can be obtained for high-performance electrodes.[58] In principle most cell geometry's can be divided into two basic groups; thin electrolyte cells (foils of about 200 μm) and thick electrolytes (tablets or pellets of mm thickness).[59,60] In order to characterize only one electrode (the working electrode), a reference electrode is inserted. For thin electrolyte cells the reference electrode has to be positioned on a surface next to a current bearing electrode, see e.g. ref.[84] For valid electrochemical experiments the alignment of the opposing working- and counter electrodes is critical within the thickness of the electrolyte.[59] For the pellet geometry the reference can alternatively be placed as a circumferential wire or a point contact in a central bore. In both cases it is desirable to position the reference electrode fairly close to the working electrode, to minimize the electrolyte resistance (series resistance, R_S) included in the measurement.[61] High series resistances cause low phase angles in the measurable impedance and large iR_S corrections for i-η curves, both inflicting on the accuracy. At the same time the bore or grove holding the reference electrode must not significantly disturb the current distribution in the electrolyte pellet. Furthermore, the reference electrode must be so small that an internal flow of current is avoided, and yet large enough that the reference impedance is significantly smaller than the input impedance of the characterization equipment.[59,62,63]
High quality electrochemical data can be obtained at OCV, using symmetrical electrodes on thin electrolytes in one common atmosphere.

A general problem is ohmic heating when passing current. This is in particular a problem for the pellet where the full electrolyte resistance contributes.[61] Demonstrations of current densities in excess of 5 A/cm^2 has been found in literature,[64] neglecting any discussion of the related heating.

The test facility geometry should have a stable reference gas such as air, the typical anode gases used are not appropriate as the sensitivity to conversion of gases affecting the Nernst potential causes artifact contributions due to concentration effects from the current-bearing electrodes.[65] Even when a stable reference electrode is used, the change of reference electrode potential with temperature should be taken into account when performing detailed analysis of a charge transfer limiting reaction step.

Impedance spectroscopy has been suggested for diagnostics of complete cells, changing the atmospheres on either electrode to identify and separate the respective contributions.[66] Whether a reasonable resolution can be obtained depends on the prior knowledge of the separate electrodes, and the difference in time constant of the respective electrode processes.

10.3.2 Transport Restrictions

Any limitation existing in the system under characterization between the voltage probes is in principle be measured, including secondary effects of processes occurring outside the borders defined by the voltage probes. Examples of the latter are ohmic heating in the electrolyte and failure to keep the atmosphere constant.
If the electrode impedance is high (kΩ), there is a fair chance that no other limitations may be significant. As the electrode impedance studied decreases, the importance of other limitations increases.

Concentration Polarization In the simplest approach perfect gas exchange over the porous anode structure is assumed. Concentration polarization in SOFC anode systems has been found to be significant under DC loading.[67-69] The conversion of hydrogen to water by even a small perturbing AC signal at open circuit potential (OCV) and at a gas utilization of less than 1% has been demonstrated to cause a significant conversion impedance at low frequencies.[70-72]

Another well-known contribution to concentration polarization is gas diffusion. Often the porous structure is focussed upon, and model calculations readily demonstrate that with a typical supported electrode thickness of less than 50 μm, reasonable porosity and not too dilute gases, the diffusion impedance in the structure is in the order of few mΩcm^2 and often insignificant.[60,73,74] However, if either of these conditions are not met, the diffusion impedance may contribute significantly. For an electrode fed through a porous cell support, the thickness and porosity of the support may cause a significant diffusion impedance.[75,76] Recently the diffusion in stagnant gas films outside the porous structure has been demonstrated to contribute significantly to measurements on high-performance electrodes.[65] Care must be taken in test facility design to ensure efficient gas exchange over the electrode surface.

Of the concentration effects only the diffusion in the porous structure (including the applied current collector structure) is relevant for the examined electrodes. In this context it is convenient to note that all the contributions to the concentration overpotential exhibit only a negligible dependence on temperature, and further the overpotential of gas conversion and diffusion in the volume above the porous structure depends on the inlet gas flow-rate. Finally the high

capacitance associated with the concentration polarization may be used for identification purpose.[77]

Auxiliary Cell Application of an auxiliary cell placed against the working electrode (e.g. of the type shown in Figure 10.7) has been demonstrated to avoid the concentration polarization problem in an efficient manner.[65,78]

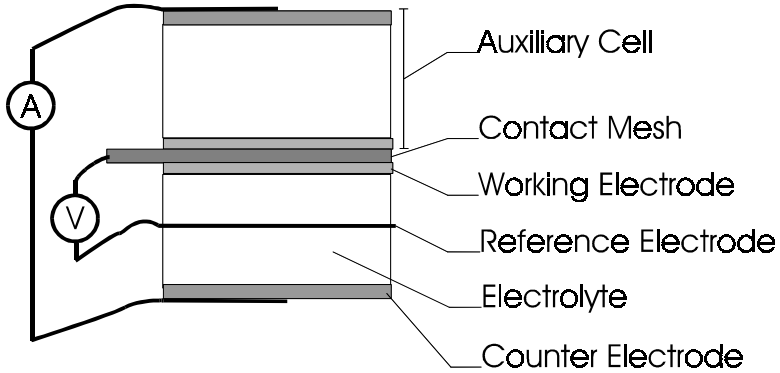

Figure 10.7 The use of an auxiliary cell with an electrode facing the working electrode at a close proximity, supplying and removing gas at a low distance from the working electrode eliminates concentration polarization even at dc conditions for reversible electrode processes.

Restrictions in the Electrolyte The resistance of ionic conductivity in the bulk electrolyte between the voltage probes referred to as R_S is in principle readily separated from the electrode response at higher temperatures. At low temperatures (e.g. 300 to 400°C) the response of the electrolyte grain boundaries can be recognized.[32,33,41] Below 750°C the impedance of pores and cracks in the electrolyte may also be observed, typically at frequencies higher than the grain boundary impedance.[79-81] At higher temperatures these effects are not measurable, and impedance spectra are typically assumed to represent only the electrode response. The geometric restriction of the current at the electrode-electrolyte interface has been modeled and discussed.[82-84] An impedance arc at high frequencies, similar to those of the electrolyte bulk response, is predicted due to the double layer capacitance allowing current to pass over the entire contact interface at high frequency, whereas only the electrochemical reaction restricted to the TPB circumference can pass a dc current.

A screening method has been applied for comparison of electrochemical properties of solid electrode materials, using single contact, point shaped (cone) electrodes.[85-87] In principle the influence of microstructural characteristics, sintering and high-temperature reactions can be avoided in this way. Often two impedance arcs are observed, the high-frequency arc is insensitive to gas composition and could only be affected by mechanical polishing of the electrolyte surface. This behavior seems to imply that the materials contact can indeed contribute to the electrode impedance.

10.3.3 Impedance Spectra

Having identified the concentration impedances as described above, it is attempted to find consistency in reported impedance spectra on Ni/YSZ electrodes at OCV. Key data are listed in Table 10.3, focussing on the summit frequency for each impedance arc.

Table 10.3 A listing of size and summit frequency of electrode-related arcs in reported impedance spectra for Ni/YSZ electrodes. Most data at 1000°C in hydrogen with 2-4% water. However, other partial pressures and temperatures are included.

Electrode type	Electrode arcs[¤]	R_P [#], Ωcm^2	Relaxation frequency [£], Hz	Other arcs present [$]
Fine cermet [51,77,88]	1	< 0.1	1-10 k	gd 100 Hz gc 1 Hz
Fine cermet [70]	1	< 0.1	1-10 k	gd 100 Hz
Fine cermet [65]	1	0.1	1-10 k	
Fine cermet[89,78]	2	0.2	10 k 1 k (70%)	
Coarse cermet,[51]	2	1.1	1-10 k 50 (90%)	gc 1 Hz
Ni rich cermet[88]	1	13	1-10 k	
Cermet[90]	1	0.15	1-10 k	gd 10 Hz
Cermet[91]	1	0.15	100-1000	gd 1-10 Hz
Cermet[102]	1	0.3	1 k	
Cermet[92]	1	1	200	
Coarse NiO in cermet[93]	2	35	14 k 2 k (95%)	
Fine NiO in cermet[93]	2	< 0.1	8000 200 (70%)	
Cermet[94]	1 (distorted)	0.6	1 k	gd ? 10-100 Hz
ZrO_2 in cermet[94]	1 (distorted)	1.7	1 k	gd ? 10-100 Hz
Coarse YSZ in cermet[95]	1	6	1 k	gd ? 1-10 Hz
50/50 coarse/fine YSZ in cermet[95]	2	1	7 k (90%) 200 (inductive)	gd ? 1-10 Hz
Fine YSZ in cermet[95]	2	0.4	10 k (80%) 200 (inductive)	gd ? 1-10 Hz
Cermet[28]	1	0.5	1 k	gd ? 1 Hz
porous Ni[51]	1	0.7	10 k	gc 1 Hz
porous Ni [78]	1	1.2	5 k	
Ni-felt[51]	2 (overlap)	27	1 k (90%) unknown	
Ni-layer[96]	1	2	100	gd 1-10 Hz
Ni-pattern[97]	1	unkn.	unknown	
Ni-point[97,98]	2 (overlap)	80	unknown	
Ni-pattern[95]	2 (overlap)	10	10-20	
Ni point[20]	2	2.3	1-10 k (80%) 100	
Ni-point[99]	2 (overlap)	85	3	
Ni-point[100,101]	1	10	500	

[¤] overlap means that arcs are inseparable, distorted means primary arc with smaller "shoulder"
[#] for point contacts the reported contact area is applied for area-correction.
[£] k indicates 10^3, percentage values in brackets are part of total R_P
[$] gd = gas diffusion, gc = gas conversion, ? = our guess based on *f* and the used setup geometry.

It is evident that measurements with only one distinct arc can be obtained, and that in several cases secondary arcs emerge at lower and higher frequencies. For similar R_P values there is also a remarkable spread in the dominant time constant caused by the capacitive values.
For cermet anodes sintered at too low temperature the situation is even more complicated, 2 to 3 arcs are observed with considerable overlap. [102,103]

In some cases inductive loops in impedance spectra have been reported for Ni/YSZ cermet anodes.[88,92,95] The effect is most pronounced under dc load, but can also appear at open circuit potential. Similar effects have been seen for Pt electrodes on Ce-doped YSZ electrolytes in H_2/H_2O.[104] Adsorption of intermediates has been suggested to cause this effect.[104]

10.3.4 Rate Limitations

In the following some of the experimental electrochemical data obtained on Ni/YSZ anodes are inspected. Mainly the electrode polarization resistance R_P is considered, and effects of concentration polarization are disregarded where identified.

Distribution of Reaction Sites and Active Thickness The effect of different series resistance connecting reaction sites in the cermet electrode to the bulk electrolyte has been suggested to cause a frequency distribution of the reaction impedance, causing an impedance arc to emerge.[105] Modeling of cermet structures and resistor networks has indicated that distortions of otherwise simple impedance arcs could occur as a high frequency "shoulder", especially if the Ni-content of the cermet is near the percolation threshold.[106,107] A distinct distortion of the impedance spectrum has been observed in agreement with this.[78] Geometric current constriction in a porous structure has been demonstrated for ion-conducting zeolites, the depression angle (and the frequency exponent n) of the related impedance arc was found to depend on the contact between particles.[108]

The active thickness of cermets has been determined, the reported values are about 10 μm at 1000°C.[51,109,110] This is in agreement with modeling results.[74,95,111] The contribution from sites in the cermet to the electrode performance has also been measured, comparing cermets with equal structure using 8YSZ and non-conducting ZrO_2, a factor of 3.5 difference in impedance was observed.[94] The active cermet thickness is limited by the sum of the reaction impedance and the transport impedance of oxide ions and electrons in YSZ and Ni, respectively. Therefore the active thickness can be expected to vary with temperature and gas composition, as the reaction impedance and the transport impedance do so.

TPB-length Specific Impedance Experiments have been conducted demonstrating that the electrode impedance scales with the TPB for Ni-stripes,[112-114] Ni-pattern electrodes,[111] Ni-pattern and Ni point contacts,[97] and from cermets with contacts in only one dimension.[115] By a combination of analyzing anode cross-sections with known exchange currents and performing a non-destructive standard porosimetry method, an attempt to develop a tool for predicting the performance of a cermet has been reported.[116]

It has been attempted to estimate the TPB-length specific polarization resistance R_P' for a number of reported anode data, arriving at values from 10^4 to 10^7 Ωcm at 700°C in dilute gases, and from 10^2 to 10^3 Ωcm at 960°C.[5] The possibility of having disperse, electrochemically active Ni-clusters on the YSZ surface from sintering might account for some of the spread in R_P', just as the electrochemical history for a specific electrode decides the amount of unconnected Ni

deposited on the electrolyte surface near the measurable TPB. Segregated Y_2O_3 rich layers and impurities on the electrolyte surface may also be important. To evaluate this effect from literature data is not straight-forward, as specific knowledge of the raw material and used preparation technique for the electrolyte surface is required.

Double Layer Capacitance The plausible double layer capacitance on the metal-YSZ interface has been approximated to a plate capacitor and estimated to be about 14 $\mu F/cm^2$ contact interface, the temperature dependence should be weak; about $T^{1/2}$.[117] The capacitive value combined with knowledge of the typical grain size may be used to estimate the TPB of cermet structures.[77]
Provided the two-phase contact area is well known, it can be established whether the measurable capacitance can at all be related to the interface, or whether capacitive adsorption processes should be considered. For Ni-pattern anodes with a rather well-defined contact area, impedance spectra with capacitive values of 1 mF/cm^2 have been reported.[95] This value is clearly inconsistent with the double layer capacitance.

Reaction Zone Width The width of the reaction zone has been considered experimentally under different conditions. A decrease in the reaction rate per TPB is expected when adjacent electrode particles or strips are positioned so closely on the electrolyte surface that reaction zones overlap. Results indicate the extent of the reaction zone to be below than 1 μm on the Ni phase in a micro-porous Ni-film anode,[96] and less than 1 μm on the electrolyte[118] concluding on another study of etched Ni-patterns.[97] At about 700°C in dilute hydrogen and water indications have been given that the extent is less than 2.5 μm on the Ni-surface.[119]

Thermal Activation The activation energy of the electrode limitation is generally found to vary from study to study. Values range from 0.5 eV to 1.8 eV, with a tendency towards fine structures having low activation energies and coarser structures exhibiting higher activation energies. See Table 6.2 in Chapter 6 for details. Identified mechanisms with activation energies of the order of 1.8 eV include electronic transport in YSZ, and OH^- bonds to Ni at lower temperatures.

The range of obtainable activation energies indicate that the electrode process can proceed without this high-activation energy reaction step being included or limiting. Another possibility is that the activation energy of the process is highly dependent on the purity of materials. Taking the Ni-redistribution by current to be significant only for coarse-structure cermets with high R_P values and in which higher gas composition gradients can be found, the electronic conductivity in YSZ might be part of the explanation. This variation of activation energy with cermet structure raises the question whether limitations in high-impedance model anodes with well-defined geometry are at all comparable to the limitations in technical anodes.

In general it has been observed that Arrhenius type plots given in literature tend to curve rather than follow straight lines, so that the apparent activation energy is lower at higher temperature.[51] An interpretation of such behavior has been given, suggesting two different processes to dominate at low and high temperature.[27]

Hydrogen Partial Pressure The apparent hydrogen partial pressure dependence at OCV is fairly weak at 1000°C with about 2-5% water. $1/R_P \propto pH_2^{\alpha}$ where typical α values range from –0.15 to +0.15, see Table 6.3 in Chapter 6 for details.
At 850°C higher α values of about 0.5 have been observed at partial pressures exceeding 0.5 atm.[78] whereas α values approaching 1 are observed for Ni-stripe anodes at even lower temperatures and low partial pressures.[112]
The weak dependence on hydrogen partial pressure at 1000°C seems to indicate that neither gaseous hydrogen, protons on the Ni-surface nor on the YSZ surface are limiting the reaction rate. At lower temperatures the situation is less clear-cut.

Steam Partial Pressure The apparent water partial pressure dependence at OCV has been demonstrated to be fairly strong at concentrations below about 0.25 atm. at 1000°C with a wide range of constant hydrogen partial pressures. $1/R_P \propto pH_2O^{\alpha}$ where typical α values are around 0.5, see Table 6.4 in Chapter 6 for details. At 850°C a tendency towards a lower α value is seen,[78] and at even lower temperatures no dependence on pH_2O is found for Ni-pattern electrodes.[112] This would appear to indicate that water promotes the reaction rate at higher temperatures. No indication of the water desorption being rate limiting is therefore present. It should be borne in mind that at OCV the balance between anodic and cathodic reactions defines the exchange current. To investigate one reaction without significant (<10%) contributions from the other, an overpotential exceeding $3\times RT/F \approx 300$ mV should be applied. Furthermore the partial pressure dependence might be an effect of a physical transport restriction, where e.g. the solubility of the diffusing species is depending on the partial pressure of water. Complex dependencies of anodic and cathodic current densities on pH_2, pH_2O and "oxygen activity at the TPB on the electrolyte" ($\approx pO_2$) have been derived at temperatures of 500 to 800°C.[119,120] Finally the links between pH_2, pH_2O, pO_2, (E,) and T in the water formation reaction and the Nernst equation should be recalled; variation of one singular parameter is not feasible.

Isotopes D_2/H_2 The classical isotope effect predicts that the shift in e.g. a pure diffusion resistance should be proportional to the change in the square root of the mass, that means for D_2/H_2 or D^+/H^+ a factor of 1.41 and for e.g. OD^-/OH^- a factor of 1.03. There is a slight difference in the energy of bonds formed by hydrogen and deuterium. Saturating the two gases with 3% natural water and heavy water, respectively, an OCV of some 14 to 19 mV over a proton conducting membrane at 500-900°C can be observed.[121] The activation energy for proton diffusion in Ni is reported to be about 10% higher for H than for D.[122] Also the rate constants for dissociative adsorption on Ni are different for the isotopes.[123]
Considering Ni electrode and Ni/YSZ cermet electrode impedance at OCV, it is found that at 1000°C virtually no isotope effect is observed, whereas at lower temperatures (down to 600-700°C) an increasing effect is seen, up to a factor of 1.25.[78,124] This change in isotope effect with temperature indicates a shift in the nature of the limiting process with temperature, presumably towards a limitation involving hydrogen or protons at lower temperature.

Catalytic Poisoning by H_2S The poisoning effect of sulfur by chemisorption on Ni-catalysts is well known,[125] it is reversible and a temperature dependent threshold exist below which no effect is observed.[126] At 700°C the threshold is about 1 ppm, at 1000°C the extrapolated value is of the order of 50 ppm.
Poisoning by sulfur has been investigated on Ni/YSZ cermet anodes in H_2 + 3% H_2O by several groups.[78,90,91] In amounts from 5 to 105 ppm an increase of about a factor of 2 in polarization resistance has been observed. The effect at 5 ppm H_2S,[90] is in contradiction with the reported

limit for degradation of Ni-catalysts performance, and no additional effect is seen applying 105 ppm. At 35 ppm the effect was found to be reversible, and to be constant with temperature from 700 to 1000°C, with or without passing anodic current and equal for low-performance porous Ni-anodes and high-performance Ni/YSZ cermets.[78] The effect was found not to be reversible at 105 ppm.[91]

Assuming that sulfur chemisorbs exclusively to the Ni-surface, the data indicate that the Ni-surface is either the location of rate limiting reactions, or that it provides a limiting species to the rate-determining reaction. It would appear that the role of the Ni-surface is fairly constant with temperature and passing of current under the given circumstances.

Considering the impedance of a full SOFC at 1000°C, the effect of 69 ppm sulfur is about 5% on the cell voltage,[127] at 800°C 10 ppm sulfur causes about 2% reduction of the cell voltage.[128] These observations are partially affected by the anode usually not being the most significant limitation for well-performing SOFC. Cells with Ni/YSZ cermet anodes have been operated with up to 2000 ppm sulfur at 950°C, maintaining output stability.[129]

Anode Metal A number of metals have been compared as porous metal anodes at 800°C in H_2/H_2O, the performance ranking was found to be Ni>Rh>Fe>Ru>Co>Pt>Pd>Au> Mn,[130-133] and in another study the order Fe>Co>Cu>Ni>Pt>Ag was obtained.[134] The order Ni>Pd>Ru>Pt was found at 1000°C using 2-3 μm thin plated metal-layers on YSZ.[135] Using the current density at the TPB of single contact electrodes, the ranking Fe>Co>Ni>Mo was obtained at 1000°C.[86]
Cermets of YSZ and metals have been compared, indicating Pt and Au to yield higher current densities than Ni.[127] However, the morphology and especially the porosity of the produced cermets is indicated as a source of discrepancy. This is probably also the cause for the discrepancies in the above rankings of metals. Measurements in a well-defined test geometry is in demand for this type of comparisons.
Other than Ni/YSZ only the Ru/YSZ system has been studied reasonably well,[136-138] and performances comparable to what is reported for Ni/YSZ has been obtained.

Using Sm doped ceria (SDC) as an anode material, the activation energy of the hydrogen oxidation reaction has been shown to change significantly by addition of 0.1 mg/cm^2 dispersed metallic catalyst in particles of up to 30 nm.[139] This observation seems to be indicative of the metal surface being important for the limiting process. It is suggested that the activation energy of the electrode reaction might be interesting to compare for various metal electrodes on YSZ as it has been done for the SOFC cathode reaction.[118]

Electrolytes Thin layers of mixed electronic and ionic conductors such as Y and Sm doped ceria (YDC, SDC)[132,140] and Sr-Fe-Co oxides[141] in a thin layer between the bulk YSZ electrolyte and the Ni/YSZ cermet have been demonstrated to enhance the performance of full cells. In another study application of La doped ceria, ceria, SDC and PrO_x had no effect on anode performance.[142] Ni-cermets with different oxides have indicated a performance ranking of PrO_x>SDC>YSZ.[133] In the same study porous Ni anodes (and Pt anodes) were compared on two electrolytes; YSZ and SDC. Very significant improvements in the anodic polarization were obtained using SDC, indicating that some of the electrolyte properties are significant.

Neither of these effects are considered to be proof of the electrolyte surface being active in the Ni/YSZ anode, as the improvements might just as well be effects of enhanced current

collection in the structure and general differences in microstructure. A true test of the importance of the electrolyte material for the electrode reaction rate is suggested to be a well-defined Ni-point contact on YSZ electrolyte surfaces with different properties such as Y_2O_3 content, ionic conductivity and electronic conductivity. An interesting experiment comparing Ni-point anodes on YSZ and a mixed electronic and oxide-/proton-conductor has been performed,[143] but the complexity of the mixed conductor in comparison to the oxide ion conductor (YSZ) makes interpretations difficult. This type of experiment has also been carried out for Pt point contacts on YSZ as SOFC cathodes in air.[55]

Blackening Reduction of zirconia (blackening) by injection of electrons[86] is known to improve the electronic conductivity significantly, especially at lower temperatures. The activation energy of the electronic conductivity is observed to be low at temperatures below 400°C.[144] Significant improvements in performance have been demonstrated at 800°C for high-impedance porous Ni and Au electrodes (R_P≈500-1000 Ωcm^2 reduced to about 40 Ωcm^2 on reduced electrolytes),[127] implying that the reduced electrolyte has a certain stability and that electrolyte blackening might be applicable as a "regenerative" anode improvement. The progression of electrolyte reduction by current is demonstrated to occur by a highly irregular front.[145] This behavior makes electrical reduction of anodes in operation a risky process, as short circuits in the electrolyte membrane might occur.

10.3.5 Modifications of the Ni/YSZ Cermet Anode

Functional Additives A few attempts have been reported for improvements of Ni/YSZ cermet anode performance. A composite of a NiO-MgO solid solution and YSZ has been made, forming a YSZ-Ni-MgO composite upon reduction where the Ni-particles are very porous.[146] Hydrogen oxidation on this composite has been shown to have an activation energy of 2.3 eV, as opposed to 1.3 eV for a pure Ni/YSZ in the same study.

Addition of MnO_2 to Ni/YSZ cermets have been shown to have a good effect on anode performance, especially in quantities around 25 m/o.[147] Modest amounts of Mn below 5 m/o have been shown to have a number of positive effects on Ni/YSZ cermet properties, R_P for a Ni/YSZ cermet of 110 $m\Omega cm^2$ and 80 $m\Omega cm^2$ at 850°C and 1000°C have been reduced to 60 and 30 $m\Omega cm^2$, respectively.[78,148] Another study of additives dissolved in the YSZ used for the cermet showed an initial effect of Cr, Mn and Ti, but after 150 hrs of operation all differences were gone, and significant differences in morphology and porosity were generally found to disrupt the results over time.[149]

Solution of Ti in YSZ not only decreases the ionic conductivity by one order of magnitude due to carrier trapping, but also enhances the electronic conductivity significantly under reducing conditions. The optimum dopant level has been estimated to be between 7 and 10%, aiming at equal electronic and ionic conductivity.[150-153] However, reported performance of cermets consisting of 35% Ni and 8YSZ with 10% TiO_2 has been low.[154,155] Providing a pure Ni/TiO_2 cermet with a plasma-sprayed electrolyte layer, very promising R_P values of 0.1 Ωcm^2 at 800°C has been observed.[156]

10.3.6 Conclusion on Anode Reaction Limitations

The following observations about the location and nature of the electrochemical processes and rate limiting steps are done:

It is apparent from materials properties and conductivities, that high current densities are attainable for a reaction taking place within an atomic distance of the TPB between Ni, YSZ and open pores. Considering the possible reactions on surfaces along the TPB, it is evident that several processes may occur in parallel. Both chemical and physical processes should be considered for identification of the rate limiting processes, although chemical processes have been argued to be negligible at the given temperatures. Impedance measurements indicate that probably two processes can limit the reaction rate on the Ni/YSZ anode, it is unclear whether purity of materials and processing are controlling the appearance of one of these contributions.

The Ni surface is most probably the site for conversion between hydrogen and protons, the current density attainable by surface diffusion of protons on Ni is orders of magnitude higher than for bulk diffusion. The poisoning effect of sulfur chemisorption on Ni indicates a role of the Ni-surface in the rate-limiting steps, the magnitude of this role is apparently constant with temperature and current load. No or little dependence on pH_2 and no isotope effect at 1000°C indicate that hydrogen supply (as molecules or protons) is not limiting the reaction rate. At lower temperatures an isotope effect and an increasing dependence on pH_2 emerges, despite that both the surface coverage and the attainable TPB current density increases.

No unambiguous evidence of the electrolyte surface as host for the electrode reaction has been established. Data on electron, proton and oxide ion mobility on YSZ surfaces are in demand.

The estimated current density at a TPB considering protons and electrons in YSZ is equal. Unconnected Ni-clusters and particles on the electrolyte surface near the TPB are suggested to provide additional reaction sites, especially for coarse structures. This process involves transport of electrons in the electrolyte, accounting for observed activation energies of up to 1.8 eV, especially for coarse structures.

Segregation of a Y_2O_3-rich phase on the electrolyte surface is well documented, and ionic transport through this layer is suggested to be a possible cause for part of the electrode impedance.

An important point to recall is, that the geometry of this electrode cannot be assumed constant. As parameters are changed the conductivities of the materials change, whereby the width of the reaction zone along the TPB may change. It is also quite possible that the active thickness of the cermet structure may change with parameters affecting the electrode reaction.

10.4 Cermet Technology

10.4.1 The Ni Anode

The primary requirements for a Ni-based anode are

i) Percolation in the Ni-phase,
ii) Stabilization of the Ni-structure against sintering,
iii) Establishing a stable and intimate contact to the electrolyte,
iv) Provide access (porosity) for gaseous species to the interface,

Sintering of Ni In pure Ni percolation is easily established. This is due to the sintering activity of Ni particles in the μm range and the high self-diffusion of Ni,[14] causing particle growth and continuous sintering at low temperatures, e.g. 750-800°C.[113,157] The melting temperature of Ni is 1455°C,[158] and 1984°C for NiO.[159]
To avoid diffusion limitations in the anode, a certain porosity must be maintained. The formation of pores is predominantly controlled by the particle size distribution, the degree of particles packing in the green state and the sintering temperature. Addition of combustible or decomposing organic pore formers has been used to increase the amount of pores of a selected diameter. Typically used pore formers are carbon fibers, carbon-black or starch with various particle sizes.[76,160] Dispersion of sub-micron ceramic particles on the surface of a porous Ni-electrode has been applied to restrain Ni-densification by sintering.[51,78,161,162]

The Ni-NiO Transformation It is relevant to consider the $Ni + ½O_2 \Leftrightarrow NiO$ transformation as it implies a volume expansion of 33% on oxidation and a volume reduction of 25% on reduction. The equilibrium pO_2,[17] is equal to a Nernst potential vs. air of about -620 mV at 1000°C and -895 mV at 500°C. The relationship is nearly linear.
Reduction of large NiO single crystals for 3 hours at 1075°C at a pO_2 of 10^{-11} atm. has been shown to occur remarkably slower than for 1 μm NiO-lamellae between oxide ion conducting YSZ lamellae, and did not go deeper than about 5 μm.[6] In cermets a high reduction rate has generally been observed,[163] but 3 μm Ni particles have been observed to retain a NiO core after reduction in 10% H_2 at 850°C.[164]

The Ni-YSZ Contact The establishment of a stable contact interface is a balance between adherence and in-plane stress between the electrolyte and the Ni anode or the NiO anode precursor structure. Ni is not wetting YSZ, the reported contact angles are 117°,[165] 117-122° on 5%CaO-SZ depending on temperature,[166] and 109.5±5.5° for CaO-SZ.[167] Addition of TiO_2 to the electrolyte has been demonstrated to reduce the wetting angle to 103°.[165,168] Excellent wetting of NiO on YSZ has been used to form high strength bonds between metals and ceramics through formation of an Ni-NiO eutect 15°C below the melting point of Ni.[158,169] The NiO-ZrO_2(cubic) interface has been investigated on epitaxially grown samples regarding preferred crystal orientation.[170]
An impregnation of the YSZ surface with a Ni-salt and subsequent heating above 1400°C has been used to enhance the adhesion of a subsequent porous Ni layer.[51,171]

10.4.2 The Ni/YSZ Cermet

Addition of YSZ to the Ni-based anode to form a cermet offers a number of advantages:

v) better TEC match with the electrolyte,
vi) increase of the TPB,
vii) better anchoring to the electrolyte.

Thermal Expansion The TEC values for TZ8Y, NiO and Ni are about 10.6-11 $\times 10^{-6}$ K^{-1},[30] 14 $\times 10^{-6}$ K^{-1} and 17 $\times 10^{-6}$ K^{-1},[172] respectively.
The TEC of NiO/YSZ composites in air has been shown to be an almost linear function of composition between the two pure phases.[172] For Ni/YSZ cermets with different phase ratios, the TEC increases only slowly with Ni-content to about 70 v/o, above which the increase is faster.[172] This is in accordance with Kerners model,[173] taking bulk, shear and Young's modulus for the metallic Ni into account. This non-linearity means that for the technically most interesting Ni-contents (30-60 v/o), the TEC of a reduced cermet is actually in better agreement with the electrolyte than the unreduced anode precursor, despite the TEC difference of the pure phases. The TEC differences have been demonstrated to be very important for cell integrity, both for supported and supporting anodes.[174,175, 103]

TPB Increase and Percolation It is known from percolation theory and Monte Carlo simulations, that mixing equally sized spheres randomly requires a minimum of about 30% of the minority phase to obtain macroscopic connectivity in both phases.[176,177] Using crystal lattices with 4 to 12 neighbors this threshold value vary from about 40 to about 20%.[176,178] Just over the threshold about 20% of the minority particles participate in the connected network, whereas 90% participates if the minority fraction constitutes about 40%.[178] Changing the size ratio of the two types of particles, the theoretical percolation threshold decreases to some 10% if the minority phase particle size is one order of magnitude smaller than the majority phase.

Provided that percolation in both Ni and YSZ is obtained in the cermet on a particle scale, TPB points can be found in the volume of the electrode. The sum of transport resistance in the solid phases and the electrode reaction itself sets the limitation on the extent of the active volume or active electrode thickness.[179] As the electronic conductivity in Ni is orders of magnitude higher than the ionic conductivity of YSZ, the active thickness of the electrode extends from the electrolyte interface. Reported active thickness for fine cermets is about 10 μm.[51,109,110]
Depending on the in-plane electronic conductivity and distance between external contact points, a practical minimum thickness of anodes exceeding the active thickness can be expected. A 40 v/o Ni cermet structure consisting of 0.5 to 2 μm particles has been found incapable of maintaining adequate contact over a 0.4 cm^2 test electrode when the thickness is less than 20 μm.[77] In another study a 20 μm cermet has been demonstrated to loose in-plane conductivity over time leading to deterioration of performance.[164]

To investigate the ionic conductivity of the YSZ structure of a cermet, it is necessary first to remove the Ni-phase by dissolution in e.g. hydrochloric acid. The conductivity of such porous systems in fine cermet anodes has been found to be about one order of magnitude lower than dense YSZ.[51,90] Application of blocking electrodes on the cermet is not sufficient to avoid internal electrode processes and electronic transport in the Ni phase. Too high a conductivity is observed by this method, see e.g. ref.[109]

The percolation in Ni-phase is observed experimentally by 4-point dc-conductivity studies on tablets or thin layers.[160,180,181] Alternatively, models for relating the electrode in-plane resistance to the discrepancy between observed and calculated electrolyte resistance of simple electrolyte geometries has been given[182] and applied. [103,93]
In practical studies the electronic conductivity is demonstrated to change abruptly at the percolation threshold. Using real particle size distributions as obtained from commercial oxides, a threshold between 30 and 40 v/o Ni has been observed.[16,132,183] Using smaller NiO particles produced by combustion methods, powders with a surface area of about 30 m^2/g has been obtained,[184] and the percolation threshold has been lowered to about 20%.[160,185] Mixed oxide powders produced in this way exhibit a remarkably gradual loss of percolation as opposed to the typical abrupt threshold.[185]

Anode Structure It is apparent that good cermet performance is essentially depending on the density of Ni/YSZ particle contacts and conductivity in the two phases. These observations leads to a compromise between small particles to enhance the contact perimeter (TPB), and larger particles of the poorer conductor (YSZ) with good sintering necks to enhance conductivity.[74,186] In technical applications of anodes a layered or graded structure is often used to enhance TPB density near the electrolyte, and conductivity in the above structure.[1,187,188] In general the formation of a well sintered and rigid YSZ structure is believed to be essential for percolation, TEC matching to the dense electrolyte and to restrain Ni-agglomeration in cermet structures.

By variation of the YSZ:NiO particle size ratio an optimum of about 1:100 has been identified for 44 v/o Ni cermets.[189] In direct contradiction a performance improvement of more than 2 orders of magnitude is found applying equally sized particles of 3 μm instead of YSZ of 0.2 μm and NiO of 12.5 μm.[93] As a more general comment it is mostly found, that smaller particles of YSZ respective to the NiO is beneficial.[190] Replacing increasing parts of the used YSZ by a finer fraction has been demonstrated to increase performance considerably,[95] but also calcination of fractions of the YSZ prior to slurry formation has been reported as beneficial.[29,191]

The results are fairly inconsistent, and it is suggested that the particle size ratio is an inadequate parameter for relating structure to performance. It might be more relevant to consider the conductivity of both phases in the cermet. E.g. for a YSZ structure both fine and coarse particles may enhance conductivity; fine particles contribute a higher sintering activity for neck formation, whereas coarse particles provide a high local conductivity to be connected by the necks.

An approach using two size fractions of YSZ in a homogeneous structure has been reported. The 48 v/o large particles (27 μm diameter) dominate firing shrinkage and TEC, whereas the fine 77/23 v/o Ni/YSZ composite in-between coarse YSZ particles provides excellent electronic conduction.[192-194] A positive effect of precalcining the NiO/YSZ mixture prior to forming the slurry or slip for depositing the anode has been reported.[102]

Anchoring The addition of YSZ to the Ni anode to form a cermet also helps anchoring of the electrode to the electrolyte surface. The sub-micron YSZ particles in the cermet have a high sintering activity, and are capable of forming sintering necks to the pre-sintered electrolyte. Good contact through these necks is a condition for the above distribution of TPB to the bulk electrode. Mechanical anchoring by electrolyte particles has also been applied prior to sintering of other electrode types where reactivity with the electrolyte limits the sintering temperature.[195]

10.4.3 Anode Performance and Durability

Ni/YSZ cermet anode polarization resistances in the order of 150 to 300 mΩcm^2 are frequently reported at 1000°C in hydrogen/water mixtures. Values of 100 mΩcm^2 have been observed after correcting for concentration limitations,[65,90,91] and even lower values have been attained.[1,78,93]
By modifications of the simple Ni/YSZ cermets with MnO_2 or MgO, values of 30 to 70 mΩcm^2 have been attained at 1000°C,[78,146] and for porous Ni on SDC electrolyte or Ni/TiO_2 cermets 100 mΩcm^2 and less have been reported at 800°C.[133,156]

The long term stability of anode performance is to a large extent linked to the microstructure in the same way as attainable performance. The effects investigated are typically in-plane conductivity of the Ni-phase, electrochemical performance and micro-structural changes. For a cermet with coarse and fine YSZ,[193] a performance of about 250 mΩcm^2 has been shown with only negligible degradation over 2500 hrs at 1000°C and 200 mA/cm^2.
Other cermet anodes with good performance have been demonstrated to be stable over 1300-1900 hrs under 300 mA/cm^2 at 1050°C (1 test) and degrade about 3 to 16 mΩcm^2/1000 hrs at 1000°C (4 tests).[89] At 850°C (4 tests) a degradation of about 80 to 110 mΩcm^2/1000 hrs was observed for identical anodes. The anode performance for two identical anodes tested at 927/1008°C and 500/300 mA/cm^2 has been observed to increase 14 and 47 mΩcm^2/1000 hrs, respectively.[199]
CElls with a Ni/YSZ cermet anode have been operated for more than 60,000 hrs with a total cell degradation of about 3.5% per 10,000 hrs.[196] Cells with cermets of Ni and CeO_2/YSZ have been demonstrated over 11500 hrs with a total cell degradation of 14% over 10,000 hrs.[197]

Sintering of Ni-particles can cause diminishment of TPB and loss of electronic percolation in the Ni-structure between TPB and current collector.[16] The effect of sintering of Ni-particles has been illustrated by electrical conductivity over the first 50 hrs at 1000°C for cermets with varying content of coarse (27 μm) and fine (0.6 μm) YSZ and fine Ni.[192] For cermets failing to have a well-formed continuous YSZ network the impedance has been demonstrated to increase a factor of 5 over 2500 hrs at 1000°C at 220 mA/cm^2.[198]

The stability of Ni in the anode is affected by high water vapor pressures at operation temperatures. $Ni(OH)_2$ has been calculated to have a significant vapor pressure, and depletion of Ni from cermet anodes at the gas inlet has been demonstrated in durability tests.[52] Judging from experimental data[50,51] the water vapor gradient in the gas around the active site under current load could be an important parameter in this mechanism of Ni transport, but the effect in fine cermet structures is difficult to predict.

The porosity of an anode support structure has been demonstrated to develop over time, presumably by Ni-agglomeration.[199] Apart from this, no structural development has been observed in the μm range of fine cermets.[89] The non-destructive standard porosimetry method reported to be useful for extremely small pore volumes should be able to provide interesting data on the structural stability of thin (supported) anodes.[116] For cathodes a change in distribution of pores in the bulk electrolyte under the electrode contact as been observed, indicating materials transport in the electrolyte.[200]

The ability of an anode to withstand accidental thermal cycles and redox cycles must also be considered part of the durability performance, as system protection against these events may be both complicated and expensive.

Thermal cycling properties of an anode is dominated by the TEC differences with respect to the contact structure and the electrolyte. Thermal cycling between 1000°C and room temperature 11 times has been demonstrated to cause about a factor 2 increase in anode impedance.[201] For other anodes hardly any development is seen over 9 cycles after a 30 $m\Omega cm^2$ increase over the first two cycles.[89] A 10% decrease in cell performance has been noted on the first cycle to 100°C (from 950°C), thereafter a combined aging/thermal cycling decrease in performance of 9% is observed over 3000 hrs with 30 cycles.[129]

Redox cycling includes dramatic volume changes of the Ni-phase with the potential to cause fracture of the sintered YSZ structure of the cermet structure. Again the cermet microstructure is decisive whether the Ni-expansion is acceptable or not. Typically more damage to anode performance is observed over redox cycles than temperature cycles.[201] The first redox cycle doubles the impedance, whereas the second cycle only cause an additional 10% increase. In other cases total failure is observed.[202] Supporting anode structures have been demonstrated to suffer no detectable degradation during redox and thermal cycles, with respect to gas adsorption, gas diffusion and permeability,[203] but the influence on the electrochemical performance and conductivity was not reported.

10.4.4 Conclusion on Cermet Technology

Porous Ni/YSZ cermet anodes are produced worldwide and anode polarization losses well below 100 $m\Omega cm^2$ at 1000°C have been demonstrated by several groups. Data reported on anode durability are scarce, but fairly low degradation rates of about 10 $m\Omega cm^2$/1000 hrs at 1000°C have been observed.

Both performance and durability are related to the microstructure of the cermet. Key parameters are conductivity in the two solid networks and the amount of TPB line established at a short distance from the electrolyte surface. The technological solution involves splitting the structure into two functional layers, a high-TPB active layer with fine particles at the electrolyte interface and a coarse well-conducting structure above.

The performance of a Ni/YSZ cermet anode appears to be enhanced by addition of small amounts of MnO_2. The main problems regarding stability appear to be Ni transport by hydroxide formation and Ni particle growth by sintering.

References

[1] S. C. Singhal, in *SOFC V*, U. Stimming, S. C. Singhal, H. Tagawa and W. Lehnert, Editors. **PV 97-40**, The Electrochemical Society Proceedings Series, Pennington, NJ. 37 (1997)

[2] S. P. S. Badwal and K. Föger, in *Third European SOFC Forum*, P. Stevens, Editor. European SOFC Forum, Oberrohrdorf, CH. 95 (1998)

[3] H. J. Beie, L. Blum, W. Drenckhanh, H. Greiner and H. Schichl, in *Third European SOFC Forum*, P. Stevens, Editor. European SOFC Forum, Oberrohrdorf, CH. 3 (1998)

[4] C. Bagger, S. Linderoth, M. Mogensen, P. V. Hendriksen, B. Kindl, S. Primdahl, P. H. Larsen, F. W. Poulsen, N. Bonanos and M. J. Jørgensen, in *SOFC VI*, accepted (1999)

[5] M. Mogensen, S. Sunde and S. Primdahl in *High Temperature Electrochemistry: Ceramics and Metals*. F.W. Poulsen, N. Bonanos, S. Linderoth, M. Mogensen and B. Zachau-Christiansen, Editors, 17th Risø International Symposium on Materials Science, Roskilde, DK. 77 (1996)

[6] G. Dhalenne, B. Bonvalot, A. Revcolevschi and F. Millot, *J. Am. Ceram. Soc*. **73** 1524 (1990)

[7] A. Bieberle, A. Mitterdorfer and L. J. Gauckler, in IEA Workshop, Wadahl, N. (1999) in press

[8] M. V. Twigg, *Catalyst Handbook, 2nd Ed*., Manson Publishing, London. (1996)

[9] A. C. Switendick, *Ber. Bunseng*. **76** 535 (1972)

[10] M. Mogensen and S. Skaarup, *Solid State Ionics,* **86-88** 1151 (1996)

[11] R. B. McLellan and W. A. Oates, *Acta Metall. Mater*. **21** 181 (1973)

[12] F. G. Jones and R. D. Pehlke, *Metal. Trans.* **2** 2655 (1971)

[13] J. Völkl and G. Alefeld, in *Hydrogen in Metals I, Basic Properties*. G. Alefeld and J. Völkl, Editors, Springer-Verlag, New York. 325 (1978)

[14] S. Skaarup, B. Zachau-Chistiansen and T. Jacobsen, in *High Temperature Electrochemistry: Ceramics and Metals*. F. W. Poulsen, N. Bonanos, S. Linderoth, M. Mogensen and B. Zachau-Christiansen, Editors, 17th Risø International Symposium on Materials Science, Roskilde, DK. 423 (1996)

[15] in CRC Handbook of Chemistry and Physics, 75th Ed., D. R. Lide, Editor., CRC Press Inc., Boca Raton, FL. 12-41 (1994)

[16] D. W. Dees, T. D. Claar, T. E. Easler, D. C. Fee and F. C. Mrazek, *J. Electrochem. Soc*. **134** 2141 (1987)

[17] A. A. Shchepetkin and G. I. Chufarov, *Russ. J. Inorg. Chem*. **17** 792 (1972), quoted in R. S. Roth, T. Negas and L. P. Cook *Phase Diagrams For Ceramists, Vol. IV*, G. Smith, Editor, Fig. 5051, The American Ceramic Society, Columbus, OH. (1981)

[18] J. Mizusaki, H. Tagawa, T. Saito, T. Yamamura, K. Kamitani, K. Hirano, S. Ehara, T. Takagi, T. Hikita, M. Ippommatsu, S. Nakagawa and K. Hashimoto, *Solid State Ionics,* **70/71** 52 (1994)

[19] B. Zachau-Christiansen, T. Jacobsen, L. Bay and S. Skaarup, *Solid State Ionics,* **113-115** 271 (1998)

[20] J. Guindet, *Contribution a L'etude de Materiaux d'Anode pour Pile a Combustible a Oxyde Electrolyte Solide*, Thesis (in french), Institut National Polytechnique de Grenoble (1988)

[21] J. Guindet, C. Roux and A. Hammou, in *SOFC II*, F. Grosz, P. Zegers, S. C. Singhal and O. Yamamoto, Editors, Commission of the European Communities, Luxemburg, L. EUR-13564-EN. 553 (1991)

[22] A. U. Seybolt, Dissertation, Yale University, New Haven, Conn. (1936), quoted in M. Hansen, *Constitution of Binary Alloys, Second Ed*., McGraw-Hill Book Company, Inc., New York. 1024 (1958)

[23] H. Yang and J. L. Whitten, *Surf. Sci*. **223** 131 (1989)

[24] R. H. Stulen and P. A. Thiel, *Surf. Sci*. **157** 99 (1985)

[25] M. Mogensen and T. Lindegaard, in *SOFC III*, S. C. Singhal and H. Iwahara, Editors, **PV 93-4**, The Electrochemical Society Proceedings Series, Pennington, NJ. 484 (1993)

[26] R. J. Aaberg, R. Tunold, R. Ødegård and S. Tjelle, in *SOFC V*, U. Stimming, S. C. Singhal, H. Tagawa and W. Lehnert, Editors. **PV 97-40**, The Electrochemical Society Proceedings Series, Pennington, NJ. 557 (1997)

[27] P. Holtappels, L. G. J. de Haart and U. Stimming, *J. Electrochem. Soc*. **146** 1620 (1999)
[28] P. Holtappels, I. C. Vinke, L. G. J. de Haart and U. Stimming, *J. Electrochem. Soc.* accepted (1999)
[29] C. Bagger, in *1992 Fuel Cell Seminar*, Courtesy Associates, INC., Washington DC. 241 (1992)
[30] R. Männer, E. Ivers-Tiffée and W. Wersing, in *SOFC II*, F. Grosz, P. Zegers, S.C. Singhal and O. Yamamoto, Editors. Commission of the European Communities, Luxemburg, L. EUR-13564-EN. 715 (1991)
[31] H. Uchida, M. Yoshida and M. Watanabe, *J. Phys. Chem.* **99** 3282 (1995)
[32] F. T. Ciacchi, K. M. Crane and S. P. S. Badwal, *Solid State Ionics*, **73** 49 (1994)
[33] S. P. S. Badwal, *Solid State Ionics,* **52** 23 (1992)
[34] J.-H. Park and R. N. Blumenthal, *J. Electrochem. Soc.* **136** 2867 (1989)
[35] C. A. J. Fisher and H. Matsubara, *Solid State Ionics*, **113-115** 311 (1998)
[36] N. Nicoloso, R. I. Merino, H. Yugami and J. Maier, in *Ceramic Membranes I*, H. U. Anderson, A. C. Khandkar and M. Liu, Editors. PV 95-24, Electrochemical Society Proceedings Series, Pennington, NJ. 106 (1995)
[37] S-L. Hwang and I-W. Chen, *J. Am. Ceram. Soc*. **73** 3269 (1990)
[38] A. E. Hughes, *J. Am. Ceram. Soc*. **78** 369 (1995)
[39] H. D. Wiemhöfer, *Brit. Ceram. Proc*. **56** 1 (1996)
[40] G. S. A. M. Theunissen, A. J. A. Winnubst and A. J. Burggraaf, *J. Mater. Sci*. **27** 5057 (1992)
[41] A. E. Hughes and S. P. S. Badwal, *Solid State Ionics,* **46** 265 (1991)
[42] S. Linderoth and A. Kuzjukevics, in *SOFC V,* U. Stimming, S. C. Singhal, H. Tagawa and W. Lehnert, Editors. **PV 97-40**, The Electrochemical Society Proceedings Series, Pennington, NJ. 1076 (1997)
[43] A. Kuzjukevics, S. Linderoth and J. Grabis, in *High Temperature Electrochemistry: Ceramics and Metals*. F. W. Poulsen, N. Bonanos, S. Linderoth, M. Mogensen and B. Zachau-Christiansen, Editors, 17th Risø International Symposium on Materials Science, Roskilde, DK. 319 (1996)
[44] Y. M. Park and G. M. Choi, *J. Electrochem. Soc*. **146** 883 (1999)
[45] Y. M. Park and G. M. Choi, *Solid State Ionics*, **120** 265 (1999)
[46] C. Wagner, *Ber. Bunseng*. **72** 778 (1968)
[47] N. Sakai, K. Yamaji, T. Horita, H. Yokokawa, Y. Hirata, S. Sameshima, Y. Nigara and J. Mizusaki, SSPC-9, Bled, Slovenia, August 1998, to be published in *Solid State Ionics*
[48] R. Hartung and H.-H. Möbius, *Chemie-Ing. Techn*., **40** 592 (1968)
[49] N. Bonanos, Risø National Laboratory, private communications (1999)
[50] R. J. Aaberg, R. Tunold, M. Mogensen, R. W. Berg and R. Ødegård, *J. Electrochem. Soc.* **145** 2244 (1997)
[51] M. Brown, S. Primdahl and M. Mogensen, *J. Electrochem. Soc*. submitted (1999), chapter 6 in this thesis
[52] A. Gubner, H. Landes, J. Metzger, H. Seeg and R. Stübner, in *SOFC V*, U. Stimming, S. C. Singhal, H. Tagawa and W. Lehnert, Editors. **PV 97-40**, The Electrochemical Society Proceedings Series, Pennington, NJ. 844 (1997)
[53] M. Mogensen and B. Kindl, US Patent 5,350,641
[54] L. Bay and T. Jacobsen, *Solid State Ionics* **93** 201 (1997)
[55] L. Bay, *Electrode Kinetics in High Temperature Fuel Cells*, Thesis, Technical University of Denmark (1998)
[56] L. D. Burke, H. Rickert and R. Steiner, *Z. Phys. Chem. NF,* **74** 146 (1971)
[57] D. Monceau, M. Filal, M. Tebtoub, C. Petot and G. Petot-Ervas, *Solid State Ionics,* **73** 221 (1994)
[58] P. V. Hendriksen and S. Primdahl, IEA workshop, January 1999, Wadahl, N. in press
[59] J. Winkler, P. V. Hendriksen, N. Bonanos and M. Mogensen, *J. Electrochem. Soc.* **145** 1184 (1998)
[60] M. Nagata, Y. Itoh and H. Iwahara, *Solid State Ionics*, **67** 215 (1994)
[61] S. Primdahl and P. V. Hendriksen, in *High Temperature Electrochemistry: Ceramics and Metals*. F. W. Poulsen, N. Bonanos, S. Linderoth, M. Mogensen and B. Zachau-Christiansen, Editors. 17th Risø International Symposium on Materials Science, Roskilde, DK. 403 (1996), chapter 2 in this thesis
[62] G. Hsieh, S. J. Ford, T. O. Mason and L. R. Pederson, *Solid State Ionics*, **91** 191 (1996)
[63] G. Hsieh, T. O. Mason and L. R. Pederson, *Solid State Ionics*, **91** 203 (1996)

[64] S. de Souza, S. J. Visco and L. C. De Jonghe, *J. Electrochem. Soc*. **144** L35 (1997)
[65] S. Primdahl and M. Mogensen, *J. Electrochem. Soc.* in press (1999), chapter 5 in this thesis
[66] N. Wagner, W. Schnurnberger, B. Müller and M. Lang, *Electrochimica Acta*, **43** 3785 (1998)
[67] M. Nagata and H. Iwahara, *J. Appl. Electrochem*. **23** 275 (1993)
[68] T. Kawada, B. A. van Hassel, T. Horita, N. Sakai, H. Yokokawa and M. Dokiya, *Solid State Ionics,* **70/71** 65 (1994)
[69] M. Nagata and H. Iwahara, in *Science and Technology of Zirconia V*, S. P. S. Badwal, M. J. Bannister and R. H. J. Hannink, Editors. Technomic Publishing Co, Inc, Basel, CH. 829 (1993)
[70] S. Primdahl and M. Mogensen, *J Electrochem. Soc.* **145** 2431 (1998), chapter 4 in this thesis
[71] S. Primdahl and M. Mogensen, in *SOFC V*, U. Stimming, S. C. Singhal, H. Tagawa and W. Lehnert, Editors, **PV 97-40**, The Electrochemical Society Proceedings Series, Pennington, NJ. 530 (1997)
[72] T. Jacobsen, *Undersøgelser over højtemperaturbrændselsceller*, thesis (in danish), Technical University of Denmark, Lyngby, DK. (1970)
[73] K.-Z. Fung and A. V. Virkar, in *SOFC IV*, M. Dokiya, O. Yamamoto, H. Tagawa and S. C. Singhal, Editors, **PV 95-1**, The Electrochemical Society Proceedings Series, Pennington, NJ. 1105 (1995)
[74] P. Costamagna, P. Costa and V. Antonucci, *Electrochimica Acta*, **43** 375 (1998)
[75] J.-W. Kim, A. V. Virkar, K.-Z. Fung, K. Metha and S. C. Singhal, *J. Electrochem. Soc*. **146** 69 (1999)
[76] S. Primdahl, M. J. Jørgensen, C. Bagger and B. Kindl, in *SOFC VI*, accepted (1999)
[77] S. Primdahl and M. Mogensen, *J. Electrochem. Soc.* **144** 3409 (1997), chapter 3 in this thesis
[78] S. Primdahl and M. Mogensen, in *SOFC VI*, accepted (1999), chapter 8 in this thesis
[79] L. Dessemond, J. Guindet, A. Hammou and M. Kleitz, in *SOFC II*, F. Grosz, P. Zegers, S. C. Singhal and O. Yamamoto, Editors, EUR–13564-EN. 409 (1991)
[80] M. Kleitz, L. Dessemond and M. C. Steil, in *SOFC Materials, Process Engineering and Electrochemistry*, ISBN 3-89336-127-8. 147 (1993)
[81] M. Kleitz, L. Dessemond and M. C. Steil, *Solid State Ionics*, **75** 107 (1995)
[82] J. Fleig and J. Maier, *SOFC V*, U. Stimming, S. C. Singhal, H. Tagawa and W. Lehnert, Editors. **PV 97-40**, The Electrochemical Society Proceedings Series, Pennington, NJ. 1374 (1997)
[83] J. Fleig and J. Maier, *Solid State Ionics* **85** 17 (1996)
[84] F. van Heuveln, *Characterisation of porous cathodes for application in solid oxide fuel cells*, Thesis, University of Twente, Holland (1997)
[85] M. Kleitz, *Réactions d'électrode dans les oxydes électrolytes solides,* Thesis (in French), L'Institut National Polytechnique de Grenoble (1968)
[86] E. J. L. Schouler and H. S. Isaacs, *Solid State Ionics*, **5** 555 (1981)
[87] P. Vernoux, *Reformage Interne Progressif du Methane dans les Piles a Combustible a Oxyde Electrolyte Solide*, Thesis (in French), L'Institut National Polytechnique de Grenoble (1998)
[88] M. Mogensen, S. Primdahl, J. T. Rheinländer, S. Gormsen, S. Linderoth and M. Brown, in *SOFC IV*, M. Dokiya, O. Yamamoto, H. Tagawa and S. C. Singhal, Editors, **PV 95-1**, The Electrochemical Society Proceedings Series, Pennington, NJ. 657 (1995)
[89] S. Primdahl and M. Mogensen, *J. Appl. Electrochem*. submitted (1999), chapter 9 in this thesis
[90] J. Geyer, H. Kohlmüller, H. Landes and R. Stübner in *SOFC V,* U. Stimming, S. C. Singhal, H. Tagawa and W. Lehnert, Editors. **PV 97-40,** The Electrochemical Society Proceedings Series, Pennington, NJ. 585 (1997)
[91] D. W. Dees, U. Balachandran, S. E. Dorris, J. J. Heiberger, C. C. McPheeters and J. J. Picciolo, in *SOFC I*, S. C. Singhal, Editor, **PV 89-11,** The Electrochemical Society Proceedings Series, Pennington, NJ. 317 (1989)
[92] J. Van herle, R. Ihringer and A. J. McEvoy, in *SOFC V*, U. Stimming, S.C. Singhal, H. Tagawa and W. Lehnert, Editors, **PV 97-40**, The Electrochemical Society Proceedings Series, Pennington, NJ. 565 (1997)
[93] C.-H. Lee, C.-H. Lee, H.-Y. Lee and S. M. Oh, *Solid State Ionics*, **98** 39 (1997)
[94] N. Nakagawa, K. Nakajima, M. Satop and K. Kato, *J. Electrochem. Soc*. **146** 1290 (1999)
[95] B. de Boer, *SOFC anode, Hydrogen oxidation at porous nickel and nickel/yttria-stabilised zirconia cermet electrodes*, Thesis, University of Twente, Holland (1998)

[96] N. Nakagawa, H. Sakurai, K. Kondo, T. Morimoto, K. Hatanaka and K. Kato, *J. Electrochem. Soc.* **142** 3474 (1995)
[97] T. Norby, O.J. Velle, H. Leth-Olsen and R. Tunold, in *SOFC III*, S.C. Singhal and H. Iwahara, Editors, **PV 93-4,** The Electrochemical Society Proceedings Series, Pennington, NJ. 473 (1993)
[98] P. A. Osborg and T. Norby, in *7th SOFC WORKSHOP, Theory and measurement of Microscale Processes in Solid Oxide Fuel Cells*. 47 (1995). IEA report obtainable from H. Nabielek, KFA-ISR Forschungs Zentrum Jülich GmbH, D-52425 Jülich, Germany.
[99] R. J. Aaberg, *Morphology and electrochemistry of metal/yttria stabilized zirconia electrodes in H_2-H_2O atmospheres*, Thesis, Institutt for teknisk elektrokjemi, Noregs teknisk-naturvitskaplege universitet, Trondheim (1998)
[100] F. Z. Mohamedi-Boulenouar, J. Guindet and A. Hammou, in *SOFC V*, U. Stimming, S. C. Singhal, H. Tagawa and W. Lehnert, Editors, **PV 97-40**, The Electrochemical Society Proceedings Series, Pennington, NJ. 441 (1997)
[101] F. Z. Boulenouar, *Etude de l'oxydation Anodique de l'Hydrogène à l'Interface Métal/Zircone Stabilisée à haute température (Métal=Platine, Nickel, Cuivre)*, Thesis, l'Institut National Polytechnique de Grenoble (1995)
[102] T. Kawada, N. Sakai, H. Yokokawa, M. Dokiya, M. Mori and T. Iwata, *J. Electrochem. Soc*. **137** 3042 (1990)
[103] S. Primdahl, B. F. Sørensen and M. Mogensen, *J. Am. Ceram. Soc.* submitted (1998), chapter 7 in this thesis
[104] E. Schouler and M. Kleitz, *J. Electrochem. Soc.* **134** 1045 (1987)
[105] J. R. Macdonald, *Impedance Spectroscopy*, John Wiley & Sons, Inc., New York. 87 (1987)
[106] S. Sunde, *Electrochimica Acta* **42** 2637 (1997)
[107] T. Kawada, N. Sakai, H. Yokokawa, M. Dokiya, M. Mori and T. Iwata, *Solid State Ionics*, **40/41** 402 (1990)
[108] E. M. Skou and T. Jacobsen, *Appl. Phys. A,* **49** 117 (1989)
[109] S. Sakamoto, H. Taira and H. Takagi, *Denki Kagaku*, **64** 609 (1996)
[110] M. Brown, S. Primdahl, M. Mogensen and N. Sammes, *J. Aust. Ceram. Soc*., **34** 248 (1998)
[111] S. Sunde, *J. Electrochem. Soc*. **143** 1930 (1996)
[112] J. Mizusaki, H. Tagawa, T. Saito, K. Kamitani, T. Yamamura, K. Hirano, S. Ehara, T. Takagi, T. Hikita, M. Ippommatsu, S. Nakagawa and K. Hashimoto, *J. Electrochem. Soc.* **141** 2129 (1994)
[113] J. Mizusaki, H. Tagawa, T. Saito, K. Kamitani, T. Yamamura, K. Hirano, S. Ehara, T. Takagi, T. Hikita, M. Ippommatsu, S. Nakagawa and K. Hashimoto, in *SOFC III*, S.C. Singhal and H. Iwahara, Editors, **PV 93-4,** The Electrochemical Society Proceedings Series, Pennington, NJ. 533 (1993)
[114] T. Yamamura, H. Yoshitake, H. Tagawa, N. Mori, K. Hirano, J. Mizusaki, S. Ehara, T. Tagaki, M. Hishinuma, H.Sasaki, Y. Nakamura and K. Hashimoto, in *Second European SOFC Forum*, B. Thorstensen, Editor. European SOFC Forum, Oberrohrdorf, CH. 617 (1996)
[115] F.P.F. van Berkel, F.H. van Heuveln and J.P.P. Huijsmans *Solid State Ionics*, **72** 240 (1994)
[116] J. Divisek, R. Wilkenhöner and Y. Volfkovich, *J. Appl. Electrochem*. **29** 153 (1999)
[117] N. L. Robertson and J. N. Michaels, *J. Electrochem. Soc.* **138** 1494 (1991)
[118] M. Kleitz, T. Kloidt and L. Dessemond, in *High Temperature Electrochemical Behaviour of Fast Ion and Mixed Conductors,* F.W. Poulsen, J.J. Bentzen, T. Jacobsen, E. Skou and M.J.L. Østergård, Editors, 14th Risø International Symposium on Materials Science, Roskilde, DK. 89 (1993)
[119] J. Mizusaki, T. Yamamura, N. Mori, H. Tagawa, K. Hirano, S. Ehara, T. Tagaki, M. Hishinuma, H.Sasaki, T. Sogi, Y. Nakamura and K. Hashimoto, in *High Temperature Electrochemistry: Ceramics and Metals*. F. W. Poulsen, N. Bonanos, S. Linderoth, M. Mogensen and B. Zachau-Christiansen, Editors. 17th Risø International Symposium on Materials Science, Roskilde, DK. 363 (1996)
[120] T. Yamamura, H. Tagawa, T. Saito, J. Mizusaki, K. Kamitani, K. Hirano, S. Ehara, T. Takagi, Y. Hishinuma, H. Sasaki, T. Sogi, Y. Nakamura and K. Hashimoto, in *SOFC IV*, M. Dokiya, O.

Yamamoto, H. Tagawa and S. C. Singhal, Editors, **PV 95-1**, The Electrochemical Society Proceedings Series, Pennington, NJ. 741 (1995)
[121] H. Matsumoto, K. Takeuchi and H. Iwahara, *J. Electrochem. Soc*. **146** 1486 (1999)
[122] H. Kronmüller, in *Hydrogen in Metals I, Basic Properties*. G. Alefeld and J. Völkl, Editors, Springer-Verlag, New York. 304 (1978)
[123] T. N. Troung, G. Hancock and D. G. Truhlar, *Surf. Sci.* **214** 523 (1989)
[124] T. Norby and P. Kofstad, In *High Temperature Electrochemistry: Ceramics and Metals*. F.W. Poulsen, N. Bonanos, S. Linderoth, M. Mogensen and B. Zachau-Christiansen, Editors, 17th Risø International Symposium on Materials Science, Roskilde, DK. 381 (1996)
[125] I. Alstrup, J. R. Rostrup-Nielsen and S. Røen, *Appl. Catal.* **1** 303 (1981)
[126] G. W. Bridger, *3rd Symposium on Catalysis of the Catalyst Society of India*, Dehra Dun, India (1977), quoted in M.V. Twigg, *Catalyst Handbook, 2nd Ed*., Manson Publishing, Ltd., London. 196 (1996)
[127] B. G. Ong, T. A. Lin and D. M. Mason, in *Electrode Mater. Processes Energy Conversion and Storage*, **PV 87-12**, The Electrochemical Society Proceedings Series, Pennington, NJ. 295 (1987)
[128] N. Minh, A. Anumakonda, B. Chung, R. Doshi, J. Ferrall, G. Lear, K. Montgomery, E. Ong, L. Schipper and J. Yamanis, in *1998 Fuel Cell Seminar*, Fuel Cell Seminar Organizing Committee, Palm Springs, CA. 262 (1998)
[129] M. A. Petrik, C. E. Milliken, R. C. Ruhl and B. P. Lee, in *1998 Fuel Cell Seminar*, Courtesy Associates, Inc., Washington DC. 124 (1998)
[130] T. Setoguchi, T. Inoue, H. Takebe, K. Eguchi, K. Morinaga and H. Arai, *Solid State Ionics*, **37** 217 (1990)
[131] T. Inoue, K. Eguchi, T. Setoguchi and H. Arai, *Solid State Ionics*, 40/41 407 (1990)
[132] K. Eguchi, T. Setoguchi, M. Sawano, S. Tamura and H. Arai, in *SOFC II*, F. Grosz, P. Zegers, S. C. Singhal and O. Yamamoto, Editors, EUR-13564-EN. 603 (1991)
[133] T. Setoguchi, K. Okamoto, K. Eguchi and H. Arai, *J. Electrochem. Soc.* **139** 2875 (1992)
[134] H. H. Eysel, Extended abstract No. 36, The Electrochemical Society Meeting, Atlantic city (1970), quoted in E. J. L. Schouler and H. S. Isaacs, *Solid State Ionics*, **5** 555 (1981)
[135] M. Nagata, T. Esaka, H. Iwahara, *Denki Kagaku* **60** 792 (1992)
[136] M. Suzuki, H. Sasaki, S. Otoshi and M. Ippommatsu, in *SOFC II*, F. Grosz, P. Zegers, S. C. Singhal and O. Yamamoto, Editors, EUR 13564-EN. 585 (1991)
[137] M. Suzuki, H. Sasaki, S. Otoshi, A. Kajimura and M. Ippommatsu, *Solid State Ionics*, **62** 125 (1993)
[138] H. Sasaki, S. Otoshi, M. Suzuki, T. Sogi, A. Kajimura, N. Sugiura and M. Ippommatsu, *Solid State Ionics*, **72** 253 (1994)
[139] M. Watanabe, H. Uchida, M. Shibata, N. Mochizuki and K. Amikura, *J. Electrochem. Soc.* **141** 2 (1994)
[140] L. S. Wang and S. A. Barnett, *Solid State Ionics*, **61** 273 (1993)
[141] S. Wang, Y. Jiang, Y. Zhang, W. Li, J. Yan, and Z. Lu, *Solid State Ionics*, **120** 75 (1999)
[142] H. Miyamoto, M.Sumi, K. Mori, I. Koshiro, F. Nanjo and M. Funatsu, in *SOFC III*, S.C. Singhal and H. Iwahara, Editors, **PV 93-4,** The Electrochemical Society Proceedings Series, Pennington, NJ. 504 (1993)
[143] T. Norby, in *Second European SOFC Forum*, B. Thorstensen, Editor. European SOFC Forum, Oberrohrdorf, CH. 607 (1996)
[144] M. Levy, J. Fouletier and M. Kleitz, *J. Electrochem. Soc*. **135** 1584 (1988)
[145] J. Janek and C. Korte, *Solid State Ionics*, **116** 181 (1999)
[146] K. Okomura, Y. Yamamoto, T. Fukui, S. Hanyu, Y. Kubo, Y. Esaki, M. Hattori, A. Kusunoki and S. Takeuchi, in *SOFC III,* S.C. Singhal and H. Iwahara, Editors, **PV 93-4,** The Electrochemical Society Proceedings Series, Pennington, NJ. 444 (1993)
[147] S. Kawasaki, JP 5-190183 (in japanese) (1992)
[148] S. Primdahl, M. J. Jørgensen, C. Bagger, M. Mogensen and O. Marina, Patent pending (1998)
[149] A. Tsoga, P. Nikolopoulos, A. Kontogeorgakos, F. Tietz and A. Naoumidis, in *SOFC V,* U. Stimming, S. C. Singhal, H. Tagawa and W. Lehnert, Editors. **PV 97-40**, The Electrochemical Society Proceedings Series, Pennington, NJ. 823 (1997)

[150] M. T. Colomer, J. R. Jurado, R. M. C. Marques and F. M. B. Marques, in *SOFC III*, S.C. Singhal and H. Iwahara, Editors, **PV 93-4,** The Electrochemical Society Proceedings Series, Pennington, NJ. 523 (1993)
[151] W. L. Worrell, P. Han, Y. Uchimoto and P. K. Davies, in *SOFC IV*, M. Dokiya, O. Yamamoto, H. Tagawa and S. C. Singhal, Editors, **PV 95-1**, The Electrochemical Society Proceedings Series, Pennington, NJ. 50 (1995)
[152] R. M. C. Marques, J. R. Frade and F. M. B. Marques, in *SOFC III*, S.C. Singhal and H. Iwahara, Editors, **PV 93-4,** The Electrochemical Society Proceedings Series, Pennington, NJ. 513 (1993)
[153] S. S. Liou and W. L. Worrell, in *SOFC I*, S. C. Singhal, Editor. **PV 89-11**, The Electrochemical Society Proceedings Series, Pennington, NJ. 81 (1989)
[154] T. Lindegaard, C. Clausen and M. Mogensen, in *High Temperature Electrochemical Behaviour of Fast Ion and Mixed Conductors,* F.W. Poulsen, J.J. Bentzen, T. Jacobsen, E. Skou and M.J.L. Østergård, Editors, 14th Risø International Symposium on Materials Science, Roskilde, DK. 311 (1993)
[155] M. T. Colomer, and J. R. Jurado, *J. Eur. Ceram. Soc*. **19** 143 (1999)
[156] H. Taimatsu, K. Kudo and H. Kaneko, in *SOFC IV*, M. Dokiya, O. Yamamoto, H. Tagawa and S. C. Singhal, Editors, **PV 95-1**, The Electrochemical Society Proceedings Series, Pennington, NJ. 706 (1995)
[157] M. M. Murphy, J. Van herle, A. J. McEvoy and K. R. Thampi, *J. Electrochem. Soc*. **141** L94 (1994)
[158] Y. C. Wu, and J. G. Duh, *J. Mat. Sci. Let*. **9** 583 (1990)
[159] in CRC Handbook of Chemistry and Physics, 75th Ed., D. R. Lide, Editor. CRC Press Inc., Boca Raton, FL, 4-78 (1994)
[160] W. Huebner, H. U. Anderson, D. M. Reed, S. R. Sehlin and X. Deng, in *SOFC IV*, M. Dokiya, O. Yamamoto, H. Tagawa and S. C. Singhal, Editors, **PV 95-1**, The Electrochemical Society Proceedings Series, Pennington, NJ. 696 (1995)
[161] T. Fukui, S. Ohara and K. Mukai, *Electrochem. and Solid-State Let.* **1** 120 (1998)
[162] R. Wilkenhöner, R. Vassen, H. P. Buchkremer and D. Stöver, *J. Mat. Sci*. **34** 257 (1999)
[163] R. J. Aaberg, R. Tunold, F. W. Poulsen and N. Bonanos, in *Second European SOFC Forum*, B. Thorstensen, Editor. European SOFC Forum, Oberrohrdorf, CH. 607 (1996)
[164] P. H. Middleton, M. E. Seiersten and B. C. H. Steele, in *SOFC I*, S. C. Singhal, Editor. **PV 89-11**, The Electrochemical Society Proceedings Series, Pennington, NJ. 90 (1989)
[165] A. Tsoga, A. Naoumidis and P. Nikolopoulos, *Acta Mater*. **44** 3679 (1996)
[166] P. Nikolopoulos and D. Sotiropoulou, *J. of Mat. Sci. Let*. **6** 1429 (1996)
[167] W. D. Kingery, in *Metal-Ceramics Interactions IV*, 42 (1954)
[168] A. Tsoga, P. Nikolopoulos and A. Naoumidis, in *High Temperature Electrochemistry: Ceramics and Metals*. F. W. Poulsen, N. Bonanos, S. Linderoth, M. Mogensen and B. Zachau-Christiansen, Editors, 17th Risø International Symposium on Materials Science, Roskilde, DK. 443 (1996)
[169] J. G. Duh, and W. S. Chien, *J. Mat. Sci*. **25** 1529 (1990)
[170] E. C. Dickey, V. P. Dravid, P. D. Nellister, D. J. Wallis and S. J. Pennycook, *Acta Mater*. **46** 1801 (1998)
[171] K. R. Thampi, A. J. McEvoy and J. Van herle, in *Ionic and Mixed Conducting Ceramics II*, T. A. Ramanarayanan, W. L. Worrell, and H. L. Tuller, Editors, **PV 94-12**, The Electrochemical Society Proceedings Series, Pennington, NJ. 238 (1994)
[172] M. Mori, T. Yamamoto, H. Itoh, H. Inaba and H. Tagawa, *J. Electrochem. Soc.* **145** 1374 (1998)
[173] E. H. Kerner, *Proc. Phys. Soc. London, Ser. B*, **69** 808 (1956)
[174] S. Majumdar, T. Claar and B. Fladermeyer, *J. Am. Ceram. Soc*. **69** 628 (1986)
[175] B. F. Sørensen and S. Primdahl, *J. Mat. Sci.* **33** 5291 (1998)
[176] M.J. Powell, *Phys. Rev. B*, **20** 10 (1979)
[177] S. Sunde, *J. Electrochem. Soc*. 143 1123 (1996)
[178] T. Kawashima and M. Hishinuma, *Mat. Trans*. **37** 1397 (1996)
[179] M. Juhl, S. Primdahl, C. Manon and M. Mogensen, *J. Power Sources* **61** 173 (1996)

[180] C. Iwasawa, M. Nagata, S. Yamaoka, Y. Seino and M. Ono, in *SOFC IV,* M. Dokiya, O. Yamamoto, H. Tagawa and S. C. Singhal, Editors, **PV 95-1**, The Electrochemical Society Proceedings Series, Pennington, NJ. 686 (1995)
[181] L. Kindermann, F. W. Poulsen and C. Bagger, in *Third European SOFC Forum, Posters*, P. Stevens, Editor. European SOFC Forum, Oberrohrdorf, CH. 133 (1998)
[182] K. Nisancioglu, in *Natural Gas Fuelled Solid Oxide Fuel Cells & Systems*, IEA Task Report, Office Federal De L'Energie, Berne, CH. 87 (1989)
[183] J. P. P. Huijsmans, E. J. Siewers and S. B. van der Molen, in *1990 Fuel Cell Seminar*, Courtesy Associates, Inc., Washington DC. 512 (1990)
[184] S. T. Aruna, M. Muthuraman and K. C. Patil, *Solid State Ionics*, **111** 45 (1998)
[185] U. Anselmi-Tamburini, G. Chiodelli, M. Arimondi, F. Maglia, G. Spinolo and Z. A. Munir, *Solid State Ionics*, **110** 35 (1998)
[186] P. Costamagna, P. Costa and E. Arato, *Electrochimica Acta*, **43** 967 (1998)
[187] C. Bagger, Danish ½ kW SOFC stack 1996, private communications, (1999)
[188] H. P. Buchkremer, U. Diekmann, L. G. J. de Haart, H. Kabs, U. Stimming and D. Stöver, in *SOFC V*, U. Stimming, S.C. Singhal, H. Tagawa and W. Lehnert, Editors, **PV 97-40**, The Electrochemical Society Proceedings Series, Pennington, NJ. 160 (1997)
[189] T. Kawashima and Y. Matsuzaki, *J. Ceram. Soc. Japan*, **104** 317 (1996)
[190] S. Murakami, Y. Akiyama, N. Ishida, T. Yasuo, T. Saito and N. Furukawa, in *SOFC II,* F. Grosz, P. Zegers, S. C. Singhal and O. Yamamoto, Editors, EUR-13564-EN. 105 (1991)
[191] T. Matsushima, H. Ohrui and T.Hirai, *Solid State Ionics*, **111** 315 (1998)
[192] H. Itoh, T. Yamamoto, M. Mori, T. Horita, N. Sakai, H. Yokokawa and M. Dokiya*, J. Electrochem. Soc.* **144** 641 (1997)
[193] H. Itoh, T. Yamamoto, M. Mori, T. Watanabe and T. Abe, *Denki Kagaku*, **64** 549 (1996)
[194] H. Itoh, T. Yamamoto, M. Mori and T. Abe, in *SOFC IV,* M. Dokiya, O. Yamamoto, H. Tagawa and S. C. Singhal, Editors, **PV 95-1**, The Electrochemical Society Proceedings Series, Pennington, NJ. 639 (1997)
[195] O. Marina, S. Primdahl, C. Bagger and M. Mogensen, in *SOFC V*, U. Stimming, S.C. Singhal, H. Tagawa and W. Lehnert, Editors, **PV 97-40**, The Electrochemical Society Proceedings Series, Pennington, NJ. 540 (1997)
[196] S. C. Singhal, in *High Temperature Electrochemistry: Ceramics and Metals*. F. W. Poulsen, N. Bonanos, S. Linderoth, M. Mogensen and B. Zachau-Christiansen, Editors, 17th Risø International Symposium on Materials Science, Roskilde, DK. 123 (1996)
[197] W. Schäfer, H. Geier, G. Lindemann and D. Stolten, in *High Temperature Electrochemical Behaviour of Fast Ion and Mixed Conductors,* F. W. Poulsen, J. J. Bentzen, T. Jacobsen, E. Skou and M. J. L. Østergård, Editors, 14th Risø International Symposium on Materials Science, Roskilde, DK. 409 (1993)
[198] S. Elangovan and A. Khandkar, in *1st International Symposium on Ionic and Mixed Conductors*, T. A. Ramanarayanan and H. L. Tuller, Editors. **PV 91-12**, The Electrochemical Society Proceedings Series, Pennington, NJ. 122 (1991)
[199] T. Iwata, *J. Electrochem. Soc*. **143** 1521 (1996)
[200] M.J. Jørgensen, P. Holtappels and C. C. Apple, *J. Appl. Electrochem.* submitted (1999)
[201] A. C. Khandkar, S. Elangovan, M. Liu and M. Timper, in *High Temperature Electrode Materials and Characterization*, D. D. Macdonald and A. C. Khandkar, Editors. **PV 91-6,** The Electrochemical Society Proceedings Series, Pennington, NJ. 175 (1991)
[202] M. Cassidy, G. Lindsay and K. Kendall, *J. Power Sources*, **61** 189 (1996)
[203] I. Drescher, W. Lehnert and J. Meusinger, *Electrochimica Acta* **43** 3059 (1998)

Chapter 11

Evaluation and Recommendations

Abstract

In this chapter the results established in the present thesis are briefly reviewed with reference to the respective chapters. The derived scientific and technological information is briefly discussed. Recommendations for further work is given based on the findings and a literature review.

11.1 Evaluation of Thesis Results

11.1.1 Interpretation of Impedance Spectra

The impedance spectra of Ni/YSZ cermet anodes at 800 to 1000°C in hydrogen/water atmospheres have been characterized, Figure 11.1, and the three distinct arcs have been described by varying primary parameters such as temperature and gas composition (Chapter 3). Experimentally this was done in a setup providing two separate atmospheres for the working electrode and for the counter and reference electrodes. It was observed that the capacitance related to the low frequency arc I was too high to be ascribed to interface layers, adsorbed layers or absorbed species in the electrode structure.

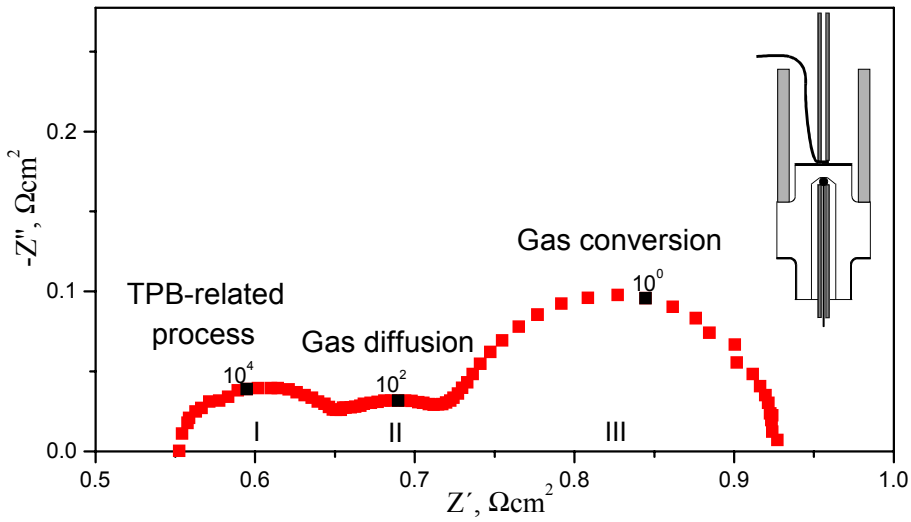

Figure 11.1 Impedance spectrum for a Ni/YSZ cermet anode at 1000°C in hydrogen with 3% water at open circuit potential. Three arcs are distinct and the respective processes are indicated. The test setup involves two separate atmospheres for working electrode and for reference and counter electrode.

By applying another setup where all three electrodes are exposed to the same atmosphere, the low frequency arc I is avoided (Chapter 4). This incontestably demonstrates arc I to be an effect of gas conversion, e.i. the variation of pO_2 in the fuel gas by the applied ac signal, with respect to the stable pO_2 of the reference gas. The quantitative expressions for the real and imaginary part of gas conversion impedance have been derived for a continuously stirred tank reactor (CSTR) volume outside the anode.

By applying current collector structures to the surface of anodes, arc II has been demonstrated to be caused by gas diffusion limitations in the gas outside the porous anode structure (Chapter 5). Simplified calculations based on the capacitance at the summit frequency of the depressed arc and a layer of stagnant gas indicate a homogeneous layer thickness of the order of 1 mm. Similar simple calculations indicate the diffusion limitation in the 50 µm thin anode structure to be negligible.

An "auxiliary" cell test approach was developed (Chapter 5), to effectively avoid the concentration polarizations of gas conversion and gas diffusion outside the porous anode structure. This approach involves placing a second cell with an "auxiliary" cell against the working electrode, using a thin conducting mesh as the joint contact, and passing current through both cells while characterizing only the working electrode, Figure 11.2. Provided the electrode processes are reversible, the working and auxiliary cell electrode will produce and consume equal amounts of gaseous species at any time. The concentration polarization over half the mesh thickness will be negligible. Furthermore the current densities will be homogeneous.

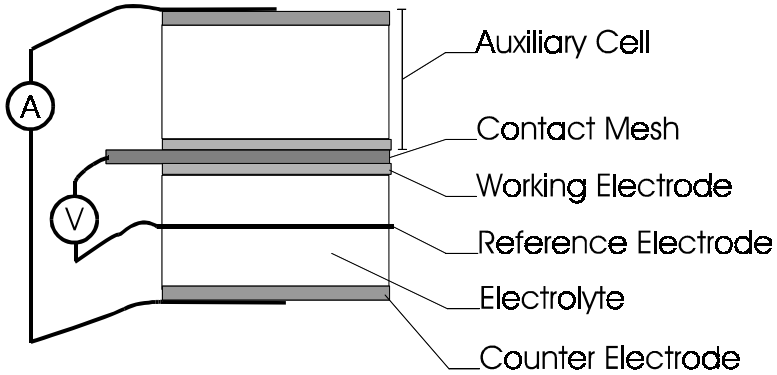

Figure 11.2 An auxiliary cell with an electrode facing the working electrode at a close proximity, supplying and removing gas at a low distance from the working electrode eliminates concentration polarization even at dc conditions for reversible electrode processes.

Having identified these concentration effects, the remaining arc III at high frequency has been demonstrated to depend on the anode microstructure, and thus ascribed to the anode (Chapter 6). In some anode structures this arc is not a simple arc, two arcs may be required for adequate data condensation by impedance fitting (Chapter 9).

The exact nature of the processes behind the anode impedance is not identified, but evidence of the process nature has been obtained (Chapter 8). By H/D isotope studies it is demonstrated how at low temperatures (700-850°C) protons are participating in the rate limiting process. At 1000°C no isotope effect is seen. By addition of H_2S known to chemisorb on Ni, it is illustrated how the Ni-surface is of equal importance to the reaction rate at low and high temperature, and with and without drawing an anodic current. The activation energy of the limiting process has been demonstrated to depend on the structure of the tested anode (Chapter 6).

By reviewing literature on Ni/YSZ cermet anodes and related subjects, two new potential contributions to the anode limitations are suggested (Chapter 10). One is electronic transport in YSZ between unconnected sub-micron Ni-particles or clusters on the YSZ surface and well connected Ni-agglomerates. Another relates to the segregation of an Y_2O_3 rich phase to the surface of YSZ at SOFC operation conditions. It is well known that for YSZ with more than 8-10% Y_2O_3 the oxide ion conductivity decreases with increasing Y_2O_3 content.

11.1.2 Technological aspects

The acquired understanding of the contributions to the impedance spectra has resulted in an "improvement" of the anode performance, as the previously reported 0.3 Ωcm^2 at 1000°C in hydrogen with 3% water for Risø cermet anodes could be corrected to about 0.1 Ωcm^2.

The durability of anodes has been studied over 1300 to 1900 hrs at 850°C, 1000°C and 1050°C at 300 mA/cm^2 in hydrogen with 3% water. At low temperatures degradation rates of about 100 $m\Omega cm^2$/1000 hrs are found, at 1000°C and 1050°C little (10 $m\Omega cm^2$/1000 hrs) or no degradation is observed (Chapter 9). Furthermore thermal cycling from 1000°C to below 100°C indicate an initial loss of 30 $m\Omega cm^2$ over the first two cycles whereafter the performance remains constant over an additional 7 cycles.

The active thickness of these electrodes has been demonstrated to be about 10 μm at 1000°C (Chapter 6). This has significant technological impact, as the electrode function can be split in a cermet structure of only 10 μm, and an overlying current collector structure. This current collector structure need not exhibit ionic conductivity, and the YSZ fraction can be substituted by a cheaper material.

The effect of sintering temperature of these anodes as fabricated from suspended slurries on pre-sintered electrolytes has been investigated and two conflicting properties are identified (Chapter 7).
To obtain adequate percolation in the Ni phase of the cermet structure a sintering temperature of 1250°C or more is required. For sintering temperatures between 1300°C and 1500°C little variation in performance at 1000°C is observed.
At the same time the thermal expansion coefficient (TEC) difference between the electrolyte and the electrodes causes stress in the structure after sintering. As the sintering temperature is increased, the stress generated during cooling increases. At 1250°C and higher sintering temperatures channel cracks emerge in the electrode structure to release the tensile stress. At sintering temperatures below 1300°C delamination between electrode and electrolyte occurs during external stress (bending). At higher sintering temperatures the adhesion between electrode and electrolyte increases, and the channel cracks propagate from the electrode into the electrolyte material and cause fracture at very low external loads.
The balance between need for high sintering temperatures and stress due to the TEC difference leads to 1300°C as the compromise sintering temperature for these anodes.

The identification of Mn as an additive for Ni/YSZ cermet anodes has improved the anode performance by a factor of two. This corresponds to about 30 $m\Omega cm^2$ at 1000°C and about 60 $m\Omega cm^2$ at 850°C in hydrogen with 3% water (Chapter 8).

11.2 Recommendations

The auxiliary cell test design is recommended for electrochemical studies on low-impedance porous electrodes. Symmetrical cells fabricated on thin electrolyte foils are found to be easy and cheap to produce, and are well suited for electrode studies at open circuit potential. For polarized studies the use of thick three-electrode pellets is recommended as the errors induced by the placement of the reference electrode are limited. In practice it is found beneficial to apply both of these geometries in an electrode research strategy.

The application of "point-shaped" electrochemically polished Ni microelectrodes on polished YSZ single crystals is suggested for comparative electrochemical experiments to examine the following points:

- How does Ni incorporation in the electrolyte surface during sintering in air affect performance ?
- Is there an Y_2O_3 rich surface film on YSZ that inflicts on performance, and can it be removed ?
- What is the effect of using YSZ electrolytes with different conductivity (Y_2O_3 content), and could it indicate whether the electrolyte surface is host to limiting anode processes ?

In this context the preparation of the electrolyte surface can be varied as freshly polished, re-sintered after polishing, sintered in air/reducing atmosphere with discrete Ni-particles on the surface, or covered by sub-micron Ni particles applied as decomposed $Ni(NO_3)_2$. A list of other topics for experiment and calculation is suggested in ref 5 of chapter 10.

Spectroscopic methods should be applied to help identify the species on the surface of both Ni and electrolyte in situ.

From a technology point of view, the performance of state-of-the-art Ni/YSZ cermet anodes makes this contribution to stack impedance less important than most other limitations. Important aspects to be addressed for Ni/YSZ are reproducibility, durability and general behavior in high water concentrations (high fuel utilization). The effect of contaminants in different NiO powders is mainly unknown. Important SOFC aspects such as redox stability and performance in methane may have to be addressed for other types of anodes.